Universidade do Minho
Escola de Engenharia

Shafagh Dinparast Tohidi

Development and structure-properties
relationship of polyamide 6 single polymer
composites reinforced by textile structures
and prepared by reactive injection molding

UMinho | 2018

June, 2018

Universidade do Minho
Escola de Engenharia

Shafagh Dinparast Tohidi

Development and structure-properties relationship of polyamide 6 single polymer composites reinforced by textile structures and prepared by reactive injection molding
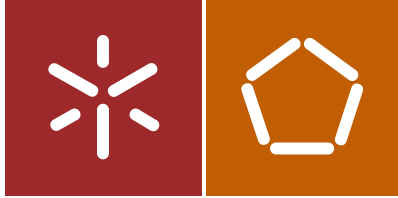
Philosophy Doctorate Thesis
Textile Engineering

Work conducted under supervision of:
Professor Doctor Ana Maria Moreira Ferreira da Rocha
University of Minho, Department of Textile Engineering
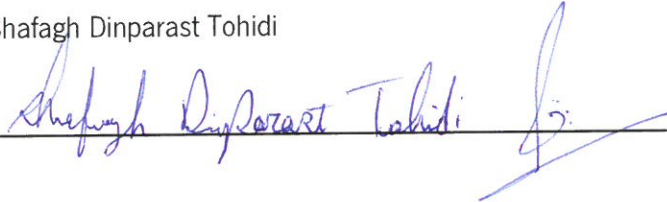Professor Doctor Zlatan Zlatev Denchev

June, 2018

STATEMENT OF INTEGRITY

I hereby declare having conducted my thesis with integrity. I confirm that I have not used plagiarism or any form of falsification of results in the process of the thesis elaboration.

I further declare that I have fully acknowledged the code of Ethical Conduct of the University of Minho.

University of Minho, 20th of June 2018

Full name: Shafagh Dinparast Tohidi

Signature: _____

Acknowledgment

performance computing (supercomputer) to perform finite element analysis of complex real-size composites and their precursors.

It's my fortune to gratefully acknowledge the support of my friends, Andre Ferreira, Mauro Rabuski, Iara Braga, Tatiana Saraiva, Duarte Fernandes, Lazaro Silva, José Amarílio Barbosa, Catarina Araújo and Mohammad Sabet for their support and generous care throughout the research tenure. They were always beside me during the happy and hard moments to push me and motivate me. I would like to extend thanks to my Persian friends and community who have encouraged and helped me during my doctorate program in Portugal.

Last but not the least, I would like to thank the people who mean a lot to me, my parents, Ali Dinparast Tohidi and Fereshteh Hannani for showing faith in me and giving me liberty to choose what I desired. I salute you all for the selfless love, care, pain and sacrifice you did to shape my life. Also, I express my thanks to my brother Shayan Dinparast Tohidi and sister in law, Naghmeh Armaniyeh and my love, Livia Araujo Rosa for supporting me spiritually throughout writing this thesis and my life in general. I would never be able to pay back the love and affection showered upon by my family.

Shafagh Dinparast Tohidi

Guimarães, June 2018

Resumo

Compósitos Laminados de Polímero Único, baseados numa matriz aniónica de poliamida 6 (PA6) e reforçados por estruturas têxteis de PA6 (tricotadas e tecidas), foram preparados com sucesso através de duas técnicas: (i) combinação de revestimento em pó de estruturas têxteis tricotadas em PA6 com micropartículas de PA6 e subsequente consolidação por moldagem por compressão (processo PCCM) ou (ii) moldagem por injeção reativa, incluindo a preparação no molde da matriz PA6, na presença dos mesmos tecidos de malha (processo NYRIM). As micropartículas (MPs) de PA6 para o processo PCCM foram preparadas por polimerização aniónica em suspensão antes da moldagem por compressão.

No processo NYRIM foi aplicado um processo de polimerização aniónica semelhante, mas realizado in situ na massa e diretamente no molde NYRIM, na presença dos reforços têxteis. Dois padrões básicos de malha (Rib1x1 e Jersey) e de estruturas tecidas (Tafetá e Cetim de 5) foram selecionados como reforços. Neste estudo foram utilizados pela primeira vez como reforços, estruturas em tafetá com pesponto, patenteadas pela empresa Jackob Muller AG® e consideradas como uma nova classe de tecidos. Todos os reforços foram tensionados e termofixados antes da moldagem. A influência da arquitetura de reforço, fração volúmica de fibra (variando na gama de 15-25%), orientação de reforço e ordem de sobreposição de camadas, nas propriedades mecânicas dos compósitos (resistência à tração, flexão e impacto Izod) foi avaliada para ambas as técnicas de moldagem.

De uma forma geral, o processo PCCM conduziu a compósitos laminados de polímero único com boas propriedades mecânicas em tensão. A técnica de NYRIM produziu laminados com baixos valores de rigidez e resistência à tração, principalmente devido à formação de oligómeros na presença dos reforços têxteis. Nos compósitos reforçados com tecidos pespontados e preparados pelo processo PCCM, verificou-se uma maior rigidez e resistência à tração até 50% e 63%, respetivamente, quando comparadas com as amostras reforçadas com estruturas de malha e com a matriz. Os compósitos reforçados com tecido demonstraram ser mais dúcteis do que os compósitos reforçados com estruturas de malha devido à elevada tensão na rotura. Todos os compósitos reforçados por malhas apresentaram propriedades de flexão e impacto melhoradas quando comparados com os compósitos reforçados com tecidos e com a matriz pura.

Verificou-se através de microscopia eletrónica e por simulação que o comportamento de todos compósitos na fratura depende da deformação estrutural dos reforços. Os resultados obtidos por microscopia eletrónica e, indiretamente, por estudos de difração de raios X sugeriram a formação de

uma camada transcristalina na interface fibra-matriz nos compósitos produzidos pelos processos NYRIM e PCCM. Neste último caso, esta camada transcristalina é ligeiramente mais espessa. Através de estudos estruturais utilizando métodos térmicos e de difração de raios X foi possível demonstrar a importância do pré-tensionamento e termofixação dos reforços têxteis na consolidação de amostras para ambos os processos. Constatou-se que as propriedades mecânicas dos compósitos laminados de polímero único estudados dependem significativamente da estrutura cristalina da matriz e dos reforços.

Abstract

Single polymer laminate composites (SPCs) based on anionic polyamide 6 (PA6) matrix and reinforced by PA6 knitted and woven textile structures were successfully prepared by two techniques: (i) a combination of powder-coating of PA6 knitted textile structures with PA6 microparticles and subsequent consolidation by compression molding (PCCM process) or (ii) by reactive injection molding including the in-mold preparation of the PA6 matrix, in the presence of the knitted textiles (NYRIM process). The PA6 microparticles (MPs) for PCCM were prepared by anionic polymerization in suspension prior to the compression molding.

In the NYRIM process, a similar anionic polymerization process was applied but carried out in situ in the bulk and directly in the NYRIM mold, in the presence of the textile reinforcements. Two basic knitted patterns (Rib 1×1 and Jersey) and woven architectures (Plain and Satin-5 harness) were selected as reinforcements. Stitched plain structures, a promising novel class of woven fabrics patented by Jackob Muller company AG®, were used for the first time as reinforcements in the present study. All reinforcements were stretched and annealed prior molding. The influence of the reinforcement architecture, fiber volume fraction (varying in the 15-25% range), reinforcement orientation and stacking order, on the mechanical properties of the single polymer composites (tensile, flexural and Izod impact) was evaluated for both molding techniques.

In general, it was found that the PCCM process leads to single polymer laminates with good mechanical properties in tension. On the other hand, the NYRIM technique produced laminates with low stiffness and strength values, the reason being the formation of oligomers in the presence of the textile reinforcements. In the composites reinforced by stitched plain fabrics and prepared by the PCCM process, a higher tensile stiffness and strength up to 50% and 63%, respectively was obtained, when compared to the knitted reinforced ones and the matrix component. Woven reinforced composites were more ductile than the ones reinforced with knitted structures due to the high strain at failure. All knitted reinforced composites showed higher flexural and impact properties when compared to the woven reinforced composites and the neat matrix. Using electron microscopy complemented and by simulation studies it was demonstrated that the fracture behavior of all composites depend on the structural deformation of the reinforcements.

The microscopy results and, indirectly, the X-ray diffraction (XRD) studies suggested the formation of a transcrystalline layer at the fiber-matrix interface in both NYRIM and PCCM composites. This

transcrystalline layer is slightly thicker in the latter case. Structural studies carried out using thermal methods and XRD pointed out to the importance of the stretch-annealing pre-treatment of the textile reinforcements for samples' consolidation in both processes. The mechanical properties of the SPCs were found to depend on the crystalline structure of both matrix and reinforcements.

Table of contents

List of Figures

xvii

xviii

List of Tables

List of abbreviations

AAROP	Activated anionic ring opening polymerization
ABS	Butadiene styrene
CF	Carbon fiber
DSC	Differential scanning calorimetry
DMA	Dynamic mechanical analysis
DTA	Differential thermal analysis
ECL	ε-caprolactam
FTIR	Fourier-transform infrared spectroscopy
FR	Final reside
GF	Glass fiber
T_g	Glass transition temperature
HPA6	Hydrolytic PA6
HDPE	High density polyethylene
IDT	Initial decomposition temperature
iPP	Isotactic polypropylene
J	Jersey reinforcement
KES	Kawabata evaluation system
KSPCs	Knitted reinforced SPCs
LDPE	Low density polyethylene
T_M	Melting temperature
M_W	Molecular weight
MMT	Montmorillonite nanoclays
MPs	Microparticles
NN	Neat plate prepared by NYRIM technique
PN	Neat plate prepared by PCCM technique
IN	Neat plate prepared by injection molding
NYRIM	Nylon resin injection molding
PCCM	Powder coated compression molding
PA6	Polyamide 6
PE	polyethylene
PW	Processing window temperature
PAMC	Producing shell-core PA6microcapsules
PA12	Polyamide 12
PTFE	Polytetra fluoroethylene
PEEK	Polyether ketone
PEMA	Polyethyl methacrylate
PP	Polypropylene
PA	Polyamide
PET	Polyethylene terephthalate
PLA	Poly lactic acid
PA66	Polyamide 66
PMMA	Polymethyl methacrylate
PLM	Polarizing light microscopy
P	Plain reinforcement
MRD	Rate of degradation
RIM	Resin injection molding
R	Rib1×1 reinforcement
SEM	Scanning electron microscope
SPCs	Single polymer composites
SDFs	Stitched diagonal filaments
R-A	Stretched-annealed Rib1×1 reinforcement
J-A	Stretched-annealed Jersey reinforcement

List of Symbols

K, $cm^3/s/cm^2$	Air permeability
A_w, gr/m^2	Area density
T_1, N	Average input tension of filaments
T_2, N	Average output tension of filaments
τ_{f2}, MPa	Adhesive shear force
B_{KES}, $\mu Nm/m$	Bending rigidity of reinforcements based KES
B_{Pierce}, $\mu N.m$	Bending rigidity of reinforcements based Pierce
L_C, mm	Critical length
E^*	Complex compression modulus
χ_c^{DSC}, %	Degree of crystallinity obtained by DSC analysis
χ_c^{WAX}, %	Degree of crystallinity obtained by WAXs analysis
T, mm	Fabric thickness
V_f, %	Fiber volume fraction
τ_{f1}, MPa	Frictional shear force
Q, W/m^2	Heat flux
IF,%	Improvement factor
I_A, KJ/m^2	Impact resistance
d, Å	Interplanar spacing with the respective indexation
$E^{''}$	Loss modulus
σ_1, MPa	Maximal longitudinal stress (strength)
σ_2, MPa	Maximal transversal stress (strength)
ρ, $g.m^{-3}$	Material density
ΔH_m^0, KJ/mol	Melting enthalpy of 100% crystalline material
N	Number of plie
L_0, mm	Original length
ν	Poisson ratio
ν_{Warp}	Poisson ratio in warp direction
ν_{Weft}	Poisson ratio in weft direction
ΔP, $N.m^{-2}$	Pressure drop
ΔH_m^i, KJ/mol	Registered melting enthalpy
C, J/mol.K	Specific heat capacity
σ, MPa	Stress
θ, degrees	scattering angle, WAXS
ε, %	strain
$E^{'}$	Storage modulus
τ_f, MPa	Shear fraction
ε_x, %	Strain at longitudinal direction
ε_y, %	Strain at transversal direction
G, GPa	Shear modulus
E_1, GPa	Young's modulus in longitudinal direction
E_2, GPa	Young's modulus in transverse direction
λ, $W/m \cdot K$	Thermal conductivity

Chapter 1

Introduction

1.1. Composite materials

Nowadays, composite materials are demanded by industries due to their higher strength per weight ratio as well as appropriate thermal and mechanical properties (in extreme environmental conditions) [1,2]. They are substituting conventional material such as metals, wood, and ceramics [3]. The ever-increasing needs for lightweight, strong (alternative to steels and aluminum), highly corrosion resistant, high fatigue life, ease of processing, high productivity and cost reduction boosted the growth of composite materials applications [4,5]. Figure 1.1a illustrates the demand, in tones, for carbon composites by region [6]. North America (particularly USA) takes 38% the lion's share of global carbon composites demand, which is driven by the aerospace and defense sectors. Europe dominates the market with 35 % carbon composites global lion's share benefitted from aerospace, the wind turbine, automotive and mechanical engineering sectors. In total, Asia and the pacific region account for 23% of global demand due to the emerging of the national program to come up with an Indian home-produced airplane company and the commercial aircraft corporation of China (Comac). Respect to the Figure 1.1b aerospace and defense industries appropriate the highest price segment although the average value in automotive construction lies far above the minimum demands.
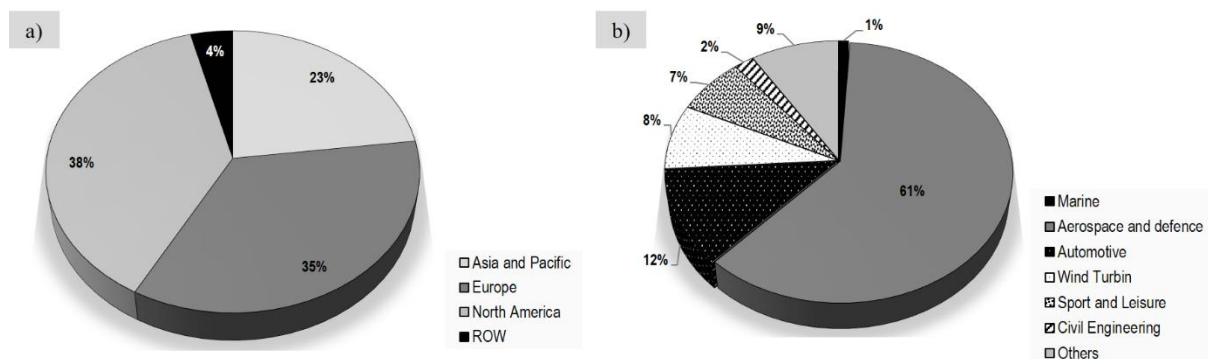
Figure 1.1. a) Carbon composites demand in 1,000 ton according to the regions (2015) [6]; b) Carbon composites demand in 1,000 ton according to the application (2015) [6].

1.2. Matrix component

Conventional composite materials contain two main components such as Matrix, and Reinforcements that are combined at a macroscopic level and are not soluble in each other. The matrix phase enhances to bind the reinforcement phase together and to protect them from the environmental influences. Moreover, they shield the reinforcements from mechanical damages by distributing the applied stresses. The role of the reinforcement component is fundamentally enriching the mechanical properties of the

neat resin system [1,5]. They can be applied in the form of fibers, fabrics, particles, or flakes. Most composite materials are categorized by homogeneous (isotropic), orthotropic (like fibrous composites) and anisotropic. The inhomogeneous body has non-uniform properties over the body in which the properties depend on position in the body [1]. An orthotropic body has material properties that are different in three mutually perpendicular directions at a point in the body and further has three mutually perpendicular planes of material property symmetry. Thus, the properties depend on orientation at a point in the body [1]. The anisotropic materials have material properties that are different in all direction at a point in the body. Depend on orientation at a point in the body of anisotropic material, there are no symmetric planes of material property. Because of the inherently heterogeneous nature of composite materials, they are studied from micromechanics and macromechanics level [1]. The general composite material classification based on the matrix components is illustrated in Figure 1.2 [2,3].
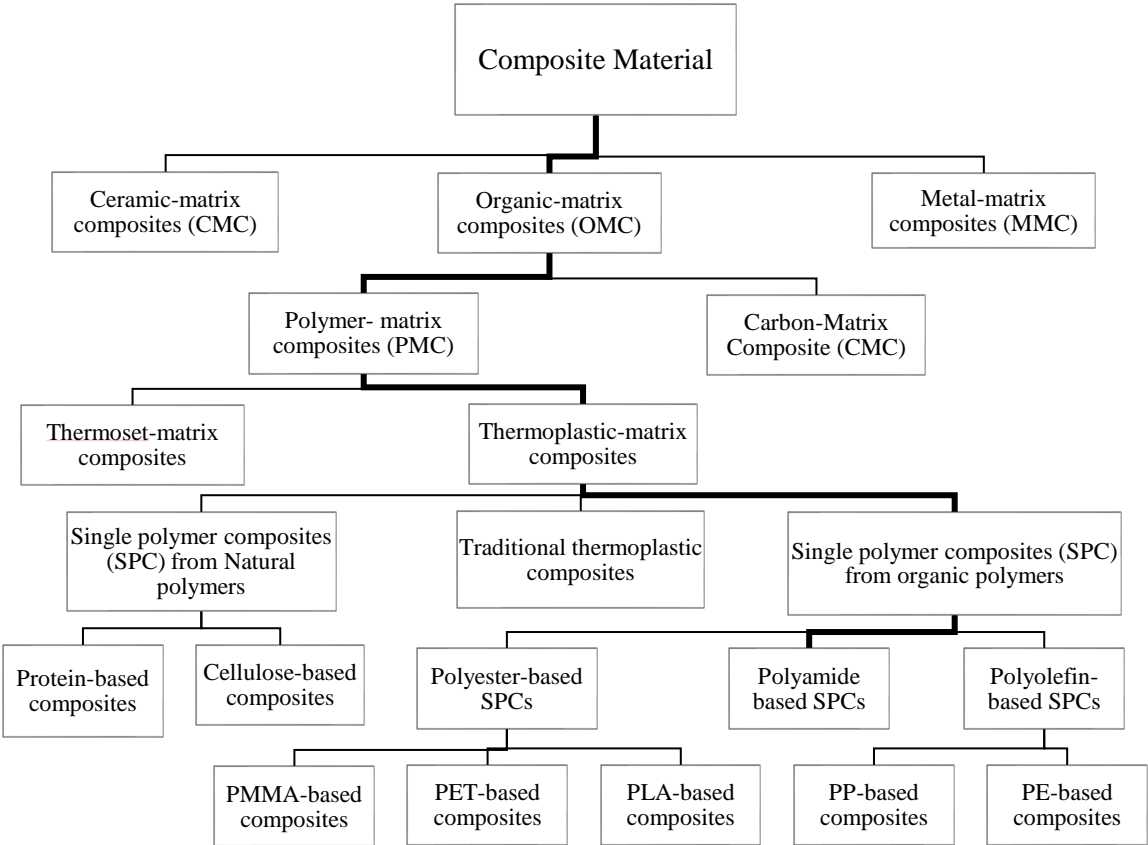
Figure 1.2. Classification of composite materials based on matrix component nature [7]

Three principal categories are mainly appropriated comprising ceramic, metal, and organic matrix base [7]. The organic matrix base composite materials are superior to other matrix types because of high specific strength, high damage tolerance, good damping characteristics and multi-functional

3

performances [4,8]. Concerning the thermal behavior, organic matrix base composites are classified into "Thermosets" and "Thermoplastics". The former such as epoxies, polyesters, and vinyl esters base composites conveniently melted and transformed from low viscosity liquids to the solid materials. Consequently, the matrix phase is diffused properly among the reinforcements. However, the final parts cannot be reshaped and recycled due to the existence of cross-links and multi monomers in the chemical morphology [2]. The later such as polyethers and cellulosic, polyamides, polyesters, polyurethanes base composites have chemical stability, better corrosion resistance, short molding cycle, low glass transition temperature (T_g) and better recyclability.

1.3. Reinforcement components classification

Fibrous reinforcements with different configurations and material properties are used in composite materials that effect the mechanical properties of the composite in different ways. Fiber reinforced polymer composite system has become increasingly important in a variety of engineering fields. The short fibers composites (e.g., prepared by the injection molding process) are demanded respect to their proper processability which makes them very cost-efficient for large production volumes. The mechanical properties of the continuous fiber (filaments) composites are dominated by the distribution of the filaments, basic mechanical properties of the filament itself, the surface interfacial bonding, fiber volume fraction and the filament orientation [2,9]. The surface interaction at the interface is controlled by the degree of bonding which is heavily influenced by the sort of treatment given to the filament surface. Low diameter filament provides higher fiber surface areas and spreading the fiber/matrix interfacial loads [10]. The filament orientation creates highly "direction-specific" mechanical properties that present more benefits as a matter of designing although the fabrication process would be costly [10].

A unidirectional fabric is one in which the majority of filaments run only in structural direction and other types may run in other directions [2]. Unidirectional fabrics are straight and un-crimped leading to the highest mechanical properties (Figure 1.3a). Prepreg unidirectional tape, where the secondary material (matrix) hold the unidirectional filaments in place, is an alternative way to improve mechanical properties of final composite [10,11]. The drape, surface quality and fabric stability, the area weight, porosity and wet ability are controlled by selecting the appropriate combination of primary and secondary filament´s count and number per centimeter and the way of structural retaining [9].

Woven fabrics are produced by the interlacing of two sets of fiber bundles those called warp (0°) and

weft (90°) piles in a regular pattern or weave style (Figure 1.3b). They are selected as reinforcements while more than one filament orientation is required. The yarns are undulated in the weave structure and the fabric's integrity is maintained by the mechanical interlocking of the filaments. Drape ability, surface smoothness, and stability of fabric are controlled primarily by the weave style. The main advantages of woven fabric composites are high tensile properties, better toughness, dimensional stability and low cost of fabrication [12]. Type of filaments, woven geometry, fabric thickness, float length as well as number of plies, interlace points, unit cell, fiber content have remarkably influences the final mechanical properties of woven fabric composites [13]. They provide more balanced properties in the fabric plane and higher impact resistance rather than unidirectional composites. The interlacing of yarns provides higher out-of-plane strength which can take up the secondary loads due to the load path eccentricities, local buckling etc. As the handling of woven fabrics is easier, fabrication procedure becomes less laborious and manufacturing errors [14]. If the properties of more than one type of filament are required, different fabrics will be considered. However, if low weight or extremely thin laminates are needed, a hybrid fabric allows two types of filament to become consolidated in just one plie [15].

Knitted structures can be categorized by basic loop formation mechanism into weft and warp knits. In the case of complex shapes of final products, knitted fabric composite are ideal candidates [16,17] owing to interlocking of loops those have the high degree of deformability (Figure 1.3c). Furthermore, knitted fabrics are considered as very loose structures with low load-carrying capability. Their advantages are possibility of near-net-shape composite production, material wastage reduction, good out of plane mechanical properties, higher impact and damage resistance and better shear strength [18].
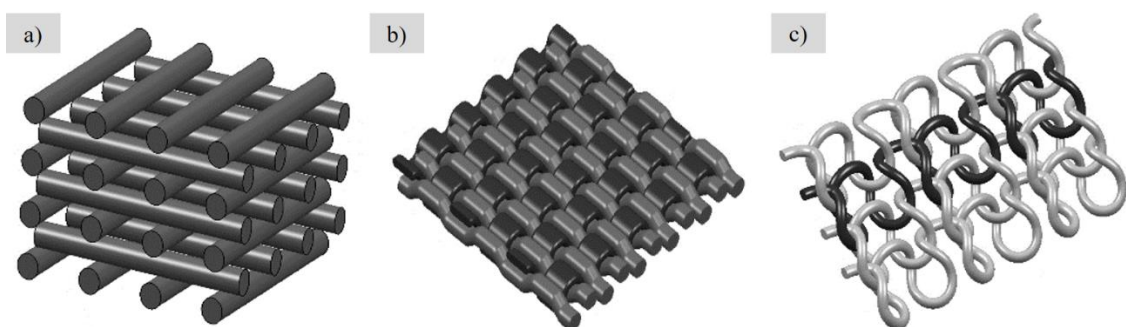
Figure 1.3. Geometrical schematic of a) Unidirectional; b) Woven and c) knitted textile reinforcements

A general comparative study based on effect of several mechanical properties of typical reinforcements in composite materials is schematically illustrated in Figure 1.4. The knitted fabric composites contain

higher the inter-laminar fracture toughness[1] than unidirectional and woven fabric composites [19]. Otherwise, the stiffness and strength of knitted fabric composites are inferior than those reinforced by woven fabrics. The processability of complex parts such as cubes, cones or spheres is difficult for woven fabric composites. To avoid excessive waste material, woven reinforcements require being cut to the precise shape before forming. In contrast, knitted reinforcements can be shaped into almost every possible profile by use of their extensional deformability. In case of fiber mat composite materials, i.e. staple fiber spray-up technique, composites easily crack in micro level at specific points and weak spots become created. The advantages of knitted fabrics are attained over the entire surface of the part, and at points of strong curvature such as corners [20].

The filament orientation and distribution in woven and knitted fabric composites are not changed significantly during molding. In contrast, in the short fibers injection molded part, the flow regime ascertains the fiber orientations and varies from point to point (Figure 1.4). The waste material is concentrated to a minimum value in fiber mat and knitted reinforced composite materials because of requiring low forces to form reinforcements and less expensive machinery and tools.
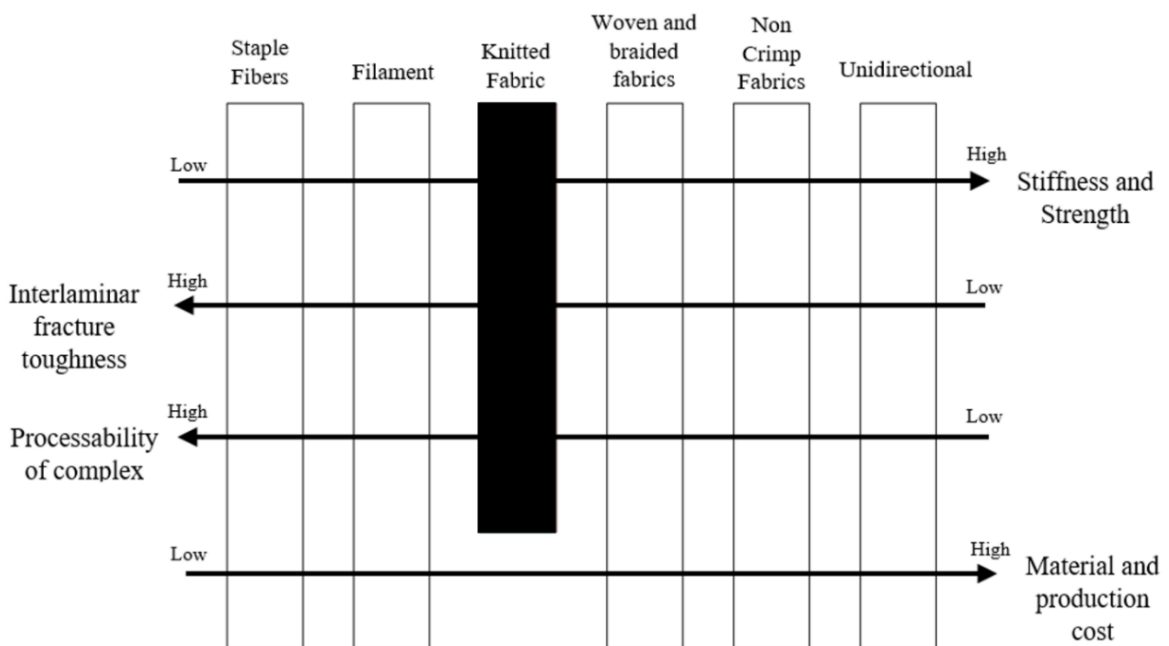
Figure 1.4. Comparison between the reinforcement architectures used in composite materials [19]

---

[1] Fracture toughness is the ability of a material containing a crack to resist fracture.

1.4.   Defects in composites

Defects in composites are included week impregnation, improper process pressure, inadequate heating, mismatch in thermal expansion between reinforcements-matrix- tool plate materials [21–23]. Moreover, the external factors containing cyclic loading, low-energy impact, moisture and temperatures alternation during composite service life are responsible for future mechanical properties blemishes. Voids and dry spots are attributed to the poor choice of the process parameter, subsurface damages, ply cracking and de-lamination (generated by external functions) [23,24]. The rate and equilibrium level of moisture absorption is increased by growing void content [25].

Weak or cracked interfaces can cause failure in composites and destruct the mechanical properties. They lead to the influx of environmental hazards such as hot gases and moisture through into the bulk of the material (filaments). Appearing critical flaws and cracks in composite structures may go undetected. A crack becomes increased in composites materials as far as the stress intensity factor at the crack tip is greater than the critical stress intensity factor[2] of the material.

Composites have neither uniform strength in all the directions nor higher fracture toughness compared to metals. The matrix components axially shrink more than the filaments, resulted from the differences on thermal expansion coefficient of the composite components and high operating temperature. Due to this fact, the matrix becomes compressed around the filaments caused voids advent. Inter-phase layer between composite components almost become generated where the atoms or molecules of the reinforcements and the matrix diffuse into each other at the interface and possess different properties from that of the filament or the matrix. This inter-phase layer may create micro-cracks or enhance to form a bond between composite components [26].

1.5.   Motivation

Glass or carbon fibers are known as conventional reinforcements those are more industrially applicable to their good stiffness, tensile strength, lower density, better process ability and compatibility with suitable sizing chemicals [27]. Beside their excellent mechanical properties, the limited recyclability, high energy requirements (end-of-life processing) and life cycle assessment are their main drawbacks [28]. Respect to inherent heterogeneous nature of the matrix and the reinforcements in composite materials, the

---

[2] The critical stress intensity is known as the fracture toughness of the material. The greater its value is, the tougher the material is. Brittle fracture is one of the main characteristic of materials with less fracture toughness.

recycling process have not well investigated. Concerning the global warming issue and the restricted landfill spaces, the demands for the recycled material has been increased to protect our environment [29,30]. Waste management regulations and current environmental legislation persuade material producers to undertake the responsibility of their product life-cycle inclusive of recycling from end-of-life and ultimate disposal [7,31,32].

Nowadays, awareness of the disastrous environmental impacts is issue of concern for governments, and it was led to declaring the concept of sustainable development [33]. Environmentally, recycling of glass fibers are challengeable both in mechanical recycling and thermal recycling [33]; hence, more attempts carried out to substitute the natural fibers that are more environmentally friendly composites. Being renewable is the main advantages of these class of composites over the glass fibers. However, the additional thermal degradation, accompanied by mechanical degradation, during reprocessing level were their drawbacks owing to the poor thermal stability of the lignocellulosic fibers and poor matrix–fiber adhesion. To some extent the conventional thermoplastic composites deal with the denoted industrial and environmental obstacles unlike being costly, possessing negative environmental impact together with the weak Van der Waals interfacial bonding between the composite components.

The recycling of composite materials, based on extensive research and development activities and various technologies commercialized in three categories such as mechanical, thermal and chemical recycling [34]. Although, all of these techniques have main disadvantages including high energy-intensive (up to 1000 °C), relatively low quality of recyclates and waste chemicals generation in the environment [35,36]. For instance, Carbon and Glass fibers are used as reinforcements in many composite products nonetheless mechanical recycling and EOL disposal through incineration (thermal recycling) brings the environmental problems [34,36]. Alternatively, the technical solutions are available so far typically produce lower grade recycled materials [28] but additional problems such as disposal of toxic solvents are their key consequences [37]. Nevertheless, chemical incompatibility of the heterogeneous composite components leads to the recycling challenges and poor interfacial bonding [34,38]. The recycling process has not well investigated because of inherent heterogeneous nature of the composite component [39].

Polyamide 6 (PA6) is generated by one type of molecule which has 6 carbon atoms and made of ε-caprolactam (ECL). Polyamides like polyesters theoretically are unreactive and they have many harmful environmental impacts. During polymerization, some percentage of monomers escapes in form of gassing or water which has environmental consequences. On the other hand, generation of unwanted ammonium

sulfate (during producing ECL) as by-product is a real culprit [40]. In the case of PA6, the toxic hydroxylamine (NH$_2$OH) and the concentrated sulfuric acid (in last two steps) are utilized in the conventional synthesis of caprolactam. As a matter of calculation, production of one ton of ε-caprolactam release 4.5 tons of ammonium sulfate (as by-product) [41] which has significantly increased mortality of crustaceans, fishes, insects, amphibians, mollusks and other organisms. The other type of the pollution can be produced in synthesis of PA6 is unreacted caprolactam monomer which is precipitated in waste water and has toxic impact in nature [42].

Depolymerizing rate of the condensate polymers would be much faster in presence of water but have more reduction in mechanical properties. Having a low density compared to the polymeric materials is the other benefit of PA6. There are two volumes of crystalline and amorphous phases in the structure of the semi-crystalline polymers (i.e., PA6) causing different percentages of crystallinity. In comparison with thermosets, processing and tooling cost of semi-crystalline thermoplastics are slightly high although decreasing the producing time and ability to reprocess molded parts reduced total expenses. Respect to environmental impact of conventional composites such as glass or carbon fiber composites, concerns for declining the man-made contaminant amount has stimulated interests in emerging a novel class of composite materials that are entitled by single polymer composites (SPCs) materials. Their main advantages are consisted pure chemical functionality, being fabricated in forms of micro and nano composites likewise higher percentage of recyclability.

1.6.   Single polymer composites (SPCs)

Four decades ago SPCs had been patented by Capiati and Porter [3] that a stronger fiber-matrix interface achieved wherein the Polyethylene (PE) powder with different melting points reinforced with oriented PE filaments. They expressed the noticeable difference in melting temperature (T_m) between PE matrix ($T_{m,PE}$ =140°C) and high-density polyethylene (HDPE)[3] reinforcement ($T_{m,HDPE}$ =131°C). The consolidation in the PE matrix was accomplished due to the higher melting temperature of the HDPE fibers. The filaments were subjected to a pull-out test subsequent of cooling-solidification process. Their results revealed the comparable interfacial shear strength with that of the glass fiber/epoxy system. Moreover, the different morphological properties were detected at the interphase region.

---

[3] Molecule chains of HDPE filaments are extended resulting in higher melting point than conventional crystallized Polyethylene filaments.

The emerge of a novel class of material, SPCs, overcome the challenges of heterogeneous composite materials [43]. A polymer matrix in a SPCs is reinforced with oriented 2D and 3D fibrous material or particles of the same polymer. They are often described as one-polymer composites, homocomposites, all (the same) polymer composites, self-reinforced, or homogeneous composites [30,44]. Because of having identical chemistry in SPCs components, the better interfacial bonding is obtained due to the existence of H-bonds or even covalent bonding across the interface [38,45,46].

1.7. Production challenges of SPCs

1.7.1.   Processing Window

A parameter of prime importance for the compression molding of SPCs is widening the processing window temperature (PW) which is considered as difference between melting temperature of monomers and reinforcements [31]. This is considered as substantial parameter due to the mutation of composite processability, interfacial bonding quality and transcrystalline layer (TCL) advent in SPCs. An optimized PW has several consequences including the deterioration in mechanical behavior of the reinforcement, different thermally induced shrinkage (relaxation), partial melting accompanied by morphology changes [47,48]. Nevertheless, time-dependent parameters such as heating/cooling rate, optimum polymerization regime and applied processing pressure are crucial parameters. Accordingly, widening the PW is supportive to avoid reinforcement weakening and disorder SPCs processing methods and conditions. Widening the processing window is an alternative way of empowering the interfacial bonding in SPCs due to the difference in crystallization-related features of composite constituents. Different melting temperature is resulted from different crystalline perfection in all semi-crystalline polymers [38].

Semicrystalline reinforcement components are prepared by several techniques such as spinning (from the melt and drawing in a temperature gradient) and stretching processes (cold drawing at different temperatures between T_g and melting temperature-T_m in several steps at increasing temperatures) [5]. Moreover, Annealing is a heat treatment usually performed under load, leading aligned and perfect crystal entities which is pronounced as memory effect. Heating and restoring in high extension status followed by the cooling process, converted isotropic counterpart to the stretching-induced superstructure. Therefore, annealing treatment increase the PW in SPCs production [45].

1.7.2.   Transcrystallinity in SPCs

Strong and durable interfacial bonding between SPCs precursors due to the same polymeric affinity is a remarkable advantage of this class of material. The similar surface energy of composite components is caused the mechanical superiority of SPCs than conventional composite materials. In case of semi-crystalline polymer composites, the spherulites grow in restricted to the lateral direction during the occurrence of heterogeneous nucleation with sufficiently high density along the interphase region. The spherulites grow in the transversal direction to the nucleating surface. Therefore, a columnar layer is created around the fibrous reinforcements named transcrystalline layer (TCL) which has a key influence on mechanical properties of final composites [32].

The mother lamellae[4], developed first, may lay edge- or flat-on at the reinforcement surface [49]. Filaments surface in composites act as heterogeneous nucleating agents and nucleate crystallization along the interface which is accompanied by a high density of nuclei [32]. Generally, TCL is created because of the crystallization conditions [50,51] and even on the molecular weight (M_w) difference between the fiber and crystallizing melt [52]. Epitaxy between fiber/matrix [39], topography of the fiber [39,53], mismatch of thermal coefficients of the fiber and the matrix [54], thermal conductivity of the fiber [55], chemical composition of the fiber surface [56], surface energy of the fiber [57,58], crystallinity of substrate, processing conditions (cooling rate, mold temperature, flow field) [54], molecular weight of the matrix [59] and surface roughness of fibers [60] are recognized as other factors of TCL generation. The TCL in composites significantly has a negative influence on mechanical properties of composites although in some cases it has improved the properties at the interface [61]. However, the real mechanism and impression of TCL in composites are still disputing.

1.8.   Summary of this Research

The present study is aimed to develop PA6 base SPCs with alternative reinforcements and provide a deeper insight into their mechanical properties, thermal analysis, fracture mechanism and polymorph characterization. Two distinctive molding techniques are employed to produce PA6 based SPCs such as nylon reactive injection molding (NYRIM) and powder coating/compression molding (PCCM) processing techniques of PA6 microparticles, previously synthetized by activated anionic ring opening polymerization

---

[4] Mother lamellae Initially is crystallized on which subsequently daughter lamellae can grow homo-epitaxially on the lateral crystalline planes.

(AAROP) from ECL in suspension as described previously [62]. AAROP was the principal polymerization method. The processing window for compression molding in this case was expected to be significantly broader than in most of the SPCs prepared by melt processing. The effect of reinforcement's architecture, fiber volume fraction, laminate orientation and stacking order on the mechanical properties of PA6 base SPCs resulting from the two methods were profoundly investigated and compared. Moreover, their bonding morphologies at interface region are studied in detail.

The morphology and the crystalline structure of PA6 based SPCs were studied to identify the main factors affecting their mechanical properties. The studies on modes of fracture under off-axial load conditions, the α-/γ-polymorph structure, the thermal properties and the crystallinity index of the samples containing various amounts and types of reinforcements were carried out to in depth analysis of mechanical properties of PA6 based SPCs. Eventually, the tested PA6 based SPCs specimens are recycled via injection molding technique and their mechanical properties are compared with the PA6 conventional injection molded and neat matrix components due to the understanding of post mechanical degradation. It is expected that the recycled PA6 based SPCs composites will combine the high temperature- abrasive- and solvent resistance of the isotropic PA6 with the high mechanical strength of the PA6 fabrics reinforcements.

The project will require innovative solutions on two levels. First, on the level of the reinforcing textile constituent, various textile structures of PA6 will be developed and thoroughly characterized based on the experience in the center for textile science and Technology (2C2T). Second, on the level of PA6 matrix creation and sample consolidation, in-mold AAROP of ECL, performed in institute for Polymers and Composites (IPC). The basic theoretical outcome of this project is expected to be the better knowledge on two molding techniques such as in-mold AAROP of caprolactam and powder coating/compression molding, in the presence of complex textile structures, as well as, their influence on the structure and mechanical properties of the final composite. The foreseen industry-relevant outcome is related with the possibility of development of a fully recyclable textile laminate composite with mechanical properties compatible with structural and semi-structural applications in automotive and aerospace industries. To achieve the goal of the project, six main tasks are foreseen:

1. Preliminary study on structural and mechanical properties of PA6 to obtain an optimum polymerization regime via two distinct molding techniques comprising in-mold AAROP of ECL (NYRIM) and powder coating/compression molding (PCCM).

2.   Preparation of the textile reinforcements and structural and surface treatment including consecutive steps like stretching and heating above glass transition temperature of the textile reinforcements.

3.   Preparation of PA6 based SPCs respect to different structural parameters such as reinforcement´s architecture, fiber volume fraction, plies orientation, stacking order.

4.   Mechanical testing and damage mechanism analysis of PA6 based SPCs with respect to the reinforcement´s structural parameters, crystalline polymorph of composite and their precursors.

5.   Investigation on fracture behavior of PA6 base SPCs using electron microscopy complemented by simulation studies.

6.   Study of the morphology and structure of PA6 based SPCs and their components.

With all these ideas in mind, the doctoral methodology of the presented thesis can be summarized as illustrated in Figure 1.5.
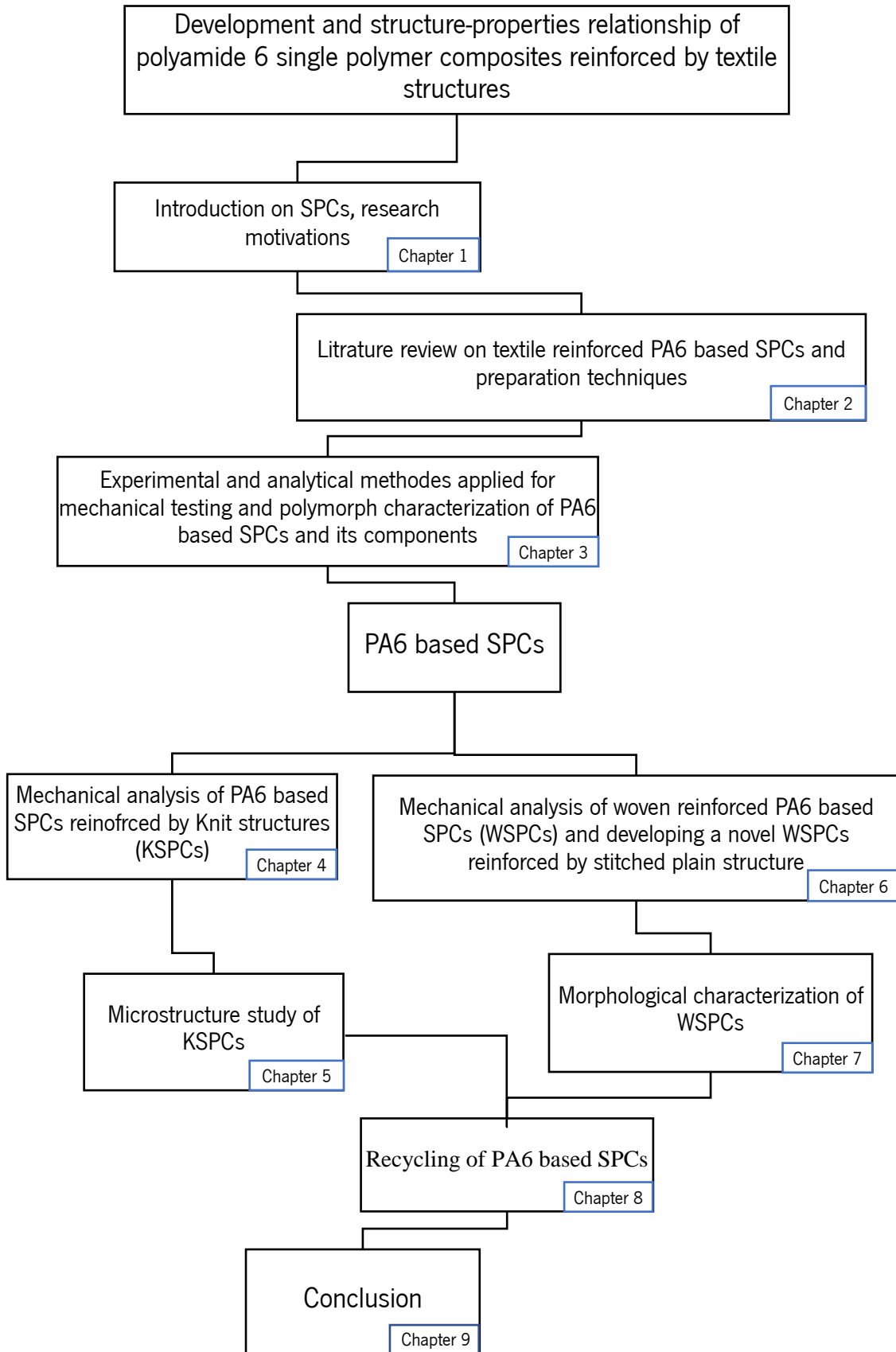
Figure 1.5. Doctoral methodology of the presented thesis

Chapter 2

State of art

2.1.   Introduction on SPCs

SPCs are a novel class of materials in which the reinforcement and matrix components are based on the identical affinity. The cause of similar polymorph structure of SPCs components results strong interfacial bonding at reinforcement/matrix interface region. Correspondingly, it causes the proper transferring internal stresses from the matrix to reinforcement components. In this chapter, a literature review on the SPCs methods of preparation, the ways of investigating their structure and the relation with mechanical properties will be presented. Furthermore, the marketing and classification of SPCs within the whole variety of polyamide based composites will be outlined. A comprehensive literature review on effect of reinforcement´s geometrical-structural parameters on mechanical properties of woven and knitted reinforced composites have been given.

2.2.   SPCs preparation techniques

Melt processing is a principal technique for SPCs preparation wherein the outer surface of constrained reinforcements is partially melted and transformed to matrix phase whereas the inner part is reformed morphologically and undertake the responsibility of reinforcement [63–65]. The delayed self-nucleation is resulted from slow crystallization of thermoplastic polymers and quenched from the fully amorphous form (melt) through the fast cooling operation. Their crystallization and softening run concurrently at processing window above their glass transition temperature (T_g) and below their melting temperature (T_m). The most applied melt-processing techniques for SPCs are film stacking [38,49], powder impregnation [45,46], solution impregnation-coextrusion [46], high temperature-pressure sintering (partially melting) [32], hot compaction [39] as well as reaction injection molding [66], mold compression [47,67], extrusion injection molding [68].

In all cases, PW, known as remarkable obstacle which does not exceed several degrees and frequently is too narrow for industrial application. For instance, the narrow PW of HDPE matrix (132°C) and fibers (139 °C) has reported by Mead, et al [69]. The PW can be elevated by several fashions such as applying the variety of polymers transition and annealing process. An alternative way is employing the same chemical composition with different chemical structures (molecular weights and chain configurations) [50,61]. For instance, growth about 20°C and 40°C PW were observed for HDPE matrix with UHMWP

reinforcement and LDPE[1] matrix reinforced by UHMWPE fibers respectively [50]. Barany et al. [52] increased the processing window up to 25°C via film stacking method. Two morphologies of polypropylene, α-PP (high melting temperature) and β-PP were applied as reinforcement and matrix respectively. Also, high PW and pressure are known as disadvantages of SPCs production techniques due to non-cost effective process and needs of precise monitoring during polymerization [54]. Following techniques briefly explained the cons and pros of SPCs molding procedure.

2.2.1. Powder impregnation

Powder impregnation is a traditional technique that involves the impregnating polymeric thermoplastic powder trough into the fiber bundles [55]. This process is one of the cost-effective manufacturing of SPCs (Figure 2.1). The impregnation process almost applied for low-molecular-weight polymer grades due to the increase of processing window. The process is relatively slow and costly because of the necessity to flow molten powder within the fiber bundles to fully wet the individual filaments. In addition, reinforcements also lose their mechanical properties because of partial melting during impregnation. This method is used for the development of SPCs reinforced by PE [56], Polypropylene (PP) [57] and Polyamide (PA) [58] fibers.
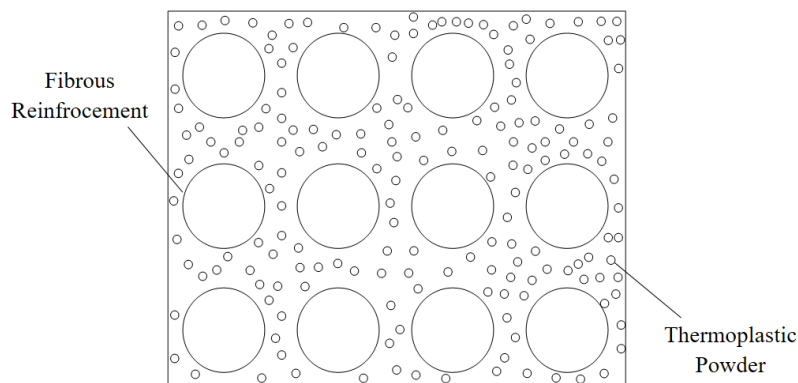
Figure 2.1. Schematic of powder impregnation method

2.2.2. Film-Stacking

In the film-stacking method, the fibrous structures are sandwiched between the matrix films that is complemented by hot pressing. The method has been applied for SPCs reinforced by PP [59], Polyethylene terephthalate (PET) [60,64], PE [65], poly(lactic acid) (PLA) [43] and UHMWPE [70] fibers.

---

[1] LDPE: Low density polyethylene

The advantages of the film-stacking method are a wide PW[2], freedom of the material selection and no expensive pre-production (Figure 2.2). The film stacking is most popular techniques due to the lower melting point of the matrix film than fibrous reinforcement [71]. The first attempt was undertaken by Bhattacharyya et al. [72] where triggering transamidation was applied to improve the interfacial properties of PA6 based SPCs. They applied antimony trioxide for powder coating of the PA6 filament before film-stacking with quenched PA6 films.
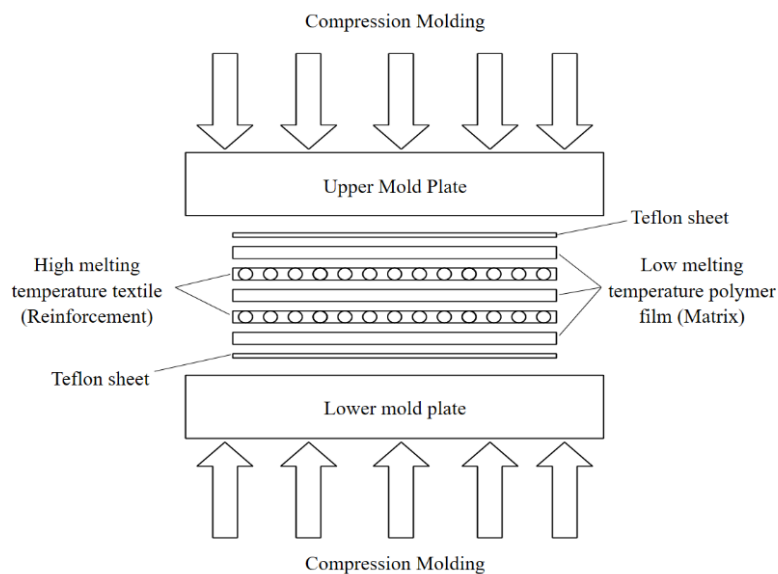
Figure 2.2. Schematic of film stacking method for composite laminate fabrication.

2.2.3. Hot compaction

A patented commercialized technique called "Hot Compaction" was developed by Ward et al [60] at the university of Leeds. Highly drawn semicrystalline filaments were installed in compressing mold where partially surface melting of filaments was converted as an isotropic matrix component of SPCs. Moreover, they continued their experience on the presented technique on SPCs based on PE [70], PP [71], PET [72], polyamide 66 (PA66) [59]. The mechanical properties of SPCs became modified compared to the isotropic (non-reinforced) polymers [72]. Karger-Kocsis [73] developed all-PP base SPCs wherein the polymers with different T_m were crystallized in two or more polymorphic modifications. The combination of hot compaction of UHMWPE filaments accompanied by in situ crosslinking had been done by Ratner et al. [74,75]. The filaments were solution coated by peroxide prior to hot compaction procedure and

---

[2] The chosen film generally has a lower melting point than the fibrous material

higher tensile modulus and strength achieved compare to the un-crosslinked reference.

The other identical technique was also investigated by other researchers called high temperature-pressure sintering [73,76–78]. All these techniques were performed in a similar manner while highly oriented polymer filaments very accurately heated (±0.5°C). As it is demonstrated in Figure 2.3, different assemblies of filaments are compacted at a temperature close to the melting onset in which approximately 10% of the polymer filaments are melted. The molten polymer flows throughout the latticework of reinforcement by applying pressure to form a continuous matrix (Figure 2.3). The sheet is then cooled (under pressure) to solidify the matrix and thermoform a rigid sheet. PP, PE, PEN, PA66, and Poly methyl methacrylate (PMMA) base SPCs are most produced via this technique [79,80].
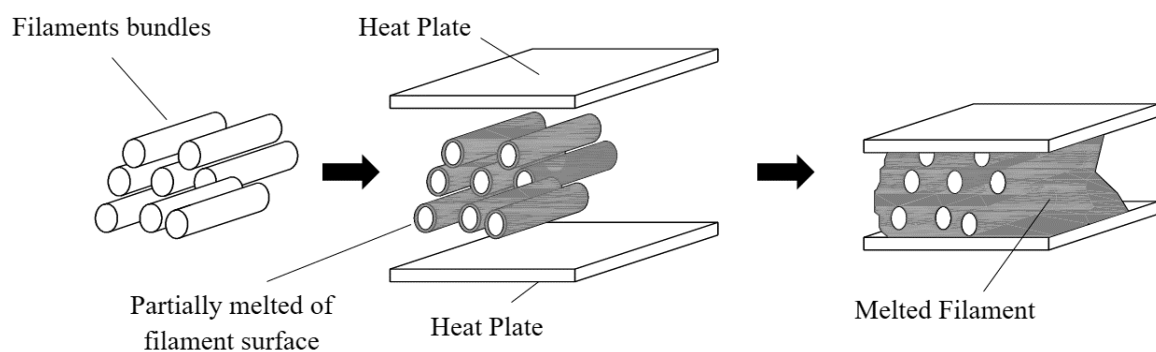
Figure 2.3. A schematic of the hot compaction process for oriented polymer filaments. The oriented filaments and the melted/recrystallized matrix are shown in white and grey colors respectively.

Constraining high fiber content (≈80 wt%) is one of its key advantages of this technique in comparison to the difficulties of impregnation process (high viscosity of polymer melt) in film stacking, powder impregnation [79]. Therefore, hot compaction technique is a proper solution to overcome the denoted shortcomings. The small processing window about 5°C is the main hindrance which brings difficulties to mold the SPCs under normal processing conditions and without annealing the filaments. Relaxation and loss of molecular orientation are resulted from overheating which is caused the poor interfacial bonding between the matrix and reinforcements at the interface. However, the processing window of hot compaction can be enlarged by applying different drawing ratios of fibrous material [80].

2.2.4. Overheating

In this technique, the constrained fibrous material (avoid shrinkage) effectively become overheated above their melting temperature. The oriented polymer fibers are embedded in a molten polymer matrix

of the same affinity. Constraining of the textile reinforcements is led to impedes the relaxation of fibers and shift the melting temperature to the higher values and enlarge processing window around 10°C [5,81]. The temperature and pressure are two main factors, managing the polymorphic transition process.

This technique is validated for two categories of semicrystalline polymers including the drawable apolar polymers (i.e., isotactic polypropylene [iPP] and UHMWPE) and less drawable polar polymers (i.e., PET and PA) [82]. The interchain interactions in apolar polymers are relatively weak and therefore a high degree of draw ability is possible. Polar polymers have relative strong inter-chain interactions and less drawable [5]. For example, in the case of iPP (high draw ratio (>14)) melting temperature shifts to more than 20°C, although, the melting temperature of ultra-drawn PE can only reach to 10°C. The main advantage of this method is to compensate the drawbacks of the hot compaction like low PW [5,79]. The reinforcements are degraded and the filaments lose their intrinsic orientation due to overheating procedures; hence, final mechanical properties of SPCs are descended. The key challenge of this technique is the lack of polymer selection.

2.2.5. Co-extrusion

Highly oriented polymer tapes are extruded from a high melting point grade of the chosen polymer (Figure 2.4). There are two main types of bicomponent set up such as side-side and skin core arrangements. During this process, a low melting point grade of the same family of polymers is extruded on the tape surface or woven fabric. Molding pressure constrains the oriented polymer tapes and increases the melting temperature of the oriented core material during consolidation and extends the PW. The outer layer of the tapes melts before the inner core of oriented polymer during post-processing into shaped components. Under pressure, this low melt grade flows throughout the fabric and becomes re-solidified (cooling process) into the form of composite [80]. The stretching, drawing steps are commonly required because of gaining higher tensile stiffness and strength for the reinforcing constituent [83,84]. The advantages of this process are wide processing window of about 20–40°C, high volume fraction of reinforcement (>90%) insertion and an excellent bonding between the tapes due to the co-extrusion process. Otherwise, the main drawback of this technique is low composite recyclability because of applying copolymers. All-PP base SPCs comprising highly oriented PP tapes have been prepared by this method.
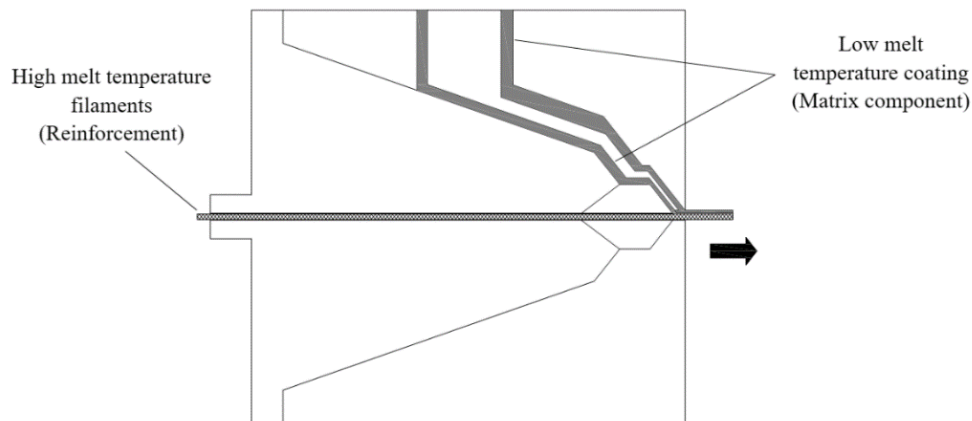
Figure 2.4. Schematic of a co-extrusion process.

2.2.6. Partially melting

In this technique, only fibrous materials are exposed partially melting. First, regular arrays of polymer filaments are constrained by lateral pressing or radial winding to avoid the shrinkage. In a few minutes, at a certain melting temperature, parts of a filament (most likely the surface having the lower degree of crystalline structure) are melted to fill the original gap between fibrous structures. Because of having less free volume and higher melting temperature, the center of filaments is not melted and intrinsically retained highly orientated. By means of a slow cooling process, the molten part begins to recrystallize to form the matrix and bonded the fibrous material together [58]. The highly orientated unmolten part of fibrous material acts as the reinforcement phase and the recrystallized part becomes matrix component. Melting the oriented filaments determine the molecular continuity between at the interface and a narrow processing window is the main drawback of this technique [58].

2.2.7. Reaction injection molding (RIM)

In the reactive processing technique, SPCs are produced in situ polymerization of low-viscosity monomers or oligomers with the presence of the reinforcements [66]. In situ means the related ring-opening polymerization is carried out in the mold giving the final shape of the product. The polymerization procedure is based on anionic or condensation mechanism in which ring-shaped molecules are opened and transformed into high molecular weight polymers. N-Polyamides (i.e., PA6) are produced through AAROP of the inexpensive ECL without generating by-products [85,86]. Mold pressures are typically very low and the process is exothermic in which polymerization is accompanied with crystallization [47,87].

21

Solid polymers are formed by cross-linking or phase separation and de-molded in less than one minute (Figure 2.5). The major reason for the growth of reaction injection molding is low viscosity during mold filling that provides many reinforcement selections. Starting with low viscosity liquids (close to water) and relatively small metering machine are caused producing larger parts. Lower void fraction, strong and stable interface (same and polar nature of both components), as well as wide processing window (about 60°C), are key benefits of this technique [48,86,87].

Complex shapes via multiple inserts, matrix low viscosity, and low-pressure requirements during filling are advantages to produce lightweight composite parts [88]. Moreover, they can be comparable with the thermoplastic injection molded (TIM) parts [88]. Correspondingly, RIM can be used for high-speed resin transfer molding. In RIM, the mold is packed by gas expansion, unlike TIM in which high pressure is required. Therefore, smaller clamps, less expensive procedure and possibility of producing large parts are its benefits. The polymerization temperature in RIM, typically is set lower than those for TIM which is led to the lower energy costs [89]. The disadvantages of RIM also are raised from low monomer viscosity. This technique is also applied to generate copolymers via various transesterification reaction [47,90]. The precise reaction viscosity controls and unevenly distribution of material are its main challenges [91]. Nevertheless, the low monomer viscosity is responsible for entrapping the gas bubbles during filling. There is difficulty to seal the molds and mold releasing increases labor costs.
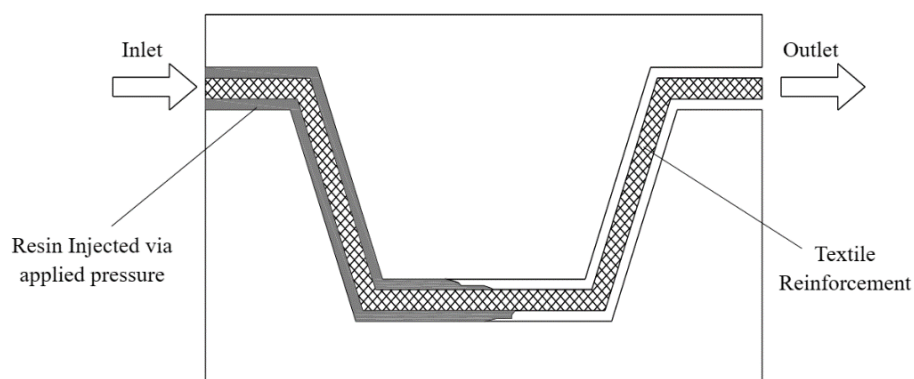
Figure 2.5. Nylon Resin Injection molding machine

2.2.8. Mold Compression

One of the common technique of SPCs preparation is compression molding methods in which the raw materials are usually applied in the form of granules, putty-like masses (Figure 2.6). They are placed in an open heated mold cavity followed by filling up the materials under pressure. The curing procedure is

carried out by maintaining heat and pressure. The overflow grooves are considered to channel away from the excess material. Aramid/polyamides based SPCs are commonly produced by this technique [47,66,84]. Fast setup time-costs, the possibility of large size parts production, variety of reinforcement selection and few wastes relatively material are the advantages of mold compression technique [83,92]. Otherwise, the production speed does not depend to the injection molding standards and there is less-than-ideal product consistency [93].
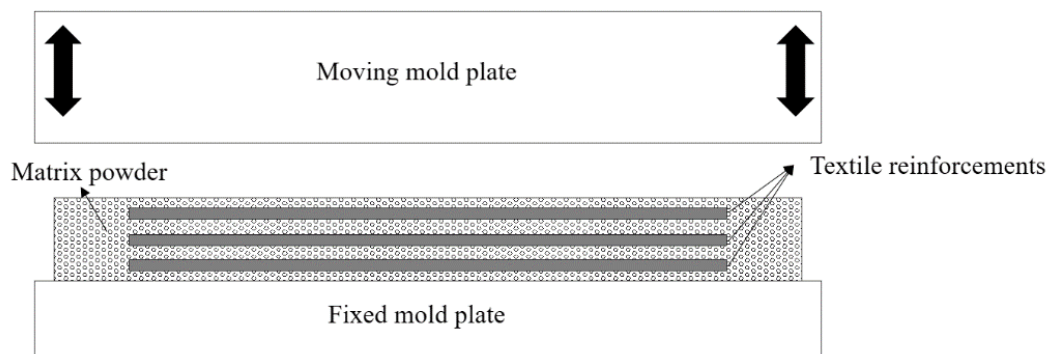
Figure 2.6. Schematic of Compression molding filled by textile reinforcements and matrix resin

2.2.9. Extrusion Injection Molding

This technique is applied often in SPCs production in which the pellets are conveyed forward by a feeding screw and injected through a die (Figure 2.7). There are two main sectors in extrusion injection molding method comprising the feed and melting sectors. The former feeds the resin into the extruder and later melt all the pellets. Fast production, material and color flexibility, low labor costs, flexibility on design and low waste are the advantages of this technique. Otherwise high initial tooling cost, part design restrictions and difficulty in accurate costing are its challenges. This technique can be adapted to the over-molding [68] wherein the molten pellets undertake the responsibility of matrix component and the reinforcements are placed in the mold cavity prior to the infiltrating with the matrix forming injected melt [94].

23
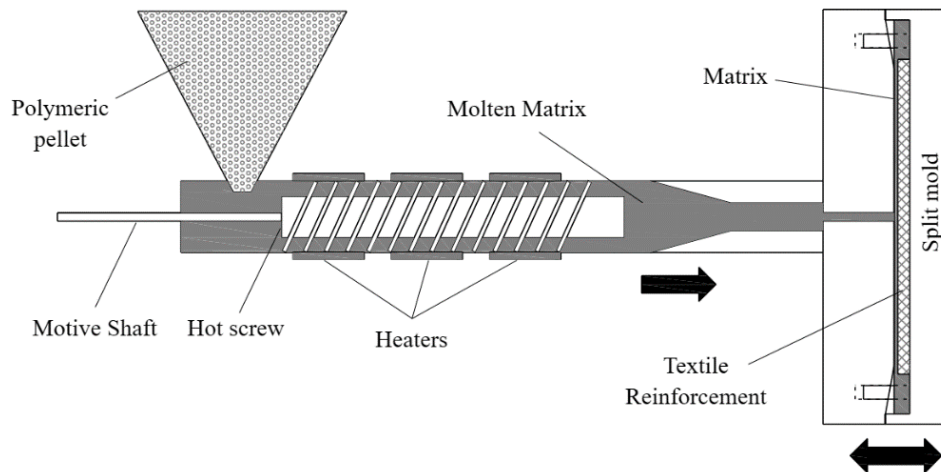
Figure 2.7. Schematic of extrusion injection molding

2.3.   Commercially available SPCs

Nowadays, single polymer composites are presented commercially by different trade names such as Curv®, PURE, PARA-LITE, Armordon, Kaypla, and Comfil. The Curv® is a SPC composed by polypropylene thermoplastic matrix reinforced by highly oriented polypropylene woven fabric. In this product, highly drawn thermoplastic fabrics are constrained and heat treated. The reinforcements become the base material to produce Curv® composite plates which are manufactured by the hot compaction technique [95]. The filament´s surface is remelted into isotropic PP and converted into matrix composite system.

The stretched filaments with different PP grades in the core and surface using a co-extrusion process are presented as Lankhorst Pure® trade mark. The antiballistic, automotive, construction and consumer products such as suitcases and sporting apparel are their ultimate applications [96]. Don & Low Ltd has presented a PP based SPCs, Armordon®, which is similar to Lankhorst Pure® production although there is a strong bond between the two different PP tapes. The tapes may directly be winded or woven into fabric format which are suitable for security industries like ballistic performance [97].

PARA-LITE is presented by Von Roll Deutschland GmbH that a very low density of (0.8 g.cm^{-3}) nonwoven PP-based tape with high tensile stiffness and impact resistance are applied [98]. Their utilities are suited for ballistic protection, building and transportation applications. It should be mentioned that Curv® is a SPC reinforced with different grades of PP base 2D reinforcement (fabrics) whereas PURE, PARA-LITE, and Armordon all reinforced by stretched 1D structures (filaments or tapes).

Kaypla is PE based SPCs, a production of Nextrusion GmbH company where the composite

constituents contain PE film matrix reinforced with a very high draw ratio PE tape (reaches to 70 GPa young modulus) [99]. Construction, automotive, and sports as well as packaging and protection, are their main utilities. Comfil-ApS is a (Danish company founded in 2001) produces a range of Polyethylene terephthalate SPCs parts. The composite component is included of low melting PET as matrix and high-tenacity PET as reinforcements in the form of yarn, fabrics, consolidated plates, rods/tapes, and pellets for injection molding.

2.4. Literature review on all polyamide SPCs

Polymers are known by two solid-state types including amorphous and semicrystalline morphologies. In an amorphous polymer, the molecules are oriented randomly and intertwined with a transparent appearance. Crystallization of polymers is a process which is contributed to partial alignment of their molecular chains. Therefore, semicrystalline materials have a highly ordered molecular structure with sharp melt points. They become soften with a temperature increment until a given quantity of heat is absorbed and then rapidly change into a low viscosity liquid. They are anisotropic in flow, shrinking less in the direction of flow. SPCs can be classified base on their polymeric morphology and crystallinity such as amorphous–amorphous[3], amorphous–semicrystalline and semicrystalline-semicrystalline phase states [100]. The overwhelming majority of the research and development works has been performed on semi-crystalline-semicrystalline type SPCs [100].

2.4.1. Polyamide 6

Polyamides (semicrystalline polymers) are applied highly in industries as fiber, plastics and adhesive applications. As fiber types, they are utilized around 50 % in tire cords, rope, thread, belts, clothes and monofilaments, brushes, sports equipment [46]. Their drawbacks are high moisture absorption, low surface energy, poor chemical reactivity below melting point [29]. Polyamides have large advantages such as good toughness, high tensile strength, strong impact resistance, low coefficient of friction as well as high melting point, good resistance to abrasion, and convenient processability [78]. Having only one monomer (repeating amide - $CONH_2$- linkages) in PA6 molecular structure is caused ease recycling.

---

[3] Dental application was caused to upbringing Amorphous-amorphous.

Otherwise, PA66 owns two monomers in its chemical structure that causes the difficulty on the recycling procedure.

2.4.2. Polymerization of Polyamide 6

Joining of two groups to form an amide linkage is essential to produce polyamides including amide bonds. The two groups involved are an amine group and a terminal carbonyl component of a functional group. The condensation reaction is applied to synthetize polyamide polymers in industry. Two main polymerization methods are applied for the producing PA6 polymer parts such as hydrolyzing the lactam by the presence of water (hydrolytic polymerization) and AAROP. RIM [88], rotational molding, centrifugal molding [101], and monomer casting [46,102] are most techniques applied in AAROP of PA6. Following sections bring a brief description on two major PA6 polymerization techniques comprising hydrolytic and AAROP.

2.4.3. PA6 hydrolytic polymerization

The hydrolytic polymerization of caprolactam is one of the most used traditional ways of polymerizing of polyamide 6 (PA6). In this technique, PA6 is made by heating caprolactam to about 250°C with 5-10% water added in which the carbonyl oxygen attracts hydrogen atoms in the water molecule (Figure 2.8). The carbonyl oxygen donates a pair of electrons to the hydrogen atom of water and generates a protonated carbonyl followed by releasing free hydroxyl group. Consecutively, the protonated oxygen atom swipes a pair of electrons from the carbonyl double bond, leaving the positive charge on the carbonyl carbon atom. As the chemical reactions in Figure 2.8. demonstrate, the carbocation[4] in the molecule possesses the possibility of being attacked by nearby hydroxide ion formed as an unstable gem-diol[5]. Subsequent of intense reshuffling of electrons, the nitrogen atom donates a pair of electrons to a hydrogen atom on one of the hydroxyl groups and stealing it away. A double bond between the oxygen and the carbon atom is created and the electrons shared by the carbon and the nitrogen shift completely to the nitrogen, severing the carbon-nitrogen bond. The circle is broken, and the reaction gives a linear amino acid (Figure 2.8).

---

[4] A carbocation is molecule in which a carbon atom bears three bonds and a positive charge. Carbocations are generally unstable because they do not have eight electrons to satisfy the octet rule.

[5] A geminal diol (or gem-diol for short) is any organic compound having two hydroxyl functional groups (-OH) bound to the same carbon atom.
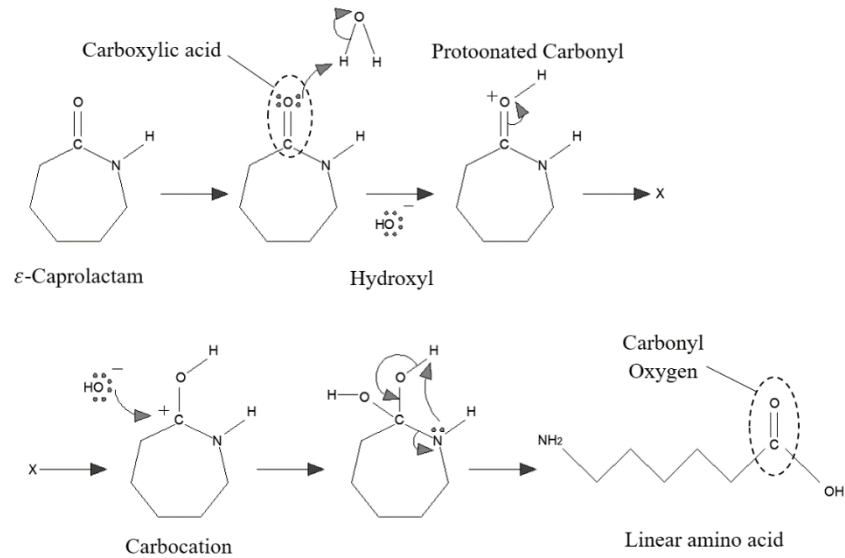
Figure 2.8. Hydrolytic polymerization of PA6 reaching to linear amino acid

The linear amino acid reacts with another caprolactam molecule. A caprolactam molecule steals the acid hydrogen from the linear amino acid and from the carbocation. This carbocation combines with any nucleophile around and an unstable ammonium species obtains. The ring nitrogen steals hydrogen from the ammonium nitrogen and opens the ring (Figure 2.9). The carboxylate group at the end of the molecule sweeps around and steals the alcohol hydrogen. This makes a new carbonyl group in the middle of the molecule and regenerates the carboxylic acid. The produced acid reacts with another caprolactam molecule and this process continues to get long chains of PA6 (Figure 2.9).
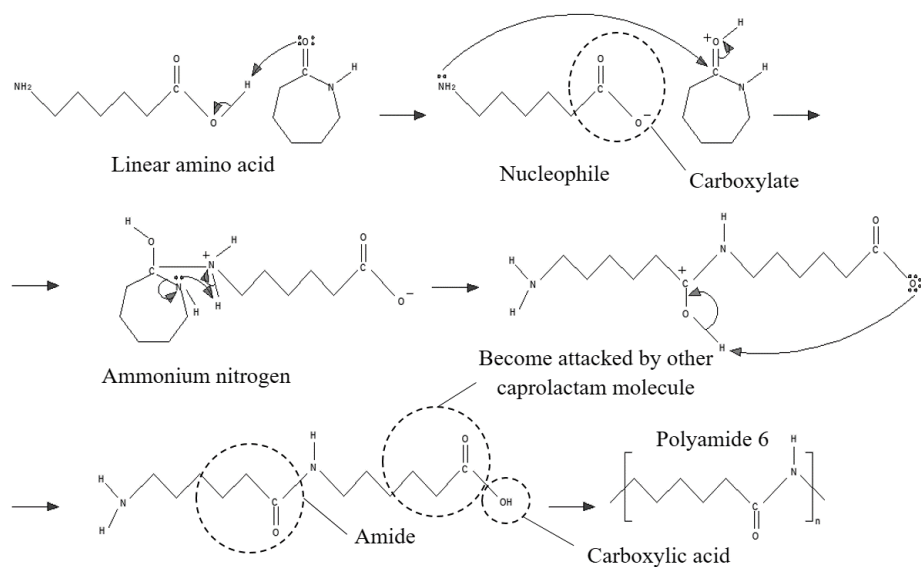
Figure 2.9. Reaction of linear amino acid with another caprolactam reaching Polyamide 6

27

4.1.1. AAROP of PA6

The principal of AAROP is opening the ring-shaped monomer molecules and transform them to high molecular weight polymers without the liberation of by-products [103]. In this polymerization method, ECL is anionically polymerized with the aid of alkaline catalysts [104]. The polymerization of ECL was first described by schlock, Joyce and Ritter [105]. They used several alkali and alkali earth metals [106] as catalyst e.g., Na, Li and Ca. Hanford and Joyce basic catalysts were then investigated, including hydrides, hydroxides, alkali metals, Gringard reagents, alkoxides and a host of other compounds [107–111].

The relationships and synergies between the catalysts and the molecular weight and molecular weight distribution of the polymeric products had been explored. This polymerization method could be defined as three main steps: i) initiator dissociation (anion formation) ii) initiator and activator complex formation iii) polymerizing at the moment of anion generation subsequent to every monomer addition [112]. Ring-opening polymerization method is divided into three main subsections such as anionic, cationic and radical ring-opening polymerization [53].

Ring opening polymerization of PA6 is an inexpensive process because of applying low-cost monomer such ECL. In case SPCs production, high processing window between composite components, reducing on processing time under anhydrous conditions [113] and growing the energy efficiency of the process is the key advantage of AAROP method. The AAROP of ECL is significantly performed at a faster rate and just in a few minutes reaching equilibrium conversion while it is compared with PA6 hydrolytic polymerization (12±24h) [114,115]. The polymerization may be successfully completed to high conversion rates at temperatures lower than in the hydrolytic polymerization [104].

As Figure 2.10 demonstrates, the first step in the anionic polymerization is the reaction of a lactam ring with the catalyst to form a lactam anion and hydrogen. Sodium hydride (NaH) is the strong base which attacks to the amide hydrogen in caprolactam and pulls it right off. The leftover sodium cation forms a salt with the negatively charged nitrogen that is left behind when the hydrogen is extracted but it's not appreciable. Therefore, some poly (ethylene oxide) is added to the reaction mixture to bring a complex sodium cation, keeping it from associating with the anionic nitrogen. The yield nitrogen contains a free anion to become more reactive.
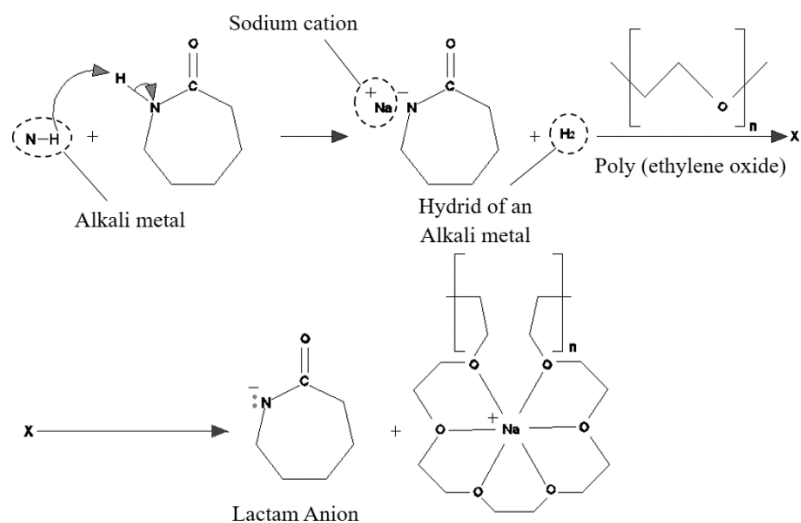
Figure 2.10. Reaction of a lactam ring with the catalyst to form a lactam anion and hydrogen

The lactam anion reacts with a lactam monomer at higher temperatures to form an imide anion (Figure 2.11). The nitrogen in lactam anion donates an unshared pair of electrons to the carbonyl carbon of another caprolactam molecule those are electron deficient and been easily attacked by anions. The caprolactam molecule ring-opens after some electron-shuffling between the carbonyl carbon and the amide nitrogen. This molecule quickly reacts with additional monomer to form a new lactam anion and a neutral N-acyllactam with an amine end-group [113,114,116].

The polymerization continues by the attack of alactam anion on the carbonyl group of the imide in which it inserts itself into the growing chain and abstract a hydrogen atom from another lactam monomer to continue the process (Figure 2.11). At low temperature, the N-acyllactam alone has no polymerization activity without the addition of strong base [117]. According to this mechanism (Figure 2.11), the polymerization and depolymerization occur largely at the imide group which is the strongest in the system.

The polymerization appears to be stalled because of the initial slow formation of the acyllactam anion [113,114,116]. The new molecule also has negatively-charged nitrogen, an amine anion which is an unstable molecule. Therefore, the activation energy is high for this step which makes the step of the reaction too slow. For this reason, there is an induction period at the beginning of the reaction before polymerization begins [118].
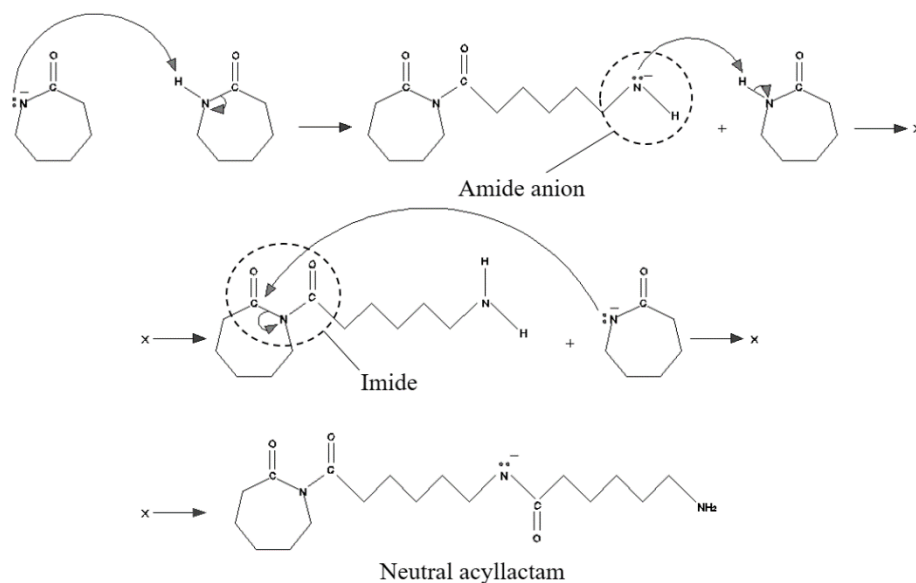
Figure 2.11. Reaction of lactam anion with a lactam monomer at higher temperatures to form a Neutral acyllactam.

The addition of imides, especially N-acyllactams to the initial reaction mixture greatly accelerates the polymerization and practically eliminates the induction period. This is because N-acyllactams possess a strong acylating power and acylate[6] lactam anions which are strong nucleophiles [107]. Acylating procedure facilitates the polymerization progression when imides or imide-forming compounds are added [119,120]. The reacting compound is an imide which is a compound with a nitrogen atom bonded to two carbonyl carbons (Figure 2.12). Imides are more reactive than amides because an imide ring-opening yields an amide anion and the product of an amide ring-opening is an amine anion. Amine anions are very unstable, but amide anions are more stable because the negative charge becomes stabilized by the carbonyl group bonded to the nitrogen atom.
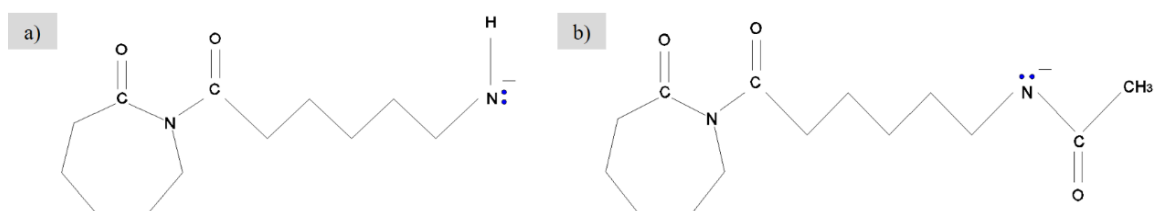
Figure 2.12. Discrepancies on chemical structure ring-opening products of a) Amine anion b) Amide anion

The anionic nitrogen steals a proton from another monomer and generates another anion of ECL. The negatively charged nitrogen attacks the ring carbonyl carbon of Neutral acyllactam. The reaction creates

---

[6] Acylation is a process of adding an acyl group (is usually derived from a carboxylic acid) to a compound.

another unstable nitrogen negative charge and it takes a proton from another ECL molecule (Figure 2.13). This trend keeps happening over and over approaching the high molecular weight of PA6.
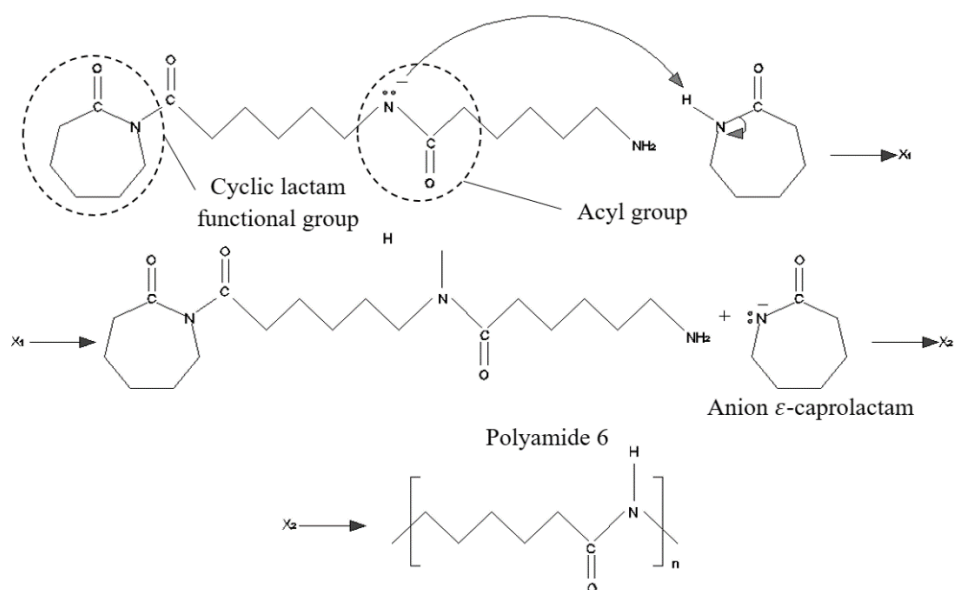
Figure 2.13. Quick reaction of imide contain molecule with another monomer reaching high molecular weight PA6

Because of the environmental impact of glass fiber reinforced polymer composites, the bloom of all polyamide base single polymer composites is becoming an attractive opportunity [77]. Polyamides are categorized into three main affinities such as Aliphatic, Polyphthalamides and Aromatic polyamides [121]. This section is dedicated to a review on the development of Aliphatic-Aliphatic and Aromatic-Aliphatic PA6 based SPCs as well as preparation techniques, reinforcement architecture influence, surface treatment and their resulting mechanical properties. Also, the effect of polymorphisms at the interface (transcrystalline layer) is appraised through hydrogen bonding or creation of nucleating spots on the reinforcements which is still the object of open discussions.

2.4.4. Aliphatic-Aliphatic PA6 based SPCs

Aliphatic polymers contain amide groups that are attached to a hydrogen atom of carbon atoms chains although the Aromatic polyamides contain the repeating benzene rings units [53]. Having a low density among other polymeric materials is their main advantage which makes them suitable to be applied in composites [122]. The foremost Aliphatic polyamides are known polyamide 6 that is generated by one type of monomer and has 6 carbon atoms and also made from ECL [91]. PA66 is also well known in Aliphatic polyamide and is polymerized from two monomers each of which contains 6 carbon atoms.

Hine et al [79] studied tensile and peeling properties of PA66 based SPCs prepared by the hot compaction and reinforced by woven PA66 multi-filaments. The influence of humidity on final mechanical properties of composites was investigated. They defined two sets of samples; immediately after hot-compaction processing (dry sample) and two weeks later in which 2% water had been absorbed by the compacted nylon sheets (wet sample). The PW obtained by 4°C. They concluded the tensile properties of dry sample was identical to PET based SPCs [67], whereas the wet sample was comparable with PP based SPCs [123]. The tensile modulus and yield strength (those properties that depended on local chain interactions) remarkably were affected by water uptake. They figured out that the value of peel load per 10 mm for wet sample PA66 based SPCs demonstrated week adhesive strength at a temperature of 80°C.

Duhovic et al [122] investigated on PA66 based SPCs prepared by film stacking technique with the processing window of 10°C. The PA66 matrix component (control sample) compression molded and then quenched in ice water. Their outcomes revealed an improvement of 28% and 160% in tensile stiffness (0.1GPa) and strength (78 MPa) compare to the starting isotropic PA66 film matrix. Moreover, the tensile stiffness was improved less than that of the hot compacted PA66 based SPCs which it was three times higher than that of the matrix-phase young modulus (5.8 against 1.9 GPa, both in a wet state) [79].

Bhattacharyya et al. [72] combined two basic techniques such as hot compaction and film stacking used for the preparation of PA6 based SPCs composed of melt-quenched PA6 film (Matrix) in the presence of PA6 high tenacity filament (as reinforcement). All reinforcements were treated by applying the antimony trioxide catalyst (Sb_2O_3) to improve the interfacial adhesion via trans-reactions. The processing window was obtained by 2°C. They concluded significant improvements on tensile modulus by 200% and the ultimate tensile strength by 300–400% as compared to the isotropic matrix film. Applying the catalyst was caused an improvement on tensile stiffness and strength by 30% and 32% for the dry samples (one-day preservation) and 8% and 20% for the wet samples (two weeks preservation) respectively.

Gong and Yong [124] studied the static and dynamic tensile properties of all-polyamide based SPCs prepared by film stacking technique. They applied acetone treated PA66 plain weave as reinforcement and PA6 film as matrix. The PW reported by 33°C. The range of cooling rate was set between 1 to 50°C/min. By descending the cooling rate, the TCL growth at the in the interphase region observed by polarizing microscope. Therefore, at the optimal processing window, the tensile strength of the composites (192 MPa) improved by 280% of the pure PA6 matrix component (69 MPa). Moreover, the

maximum loss tangent value of the composite at optimum processing window was achieved due to the better interfacial bonding of composite components (Figure 2.14).
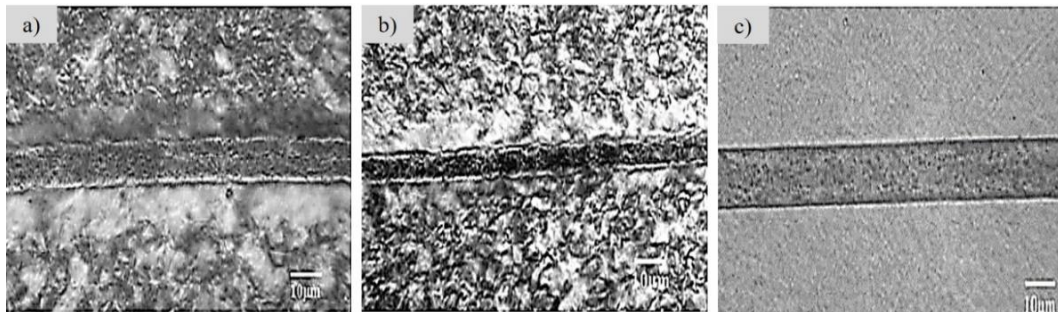
Figure 2.14. Transcrystallization of PA6 matrix on the PA66 fiber surface after different cooling methods in the a) hot press, b) air, c) water [124]

Gong et al [85] continued on the in situ anionic ring opening polymerization (AROP) of ε-caprolactam to prepare aliphatic PA6 based SPCs reinforced by PA6 Plain weave fabric. The tensile properties of PA6 based SPCs at mold temperatures of 140, 160, 180, and 200°C were studied. The optimum processing window of 20-80°C, high reaction degree (>93%), low void fraction (<2.5%) and strong and stable interfacial bonding were gained. Their results demonstrated better tensile strength (154 MPa) of PA6 based SPCs at optimum molding temperature (160°C) which was 108% modified than tensile strength of neat PA6 polymer (74 MPa) at the same molding temperature.

Gong and Yong [58] studied the effects of mold temperature (222–228°C), on tensile properties of PA6 based SPCs by partially melting the recycled PA6 cloth. The incipient melting temperature and the melting peak of constrained PA6 fibers were 222.7°C and 228.0°C, respectively. They concluded that the 31% of PA6 filaments were exactly melted to form the matrix at the optimum mold temperature of 226°C. Also, the tensile strength (138 MPa) of PA6 based SPCs was improved by105% of the one of neat PA6. Selection of higher mold temperature (228°C) was caused melting of a majority of PA6 filaments (82%) because of descendant orientation degree of PA6 molecules along fibers direction and reduction of the void fraction.

Dencheva et al [86] investigated on the influence of acetone surface treatment of PA6 filaments (as reinforcement) on tensile properties of PA6 based SPCs prepared by in-mold activated anionic ring-opening polymerization (AAROP) of caprolactam. Three polymerization temperatures such as 160, 165 and 170°C were employed. To obtain control specimen, the hydrolytic PA6 produced by compression. The polarized light microscopy (PLM) images showed the presence of oriented TCL at the interphase

region (Figure 2.15). Their results demonstrated that the PA6 based SPCs with 15–20 wt% reinforcements and solvent-pretreated of reinforcements prior to AAROP had remarkable improvement in stress at break of 70–80% and deformation at break (up to 150–190 %) using solvent-pretreated reinforcements outperform the neat APA6 matrix. Optimum temperature and processing window diagnosed by 165°C and 40-60°C respectively. The neat matrix APA6 anionically produced at 160°C displayed significant improvements on tensile stiffness (55%) and strength (44%) compare to hydrolytic PA6 sample.
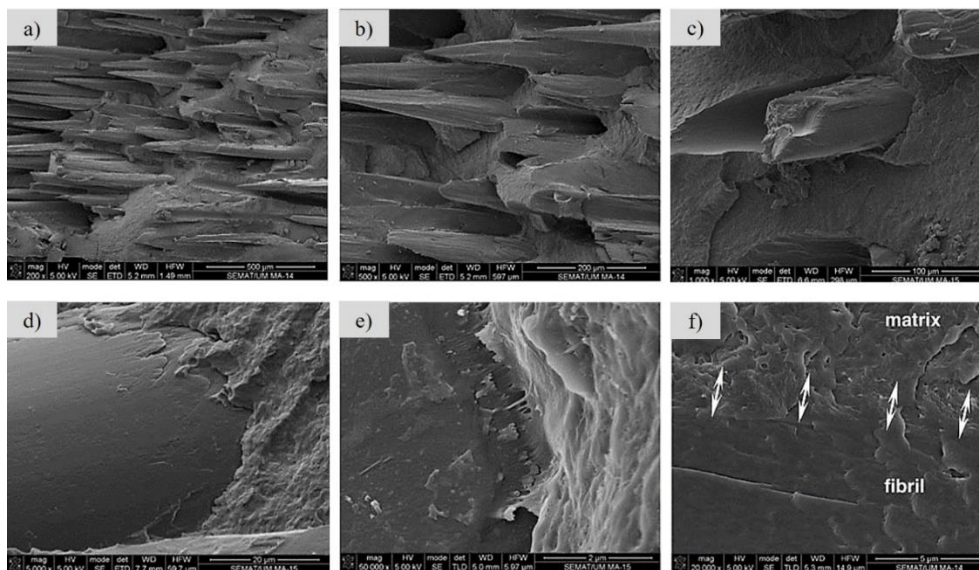
Figure 2.15. SEM images at different magnifications of the SPC sample with 20 wt% of PA6 monofilaments with acetone treatment. Arrows in image f indicate the thickness of TCL [86]

The recent work of Dencheva et al [125] disclosed new two-stage strategy for the preparation of all-polyamide laminate composites based on PA6 matrices reinforced by high volume fractions of PA66 textile structures and three different types of nano-clays. In the first stage, PA6 microcapsules loaded with montmorillonite nano-clays (MMT) were synthesized by solution/precipitation AAROP of ECL in the presence of three different organically treated MMT brands. In the second stage, the MMT-loaded microcapsules obtained with controlled molecular weight, composition and granulometry were compression molded in the presence of PA66 textile structures to produce the final dually reinforced laminate composites. Mechanical tests in tension, flexion, and impact for selected composites in this study showed up to 73% increase of the Young's modulus, up to 142% increase of the stress at break, and more than a fivefold increase of the notched impact resistance. One of the outcomes of this work was that the PA6 microcapsules (empty and with MMT loads) were produced with melting temperature of 206-207°C which is by 18°C lower than the melting point of hydrolytic PA6 brands typically used to produce PA6 textile structures.

Tohidi et al [126] investigated on textile reinforced SPC laminates produced by compression molding of PA6 knitted textile structures powder-coated of PA6 microparticles obtained by AAROP. The tensile properties of composites were studied in relation to the knitted reinforcement architecture (Rib1×1 and Jersey), fiber volume fraction (15, 20 and 25 V_f %), ply orientation (wale and course) and stacking orders (0/45/0 and 90/45/90). Polarized light microscopy and SEM studies evidenced a homogeneous distribution of PA6 monofilaments in the knitted reinforcements, without damage caused during the consolidation of the laminates by hot pressing. At the interface region, presence of a transcrystalline layer (TCL) was supposed based on thickness discrepancies between the annealed monofilaments and the ones embedded in the PA6 based SPCs (Figure 2.16). The results showed that the Rib reinforced PA6 based SPCs with fiber content 15% and all plies aligned along the wale direction, displayed the best improvement of tensile stiffness and strength as compared to anionic and conventional hydrolytic PA6 matrix. The fracture behavior of the PA6 based SPCs was found to depend on the deformation of the knitted reinforcements, in which crossover points were the main factors responsible for tensile failure.
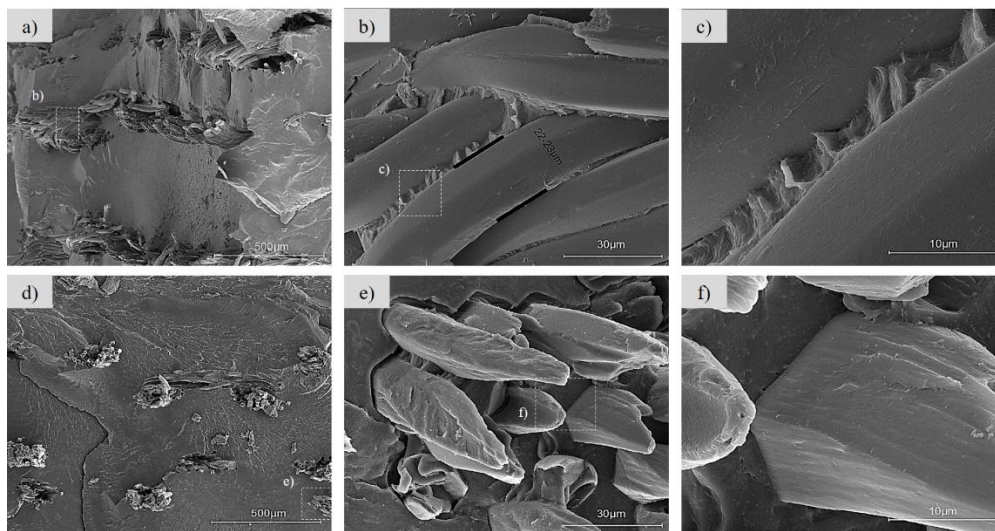
Figure 2.16. SEM images after cryofracture of PU-R15 composite; a-c) course direction d-f) wale direction [126].

Oliveira et al [127] studied on multiscale thermoplastic laminate composites based on PA6 dually reinforced by carbon fiber woven textile structures and different micron-sized metal particles using microencapsulation strategy. Two main steps appropriated comprising producing shell-core PA6 microcapsules (PAMC) loaded with 13–19% metal activated via AAROP of ECL in the presence of different metal particles. In the second step, the loaded PAMC were distributed between textile plies with fiber volume fractions $V_f = 25\%$ or $V_f = 50\%$. These structural results were correlated with the tensile and the

electrical properties. Their results showed a notable increase of the d.c electrical conductivity in 7 orders of magnitude for the CFT-metal laminates compare to the neat PA6. Moreover, this increase was concurrent by a 2.5–3.0 times growth of the tensile stiffness and stress at break. They concluded the microencapsulation strategy can be applied to produce multifunctional textile-metal-PA6 thermoplastic composites with tailored electrical and improved mechanical properties for advanced applications.

2.4.5. Aromatic-Aliphatic SPCs

A DuPont production composed of poly (para-phenylene terephthalamide) named Kevlar, is the other most used affinity of polyamides which is applied as the multipurpose reinforcing for polymer composites material. Kevlar is one of the important affinity of Aromatic polyamides produced from carbamide (urea). Unlike Aliphatic polyamide, the benzene rings join the chains of carbon atoms together. The two monomers are benzene-1,4-dicarboxylic acid and 1,4-diaminobenzene which are synthesized by removing water between the -COOH and -NH2 groups. Aramid filaments are used as reinforcements and because of containing highly crystalline microstructure, the better interfacial bonding and tensile properties are achieved [92]. Chemical, thermal, plasma treatments and in-situ polymerization of monomers onto functionalized fibers are applied to modify the electrostatic, adsorption interactions and interphase chemistry and morphology of Kevlar filaments in composite systems [121,128,129]. The properties of Aromatic-Aliphatic SPCs widely studied by many researchers owing to the wide processing window [128,130,139–141,131–138]. Although obtaining the proper interfacial bonding becomes a challenging issue [142–145]. Accordingly, the following literature reviews demonstrates the importance of interfacial bonding modification in Aromatic-Aliphatic SPCs.

Kukureka et al [130] studied the effect of fiber reinforcement on the friction and wear properties of injection molded carbon fiber-PA66 composite and aramid fiber-PA66 SPCs in rolling-sliding contact. The glass fiber-PA66 composite was prepared via extruded bar as reference sample. The aramid fiber reinforcement did not significantly change the friction of the matrix material although, both the carbon and glass fiber reinforcements reduced the coefficient of friction. Wear properties of the aramid and carbon fiber composites was essentially linear with time and generally around ten times greater than that of the unreinforced material. Reinforcing the PA66 with aramid fiber produced a significant increase in wear rate.

Interfacial bonding at the interface of aromatic-aliphatic SPCs was investigated by several researchers. Khondker et al [128] studied on Aramid-PA6 knit reinforced SPCs via combining film-stacking and hot compression molding techniques. Also, they prepared Aramid-epoxy knitted composite to compare interface region polymorphs. The degree of anisotropy in the mechanical properties was less severe in the Aramid-PA6 knit reinforced SPCs than Aramid-epoxy composite. Moreover, Aramid-PA6 samples exhibited relatively better interfacial adhesion property than aramid-epoxy composites. Eagles et al [131] investigated on interfacial properties of Kevlar 49-polyamide 12 (PA12) SPCs with two different surface treatments such sizing and water boiling (for six and half days). Five thermoplastic resins base comprising Ionomer, PE, PA12, polycarbonate and PMMA were applied as matrix components. The interfacial bond strength and frictional shear strength of sized Kevlar 49-PA12 SPCs increased due to the existence of hydrogen bonds between amide groups of Kevlar 49 and PA12.

Gordon et al [132] explored on wear and frictional properties of Aramid-PA46 SPCs under variations of the cycles number. The wear results from the twin-disc wear test rig showed an initial rapid rise in temperature (using a thermal video camera) followed by a slow decrease or a plateau trend. The SPCs failed by pitting and large cracks/fractures occurred at the relatively high loads and velocity. They were known as suitable materials for tribological applications like plastic gears. The friction and wear properties of chopped aramid fiber-PA66 SPCs had been investigated by Bolvari et al [133] wherein the PA66 was filled with and without polytetrafluoroethylene (PTFE). Their results showed that the tensile strength increased with higher fiber volume fraction and addition of PTFE was caused the reduction of the dynamic friction coefficient.

The weighted average orientation is determined by geometrical factors including the fiber volume fraction and the density of nucleation sites on the fiber surface. Klein et al [134] investigated on TCL properties of aramid fiber (Kevlar 29 and 49)-PA 66 SPCs. They prepared carbon-PA66 composites as reference sample. They concluded that most of the crystallites are not parallel to the fiber axis and their c-axis (the direction of the polymer chain) are inclined at right angles to the fiber axis which is a consequence of the crystal growth mechanism. They hypothesized six possible preferential arrangements of polymer chains in the TCL relative to the fiber axis. It was led to crystallite alignments that were consistent with the observed equatorial and meridional orientations (Figure 2.17). The X-ray diffraction patterns showed an alignment with either model (d) or (e) (Figure 2.17). In the nucleation and initial growth stages the first lamina (at the fiber surface) was oriented in such a way that the a-, b- and c-axis

of the constituent crystallites which was aligned in the radial, tangential and axial directions, respectively.
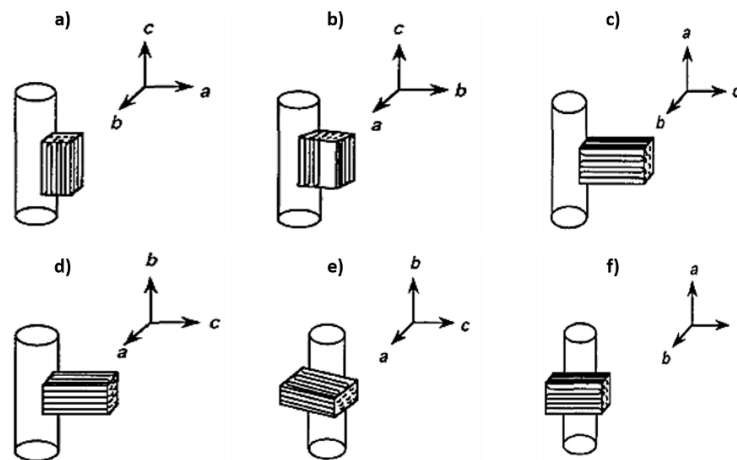
Figure 2.17. A schematic presentation of the six possible arrangements of the polymer chain in the transcrystalline layer relative to the fiber axis [134,146].

YU et al [135] dealt with the characterization of the mechanical properties of acetone treated Kevlar 29-polyamide SPCs. Two types of chemical treatments such as surface hydrolysis, and chemical grafting with succinyl chloride reactions and suberoyl chloride reactions performed on the fiber surface. Three types of polyamide matrices comprising PA6, PA11 and PA66 were selected in which the mechanical properties of chemical grafted Kevlar 29/PA6 SPCs remarkably were modified. The destructive influence of methacryloyl chloride was attributed to the polar nature of polyamide 6 whereas the end of the grafted molecule of methacryloyl chloride was non-polar. The size of the TCL zone and its crystal structure were affected by chemical treatments performances. Applying the Kevlar fibers induced a change in the crystallization at the interface while they were embedded in PA6, PA11 matrix and the chemical treatment of the reinforcements modified the nucleating ability.

Nuriel [136,137] investigated on two sets of unidirectional Kevlar-29-PA66 SPCs. They applied special fiber micro positioning device to produce unidirectional micro-composites by aligning filaments accurately on a PA66 film. The effective contribution of the TCL was generated only when the c-axis (chain axis) of the polymer in the TCL was parallel to the fiber (see Figure 2.17). The improvement in the longitudinal strength and stiffness was attributed to TCL advent and misalignment of the c-axis of the TCL.

Klein et al [138] investigated on the use of nucleating agent on the melt of PA66 in the presence of carbon and aramid (Kevlar29 or Kevlar49) fibers. The fibers found to behave like a giant nucleating site

producing a uniform TCL with the morphology and crystallization kinetics different from those of the bulk matrix. The values of activation energy were higher for the PA66 based SPCs than neat PA66. The presence of fibers with nucleating agent led to the development of a more ordered structure that required a larger amount of energy for crystallization (TCL). Shi et al [139] studied the formation TCL in Kevlar-129 fiber/PA6 SPCs. A single Kevlar fiber fixed onto a piece of glass slide with several pallets of PA6 and was then put into an oven for melting. The TCL appeared on the surface of Kevlar 129 fiber in the temperature range 130–190°C. Respect to presented six possible arrangements of the polymer chains in the TCL relative to the fiber axis (see Figure 2.17), model (b) diagnosed reasonable due to generation of epitaxial crystallization (hydrogen bonding) between composite component [134].

Feldman et al [140] investigated on induced different morphologies of the TCL in Kevlar 49 fibers-PA66 SPCs. All reinforcements were surface treated by two different methods to etch the Kevlar 49 fiber surface. The roughness of the fiber surface was increased and bi-layered structure comprising a compact inner layer (TCL) was generated (Figure 2.18a-c). The bi-layered structure was associated to a crystallographic transition "a" triclinic crystal structure to the "b" triclinic isomorph of PA66 (see Figure 2.17).
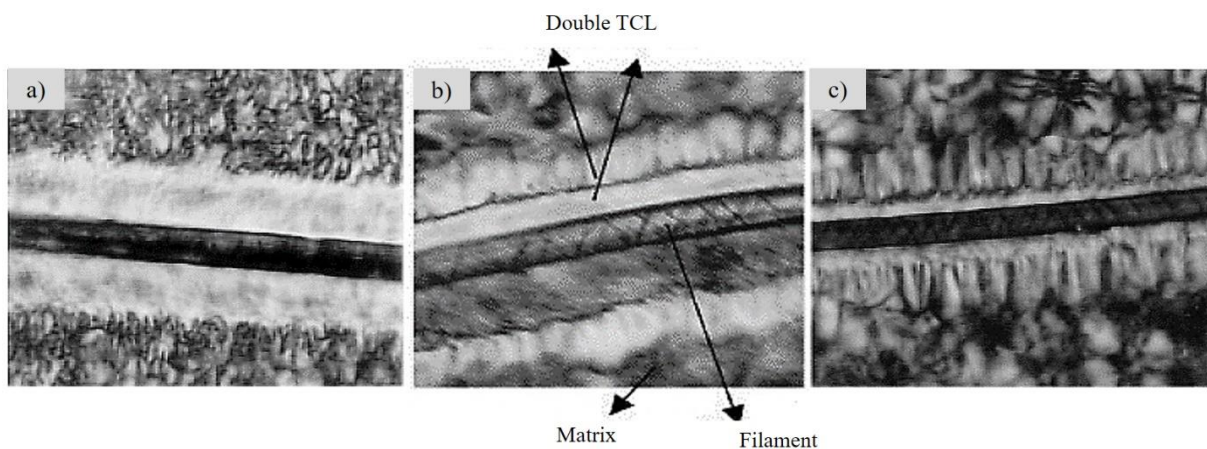
Figure 2.18. a) Polarized light microscopy pictures of transcrystallinity in aramid fiber reinforced nylon 66 with pristine (a), Br/NH3 treated; b) and chlorosulfonated fibers [140].

Feldman et al [141] investigated on microstructure behavior of the TCL under tensile stress on Kevlar 49 fiber-PA66 SPCs. The TCL was grown under a range of isothermal crystallizing temperatures from 170°C to 250°C using ice water quenching. The samples, crystallized at 220°C exhibited the stiffest TCL. That was in good agreement with XRD and mechanical results wherein the maximum value for tensile stiffness (1.8 GPa) and strength (68 MPa) were achieved.

2.5. Literature review on mechanical properties of textile reinforced composites

Textile reinforced composite have been receiving greater attention for likely structural applications such as aircraft and automotive industries due to the need for improvements in interlaminar shear strength, damage tolerance and through-thickness properties of composite materials. They are acquiescent to automated and efficient manufacturing techniques although having a complex geometrical structure of the textile reinforcement is caused numerous strength properties controlling [147]. Conventional textile techniques such as weaving, braiding, knitting and stitching are used to reinforce organic and inorganic materials and offer adequate structural integrity and shape-ability for near-net-shape manufacturing. This accomplish producing a wide range of two- and three-dimensional textile reinforced composites. Table 2.1 demonstrates alternative techniques of manufacturing textile reinforced composites.

Table 2.1. Various techniques of manufacturing textile reinforced composites (adapted from ref.[148]).

Textile reinforcements	2D structure	3D structure	Textile reinforcements	2D structure	3D structure
Woven	Biaxial	Biaxial	Nonwoven	Mechanical process	-
	Triaxial	Triaxial		Chemical process	-
		Multiaxial			
Knitted	Warp	Warp	Combination	Knitting + Weaving	Knitting + Weaving
	Weft	Weft		Knitting + Nonwoven	Knitting + Nonwoven
Braid	Flat	2 steps	Stitched	-	Lock
	Circular	4 steps		-	Chain
		Solid			

Mechanical properties of composites reinforced with woven, knitted and braided fabric have been studied extremely [149,150,159–168,151,169,152–158]. Meanwhile, a comprehensive review on reinforcement´s geometrical influences on mechanical properties of woven and knitted reinforced composites have been given in following paragraphs.

Knitted reinforcements are formed by a continuous length of filament into vertically intermeshed loops. Knitting methods is a method of interloping formed filament into loop which is released only after a succeeding loop and then intermeshed with it. They require a relatively fine, smooth and strong filament

with good elastic recovery properties. Afterward a secured ground loop structure is gained. Regard to the filaments feeding and knitting direction, knitted structures are basically classified into warp- and weft-knit structures. Warp knitted reinforcements are made by forming loops from filaments coming in parallel sheet configuration that run in the direction of fabric formation. Large numbers of filaments in parallel sheet form are supplied from warp beams [149].

In weft knitted structure, the filaments run in the widthwise direction with reference to the direction of fabric formation. In weft knit reinforcements, knitted loops are arranged in rows and columns known as wale and courses[7]. Sum of courses and wales individually are representative of length and width knit fabrics respectively. Moreover, Stitch Density[8] is a major terminology in knit reinforcements describes a total number of loops in a measured area of fabrics ($1.\,cm^{-2}$). In general, the structural filaments in weft knitted reinforcements are perpendicular to the fabric selvedge. Although, in the case of warp knitted reinforcements, the structural filaments run along the fabric length approximately parallel with the selvedge [150]. Weft-knit reinforcements are less rigid compare to the warp-knit structures. Warp knitted reinforced composites owns good stiffness and strength properties compare to those reinforced with weft knitted structures. Thus, they are suitable for primary and secondary load-bearing structural applications.

Producing complex and intricately shaped polymer composite parts containing good impact energy absorption and better drapeability require optimum molding condition. Meanwhile, to reduce the damage probability during the thermoforming process, replacing weft knitted reinforcements with the warp knitted and woven structure in the composite material is essential [151,152]. The main privileges of applying Knitted reinforcements as reinforcements are the milling procedure, material waste reduction and labor time-cost optimization. All these benefits are gained because of the par shape conformation of knit loop in weft knitted reinforcements.

Many researches have been conducted preliminary experimental studies to explore the effects of variables such as stitch density, knitted-fabric structure, number of plies of knitted fabrics, percentage pre-stretching of knitted fabrics, inlay fibers, tow size of yarn bundles on the mechanical properties of warp-knit [153–155] and weft-knit [151,152,156–162] reinforced composites. Following studies review the influences of filaments types, reinforcements architectures and fiber volume fraction, as well as

---

[7] Course density (CPC) ($\frac{1}{cm}$) is number of rows of loops across the width of fabric. In return, Wale density (WPC) $\frac{1}{cm}$ is number of column of loops across the length of fabric.

[8] Stitch Density=WPC×CPC

stacking order, on the mechanical properties of knitted reinforced composite materials.

Leong et al [170] investigated the effect of wale and course wise knit loop deformation on tensile and compressive properties of weft knit Milano composites. They found out the loop deformation transforms the transverse to shear mechanical failure in either loading axis, although the compressive fracture mode was insensitive to the fabric deformation. The loop leg and fiber crossover points were detected as prevalent tensile failure.

Khondker et al [171] studied the tensile behavior of the thermoset composites reinforced by Jersey and Milano knit textile structures along the wale and course directions. The fracture mechanism demonstrated that structural parameters such as fiber bending, crossover points and the relative fiber distribution along the two principal loading axes were largely distinguished as the state of the microstructural imperfections.

The influence of interfacial bonding on overall mechanical properties of thermoplastic weft knit aramid/nylon composite by varying molding time was studied by Khondker et al [128]. They compared the interfacial adhesion at the matrix/reinforcements interface by preparing the Aramid/epoxy composites as a control sample. They disclosed dialectic correlation between optimum mold condition and processing time with tensile properties of composites. The fractography analysis showed the better debonding forbearance (Figure 2.19).

They followed profound investigation on the effect of knit structural deformation for in-plane tension/compression properties and damage resistance of thermoset knitted Jersey, Rib1×1 and Milano-rib reinforced composites [172]. Their results revealed that deformation of knit-structural parameters such as loop curvature and crossover points were broadly correlated to the mechanical failure of the knitted reinforced composites.
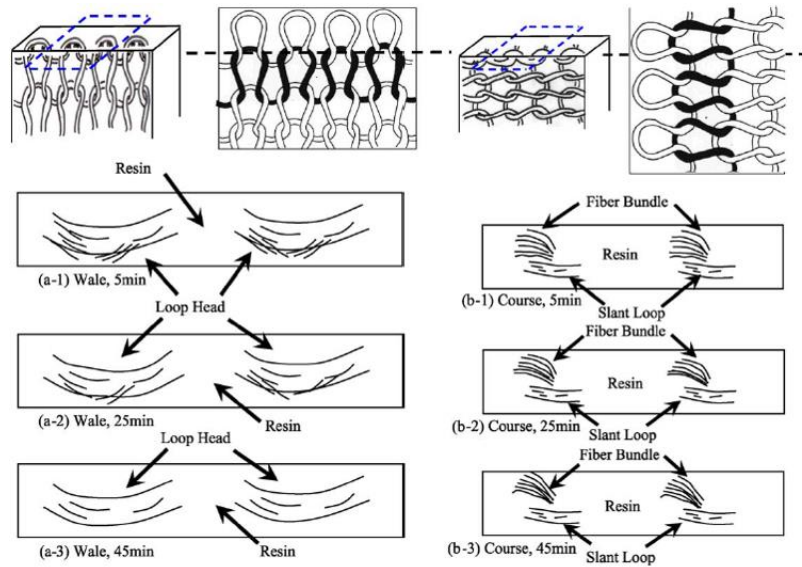
Figure 2.19. Schematic drawings of the fracture surface aspects in aramid/nylon plain weft knitted composites [128]

Ramakrishna and Hull [160] studied on tensile properties of Rib1×1 knit carbon/epoxy composite material via increasing fiber content. Their results showed that applying tow size spun yarn, inlay filament insertions and fiber content increment were led the mechanical improvement. Bini et al [173] studied the tensile properties of Jersey knit Kevlar/epoxy composites. Tensile tests performed at different off-axial angles (0°, 30°, 45°, 60° and 90°) with respect to the wale direction. The anisotropic study was carried out on both single-layered and multilayered (four-layered) knitted fabric composites. The elastic modulus and tensile strength were found to be the highest in the wale direction (110 MPa) but descended gradually towards the course direction (35 MPa). The tensile strength of the knitted fabric composite was higher while the loops were perfectly aligned parallel to the wale direction.

The mechanical properties of the tuck stitches knit fiberglass/epoxy composites have been studied by Alpyildiz et al [174]. Different knit patterns such as full Cardigan derivative knitted and Rib1×1 have been applied (Figure 2.20). It was found that the tuck stitches did not have a contributive effect on the tensile and compressive properties. The highest tensile strength (120 MPa) obtained for composites reinforced by Rib1×1 in wale directions although, in case of full cardigan composites, the tensile strength was identical in two principal directions (85-90 MPa).
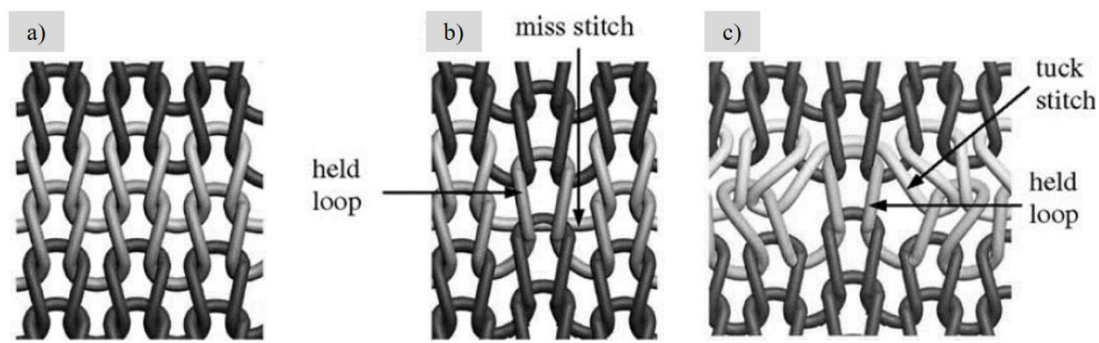
Figure 2.20. simulated Loop types, a) knit stitch; b) miss stitch; c) tuck stitch [175,176]

Putnoki et al [177] studied on tension, compression, impact and flexural properties of in tension deformed Jersey knit glass/PET composite prepared by hot press. Two types of PET matrix such as amorphous and semicrystalline polymorphs were considered in their study. They demonstrated embedding un-stretched reinforcements caused better flexural modulus and strength in wale direction by ca., 0.25 GPa and 600 MPa respectively. The increasing reinforcement deformation was due to the raise of flexural anisotropy and perforation impact energy of final composites.

Karger-Kociss and Czigany [178] characterized the dynamic-mechanical/thermal analysis spectra of hot pressed Jersey glass/PP composite under biaxial tensile and flexural loading. The lofting (thermal expansion) of composites explained the high residual thermal stresses in the matrix. It was resulted in the poorly bonded, "overstressed" glass fiber knits. The reason of the driving force of lofting lied on elastic recovery in the transverse direction. Meanwhile, the poorly bonded composite was not being kept in balance by the in-plane stress field where the interfacial shear stress was the dominating factor.

Gobi Kannan et al [179] were explored on Flexural and Izod impact properties of uni- and multi-directional flax yarn Jersey and Rib1×1 knit-PLA composites prepared via film stacking technique. They concluded that unidirectional lamination in wale direction had highest flexural (≈11 MPa) and impact (≈80 J/m) strength. Huang [180] studied the failure mechanism of four-point flexural tested of Jersey reinforced composite (six plies) beams. The composites were laminated by the stacking orders of $[(0)_6]$, $[(90)_6]$, $[0/(90)_4/0]$, $[90/(0)_4/90]$, and $[0/45/(-45)_2/45/0]$. They figured out the highest flexural strength (180.7 MPa) was obtained for unidirectional knitted reinforced composites (Figure 2.21).
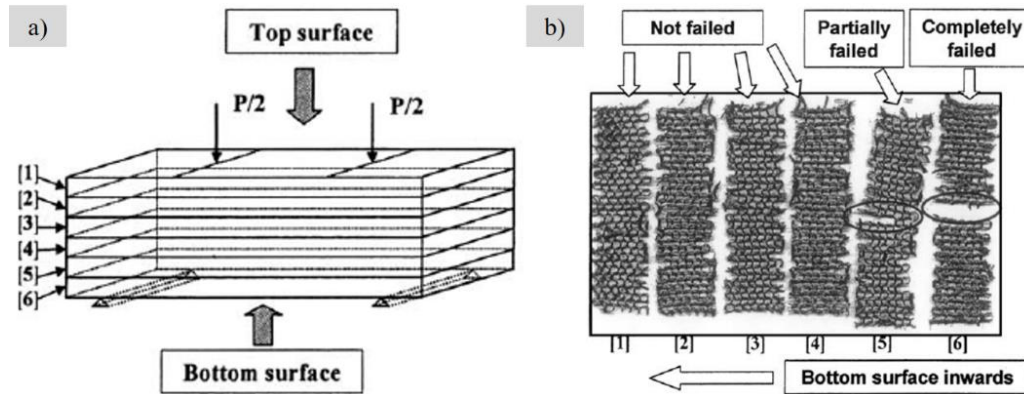
Figure 2.21. Failure mode of a laminated beam with knitted fabric reinforcement after four-point bending test: (a) beam schematic, b) fabric details after matrix combustion [180].

Pandita et al [181] investigated on the drop weight impact properties (3, 5, and 7 Joule/mm incident kinetic energies) of Rib1×1, Milano, Full cardigan and Interlock knit reinforced composites. They considered two types of impact load such as dynamic and static indentation loads. The former dedicated to gradually decreasing of projectile velocity while the kinetic energy had been absorbed by the test sample and the later was allocated to the constant projectile velocity. Rib1×1 reinforced composites owned higher degree of anisotropy (via ultrasonic C-scan analysis and X-ray tomography) caused to confine perpendicularly impact damage region to the weakest direction of the tensile properties (course direction). Although the impact fracture was distributed in all direction for knit Milano reinforced composites because of containing the low degree of anisotropy.

Khondkera and colleagues [172] dealt with the effect of Milano, Rib 1×1 and Plain architecture on the low-velocity drop weight impact (with 1.7 and 27.3 J incident impact energies) of glass/vinyl-ester composites. Their results showed that apparent mesh size[9] of the knit structures decreased by the higher value of total loop density which provided better through-thickness-strength of knit composite materials. Moreover, the interlaminar fracture toughness was improved by better knitted-mesh generation and followed by proper impact resistance to damage.

Karger-Kocsis et al [182] studied on low-energy and perforation impact conditions of Rib1×1 knit carbon/poly(ethyl methacrylate) (PEMA) and poly(ether ketone) (PEEK) with 35 and 51 % volume fraction respectively. The highest thickness-related perforation impact energy was found for the composites with

---

[9] The inverse value of volumetric total loop density or the integrity index, presented as following equation:

$$\text{Apparent mesh size} = \frac{\text{Specimen tickness (mm)}}{\text{Fabric areal loop density} \left(\frac{\text{Loops}}{\text{mm}^2}\right) \times \text{numberof fabric layers}}$$

PEEK matrix component ($\approx$15 J/mm) due to the high fiber content, high matrix ductility, and better fiber/matrix bonding. Aktas and colleagues [183] investigated the effect of impact behavior (applying 5–25 J impact energies) of eight layers Plain, Milano, and Rib1×1 E-glass/epoxy composite plates. Their results revealed that the maximum and minimum contact forces belonged to Rib1×1 and Jersey knitted fabric composites respectively. The failure modes were categorized by fiber splitting and the cracking at the level of penetration and perforation.

Filament´s orientation determine the stiffness properties and thermal expansion coefficients of composites. Thus, woven fabric composites are applied commonly while more than one filament orientation is required. A woven reinforcement is composed of two sets of interlacing, mutually orthogonal yarns and is woven on a loom in which its architecture is illustrated by the interlacing pattern of the warp and weft filaments. A small repeating unit cell (RUC) are identified as the periodicity of the repeating pattern in a woven structure that is sufficient to describe the fabric architecture. The yarn undulation or 'crimp' is created by the interlacing of the yarns in woven fabric.

The mechanical properties of woven reinforced composites are governed by weave parameters such as weave architecture, yarn sizes, yarn spacing, yarn crimp and laminate parameters including stacking orientations and overall fiber volume fraction. The explicit architecture of woven reinforcements in composites is causes higher specific mechanical strength, superior corrosion resistance and better fatigue properties compare to those reinforced by knitted structures.

Influence of woven fabrics geometrical parameters on mechanical properties of composite materials have long taken the attention of many researchers [13,163–169,184]. Junior et al [163] studied the effect of the fiber volume fraction (25% to 45%) and orientation of the ramie fibers in plain woven hybrid ramie-cotton/polyester composites. Their results showed an improvement in the tensile strength of composites with 45 wt% fiber contents (warp direction) up to 338% compare to the reference neat polyester resin. Influence of different woven geometries and plie orientations on tensile and flexural woven thermoplastic composites based on E glass[10] impregnated tow-preg tape/acrylonitrile butadiene styrene (ABS) investigated by Mariatti et al [13]. They applied woven reinforcements with different patters such as plain, (2x2) basket, (2x1) twill and 4-end satin. They concluded that the mechanical properties of satin

---

[10] E-glass is known for its strength and electrical resistance and mostly applied in the fiber reinforced polymer composite industry.

reinforced composites were higher than those reinforced by other structure.

Osada et al [164] studied the influence of micro-fracture behaviors of glass Plain and Satin woven/acryl silane coupling agent and vinyl ester composites on tensile properties. The effect of reinforcement structural parameters such as geometry of textile fabric (Plain and Satin), crimp ratio and aspect ratio on the initial fracture behavior of composites (knee point) were observed via edge surface replica observation. They showed that the low crimp ratio of warp fiber bundle in satin architecture was led to difficulty in bending deformation to the weft fiber bundle. Moreover, the stress concentration in the smaller aspect ratio of fiber bundle scarcely was occurred and gave rise to the onset of the transverse crack in which the higher knee point stress was detected (Figure 2.22).
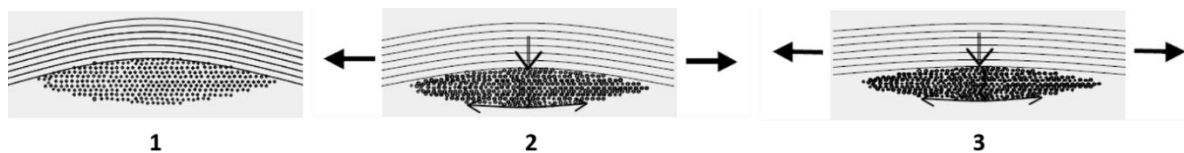
Figure 2.22. Initial fracture mechanism in plain woven fabric composite [164]

Gao et al [165,166] investigated on damage development of fiber eight-harness satin carbon/polyimide composites. To detect the fracture mechanism, quasi-static (discontinuous) tensile tests performed wherein the composite materials were loaded up to progressively higher strain. Moreover, Acoustic emission monitoring applied to illustrate the onset and accumulation of transverse matrix cracking. The transverse matrix cracking and delamination at crimp regions was the major fractural parameters. The maximum length of the delamination was identical with the crimping length causing the minor tensile stiffness of the laminates.

Todo et al [184] evaluated the effect of various strain rates ranging from 1×10^{-2} to 1×10^{1} s, on tensile properties of four different plain woven/polyamide composites. Two types of reinforcement´s material type such as carbon fiber (CF) and glass fiber (GF) and two kinds of matrices comprising polyamide-6 (PA6) and modified polyamide-6 (mPA6) were used. Their results demonstrated an increase in tensile strength and failure strain of the composite materials via strain rate elevation. The better tensile performance in all testing rates was achieved for CF-mPA6 composites. The extensive microcracking was detected in the matrix and transverse region of yarns prior to breakage via polarized light microscopy studies.

The bearing strength of woven GF-epoxy composites pinned joints with three different linear densities (200, 270, and 300 g. m^{-2}) was studied by Asi et al [167]. Aside woven fabric linear densities, fiber volume fraction, void content, and geometric parameters were determined as key parameters on bearing strength properties. Three different failure modes consist of bearing and shear out and net-tension were detected in association with geometric parameters. Increasing the reinforcement linear densities increased the void content.

The internal micro- and meso-geometry of the reinforcement are the main part of damage mechanism in textile reinforced composites. The test sequence intended to characterize tensile damage of tri-axial braid quasi-unidirectional woven/epoxy composites had been investigated by Lomov et al [168]. A full-field strain measurement on the surface and acoustic emission (AE) registration had been carried out to detect the first (ε_1), well-developed (ε_2) and just before the final (ε_3) fracture of the samples. They concluded that the damage initiation established by of transverse cracks (inter-filament, intra-yarn failure), delamination on the fiber bundle´s boundaries and the onset of filament failure at the ultimate failure of the sample.

Pandita et al [169] studied on anisotropic tensile fatigue behavior of fiber E-Glass plain woven-epoxy composites. SEM and acoustic emission techniques were applied due to detecting the influence of fatigue stress ratio and frequency in either principal test directions. They concluded the fatigue damage in the on-axis directions began transversely (Figure 2.23). Afterward, it grew and deflected through the matrix component and along the filament length. Embedded filaments showed vulnerable durability during off-axis test direction in which the residual properties declined quickly.
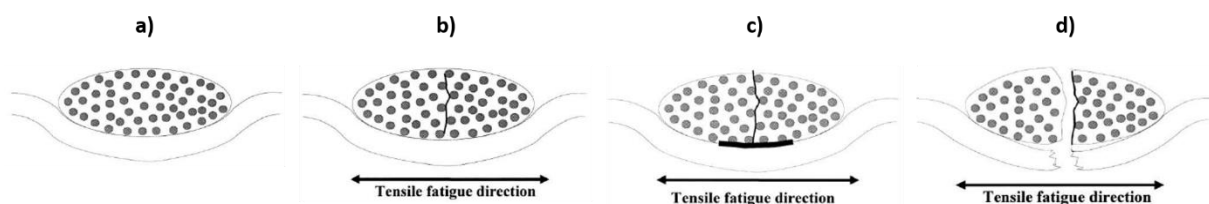
Figure 2.23. Schematic of the tensile fatigue development in woven reinforced composites subjected to a tensile fatigue load at the weft direction a) no fatigue failure; b) Crack in transverse filament; c) Meta delamination d) filaments fracture at the longitudinal direction [169].

Chapter 3

Experimental and test methods

3.1. Introduction

The present chapter begins with the preparation of SPCs precursors and the equipment used to the determined purposes. Subsequently, description of physical analysis of knitted and woven reinforcements is given in next section. This is followed by an introduction on thermal and polymorph characterization. Eventually the mechanical characterization techniques including tensile, flexural and impact test are described in this study.

3.2. Materials

3.2.1. Textile Reinforcements

Three different reinforcements were selected in this study such as knitted, woven and stitched plain fabrics. The air jet textured[1] PA6 continuous filament (160 dtex[2]) was applied to prepare the textile reinforcements and commercialized by QTT, Portugal. The selection of air jet textured yarns essentially was caused introducing bulkiness into yarns structure followed by the probability of mono-filament's entanglement. To minimize contaminations, all reinforcements were pre-washed with $1\,\mathrm{g.\,L^{-1}}$ of non-ionic detergent solution at 40°C for 30 min and then rinsed with reverse osmosis water for another 15 min. All Reinforcements were immersed in acetone for 30 min and dried for 2 h at 60°C due to the elimination of any non-chemically bonded finish on filaments surfaces.

In this study, two alternative reinforcement architectures comprising Jersey and Rib 1×1 were selected (Figure 3.1a-c). Jersey knit reinforcements are known as the simplest and most basic knit structure in which all the loops are intermeshed in the same direction and produced by only one set of the needles (Figure 3.1a-b). Rib 1×1 architectures are the second basic family of weft knit structures those require two sets of needles operating in between each (Figure 3.1c). Compare to the Rib 1×1 architecture, Jersey reinforcement contains the different front and back technical faces, less expensive, lighter structure, less extensible, thinner and have the tendency to curl.

---

[1] Air jet texturing is carried out by feeding a wet a single type of yarn or with a blend of filament yarns or a dry yarn plus a small amount of water into a high-speed jet of air.

[2] dtex is a unit of measure for the linear mass density of fibers, yarns and filaments which is defined as the mass in grams per 10000 meters.
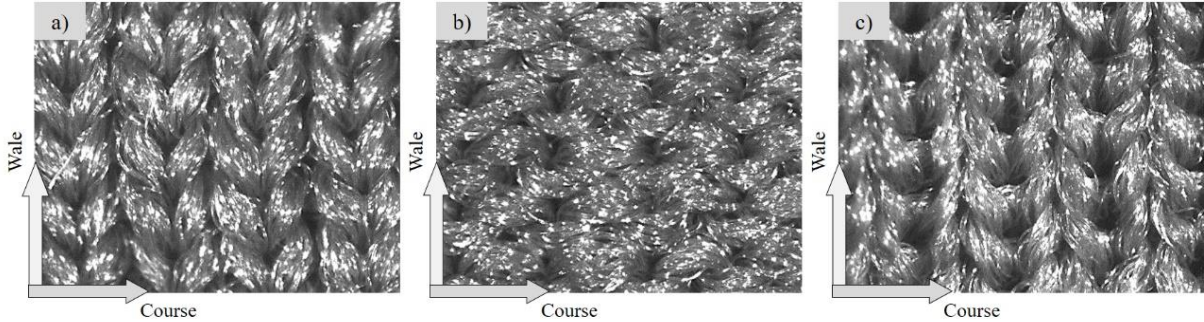
Figure 3.1. The architecture of weft knitted reinforcements a) Jersey-Technical front face b) Jersey-Technical back face c) Rib 1×1

In this study, all woven reinforcements were produced by the NHJM2 53 6/42 Z4 machine and delivered from Jackob Muller Company AG®, Switzerland. The Jakob muller loom is an electronically controlled narrow fabric needle loom for Jacquard-patterned articles with a warp effect and unlimited repeat lengths, which can be linked with optional MUCAD MINI/MICRO direct transfer software (Figure 3.2a). The interlacing of the warp (0°) and weft (90°) filaments in a regular pattern produced the woven fabrics in which the mechanical interlocking of the filament maintains the fabric's integrity.
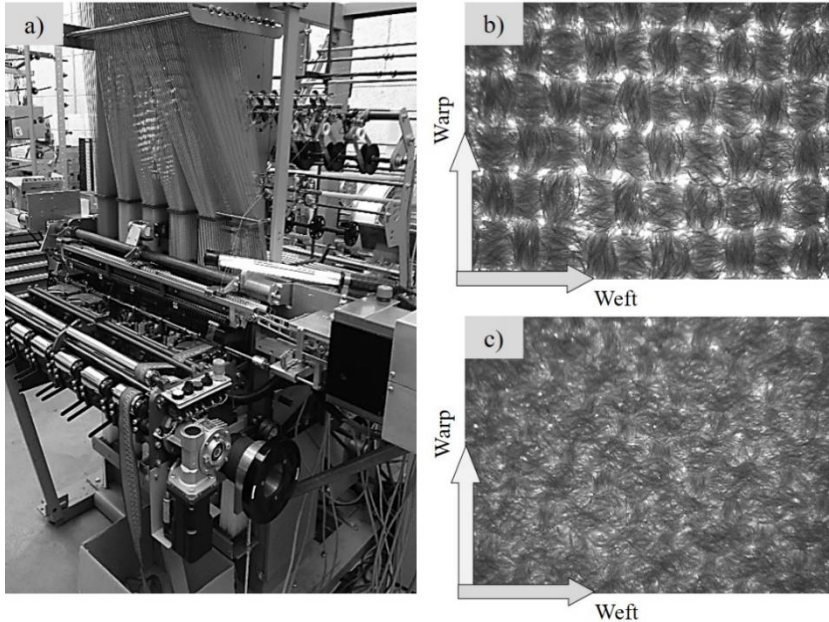
Figure 3.2. a) Patented NHJM2 53 6/42 Z4 machine by Jackob Muller (JM) Company AG®, Switzerland; b) Untreated Plain; c) Untreated Satin reinforcements

In the present study, two basic alternative reinforcement patterns such as Plain and Satin (5 Harness[3])

---

[3] The total number of fibers crossed and passed under, before the filament repeats the pattern is called Harness which is typically 4, 5 and 8 in the designation.

were selected (Figure 3.2b-c). The plain reinforcements patterned by alternatively undulation of warps under and over each weft filaments. The warp and weft density ($1. cm^{-1}$) are presented by WAPC and WEPC respectively. Being symmetrical, good stability and reasonable porosity, as well as drape less and the high level of filament crimp ratio, were their main advantages. Satin patterns were selected to produce fewer intersections of warp and weft. low stability, low crimp ratio and asymmetric pattern were their main benefits. Satin reinforcements own asymmetric structure. In one face, filaments run predominantly in the warp direction although the other face has filaments running mostly in the weft direction.

Stitched woven reinforcement are novel woven fabrics affinity (patented by JM) that contained two different sets including the base woven structure and the stitched diagonal filament (SDF) (Figure 3.3a). The woven base structure is made of any conventional woven patterns and SDF seams in spiral path at the determined spots. Defining the stitching spots set the gradient of the spirals. Three stitch gradients 30°, 45° and 60° with the plain weave substrate were selected in this study (Figure 3.3b-d). To weave stitched woven reinforcements, the feeding system in NHJM2 53 6/42 Z4 machine (see Figure 3.3e) was driven by separate stepper motors and became smoothly aligned with the warp and weft filaments arrangement.
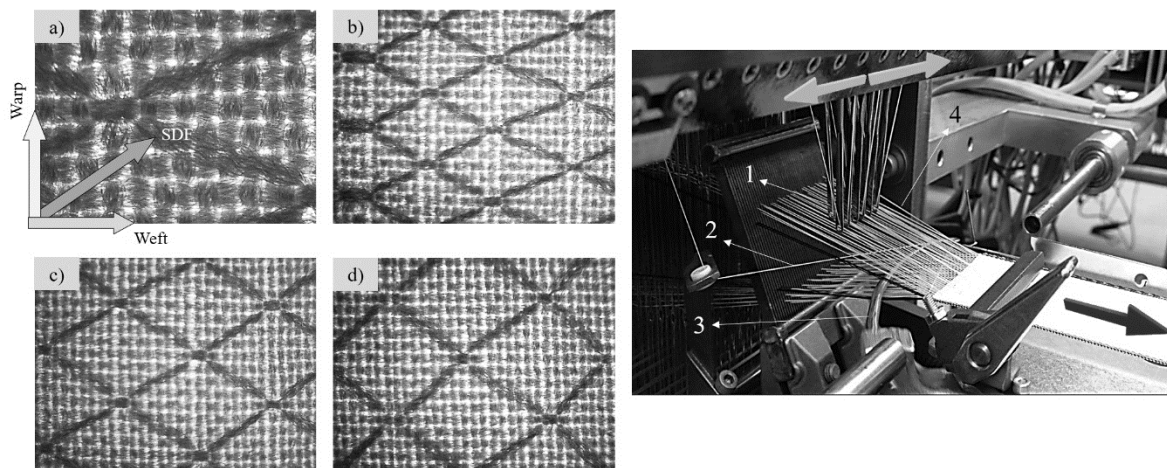
Figure 3.3. a) Back lighted microscopic images of Stitched Plain reinforcements. Structural demonstration of stitched woven fabrics with b) 30°; c) 45°; d) 60° SDF gradients; e) Dynamic illustration of weaving stitched woven fabrics with patented NHJM2 53 6/42 Z4 machine (1- SDF translating feeder, 2- Weft System, 3- Weft feeding system, 4- Warp System).

Table 3.1 demonstrated the major physical properties of all reinforcements such as sample designation, areal weight and thickness of all reinforcements.

Table 3.1. Summary of physical properties of all applied reinforcements

Woven Reinforcements	Designation	Areal weight ($g.m^{-2}$)	Thickness (mm)	WPC×CPC	WAPC×WEPC
Rib	R	207.72 ± 4.08	0.79 ± 0.01	16×25	-
Jersey	J	159.95 ± 3.69	0.54 ± 0.01	16×30	-
Plain	P	147.63 ± 1.72	0.58 ± 0.01	-	22×16
Satin	S	142.39 ± 2.31	1.00 ± 0.02	-	22×16
Stitched Plan with 30° SDF	SP30	138.44 ± 0.95	0.61 ± 0.01	-	22×14
Stitched Plan with 45° SDF	SP45	128.80 ± 1.81	0.55 ± 0.01	-	22×14
Stitched Plan with 60° SDF	SP60	131.31 ± 2.04	0.55 ± 0.01	-	22×14

3.2.2. Stretching-annealing treatment of textile reinforcements

The stretching-annealing treatment is a thermo-mechanic treatment to heat a material above its recrystallization temperature. This process is followed by cooling procedure to improve their mechanical properties. Materials made of linear and branched polymers hold their configuration during the cooling process. However, by applying heat, these materials become soften and eventually molten. At this level, the molecules do not cross-link by covalent bonds and overcome the intermolecular forces and flow past one another. Therefore, annealing procedure aims reducing tensions and ensure the formation of an even crystalline structure in the textile reinforcement. In this study, to optimize the mechanical properties of the textile reinforcements, all of them were stretched to 30% of their original length along the two principal directions, using a screen stretching apparatus (Figure 3.4a). Once stretched, the reinforcements were annealed with fixed ends at 170 °C for 90 min using a specially designed metal frame (Figure 3.4b).
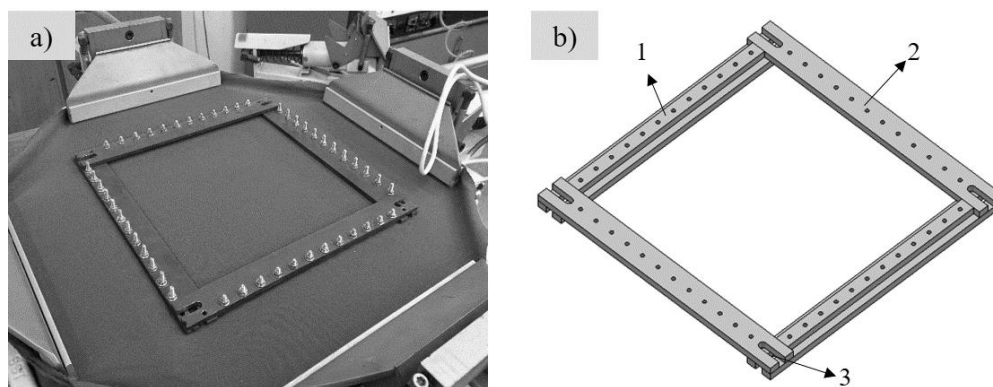
Figure 3.4. Preparation of the textile structures: a) biaxial stretching screen stretcher apparatus; b) adjustable metallic frame applied in the stretching-annealing treatment with fixed ends (1- Constant coupler, 2- Versatile coupler, 3- Fixation joint).

Table 3.2 shows the sample designation, measured areal weight and thickness of all textile

reinforcements before and after the washing, drying and annealing cycle designated as "treatment". Comparing Table 3.1 and Table 3.2 shows that the remarkable structural-physical differences textile reinforcements after stretching-annealing.

Table 3.2. Summary of All reinforcements physical properties after annealing process

Woven Reinforcements	Designation	Areal weight $(g.m^{-2})$	Thickness (mm)	WPC×CPC	WAPC×WEPC
Annealed Rib	R-A	108.46 ± 1.58	0.60 ± 0.01	13×18	-
Annealed Jersey	J-A	101.86 ± 1.53	0.41 ± 0.01	15×25	-
Annealed Plain	P-A	111.04 ± 2.10	0.42 ± 0.01	-	20×12
Annealed Satin	S-A	106.49 ± 1.58	0.46 ± 0.01	-	20×12
Annealed Stitched Plan with 30° SDF	SP30-A	111.78 ± 2.01	0.41 ± 0.01	-	19×12
Annealed Stitched Plan with 45° SDF	SP45-A	108.67 ± 1.60	0.37 ± 0.01	-	19×12
Annealed Stitched Plan with 60° SDF	SP60-A	110.37 ± 2.15	0.38 ± 0.01	-	19×12

3.2.3. Chemical reagents and solvents

All the solvents used in this work ("purum" grade) were obtained from Sigma Aldrich and used as received. The ε-caprolactam (ECL) monomer with reduced moisture content suitable for AAROP was delivered by Brüggemann Chemical, Germany. Before use, it was kept under vacuum for 1 h at 23°C. As polymerization activator, Bruggolen C20P (C20) from Brüggemann Chemical, Germany was applied. According to the manufacturer data, C20 contains 80 wt% of blocked diisocyanate in ECL. The initiator sodium dicaprolactamato- bis-(2-methoxyethoxo)-aluminate (80 wt% in toluene, DL) was purchased from Katchem and used without further treatment.

3.3. Preparation of SPCs

3.3.1. Polyamide 6 microparticles synthetization

As known from detailed earlier studies [62,185], the initiation and propagation of lactam AAROP require an anionic initiator and an activator including imide links C(O)-N-C(O)-. Being expensive and high melting temperature (>260°C) and requiring more production cycles were known to prefer caprolactam rather cyclic oligomers [59]. The C20 was comprised of two performed imide links to propagate the

reaction [86,186]. Organo-aluminum compound, containing a stabilized caprolactamate anion in initiator enhanced to delocalization of negative charge [86]. This is because of the existence of lactam anion leading to declining the nucleophility and coordinate Al atom with the lactam carbonyl oxygen [187]. Thus, this initiator reacts slower rather than simple sodium caprolactamate.

The solution-precipitation AAROP of ECL to PA6 microparticles (MPs) was performed as described previously [62,185]. The lactam was dissolved in a 1:1 v/v toluene/xylene mixture (purchased from Sigma-Aldrich) under nitrogen atmosphere refluxing the reaction mixture for 10-15 min. In several minutes, clear solutions were obtained and the components of the catalytic system DL and C20 were introduced in a molar ratio 1:2. The reaction time was 1 h, keeping the temperature in the 125-135°C range at constant stirring. Thus, MPs were produced in the form of fine powder, separated from the reaction mixture by vacuum filtration, washed with methanol and dried. The chemical reaction of AAROP in this study is schematized as shown in Figure 3.5.
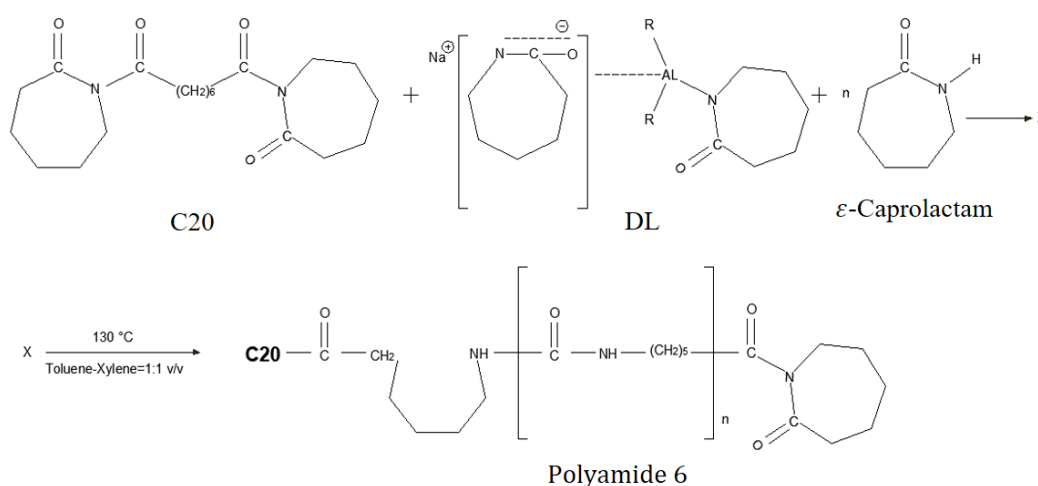
Figure 3.5. Chemical reactions occurring during AAROP in solution (R=OCH$_2$CH$_2$OCH$_3$).

The polymerization of ECL to MPs was performed using a mixed hydrocarbon solvent able to dissolve all the components of the reaction mixture. It is important that this catalyst system should remain active in the presence of solvent employed. The growing PA6 chains began form initially viscous, low molecular weight particles. Subsequently, the final MPs upon additional propagation, coalescence and crystallization was produced (Figure 3.6a-c). The diameter ranges and average roundness ($\frac{d_{max}}{d_{min}}$) of MPs were measured between 35-50 μ_m and 1.2-1.3 respectively.
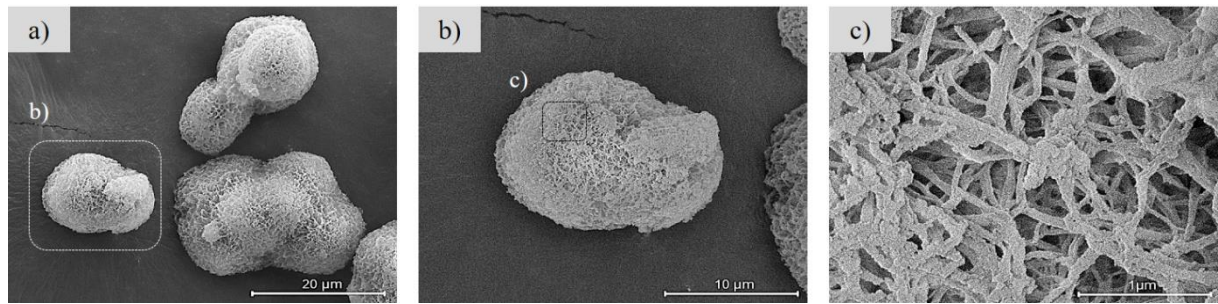
Figure 3.6. a-c) Selected SEM micrographs of PA6 microparticles (MPs) at three different magnifications.

3.3.2. Preparation of SPCs via NYRIM technique (N-composites)

One of the techniques used to prepare SPCs for this study is based on the activated anionic polymerization of ECL in a specially designed prototype equipment developed for reactive injection molding to nylons (NYRIM) (Figure 3.7a). In a typical preparation, 0.33 mol ECL was heated to 90°C under nitrogen flux and then 1.5 mmol of the DL initiator were added. After 60 min at temperatures between 90–110°C, 0.75 mmol of activator C20 was added to the mixture at once. The resulting activated monomer/initiator mixture was injected into the mold (80×80×3mm), preheated to 120°C, where the annealed reinforcements were already installed, oriented in the wales direction (0) (Figure 3.7b). In case knitted textile structures, the elliptical perforations on the vertices of reinforcements helped to keep the knitted structure in place, avoiding fabric jamming (Figure 3.7b).
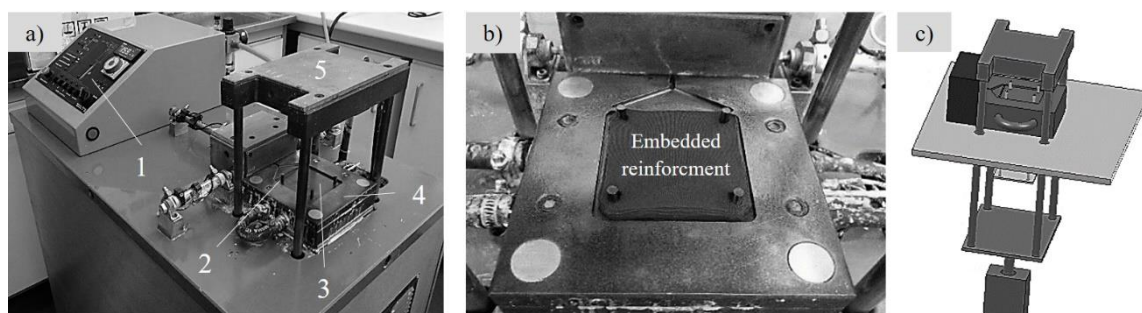
Figure 3.7. a) Prototype equipment for reactive injection molding of nylons (NYRIM) (1-Thermal hydraulic controller, 2-Extractor beam, 3- Mold cavity, 4- Fixed bottom mold, 5- Dynamic top mold); b) In-mold reinforcement installation; c) CAD Progression due to reinforcement installation assessment.

The polymerization temperature was kept in the range of 160–170°C, setting the reaction time at 15 min. After that time, the mold was cooled down automatically to 65°C at a cooling rate of $40°C. \text{min}^{-1}$ followed by demolding of the laminate plate prepared by NYRIM technique (N-composites). To optimize the in-mold installation of textile reinforcement, the NYRIM mold was simulated using SolidWorks, version 2014-2015 (Figure 3.7c).

3.3.3. Preparation of SPCs via PCCM technique (P-composites)

The solution-precipitation AAROP of ECL to PA6 microparticles (MPs) was performed as described in detail previously [62,125,185,188,189]. The chemical reaction of AAROP in this study is schematized in (Figure 3.5). Summarizing the preparation procedure, the amount of 2 mol ECL was dissolved in a 1:1 v/v toluene/xylene mixture under nitrogen atmosphere refluxing the reaction mixture for 10-15 min. In several minutes, clear solutions were obtained and the components of the catalytic system DL and C20 were introduced in a molar ratio 2:1. The reaction time was 1 h, keeping the temperature in the 125-135°C range at constant stirring. Thus, the MPs were produced in the form of fine powder, separated from the reaction mixture by vacuum filtration, washed with methanol and dried.

The SPCs were produced by the Powder coated compression molding (PCCM) method (P-composite) in the following way. The plies of reinforcements and previously calculated amounts of MPs were deposited into the mold before compression molding (Figure 3.8a). For the preparation of laminate composites of k plies, the MPs were divided into (k+1) equal portions and the respective ply sets were prepared. The consolidation of the ply sets by compression molding was performed in a Moore hydraulic hot press (UK) using a mold with dimensions 70×70×2mm. The pressure applied was 5 MPa for 10 min at 215°C and the samples were subsequently cooled down to 50°C at a rate of ca. $50 \, °C.\min^{-1}$ (Figure 3.8b-c).
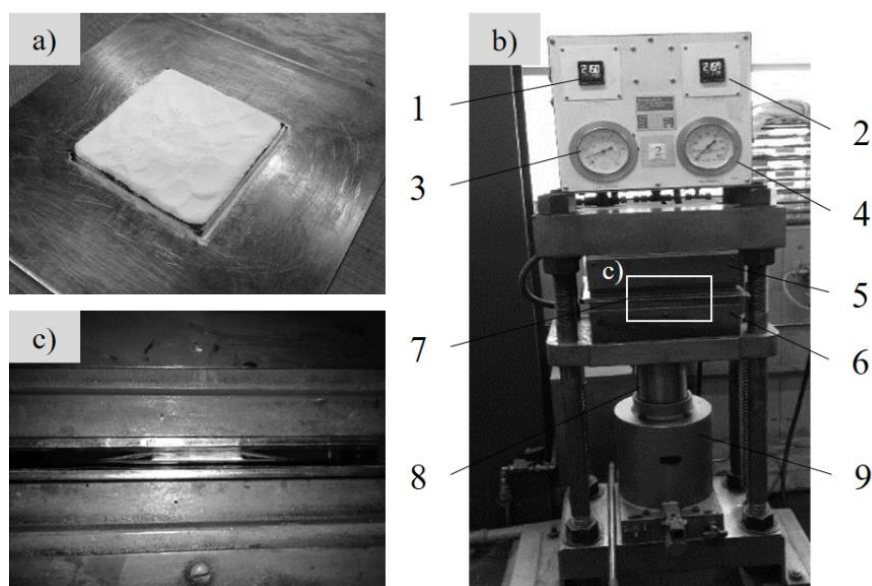
Figure 3.8. a) Stacking set of knitted reinforcements and MPs; b) hydraulic hot press and parts description (1- Top thermo-controller, 2- Bottom mold thermo-controller, 3- Top mold hydraulic pressure indicator, 4- Bottom mold hydraulic pressure indicator, 5- Dynamic top mold, 6- Fixed bottom mold, 7- Sample, 8- hydraulic jack, 9- Manual mold pressure controller)

In such a way all SPCs with three fiber volume fractions V_f were prepared, i.e., 15, 20 and 25%. The necessary number of textile plies for each V_f value was determined according to Eq. 1 [190].

$$V_f = \frac{A_w.N}{\rho_f.T} \tag{3-1}$$

wherein A_w $(g.m^{-2})$ is the area density of the reinforcement textile, N is the number of plies, ρ_f $(g.m^{-3})$ is the density of the PA6 textile filaments and T in (m) is the laminate thickness. The knit reinforcements were stacked unidirectionally or in different directions.

The stretched and annealed Rib and Jersey reinforcements had thickness of 0.6 mm and 0.4 mm, respectively which were higher than woven structures. Five plies of R-A and six plies of J-A reinforcements corresponding to 25% of fiber content was the maximum that the mold with 2 mm thickness could accommodate without textile damage after compression molding. The attempt to compression mold higher volume fraction of fibers i.e., 30% caused rupture of the embedded knitted structures. The Figure 3.9a-b illustrates the said textile rupture. So the maximum fiber content of 25% was used in this work, adding two more fiber concentrations of 15% and 20% to study the effect of fiber content on the mechanical properties.
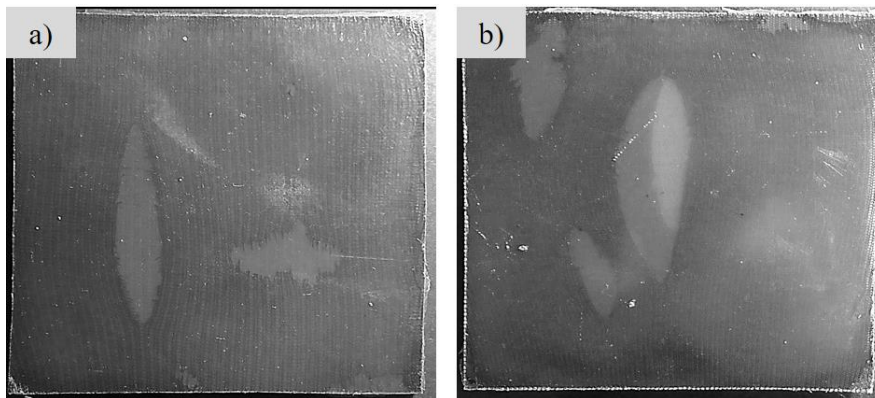
Figure 3.9. High internal pressure and rupturing of the embedded knitted textile reinforcements due to the in-mold fiber content overloading; a) Rib reinforced KSPCs; b) Jersey reinforced composites with 30 V_f, %

Back to the selection of 15% V_f as optimum volume fraction, multidirectional knitted reinforced SPCs were prepared through the PCCM technique. Therefore, two sets of multidirectional laminations such as (0/45/0) and (90/45/90) were chosen. Embedding 45° inclined lamina enhanced to comprehend the effect of symmetrical multidirectional lamination on final mechanical properties of these class of composites.

3.4.   Recycling of the SPCs by injection molding

To recycle SPCs, the fractured samples were categorized based on the reinforcement architectures and polymerization techniques. Materials in injection molding were fed through a hopper into an extruder. Afterwards a reciprocating screw mixes and melts the material and then injects it into a mold. The clamping force was applied to keep the mold closed during the process. All samples were inserted in a shredding machine (Figure 3.10a) and the chopped SPCs were sieved of any other contaminants (Figure 3.10b). Then the shredded SPCs and the conventional PA6 granules as reference sample were molded by injection using a BOY 22A reciprocating screw injection molding machine (Figure 3.10c) with a clamping force of 220 KN and a maximum stroke volume of 2.05 in^3. The constant volumetric flow rates were set at 40 $mm.S^{-1}$. The maximum injection pressure was 80 bars. End-gated dumbbell shaped bars for tensile property contained the 55×3×2mm dimensions (Figure 3.10d-e).
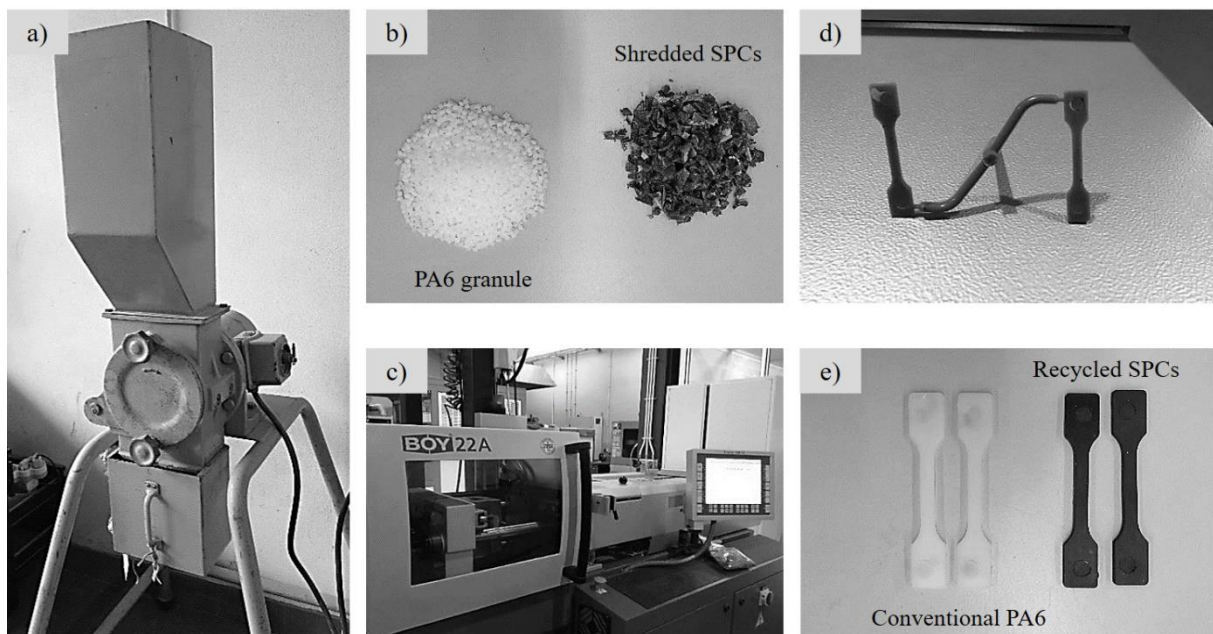
Figure 3.10. a) Inserting the fractured test sample into the shredding machine; b) the PA6 granule and shredded SPCs test samples; c) BOY 22A reciprocating screw injection molding machine; d-e) End-gated dumbbell shaped bars for tensile test specimen.

The melting of the PA6 resin happened because of the frictional heating from the screw rotation inside the barrel to keep the resin at the appropriate temperature. Typically, four temperature zones are defined on the cylinder (Figure 3.11). The rules for setting the heater band temperatures were applied in this study under which the temperature gradually decreased from the nozzle zone to the zone nearest the hopper. The last temperature zone was set 40° to 50°C lower than the calculated melt temperature, to give better transport of plastic pellets during plasticization. The following melt temperature were used to

set the heater band temperature:

1. 195°C at the rear zone
2. 195°C at the middle zone
3. 200°C at the front zone
4. 200°C at the nozzle zone

The heater band at the nozzle zone was set to the calculated melt temperature to keep the temperature uniform. Drooling at the nozzle and degradation or color changes in final product are caused by improper heater band temperature settings.
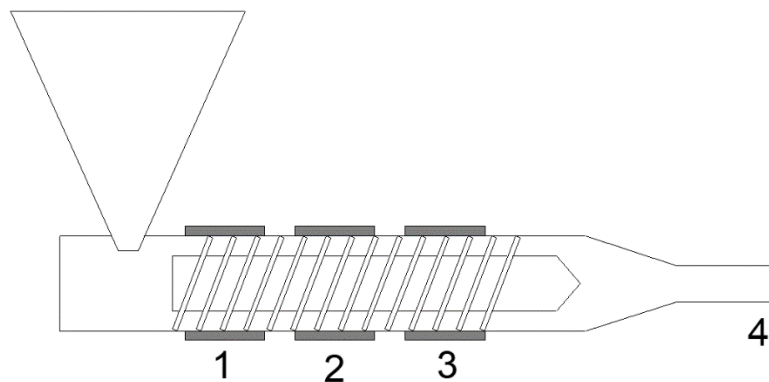
Figure 3.11. Four basic barrel zones on an injection molding machine along with the nozzle body and tip. 1- Rear zone, 2- Middle zone, 3- Front zone, 4-nozzle zone.

3.5. Reinforcements physical analysis

3.5.1. Reinforcements Air permeability

Air permeability is a hygienic property of textiles which influences the flow of gas from one side of fabric structure to the other. Evaluation on air permeability of textile structures determines the reinforcement´s porosity that enhances to evaluate matrix permeation through textile reinforcements. In this study FX-3300 air permeability tester was used regard to the standard test method, ISO 9237. The rate of air flow passing perpendicularly through an identified area was measured under 100 Pa air pressure. A suction fan pumped the air perpendicularly through the reinforcements and the flow was adjusted gradually while the required pressure drops achieved across the test region. The transducer determined velocity of air flow by dividing the volumetric flow rate $(m^3.s^{-1})$ over the specimen area (10 cm^2). The pressure drop for all textile reinforcements was set to 1000 Pa, with an accuracy of at least

2%. The air permeability (k) is calculated according to Darcy's law [191] as follow:

$$k, cm^3/s/cm^2 = \frac{\mu L \nu}{\Delta p}$$
(3-2)

where μ, L, ν are the fluid viscosity, flow length and the fluid velocity respectively. The Δp is the pressure drop.

3.5.2. Reinforcements thermal conductivity

Computer-controlled portable instrument ALAMBETA is the fast and non-destructive measurement of transient and steady-state thermos-physical properties of any compressible materials, particularly the textile fabrics. Alambeta apparatus, Czech Republic was applied to study the thermal conductivity and distribution of reinforcements respect to the standard ISO EN 31092-1994. Contact pressure was set on 200 Pa and temperature difference of 10°C between the bottom and top hot plates was led to the transitional heat. Average of 10 reading was taken for each reinforcement on either technical face. The transmission of heat quantity through a unit thickness in a direction normal to a surface of unit area was identified by thermal conductivity which was not time-dependent factor due to a unit temperature gradient under steady-state conditions. The thermal conductivity of homogenous materials was obtained by the following equation [192,193].

$$\lambda \left(\frac{W}{m.k} \right) = \frac{Q}{A.\frac{\Delta t}{h}}$$
(3-3)

where λ, Q, A, Δt and h are the thermal conductivity, the heat transmitted, the area, the temperature and the sample thickness respectively. Thermal diffusion is known the heat flow through the air in fabric structure which was calculated by equation (3-3) [193].

$$a \left(\frac{m^2}{s} \right) = \frac{\lambda}{\rho.c}$$
(3-4)

where a, ρ and c are the thermal diffusion, the material density, the area and the specific heat capacity respectively. Moreover, Thermal absorption for homogenous textile reinforcements gained by the following equation [193,194].

$$b \left(\frac{Ws^{\frac{1}{2}}}{m^2K} \right) = \sqrt{\lambda \rho c}$$
(3-5)

3.5.3. Shirly Winding Drum test

Shirley winding drum tester (Shirley developments) was used to evaluate the coefficient of friction of the yarns based on ASTM D3108 (Figure 3.12). A length of the filament was run at known speeds and in contact with either single or multiple friction surfaces using a specified winding angle. The essential dimensions comprising AB, AC, PD and $\overset{\frown}{BCP}$ were 10.16 cm, 5.08 cm, 45.72 cm and 120° respectively. The radii of pulleys B and C was 2.54 cm although the radii of both pulleys at A was 0.635 cm. After pre-tensioning, the yarn passes round on beneath of two concentric pulleys, A, thence to pulley B, round the test cylinder D to pulley C and on to a winding drum via the upper pulley at A. The filament input and output tensions was measured. Amonton law was applied to calculate the coefficient of friction using following equations:

$$\text{Exp}(\mu\theta) = \frac{T_2}{T_1} \tag{3-6}$$

$$\mu = \frac{(\ln T_2 - \ln T_1)}{\theta} = \frac{\ln(\frac{T_2}{T_1})}{\theta} \tag{3-7}$$

where μ is coefficient of friction, T_1 (mN or gf) is average input tension, T_2 (mN or gf) is average output tension and θ is cumulative wrap angle, radians. The system pivoted at P is acted upon by forces due to the initial tension, T_1, in the yarn approaching D and the final tension, T_2, of the yarn leaving D. The initial tension was applied by running the yarn between sintered aluminum oxide discs and around the pulley of an American G.E. hysteresis brake. The torque exerted by the yarn tension was opposed by the torque between a ferromagnetic disc, fixed to the pulley, and two small permanent magnets. The tension introduced into the yarn was varied by changing the distance between the disc and the magnets.

The yarn run through a 'null-point' indicator between the brake and A. The yarn tension was balanced against a weight through a double cantilever. A pointer on this instrument was brought to its equilibrium position by adjustment of the hysteresis brake. In this condition, the yarn tension, T_1, was equal to the weight applied. The outer layers of yarn on the bobbin were run off. From the mean, the corresponding value of T_2 was found. In general, the over-all mean value of μ was obtained from readings on ten bobbins.
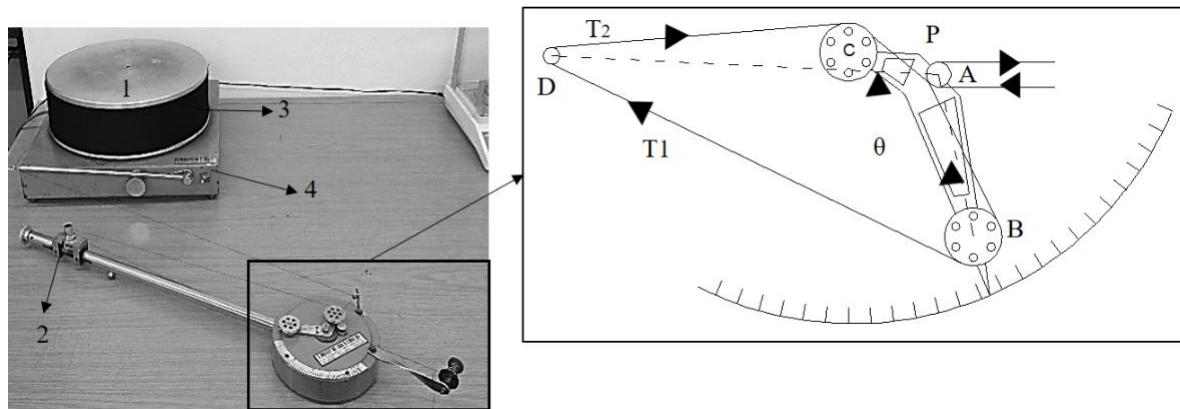
Figure 3.12. Shirley winding drum tester (1- American G.E. hysteresis brake; 2- Sintered aluminum oxide discs; 3- Filament; 4- Winding electromotor)

3.6. Thermal and morphological characterization of SPCs

3.6.1. Polymorph topography and microscopy

Olympus BH-2 light microscope equipped with Leica Application Suite 4 software was employed to visualize and analyze optical microscopy images of SPCs studying the distribution of plies in samples prepared by microtoming. The scanning electron microscopy (SEM) studies were performed in a NanoSEM-200 apparatus of FEI Nova (USA) using mixed secondary electron/back-scattered electron in lens detection. Au/Pd alloy was used to sputter-coat the samples to be observed.

3.6.2. The average viscometric molecular weight

The average viscometric molecular weight M_v of the composite components was determined by intrinsic viscosity measurements in 97% sulfuric acid at a concentration of $0.2 \, \mathrm{g. \, dL^{-1}}$ using a suspended level Ubbelohde viscometer thermostatted at 25°C. The Mark-Houwink equation for PA6 was used with $K = 5.066 . 10^{-4}$ and $\alpha = 0.74$ [195]. Average of at least five runs designated to achieve the flow times.

3.6.3. Differential Scanning Calorimetry

The differential scanning calorimetry (DSC) measurements were carried out in a 200 F3 equipment of Netzsch at a heating rate of $10°\mathrm{C. \, min^{-1}}$ under the nitrogen purge. To remove the thermal history of the specimens, two consecutive heating scans were performed, whereby the crystallization between them was made with a cooling rate of $10 \, °\mathrm{C. \, min^{-1}}$. The temperature of glass transition T_g of the samples,

63

the melting temperature T_m and the DSC crystallinity index were obtained for each sample. The typical sample weights were in the 5-15 mg range. The DSC crystallinity index $X_c^{DSC}(\%)$ of the samples was calculated according to the following equation.

$$X_c^{DSC},(\%) = \frac{\Delta H_m^i}{\Delta H_m^\circ} \qquad (3\text{-}8)$$

where the ΔH_m^i is the registered melting enthalpy of the current sample and ΔH_m° is the melting enthalpy of a 100% crystalline PA6 (230 J/g) [196,197].

3.6.4. Thermogravimetric analysis

Thermogravimetric analysis was performed on a modulated TGA Q500 from TA instruments. The TGA trace was obtained in the range 40–600°C under the nitrogen atmosphere with a flow rate of 20 $mL.\,min^{-1}$, the heating ramp being $10°C.\,min^{-1}$. Before the test the samples were dried at 60°C for 1h. TGA curve, its first derivative, as well as the DTA curve were obtained and analyzed for all samples.

3.6.5. Wide Angle X-Ray Scattering (WAXs)

The 1D WAXS curves were also corrected for background scattering, irradiated volume, and beam intensity. All WAXS patterns were collected in a Bruker D8 Discover θ-θ diffractometer working with Cu Kα radiation ($\lambda = 1.541$ Å). Their scattering angle axis was calibrated with the angular position of the reflections of a standard crystalline poly (ethylene terephthalate) sample (Figure 3.13). XRD patterns were collected in the 2θ range of 5-45° with a step time of 2 s and step size of $0.1\ deg.\,min^{-1}$. Curve fitting of the XRD patterns was made as previously shown [198] using a commercial peak-fitting software. All WAXS curves were fitted with Gaussian peaks. The XRD crystallinity index X_c^{XRD} was calculated according to:

$$X_c^{XRD} = \frac{\sum A_c}{\sum A_c + \sum A_a} \qquad (3\text{-}9)$$

where $\mathbf{A_c}$ is the integrated area underneath the respective crystalline peaks and A_a is the integrated area of the amorphous halo.
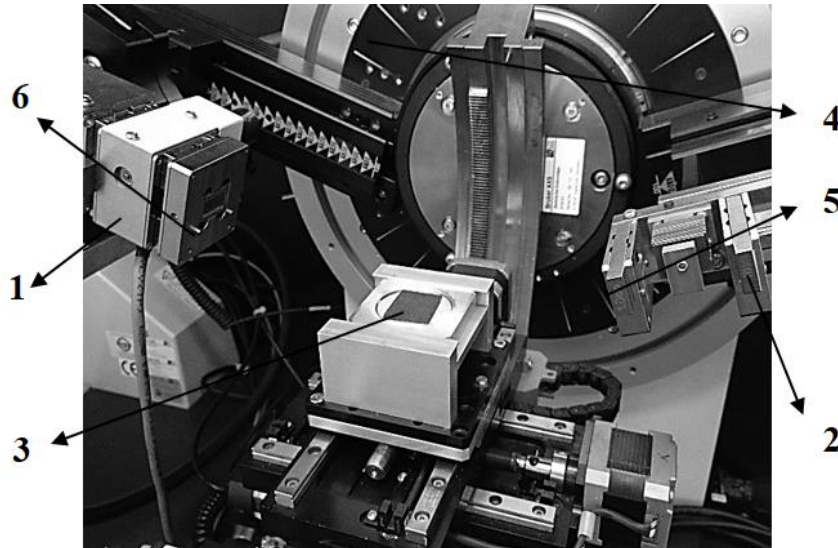
Figure 3.13. The Bruker D8 Discover θ-θ diffractometer wide angle X-ray apparatus. (1- X-ray tube; 2- Detector; 3- Sample; 4- Goniometer; 5- Collimator; 6- Adjustable slots)

3.6.6. Fourier transform infrared (FTIR)

The total reflectance ATR-FTIR spectra of the SPCs components were recorded on a Nicolet Avatar 360 FTIR spectrophotometer (Madison, USA). The spectra were collected in the region of $4000-400 \text{ cm}^{-1}$ and at a resolution of 16 cm^{-1}. Furthermore, all moisture eliminated from investigated system to avoid water-PA6 H-bonds formation and may obscure absorption bands owing to the PA6 polymorph.

3.7. Mechanical characterization of SPCs and the components

3.7.1. Reinforcements Tensile test

The Standard method of ASTM D5034, grab test, had been appropriated for tensile analysis of all reinforcements before and after stress-relaxing treatment. All reinforcements had been tensile tested in two principal directions although knitted reinforcements also were stretched in diagonal direction (Figure 3.14). The 150×100mm samples were stabilized in a temperature controlled environment at 23°C for at least 5 hours. The tensile test had been performed in an Instron 4505 universal testing machine with a standard load cell of 2.5 kN and at a constant crosshead speed of 2 mm.min^{-1}. All textile reinforcements instantaneously inserted after stretching-annealing treatment to avoid the water intake.

65

Figure 3.14. Dynamometer cyclic tester Hounsfield tester H100KS and the tensile test set based on ASTM D5034, grab test (1- Textile sample; 2- Dynamic cross head; 3- fixed cross head 4- Strain gauge loadcell; 5- Drive unit; 6- Wedge grips; 7- Digital display)

3.7.2. Reinforcements Bending Test

The anisotropy bending rigidity (B_{KES}) of untreated and annealed knitted reinforcements toward wale (0°), diagonal (45°) and course (90°) directions had been measured using the KES-FB$_2$ Pure Bending tester applying constant rate, from a curvature 2.5 to −2.5 cm^{-1} (Figure 3.15a). All reinforcements were cut in 20×20cm pieces and the distance between grips was 1cm. Each sample was gripped between fixed and dynamic clamps and bending procedure was followed a circular path. The KES test was carried out for five consecutive test samples regarding double technical faces. Figure 3.15b demonstrates a typical momentum-curvature curve of knitted reinforcements after annealing. The angular momentum was recorded during structural deformation and final momentum–curvature curve. The slope of the curve was determined between ±0.5 and ±1.5 cm^{-1} expressed as bending rigidity of textile reinforcements.

$$B_f = \tan \alpha = \frac{A-B}{1.5-0.5} \tag{3-10}$$

$$B_{KES} = \frac{B_f - B_b}{2} \tag{3-11}$$

66
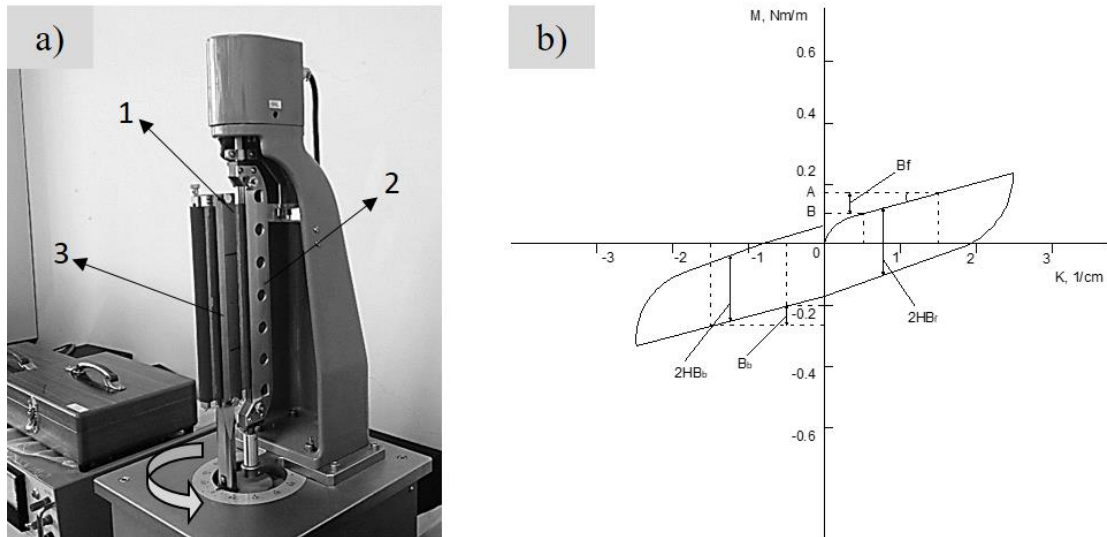
Figure 3.15. a) KES-FB$_2$ Pure bending apparatus; b) Typical momentum–curvature curve of textile reinforcement.

Bending stiffness (B$_{Pierce}$) of Woven and Stitched woven reinforcements determined by Peirce cantilever test [199]. All specimens were cut by 200×25mm. They progressively became slipped over the edge of the top-surface, until the leading edge of the fabric in which was in contact with the angled surface of the device. The overhanging length of the specimen was measured using a graduated ruler (Figure 3.16).
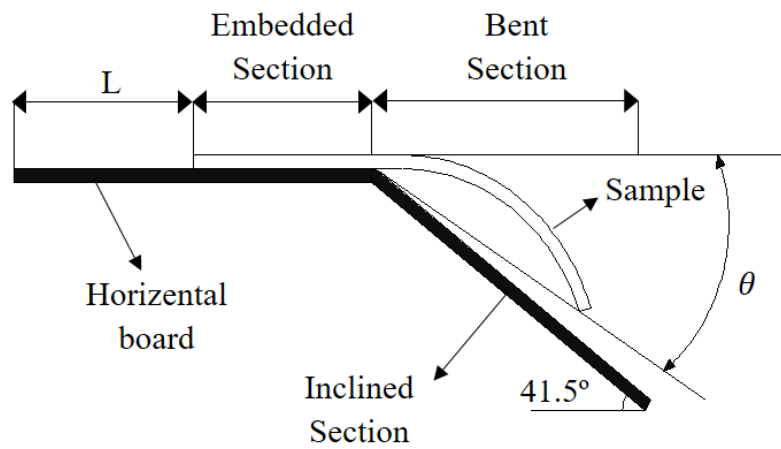
Figure 3.16. Cantilever principal for bending rigidity evaluation of woven and stitched woven reinforcements

Respect to the ASTM standard (D1388), a fixed angle θ = 41.5 ° is used for the inclined surface [199]. Pierce equation due to the measuring of bending rigidity expressed by following equations.

$$c = l \times f(\theta) = \left(\frac{\cos\frac{\theta}{2}}{8.\tan\theta} \right)^{\frac{1}{3}} \tag{3-12}$$

$$B_{Pierce} = 9.81 \times 10^{-12} \times w \times c^3 \tag{3-13}$$

where c (mm), w (g. mm^{-2}) are bending length and areal weight of reinforcements.

3.7.3. Dynamic mechanical analysis (DMA) of reinforcement

The viscoelastic compression response of all reinforcements was studied by isothermal dynamic mechanical analysis (DMA), DMA7e Perkin-Elmer apparatus, using the compressive mode. A rectangular specimen of 8×8 mm was subjected to oscillating compression plates (Figure 3.17). A continuous flow of high purity helium (flow rate ≈ 65 $\text{cm}^3. \text{min}^{-1}$) was applied to improve the heat transfer in the experimental set-up. The static preload selected was $2.4 \times 10^5 \text{Pa}$ on which an oscillating load $2.3 \times 10^5 \text{Pa}$ (sinusoidal wave) at 1Hz was superimposed. The isothermal temperature was set at 30°C. The amplitudes of these stresses were small enough to warrant the study of the sample in the linear viscoelastic regime.
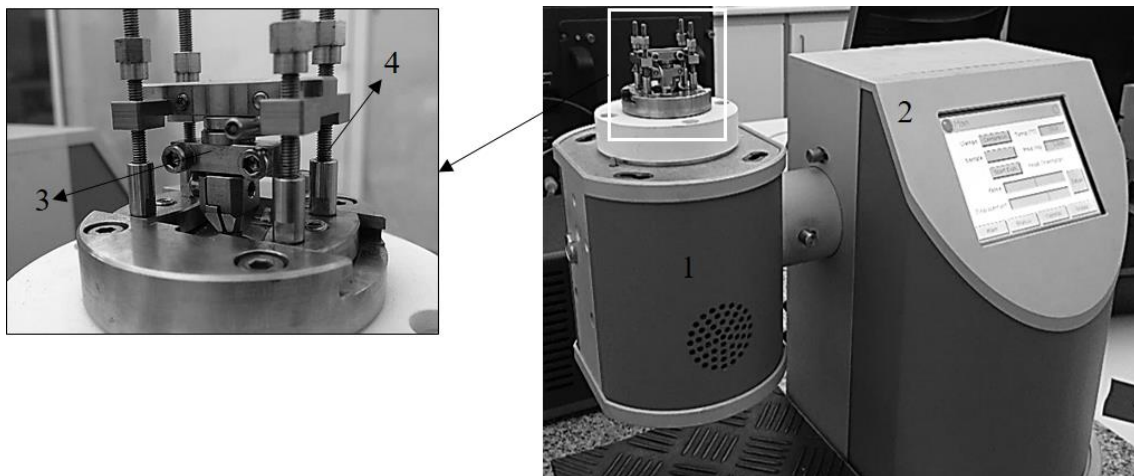
Figure 3.17. DMA7e Perkin-Elmer apparatus (1- Stepper motor; 2- Microcontroller; 3-Textile specimen; 4- Drive shafts)

3.7.4. Test specimen cutting

A commercial CNC laser cutting machine was applied to gain uniform Tensile, flexural and Izod impact test samples. The standard samples for each test were laser cut from one and the same composite plate to ensure reproducibility (Figure 3.18). Power density, wavelength of emission, interaction time as well as melting and vaporization temperatures, thermal conductivity and heat capacity were attributed to the influence of laser beam on a material. The energy transferred from the laser beam to the material by means of laser energy absorption in a superficial zone of the material. The lens of focal length and the power density at the focus of 0.25mm in diameter were 60 mm and 96 $\text{W}. \text{cm}^{-2}$ respectively. Adjusting

work-piece movement was accomplished by a numerically controlled table. The residual parts were employed for thermal and structural characterization test specimens.
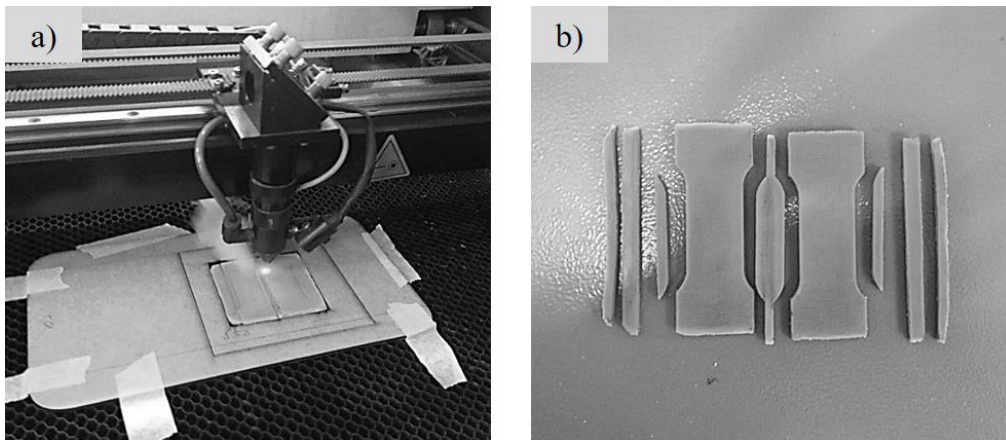
Figure 3.18. a) CNC Laser cutting machine for thermoformed parts whether for clean contours or hair-thin perforations; b) laser cut tensile test specimens.

3.7.5. Tensile test of SPCs

Tensile test samples stored for ca. 30 days at 23°C and 65% relative humidity owing to condition procedure. The tensile test was performed on an Instron 4505 testing machine (USA) at 23±2°C with a standard load cell of 50 kN and at a constant crosshead speed of 2 mm.min^{-1} (Figure 3.19a). The standard specimens were cut out according to ASTM D638 with a gauge length of 38 mm (Figure 3.19b). At least five specimens of each sample were selected to calculate the average values and their standard deviation. It should be mentioned that the SPCs and PA6 neat matrix specimens were shattered at the gage region (Figure 3.19c). The Young´s modulus (E) was measured from the stress–strain curves as the tangent at 1% strain. The improvement factors IF were calculated comparing the average Young´s modulus or maximum tensile strength values of the SPCs to those of the matrix material plate according to equation (3-13):

$$\text{IF, (\%)}_{\text{matrix}} = \frac{P_i^{\text{SPC}} - P_i^{\text{matrix}}}{P_i^{\text{matrix}}} \tag{3-14}$$

where P_i^{SPC} and P_i^{matrix} are the respective parameters of the composite and matrix materials.
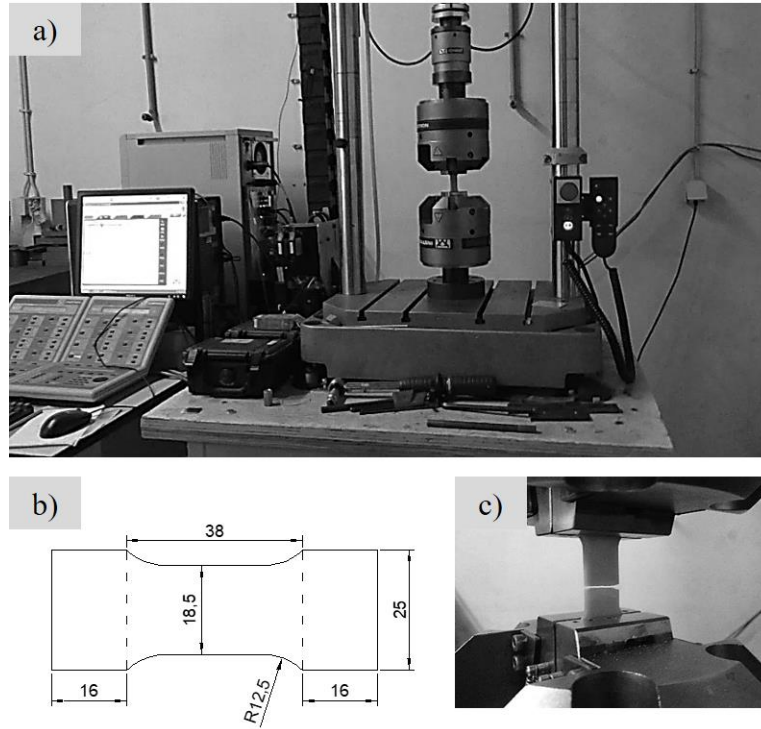
Figure 3.19. a) Instron 4505 testing machine (USA); b) Tensile fracture of SPCs at the middle of gage section; c) Tensile test dimension

3.7.6. Flexural Test SPCs

The flexural properties of the SPCs were carried out in the same Instron 4505 testing machine according to ASTM D 790-03 (Figure 3.20). In this test method, a three-point loading system with a simply supported beam was applied using a rate of 2 $mm.min^{-1}$, a load cell of 2.5 kN and the distance between the points of support of 40 mm. Following equations had been applied to calculate the Flexural modulus (GPa), Strength (MPa) and Strain (%):

$$E_f(GPa) = \frac{L^3.m}{4bd^3} \tag{3-15}$$

$$\sigma_f(MPa) = \frac{3PL}{2bd^2} \tag{3-16}$$

$$\varepsilon_f(\%) = \frac{6Dd}{L^2} \tag{3-17}$$

where L is the distance between the points of support, m is the slope of force-deflection curve. b and d are the width and the thickness of the sample (mm) respectively. D is the maximum deflection in mm and P is the applied force (N).
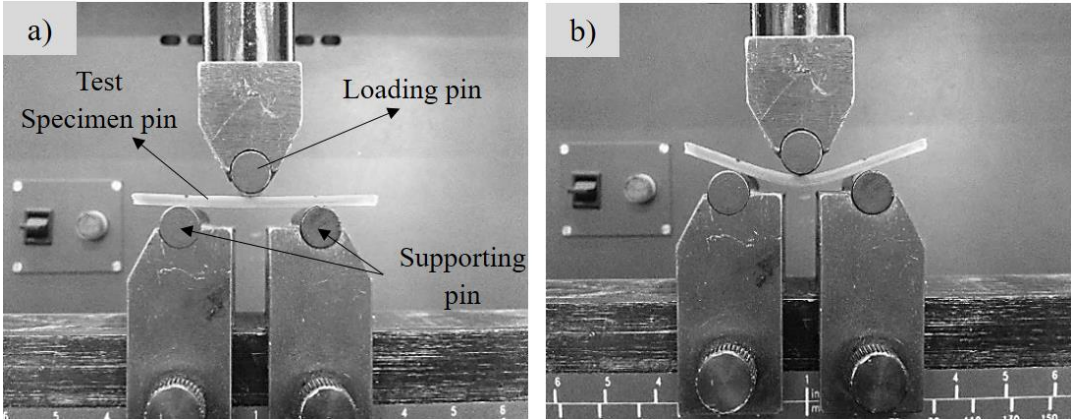
Figure 3.20. Three-point flexural test wherein the loading force is applied in the middle of bar by means of loading pin a) before b) after applying flexural force

3.7.7. Unnotched Izod impact Test

Unnotched Izod pendulum impact test according to ASTM D 256-04 have been chosen to study the impact strength of the composite materials (Figure 3.21). The specimen absorbed energy until it yields while the striker impacts the specimen. The impact strength (IS) was measured as the impact energy absorbed relative to the test bar cross-section according to the below equations:

$$I_A \left(\frac{KJ}{m^2} \right) = \frac{E_{composite} - E_i}{A} \qquad (3\text{-}18)$$

where in E_i and $E_{composite}$ are the energies registered in the impact equipment without and with sample bar, respectively, A is the area of the unnotched sample.
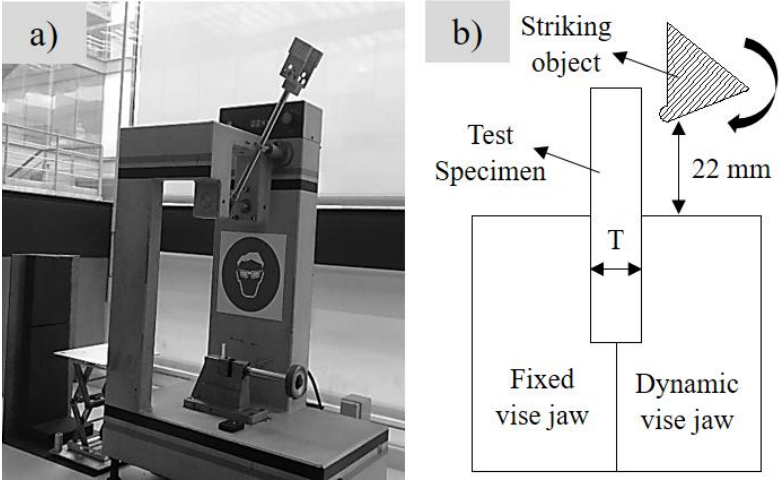
Figure 3.21. a) Cantilever Beam (Izod-Type) Impact Machine; b) Relationship of vise, specimen, and striking edge to each other for Izod test method, T=bar test specimen thickness.

Mechanical analysis and structure relationship of KSPCs

4.1.   Introduction

No systematic studies have been reported on the structural relationship of polyamide 6 based Knitted single polymer composites (KSPCs). Research work identifying the effects of various parameters such as loop configuration and orientations are not available in the open literature. In the present chapter single polymer laminate composites based on anionic polyamide 6 matrix reinforced by polyamide 6 knitted textile structures (KSPCs) were produced by nylon reactive injection molding (NYRIM) and powder coating/compression molding (PCCM) processing techniques. The MPs were synthesized by solution/precipitation activated anionic ring-opening polymerization of ε-caprolactam. The mechanical properties (Tensile, Flexural and Izod impact) of KSPCs resulting from the two methods were investigated and compared in relation to the knitted reinforcement architecture, fiber volume fraction, ply orientation and stacking orders. The mechanical behavior of the KSPCs was correlated with the geometry parameters of the knitted reinforcements. The fracture behavior of KSPCs was investigated by electron microscopy complemented by simulation studies.

4.2.   Knit Reinforcement mechanical properties

4.2.1. Structural simulation of knitted reinforcements

To better understanding the structural analysis of reinforcements in relation with mechanical failure analysis of KSPCs, the real size geometrical Rib1×1 and Jersey reinforcements had been virtually modeled. To simulate the real size knit reinforcements, Kurbak's geometrical model for Jersey knitted loop shape [200,201] was taken as starting points and the modifications were generated to obtain the geometrical model for the stretched-annealed Rib1×1 and Jersey knit reinforcements. The continuity of the curves in the loop partitions were defined by repeating unit provided throughout the model.

Inspired by Kurbak's geometrical model [200–204] , Rib1×1 reinforcement yarn axis are drawn with the six virtual circular cylinders, used to simulate loop partitions at crossing section made 90° with the fabric plane. The drawing procedure was initiated from point A and then the whole geometry was mirrored on the axis normal to this point (Figure 4.1a). Two virtual circular cylinders comprising loops leg and sinker loops were joined at point B and sinker loops cylinder making an angle with the fabric plane at point C (Figure 4.1a-c). It should be mentioned that virtual cylinders were applied as the base structure to sketch the yarn axis superficially and eliminated after concluding the final kernel geometry. The Jersey

architecture was simulated with two virtual circular cylinders shown in Figure 4.1d-f. Therefore, a similar strategy is applied to draw the kernel geometry of annealed Jersey reinforcement.
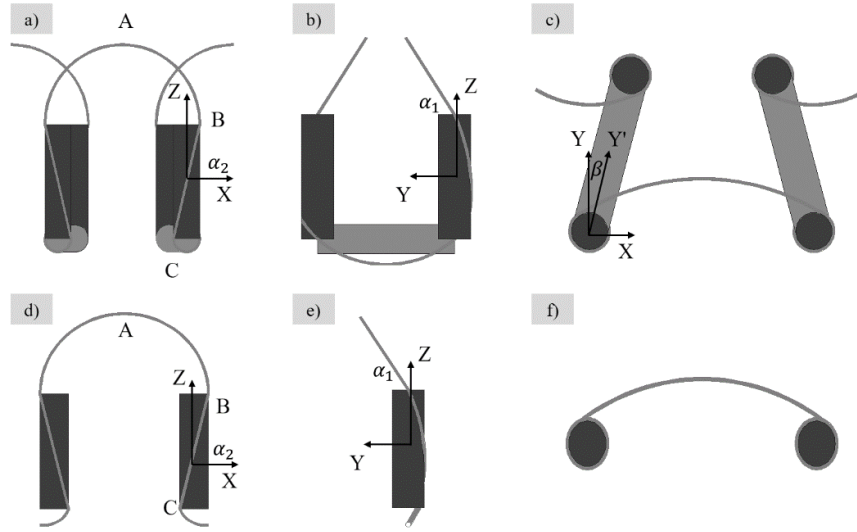
Figure 4.1. General view of the Rib model created. a) Arrangement of representative circular cylinders on the central axis of yarn; b) drawing of 3D yarn central axis of the model with effective yarn diameter.

The loop head in Rib1×1 and Jersey architecture is located on a plane that has an angle α_1 respect to the plane normal to fabric plane (Figure 4.1b,e). Loop head geometry was measured by equation (4-1).

$$x = a \sin \theta, \ y = a \cos \alpha_1 \cos \theta, \ z = a \sin \alpha_1 \cos \theta, \ 0 \leq \theta \leq \frac{\pi}{2} \qquad (4\text{-}1)$$

where a is the radius of loop head and α_1 is calculated in equation (4-2) due to equalizing the radii of curvatures of the upper part of the loop and the helix of the loop legs at point B.

$$\cos^2 \alpha_1 = \frac{ra}{b^2} \qquad (4\text{-}2)$$

where a and b are the major and the minor radii of the loop head ellipse. For most of the tightness values used in practice, r, the radius of loop leg cylinder, can be taken as the half of the yarn diameter, is given by:

$$r = \frac{\eta d}{2} \qquad (4\text{-}3)$$

where d is the effective yarn diameter and η is yarn swelling or compression parameter. Because of rigorous structural deformation of knitted reinforcements after stretching-annealing procedure,

determination of η value was complicated. In this study, to simplify the simulation knit model, some basic

assumption is required to be taking into considering such as 1) touching two neighboring loops in the

same face and at the same course, measured by visual image analysis 2) interlocking loops in the same

wale are touching each other at their widest points. Therefore, α_1 measured by considering the mentioned

assumptions (Figure 4.2a). Ten digitalized superficial microscopic images had been captured from the

top surface of each knitted reinforcements. Subsequently, the AutoCAD® computer program, version

2016 was used to determine of virtual vertical circular cylinders dimensions due to draw the filament

kernel geometry. Eventually, an elliptical profile regarding the yarn geometry after annealing procedure

was swept over the kernel geometry (Figure 4.2b).
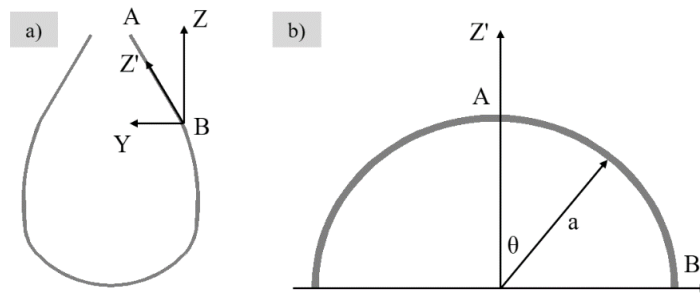
Figure 4.2. The filament axis curve used to draw the loop head in knit reinforcements. a) The illustrative location of loop head curve; b) loop head curve shown in its Z'-X plane.

To simulate the loop leg curves, the filament central axis was wrapped around virtual cylinders in which

following formula were used to describe helix configuration.

$$\begin{cases} x(t) = \cos(t) \\ y(t) = \sin(t) , \qquad \pi - \beta < t < \pi + \beta \\ \quad z(t) = t \end{cases} \qquad (4\text{-}4)$$

The total wrapping angle (t) is changing between π – β to π + β influenced by the tightness of the

Rib1×1 or Jersey structure. In case R-A structures, Figure 4.3 shows the axes of circular cylinders lied in

the X-Y plane. The yarn axis is wrapped around the cylinder of crossing section in the same manner with

the loop leg. Point B is known as junction axes of those cylinders where the radii of curvatures of yarn

axes are taken to be the same. Three simulating assumptions for R-A are illustrated in Figure 4.3a-c.

Respect to the microscopic images of R-A and J-A structures (Figure 4.3d-e), the model, shown in Figure

4.3c is selected to sketch the virtual circular cylinders and draw the kernel geometry of all knitted

reinforcements.
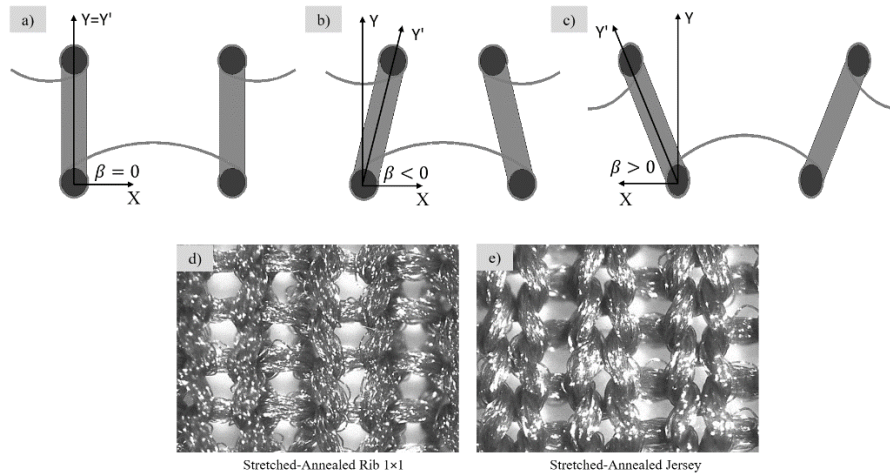
Figure 4.3. The upper view of possible curves used for the loop arms of annealed Rib1×1 reinforcement. a) β = 0; b) β is negative; c) β is positive; d) R-A 1×1 e) J-A

Three major hypothesizes were propounded to conclude final geometrical model 1) The filament cross-section was considered elliptical 2) The constant sweeping of elliptical cross-section through the kernel geometry 3) No dimensionally deformation at the cross over points. As it can be seen in Figure 4.4a-b, the kernel structure imported into the SolidWorks® software-version 2015 to sweep the cross-section profile though upon it. At the end, virtually clash test had been run to evaluate contact situation at the interface regions via SolidWorks® software program. A loop unit cell was extracted from reinforcement structure and partitioned such as loop head, loop leg and sinker loop (insets Figure 4.4a-b).
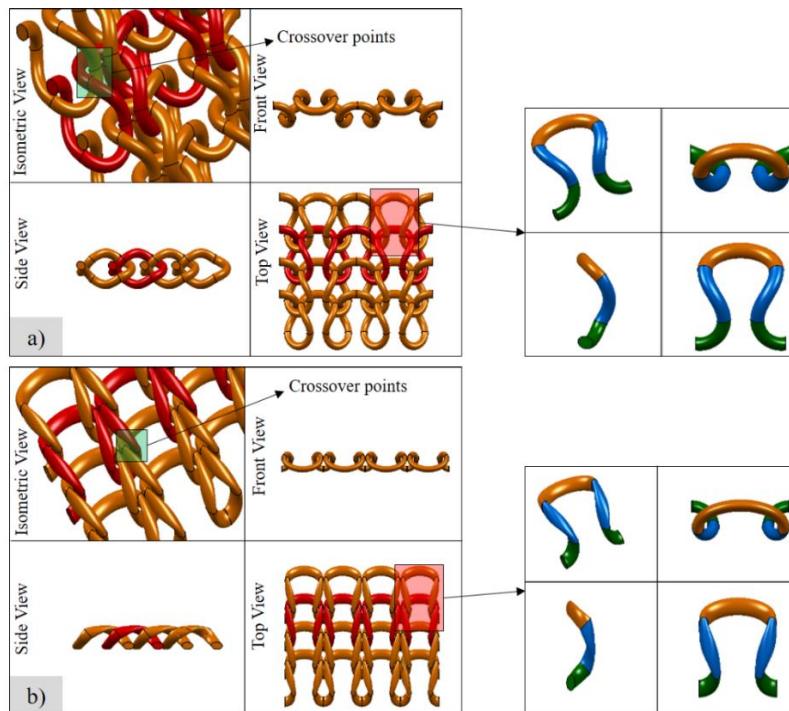
Figure 4.4. Simulated real size annealed knit structures detailed by loop unit-cell configuration a) Rib1×1 and b) Jersey Reinforcements

77

4.2.2. Tensile properties

Polyamide filaments undergo various heat-setting processes during spinning, drawing, texturing, and fabric finishing. Annealing (stress-relaxing) is used to modify the microstructure and impart stable crystalline configuration to semicrystalline polymers. Since filaments are usually oriented, annealing led to changes in both the amorphous and the crystalline phases. Structural changes are influenced by the temperature, time and the dimensional constraints imposed on the filaments. On the contrary, heat setting may lead to a loss of mechanical properties [205,206]. Annealing PA6 knitted fabrics increases crystallinity, crystallite size, the crystalline perfection of the polymer and modify the low glass transition temperatures [207]. Since the mechanical properties of a laminate composite depend strongly on the strength and stiffness of the reinforcements, single textile plies of both Jersey and Rib 1×1 type were first tested in tension, before and after the stretching-annealing procedure, as well as applying the strain at different angles in respect to the wale direction. Figure 4.5 shows the stress-relaxation process was caused the significant improvement on tensile properties of knitted structures. Top figures display also that all the annealed knitted reinforcements developed larger empty spaces between the knitted loops upon stretching.
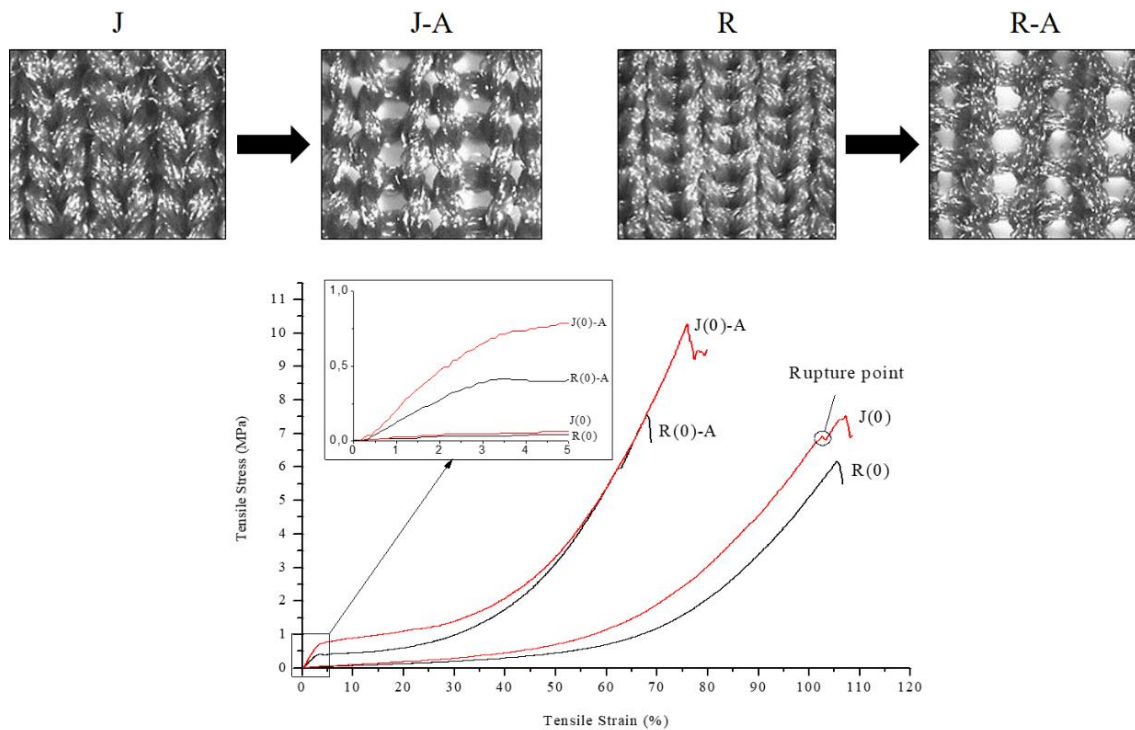
Figure 4.5. Stress-strain curves in tension of Rib1×1 and Jersey textile reinforcements before and after the stretching-annealing procedure.

78

Stress-strain behavior of knitted reinforcements typically illustrates a gradual increase reaching to the rupture point (Figure 4.5). The annealing process was caused to emerge of superior rigidity at the rudimentary tensile strain (within approximately 5%) on knit structure followed by instantaneous slump on reinforcement tensile stiffness. Therefore, two different structural rigidities were diagnosed from the stress-strain graph of the annealed knit structure at the inflection point. The tensile strength of knit reinforcements was significantly modified by applying annealing procedure.

As seen from Figure 4.5 (R-A, J-A curves), stretching to 30% accompanied by heating at 170°C for 90 min resulted in the appearance of the clear elastic region in the stress-strain curves between 0-5% relative strain that was absent in the R and J samples. Moreover, the second elastic region in both annealed samples observed above ε = 40% had the larger slope as compared to that of the untreated textiles indicating a higher E-modulus in the former case. As the tensile behavior of the knitted reinforcements clearly affect the mechanical properties of the composite laminates, single plies of jersey and rib 1x1 fabrics were tested, before and after the stretching-annealing treatment, in wale (0˚), bias (45˚) and course (90˚) directions. As it can be seen in Figure 4.6a-c, the stretching-annealing treatment applied to the knitted reinforcements at different angles (0°, 45° and 90°), was led to an increase of their tensile stiffness and strength and to a decrease in elongation. As it is known, an externally applied load (force) to a composite is partly borne by the matrix and the reinforcements.
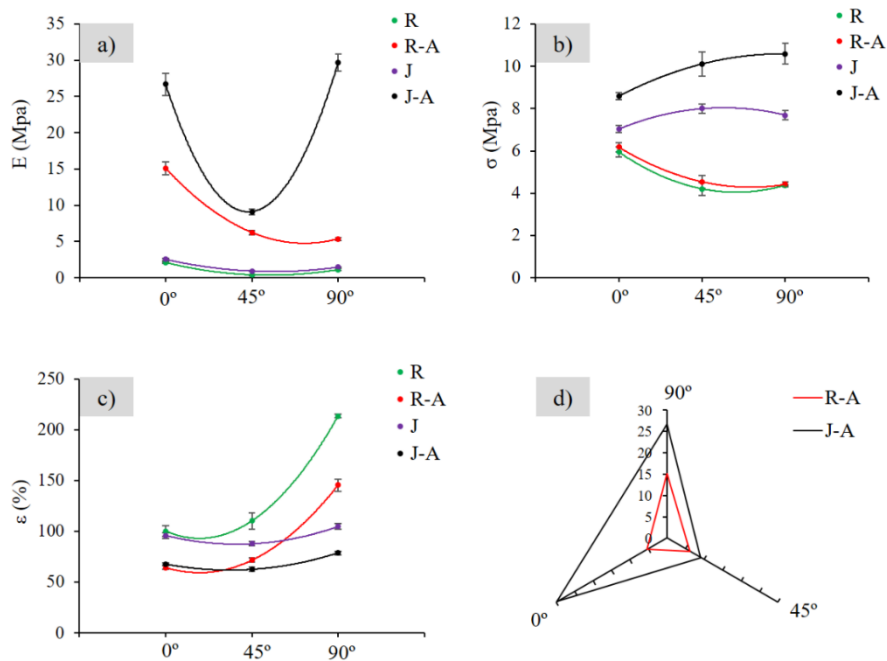
Figure 4.6. Comparison on Tensile properties of all untreated and annealed knitted reinforcements a) stiffness; b) Strength and; c) Strain at different orientation. d) Analogy of tensile stiffness anisotropy in annealed knitted reinforced. For sample designation see Table 3.1 and Table 3.2.

Furthermore, the J-A depicted higher tensile stiffness (Figure 4.6a) and strength (Figure 4.6b) , but lower elongation than the R-A structures (Figure 4.6c). The anisotropic behavior of the "treated" knitted structures was analyzed based on the tensile properties obtained under the different loading angles (0°-wale, 45°- bias and 90°- course directions). Figure 4.6d, shows the anisotropy on the tensile stiffness of the J-A and R-A samples. Higher anisotropy was presented by the J-A reinforcements.

4.2.3. Bending strength

The bending rigidity of knitted reinforcements before and after annealing procedure was evaluated by Kawabata evaluation system (KES). The typical momentum–curvature curve of knitted reinforcement is demonstrated in Figure 4.7. The influence of annealing process, orientation and the reinforcement's architecture on bending rigidity of knitted reinforcements have been investigated to be linked with flexural properties of KSPCs.

$$B_f = \tan \alpha = \frac{A - B}{1.5 - 0.5}$$

$$B_{KES} = \frac{B_f - B_b}{2}$$
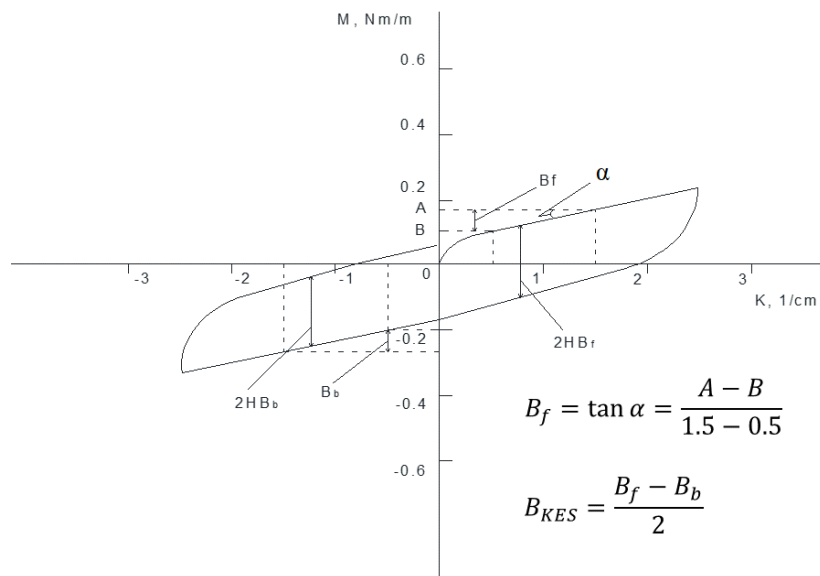
Figure 4.7. A typical momentum–curvature curve of knit reinforcement after annealing process.

The bending properties of knitted reinforcement was performed to analyze the effect of textile reinforcements on flexural properties of KSPCs. Figure 4.8 shows annealing process increased the bending rigidity of knit structures. The R(90)-A sample, merely, owned highest bending stiffness (101 μN. m). The diagonal direction in all knitted reinforcements contained the bottommost bending rigidity. Excluding R(90)-A and J(0)-A samples, knitted structures resist identically against bending forces for either technical faces. Significant differences on bending rigidity of the R-A sample respect to the three determined test directions evidenced their higher anisotropic manner. Although, the J-A showed stable

80

properties in those directions.
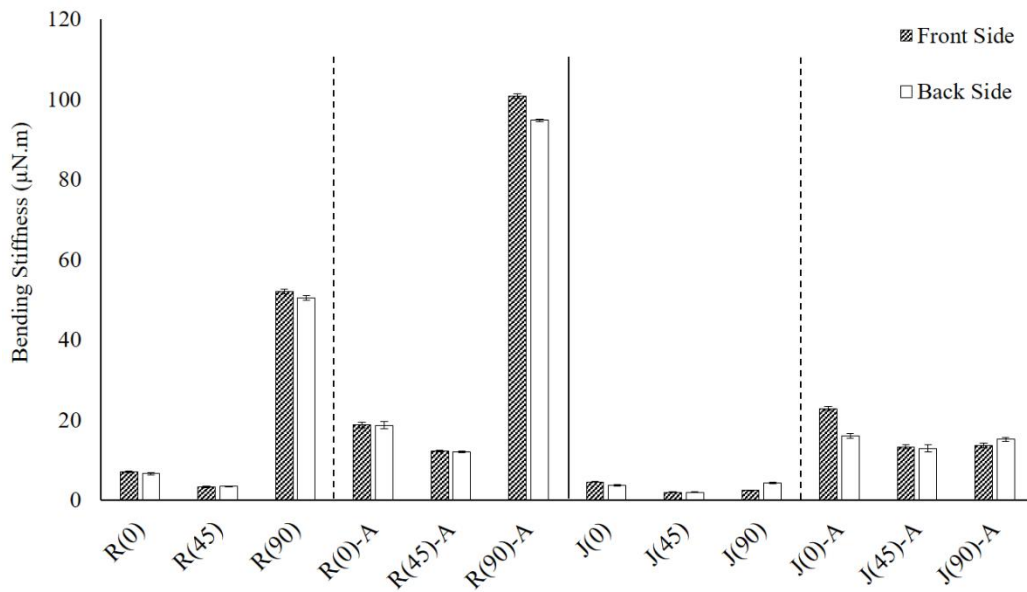
Figure 4.8. Comparison on KES Bending rigidity of knitted reinforcements before and after annealing for front and back technical faces. For sample designation see Table 3.1 and Table 3.2.

4.2.4. Air permeability

Knitted reinforcement structural analysis had been performed to correlate the mechanical properties of KSPCs with the reinforcement structural deformation. Table 4.1 exhibits the construction factors like annealing procedure significantly influenced the air permeability of knit structures which is led the better matrix penetration through the plies during the molding process. Although, reinforcement architecture after stretching-annealing did not significantly change the air permeability of knitted structure.

Table 4.1. The effect of annealing process on Air permeability of knitted reinforcements. For sample designation see Table 3.1 and Table 3.2.

Specimens	Air permeability ($\frac{\frac{L}{S}}{m^2}$)	
	Front Face	Back Face
J	1106.7 ± 20.8	1063.3 ± 15.3
R	1032.5 ± 12.6	1017.7 ± 29.3
J-A	5036.0 ± 72.3	5033.6 ± 40.7
R-A	5344.0 ± 63.1	5275.0 ± 76.8

4.2.5. Thermal properties

Heat transfer analysis of all knitted reinforcements performed to comprehend a comparison on thermal conductivity (λ), thermal diffusion and thermal absorptivity of knit structures (Table 4.2). Annealing process declined thermal conductivity of the knitted reinforcements. In general, Rib1×1 reinforcements had better heat transferring than Jersey structure. The higher thermal conductivity of R-A reinforcements led to the better heat transferring through laminates during molding and the better monomer conversion and interfacial bonding among composite components.

Thermal diffusion is an ability of the heat flow through the air in the knitted reinforcements. The thermal diffusion of the textile materials is not instrument parameter. Thermal diffusion of knitted reinforcements represents in what manner the heat moves rapidly through them. Whatever a material is highly thermal diffusive, it conducts quickly the heat relative to its volumetric heat capacity. Table 4.2 shows annealing process increased the thermal diffusion of the knitted reinforcements up to 46%. Technical faces in knit structures had no significant influence on heat conductivity and thermal diffusion parameter. Higher thermal diffusion of J-A reinforcements proved to entrap a large amount of air in the structure.

Table 4.2. The thermal data of knitted reinforcements comprising thermal conductivity, thermal diffusion and thermal absorptivity. For sample designation see Table 3.1 and Table 3.2.

Specimens	Thermal conductivity ($\times 10^{-3}$) ($W\ m^{-1}\ K^{-1}$)		Thermal diffusion ($\times 10^{-6}$) ($m^2 s^{-1}$)		Thermal absorptivity ($W\ m^{-2}\ s^{\frac{1}{2}}\ K^{-1}$)	
	Front Face	Back Face	Front Face	Back Face	Front Face	Back Face
J	48.3 ± 1,0	48,2 ± 1,0	1,3 ± 0,2	1,4 ± 0,2	134,5 ± 8,5	140,4 ± 9,0
R	52.6 ± 1,0	52,7 ± 1,1	1,5 ± 0,2	1,5 ± 0,2	134,1 ± 9,5	132,2 ± 8,3
J-A	32,3 ± 0,4	32,9 ± 0,5	1,9 ± 0,1	2,0 ± 0,1	85,6 ± 1,3	87,2 ± 2,0
R-A	37,9 ± 0,5	37,7 ± 0,5	1,7± 0,1	1,8 ± 0,1	90,5 ± 2,6	91,2 ± 1,5

As seen in Table 4.2, stretching-annealing treatment significantly decrease the thermal absorption of knit structures. Thermal absorption is a transient parameter that not influence from either the temperature gradient between the surface of the knit reinforcements and environment or the measurement time. The validity of thermal absorption measured by Alambeta device confirmed that the R-A sample owned higher thermal absorptivity compared to the J-A. The differences on thermal absorptivity of Jersey reinforcements respect to either technical faces were related to its unsymmetrical structure.

The high thermal absorptivity and thermal conductivity in R-A explained the better distribution of heat between plies during molding. Higher thermal diffusion in J-A represented the porous structure due to the existence of large amount of air though the structure which was caused appropriately impregnation of the matrix through the embedded plies.

4.2.6. Dynamic mechanical analysis

In compression mode, an axial load was applied to the one-dimensional knitted reinforcements held between two parallel plates whereas bulk compression effects a three-dimensional change. The determined uniaxial compression was caused the stretched-annealed reinforcement to buckle. The isothermal compression properties of all knitted reinforcements were evaluated by dynamic mechanical analysis (DMA). The measurement of the bulk compression properties accompanied by tensile properties of treated knitted reinforcements provided the structural analysis on impact properties of KSPCs. The viscoelastic parameters, elastic (storage) modulus ($E^{'}$), viscous (loss) modulus ($E^{''}$) and tangent delta (δ) of all knit reinforcements before and after stretching- annealing were calculated using the following equations. The isothermal compression properties of knitted reinforcements performed by dynamic mechanical analysis (DMA) illustrated in Figure 4.9a-b. Storage modulus ($E^{'}$), loss modulus ($E^{''}$) and tangent delta (δ) of all knit reinforcements with and without annealing are calculated by following equations.

$$E^{'} = |E^*| \times \cos \delta \tag{4-5}$$

$$E^{''} = |E^*| \times \sin \delta \tag{4-6}$$

$$\delta = \tan^{-1} \frac{E^{''}}{E^{'}} \tag{4-7}$$

where the phase angle (or shift) δ (rad) is the phase difference between the dynamic stress and the dynamic strain in a viscoelastic material subjected to a sinusoidal oscillation. The complex compression modulus E^* is given by the ratio between the stress and the strain amplitudes and represents the overall resistance of the material to compression (equation (4-5)).

$$|E^*| = \frac{\sigma_A}{\varepsilon_A} = \sqrt{(E^{'2}) + (E^{''2})} \tag{4-8}$$

$$\begin{cases} \sigma_A = \sigma_0 \ \sin(wt + \delta) \\ \varepsilon_A = \sigma\varepsilon_0 \ \sin(wt + \delta) \end{cases} \tag{4-9}$$

$$\varepsilon_A = \sigma\varepsilon_0 \; \sin(wt + \delta) \qquad\qquad (4\text{-}10)$$

where w, t and δ are the frequency of strain oscillation, time and phase shift between stress and strain, respectively. The Elastic storage modulus E' is a measure of the elasticity of the material and is proportional to the energy stored during a loading cycle. Therefore, it represents the ability of the materials to store energy and is roughly similar to the elastic modulus for a single, rapid stress at low load and reversible deformation [208]. The Viscous loss modulus E'' is defined as being proportional to the energy dissipated during a loading cycle. The tan delta (δ) is a measure of material mechanical damping or internal friction in a viscoelastic system. When tan delta (δ) is > 1, the material can be considered more viscous than elastic, and the opposite when it is < 1, i.e. when E' is higher than E''.
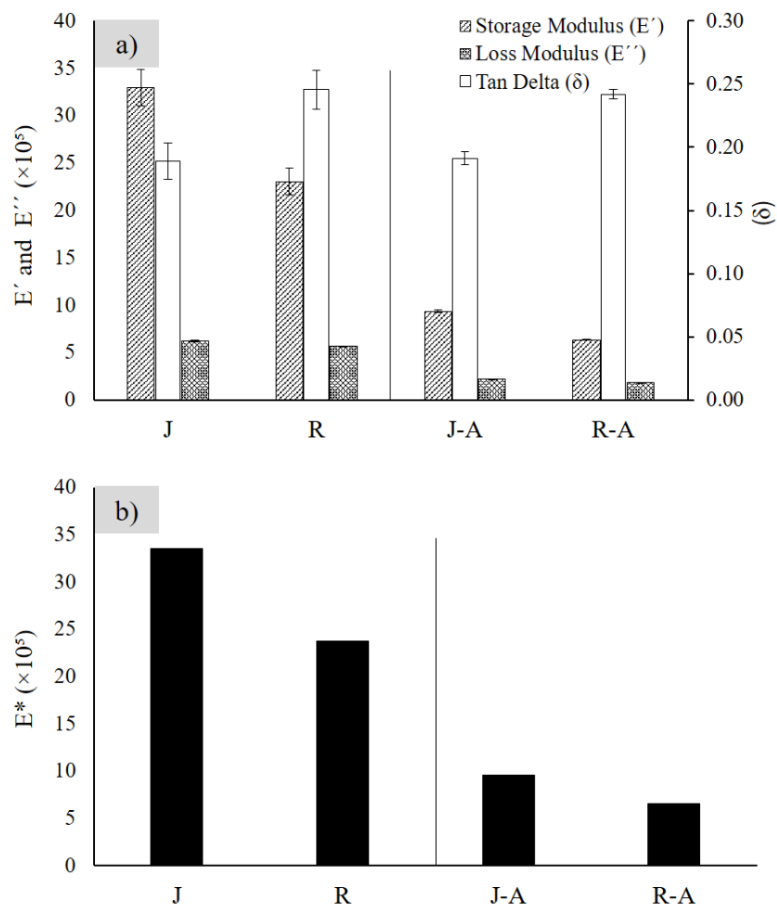
Figure 4.9. a) Comparison on Dynamic mechanical analysis (DMA) of knit reinforcements before and after annealing procedure; b) compression stiffness of all knitted reinforcements. For sample designation see Table 3.1 and Table 3.2.

Figure 4.9a-b shows that the stretching-annealing treatment clearly affected the viscoelastic compression parameters of the knitted reinforcements, significantly decreasing the elastic (E') and viscous (E'') moduli and the overall stiffness (E*) of the "treated" reinforcements. Furthermore, it is also

84

apparent that the untreated jersey structures showed significantly higher storage (E') and loss (E'') moduli than the Rib1x1 ones. Between the "treated" samples, these parameters are not considered different (Figure 4.9a).

The tan delta (δ) of both knitted architectures before and after the stretching-annealing treatment are lower than 1, but it is higher in the Rib 1x1 reinforcements. Figure 4.9b demonstrates the superior compression stiffness (Complex modulus) of the jersey reinforcements before the stretching-annealing treatment. After this procedure, the complex moduli of both reinforcements are similar. The reasons are lied on decreasing the stored energy and energy dissipation of treated knitted reinforcements which are resulted from stiffening the monofilaments after stretching-annealing treatment.

4.3. Mechanical Properties of KSPCs

The mechanical properties of all KPCs prepared by PCCM (PK-composite) and NYRIM (NK-composite) techniques were studied in relation to the knitted reinforcement architecture, fiber volume fraction, ply orientation and stacking orders. Table 4.3 demonstrates all NK- and PK-composite samples and explains their designations. The reinforcements unidirectionally oriented upon each other. In such a way KSPCs with three fiber contents were prepared, i.e., 15, 20 and 25 V_f%.

Table 4.3. The designation and detail description of NK- and PK-composites.

KSPCs designation	Knit reinforcement architecture	V_f,%	Plies Number (PCCM)	Plies Number (NYRIM)	Plie Orientation
P/N[a]U-J([b])-15		15	3	5	
P/N[a]U-J([b])-20	Jersey reinforcement after stretching and annealing	20	5	7	Unidirectional[b]
P/N[a]U-J([b])-25		25	6	8	
PM-J([c])-15		15	3	-	Multidirectional[c]
P/N[a]U-R([b])-15		15	3	5	
P/N[a]U-R([b])-20	Rib reinforcement after stretching and annealing	20	4	6	Unidirectional[b]
P/N[a]U-R([b])-25		25	5	8	
PM-R([c])-15		15	3	-	Multidirectional[c]

[a] P or N represent the PCCM and NYRIM molding techniques respectively in this study.

[b] Unidirectional laminating of Knit textile reinforcements in which 0 for wale-wise or 90 for course-wise directions.

[c] Multidirectional laminating of Knit textile reinforcements via combination of wale (0), course (90) and diagonal (45) orientations. Therefore, the designations of A and B represent the stacking orders of 0/45/0 and 90/45/90 respectively.

4.3.1. Tensile properties of PA6 matrices

The basic in-plane tensile test was carried out to explore the influence of polymerization technique on tensile behavior of PA6 matrix component. The stress–strain graphs of PA6 matrix component prepared by PCCM and NYRIM techniques are illustrated in Figure 4.10. As the axial stress is gradually increased in increments, the total elongation over the gauge length is measured at each load increment and this is continued until failure of the matrix sample.

Two major tensile stress values of interest are recognized in stress-strain plot of PA6 matrix components such as (1) The maximum value of tensile stress where the material can withstand and (2) the fracture stress which is the value of the stress at fracture. The tensile stiffness is basically the ratio of stress to strain and is measured from the gradient of the linearly elastic region. The tensile ductility of PA6 matrix is represented at the strain in which the material undergoes large strain before fracture. As Figure 4.10 demonstrates, the stress-strain graph of NN matrix sample followed ductile behavior although the PN matrix sample failed in brittle manner.
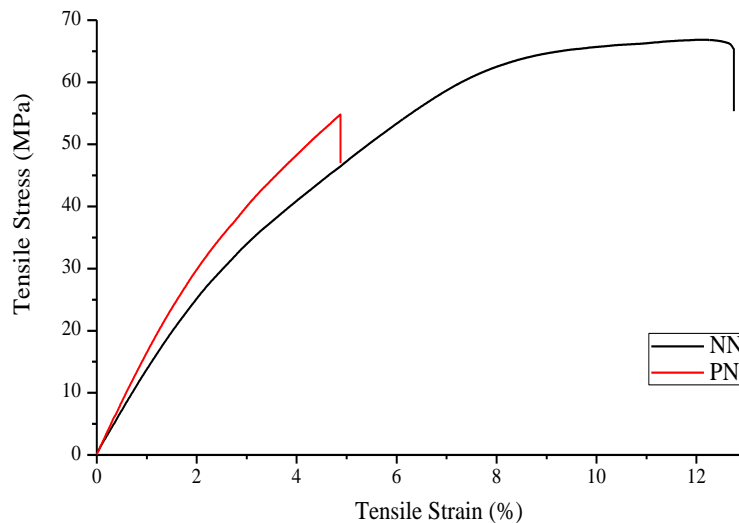
Figure 4.10. The stress–strain curve of PA6 matrix component prepared by PCCM and NYRIM techniques.

Refer to the stress-strain graph of PN and NN (Figure 4.10), the elastic zone was determined at the tensile test onset (the tensile strain of 0.5-1.5 %). Moreover, the stress-strain graphs of stretched-annealed knitted reinforcements showed dual elastic behavior that dispersed from inflection point. Correspondingly, the elastic zone before this point had been selected to measure the reinforcement tensile stiffness. Thus, the elastic modulus of annealed knitted reinforcements was calculated at the matching strain range of the matrix components.

The tensile data analysis in Table 4.4 evidenced higher tensile stiffness of PN matrix component (25% IF_{NN}). In return, the NN sample owned high tensile strength (σ_{max}=66 MPa) compare to the PN matrix sample (σ_{max}=56MPa). The region between stresses at max and fracture point represents the "necking" or "neck down" which is s a mode of tensile deformation that large amounts of strain are localized disproportionately in a small region of the material. Therefore, overlapping of max tensile stress with stress at fracture evidences no necking effect. The NN matrix samples showed higher ductility due to the higher tensile strain at fracture (133% IF_{PN}). Moreover, their great ductility permitted large local deformation on the vicinity of the highly stress concentration area (i.e. the cracks, rivet holes), thereby preventing the occurrence of sudden, catastrophic failures.

Table 4.4. Data about the tensile properties of matrix component prepared by PCCM and NYRIM techniques.

Specimens	Young´s modulus E(GPa)	Stress at max σ_{Max}(Mpa)	Stress at break σ_{Br}(Mpa)	Strain at max ε_{Max}(%)	Strain at break ε_{Br}(%)
PN	1.73 ± 0.02	56.71 ± 1.77	56.71 ± 1.77	5.19 ± 0.11	5.19 ± 0.11
NN	1.38 ± 0.05	66.20 ± 2.96	65.02±2.69	11.61 ± 0.94	12.11 ± 1.07

4.3.2. Tensile properties of PK-composites

The influence of the type of knitted architecture (Jersey or Rib1×1), V_f,% (15,20 and 25%) and ply orientation (wale-0°, course-90°) on the tensile properties of KSPCs is shown on Figure 4.11a. The stress-strain curve of neat anionic matrix PN is presented to enable comparison. Changing the strain direction to 90° in respect to wale resulted in the stress-strain curves in Figure 4.11b. During the early stages of loading, all Unidirectional KSPCs behave a linear elastic manner followed by pseudo-plastic before reaching an ultimate stress. Eventually, it is tracked by an abrupt drop in stress magnitude corresponding to final failure of the composite material which is resulted from a brittle failure.

Their shape remained unchanged whereby the E and σ_{max} values dropped slightly becoming close or slightly below those of the PN reference. The representative curves of KSPCs reinforced by unidirectional laminate sets of J-A and R-A reinforcements strained along the wale direction (Figure 4.11a) showed very similar slopes in the 0<ε_{br}<2% range, which is used to calculate the E modulus. In general, the σ_{max} values of all KSPCs converge to values up to 70 MPa, i.e., clearly above that of the PN matrix material. Most all ε_{br} values in this series are below 10%, i.e., slightly larger than the value of the PN reference.
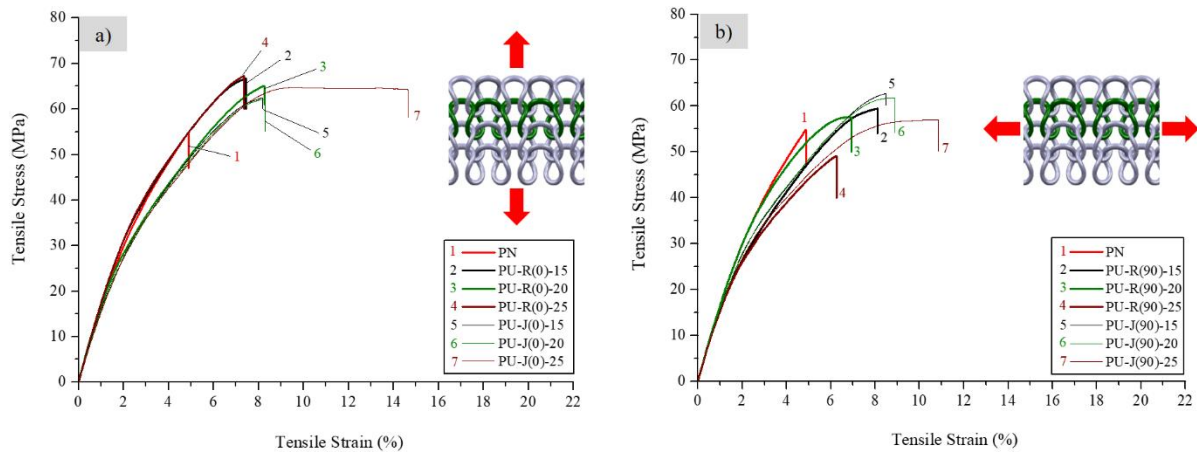
Figure 4.11. Stress-strain curves in tension of SPCs: (a) Strain applied along the unidirectional alignment of the ply set; (b) Strain normal to the ply set alignment; For sample designation see Table 4.3.

Figure 4.12 presents a comparison between the stress-strain curves of unidirectional (PU series) and multidirectional (PM series) laminates with three textile plies (V_f =15%). The failure mode of multidirectional KSPCs became prolonged after maximum tensile stress (plateau region). Likewise, there is a marginal difference on tensile stiffness and strength of uni or multidirectional KSPCs.
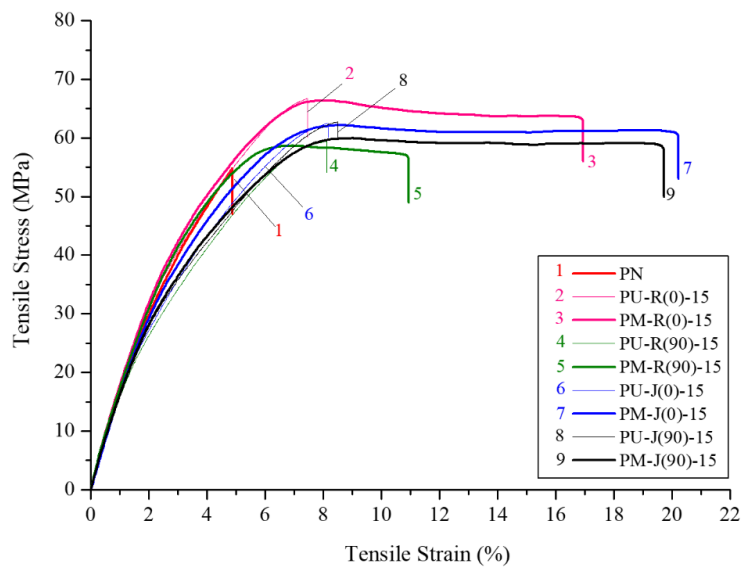
Figure 4.12. Stress-strain curves in tension of KSPCs materials with three uni- or multidirectional plies of both types, strain applied in two perpendicular directions. In all stress-strain curves the neat anionic matrix PN is presented for reference. For sample designation see Table 4.3 and the text.

Notably, the PM composites displayed higher ε_{br} values compared to the PU homologues, best expressed in the KSPCs with J-A reinforcements. On the other hand, the highest σ_{max} and E-values were obtained in the composites with either uni- or multidirectional ply sets containing R-A reinforcements (Figure 4.10, curves 2,3). Higher ductility (strain-to-failure) of multidirectional KSPCs is quantified by the fracture strain and reduce of area at fracture which is due to increase the impact force absorptivity of

88

composites.

Deep analysis of tensile properties of KSPCs illustrates distinctly in which the influence of reinforcement orientation, architectures, and volume fractions had been specified. As seen from the averaged mechanical data tabulated in Table 4.5, the reinforcement architecture does not significantly influence the composites' tensile stress, but slightly affects the tensile strain, being lower for the R-A reinforced ones.

Except for sample P-J-25, these KSPCs display a brittle behavior. The increase in fiber volume fraction also had a minor effect on the tensile behavior of the KSPCs produced by the PCCM technique. R-A structure strengthened tensile properties of KSPCs; hence, the best tensile stiffness (ca. 1.9 GPa) and strength (ca. 68 MPa) achieved for R-A reinforced KSPCs respect to the wale (0) direction.

Table 4.5. Data about the tensile properties of PK-composites. For sample designation see Table 4.3 and the text.

Sample designation	Young´s modulus E(GPa)	Stress at max σ_{Max}(Mpa)	Stress at break σ_{Br}(Mpa)	Strain at break ε_{Br}(%)
PN	1.73 ± 0.02	57.3 ± 0.9	56.7 ± 1.8	5.2 ± 0.1
Durethan B30S*	1.03 ± 0.04	51.2 ± 2.0	65.5 ± 1.3	37 ± 6.0
PU-R (0)-15	1.93 ± 0.03	65.9 ± 0.7	63.9 ± 1.1	9.2 ± 0.5
PU-R (0)-20	1.68 ± 0.02	64.2 ± 0.6	67.8 ± 1.1	8.5 ± 0.4
PU-R (0)-25	1.87 ± 0.03	67.4 ± 0.4	58.1 ± 1.6	10.3 ± 0.1
PU-R (90)-15	1.62 ± 0.01	58.7 ± 0.6	55.9 ± 1.5	8.4 ± 0.6
PU-R (90)-20	1.72 ± 0.04	55.3 ± 0.6	43.0 ± 0.7	7.1 ± 0.1
PU-R (90)-25	1.63 ± 0.05	43.0 ± 0.7	61.7 ± 1.1	6.4 ± 0.2
PU-J (0)-15	1.66 ± 0.05	62.1 ± 0.3	62.8 ± 1.4	8.9 ± 0.4
PU-J (0)-20	1.61 ± 0.03	62.3 ± 0.5	64.6 ± 0.5	9.7 ± 0.6
PU-J (0)-25	1.65 ± 0.03	65.3 ± 0.8	62.8 ± 0.4	19.8 ± 0.3
PU-J (90)-15	1.69 ± 0.01	63.1 ± 0.3	61.4 ± 0.4	13.6 ± 0.5
PU-J (90)-20	1.58 ± 0.03	61.3 ± 0.6	60.7 ± 1.2	13.8 ± 0.7
PU-J (90)-25	1.53 ± 0.01	61.9 ± 0.6	62.1 ± 1.3	11.8 ± 0.7
PM-R (0)-15	1.78 ± 0.03	63.6 ± 0.4	57.9 ± 1.1	16.9± 0.1
PM-R (90)-15	1.76 ± 0.02	59.3 ± 0.5	60.3 ± 0.4	11.0 ± 0.2
PM-J (0)-15	1.69 ± 0.02	62.2 ± 0.2	58.5 ± 1.0	19.6 ± 0.8
PM-J (90)-15	1.67 ± 0.02	59.8 ± 0.6	56.7 ± 1.8	20.0 ± 0.7

* Commercial neat hydrolytic PA6 of BASF, Germany, compression molded granulate [209]

The multidirectional stacking order outstandingly increased the ductility of KSPCs although the changes were considerable for J-A reinforced KSPCs (Table 4.5). Unlike unidirectional reinforced KSPCs, laminating the knitted reinforcement with different stacking order caused significant discrepancy between the maximum tensile stress and stress at failure. This difference represents the necking behavior of the KSPCs in which large amounts of strain are localized disproportionately in a small region of the material (Table 4.5).

Figure 4.13 compares the tensile stiffness and strength improvement factors of all KSPCs respect to the PN reference. In this radar chart, the orbit with 0 index represent the base compared factor known as PN reference. The out-layer orbits display the tensile properties improved values compare to the PN reference (IF_{PN}, %). To select the best sample, coincidence of tensile stiffness and strength is a major criterion. Therefore, wale-oriented composites reinforced by R-A architecture, as well as, 15% fiber volume fraction identified as the best sample due to the superior tensile stiffness and strength. It should be noticed that J-A reinforced KSPCs owned steady tensile properties in different orientations albeit the IF_{PN} values for R-A reinforced KSPCs fluctuated around the reference orbit. This can be explained by anisotropic behavior of annealed Rib reinforcements in two principal (0° and 90°) directions. Moreover, the necking behavior of multidirectional KSPCs become observable by the discrepancies between radar charts of stresses at max and break in which the area under former chart overlaps on the latter.
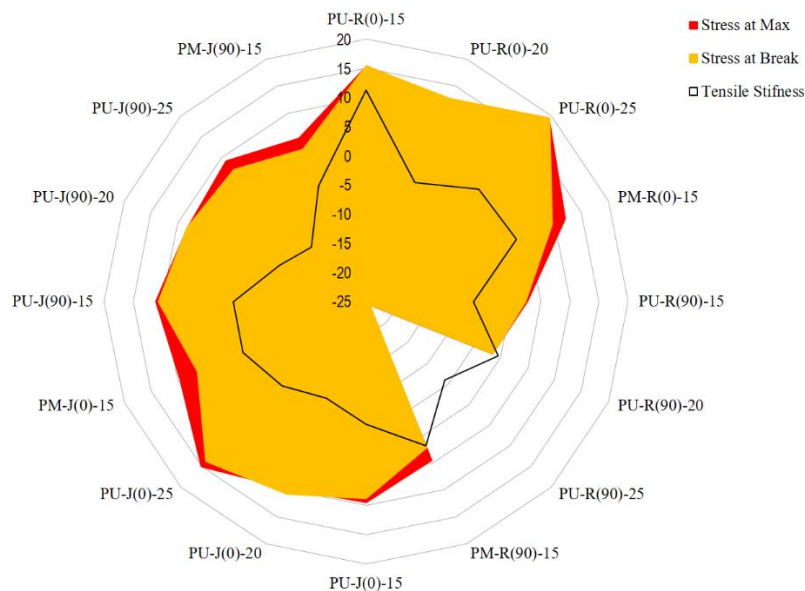
Figure 4.13. Calculated tensile stiffness and strength improvement factors of all PK-composites compared to the PN reference. For sample designation see Table 4.3 and the text.

4.3.3. Tensile properties of NK-composites

The influence of knitted reinforcement architecture (Jersey and Rib 1x1) and fiber volume fractions (15, 20 and 25 V_f,%) on the tensile behavior of KSPCs laminates prepared by NYRIM techniques (NK-composites) was investigated. Examples of the stress–strain curves obtained in the wale direction are shown in Figure 4.14. Regarding the tensile properties of NK-composites (Figure 4.14), it is apparent that the in-mold polymerization of ECL caused an increase in ductility (from 5 to 17%) and tensile strength of

the matrix component (from ca. 55 MPa to 60 MPa), as illustrated by the stress-strain curve of the neat matrix (NN). However, the tensile stress of all NK-composites was significantly lower than in the PCCM samples. The explanation of this experimental result should be related to the finishing of the reinforcing textile structures.

It can be hypothesized that irrespective of the preliminary washing, traces of the finishing probably still remained on the textile fibers and hindered the sensitive in-mold AAROP process that forms the PA6 matrix in-situ during NYRIM. This hindrance resulted in a lower degree of conversion of ECL to high molecular weight PA6 leading to the deterioration of the mechanical performance of the NK-composites. Since the PCCM samples are produced with already existing PA6 powders, textile finishing does not have any influence there.
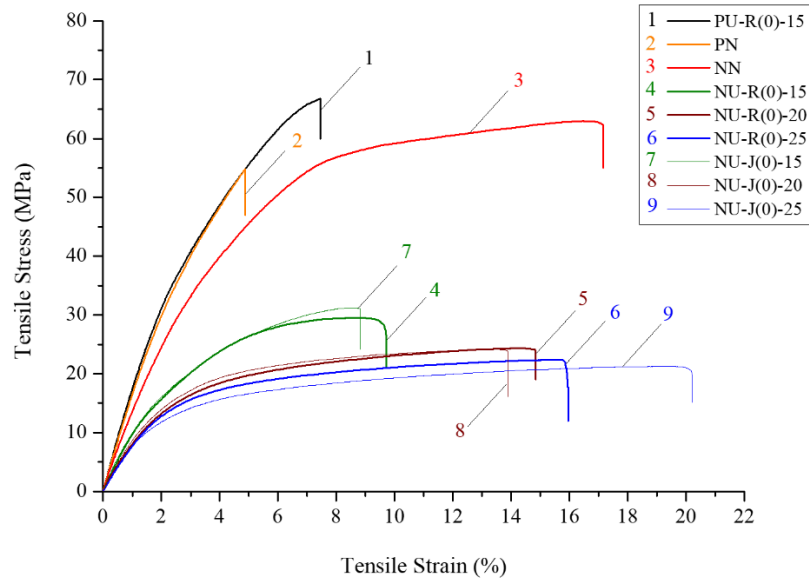
Figure 4.14. Comparative study on stress–strain characteristics for NK- and PK-composites and influenced by reinforcement architectures and fiber volume fractions. For sample designation see Table 4.3 and the text

The tensile properties of all the NK- and PK-composites are presented in Figure 4.6. From the obtained results, the knitted reinforcement architecture exclusively affected the tensile stiffness of the PK-composites. The increase in the fiber volume fraction tended to reduce the tensile rigidity and to increase the tensile strength and strain at break of these KSPCs laminates, but are not considered significant. In the case of NK-composites, a clear increase in the strain at break is observed with an increase with fiber content, together with a decrease in tensile strength and stiffness. In the following sections, morphological and crystallographic studies will be presented to investigate possible causes for this behavior. It should be noticed that all KSPCs designations in following sections are merely represent the PK-composites.

91

Table 4.6. Data about the tensile properties of NK-composites. For sample designation see Table 4.3 and the text

Specimens	Young´s modulus E(GPa)	Stress at max σ_{Max}(Mpa)	Stress at break σ_{Br}(Mpa)	Strain at break ε_{Br}(%)
PN	1.73 ± 0.02	56.71 ± 1.77	56.7 ± 1.8	5.19 ± 0.11
NN	1.38 ± 0.05	67.82 ± 0.96	66.4 ± 1.08	12.65 ± 0.54
NU-R(0)-15	1.04 ± 0.01	28.88 ± 0.60	28.10 ± 0.85	7.13 ± 0.13
NU-R(0)-20	0.83 ± 0.02	23.91 ± 0.76	22.92 ± 1.06	12.33 ± 0.58
NU-R(0)-25	0.77 ± 0.02	23.45 ± 0.16	20.0 ± 0.53	18.03 ± 0.16
NU-J(0)-15	1.08 ± 0.07	28.76 ± 0.40	28.40 ± 0.49	9.91 ± 0.64
NU-J(0)-20	1.02 ± 0.03	24.62 ± 0.51	23.01 ± 1.00	14.05 ± 0.39
NU-J(0)-25	0.89 ± 0.01	21.81 ± 0.68	20.53 ± 0.98	20.84 ± 0.39

Figure 4.15 distinctively exhibits the differences of stress-strain graphs of PU-R(0)-15 sample and its components. Knitted reinforcement demonstrates dramatically feeble tensile properties in comparison with matrix component. Therefore, higher tensile stiffness of KSPCs, merely, cannot be related with the tensile properties of knitted reinforcements. Because the R-A reinforced KSPCs illustrated better tensile properties despite J-A reinforcement had superior tensile properties (see Figure 4.5). In this study, it is believed that reinforcement structural parameters, crystalline morphology and crystalline division can explain the different tensile behavior in KSPCs.
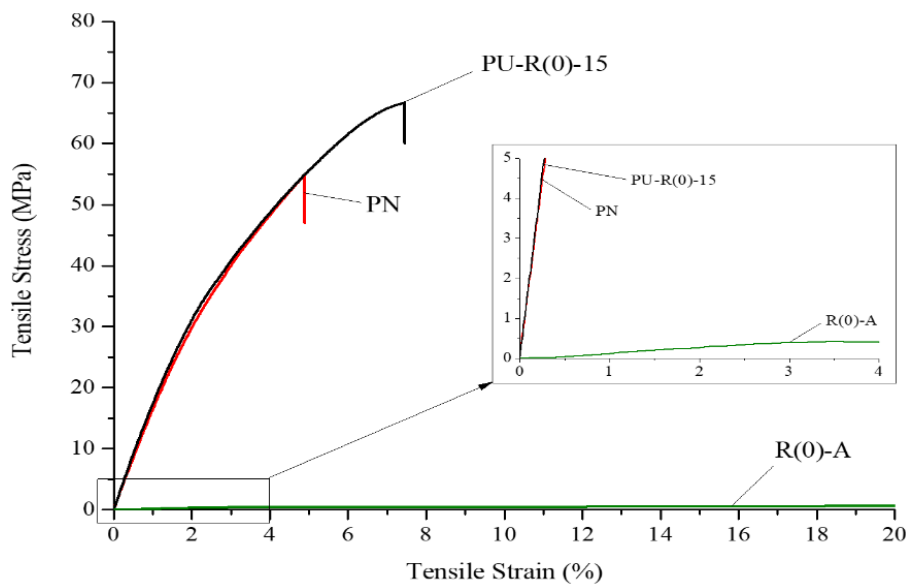
Figure 4.15. Comparison on stress-strain graph of PU-R(0)-15 and its components

4.3.4. Flexural Properties of KSPCs

The flexural stress-strain graphs of uni- or multidirectional KSPCs in wale (0°) and course (90°) directions with the flexural displacement of 10mm is demonstrated in Figure 4.16a-b. The flexural stress-

strain curves show noises which may results from vibrations of the supports, delamination in the top and bottom faces of composite plates and initiation of damage in the sample. The linearity in flexural curve explains the elastic deformation of the KSPCs. This trend is followed by reaching max flexural stress and then continued to sustain the load (plateau region). The maximum failure stress on the tension side of a flexural specimen was considered the flexural strength.
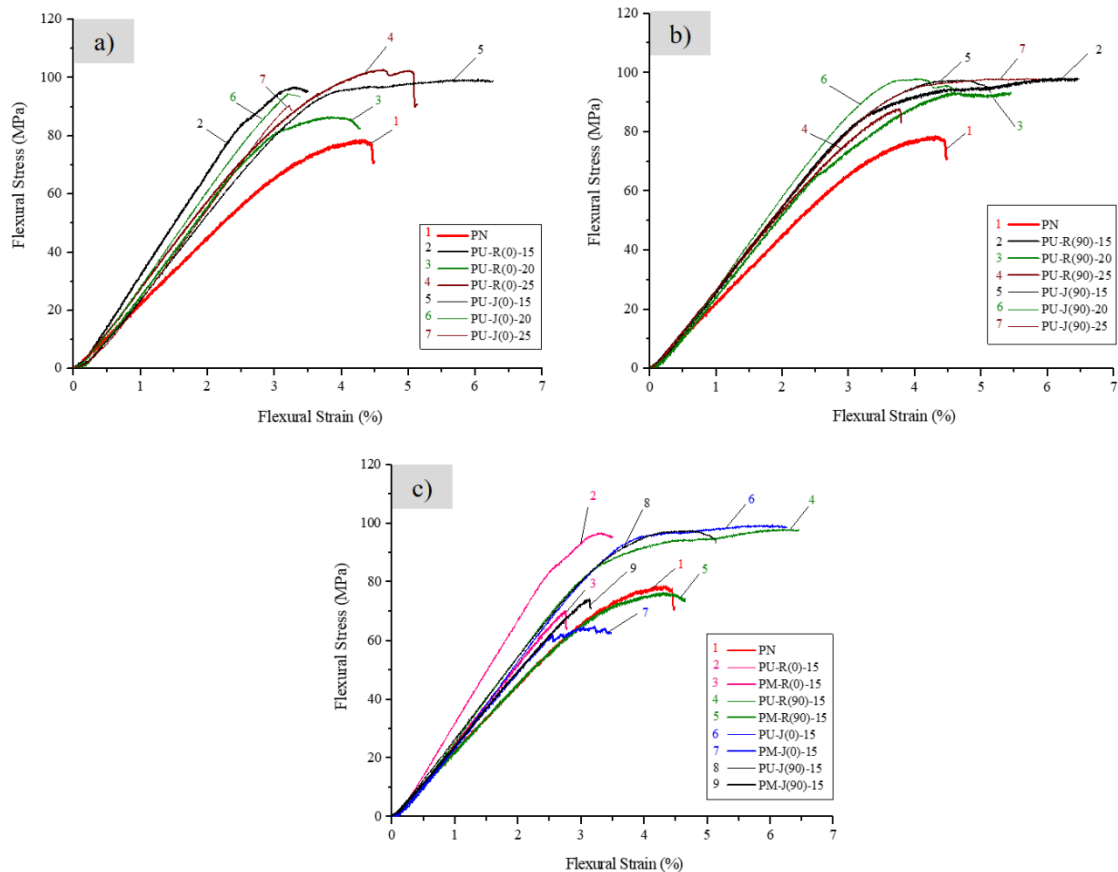
Figure 4.16. Stress-strain curves in flexural of unidirectional KSPCs in a) Wale b) Course Direction; c) A comparative study on Flexural Stress-strain graphs of uni- or multi KSPCs. For sample designation see Table 4.3.

The flexural data analysis of KSPCs influenced by knit architecture (Jersey, Rib1×1), fiber volume fraction (15, 20 and 25 V_f%) and reinforcement´s direction (0° and 90°) is shown in Figure 4.17. The knitted reinforcements remarkably enriched the flexural properties of the matrix component in two principal directions (Figure 4.17a–b). The flexural properties of matrix component remarkably improved by applying knitted reinforcements in two principal directions. Figure 4.17c displays that multidirectional KSPCs own higher flexural properties compared to the PN reference although diagonal lamination of knitted reinforcements did not improve the flexural behavior of KSPCs while they were compared to the unidirectional KSPCs.
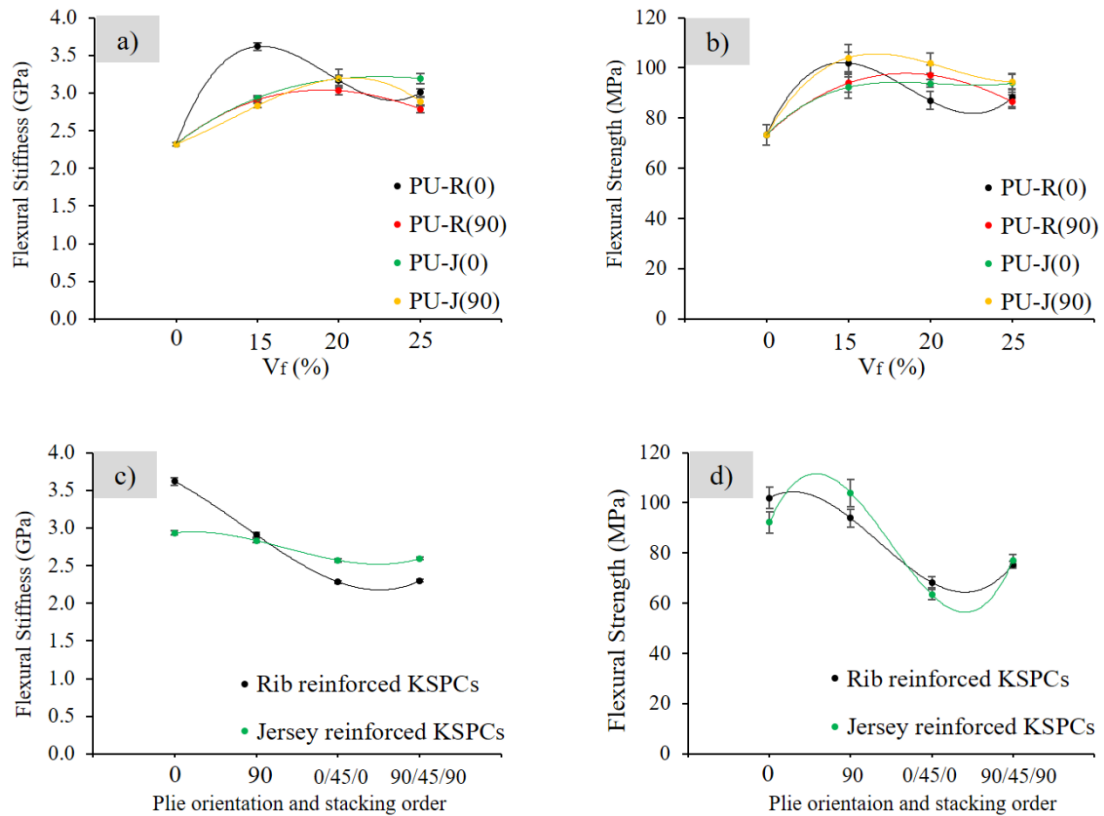
Figure 4.17. Flexural properties of unidirectional KSPCs: a) stiffness (GPa) and b) Strength (MPa) in function of the knitted architecture, fiber volume fraction and reinforcement plies orientation; Flexural properties of uni and multidirectional KSPCs reinforced with 15% fiber volume fraction: c) stiffness (GPa) and d) Strength (MPa) in function of the knitted architecture, reinforcement plies orientation and stacking. The designations are presented in Table 4.3.

Applying knitted reinforcements improved significantly the flexural properties of KSPCs. The higher increase on the flexural stiffness and strength was obtained with the R-A reinforced KSPCs containing the lowest fiber volume fraction (15%) and plies oriented in the wales direction (PU-R (0)-15). The flexural stiffness (Figure 4.17a) and strength (Figure 4.17b) of unidirectional stacked KSPCs was not significantly changed by fiber content increment, except for the Rib laminates where an increase from 15 to 20 V_f% led to a significant decrease in the flexural properties. The higher increase on the flexural stiffness and strength was obtained with the R-A reinforced KSPCs containing the lowest fiber volume fraction (15%) and plies oriented in the wales direction (PU-R (0)-15).

For the same fiber volume fraction, the KSPCs with J-A embedded in the course direction (90°) showed the highest flexural strength (≈100 MPa). The composites with 15 V_f% were higher resistant to flexural loads. Figure 4.17c-d compares the flexural properties of rib and jersey KSPCs with 15 V_f% and plies uni and multidirectional stacked.

Flexural properties improvement factor (IF_{PN}) of all KSPCs is illustrated in Figure 4.18 wherein R-A

reinforcements oriented in wale direction, modified the flexural properties of PA6 neat polymer up to 60%. Despite higher bending rigidity of course wise R-A structures (see Figure 4.8), unidirectional R-A reinforced KSPCs owned feeble flexural rigidity in that direction. As conclusion, the different flexural behavior of KSPCs specimens cannot be correlated merely with the bending rigidity of knitted reinforcements. The influences of knitted reinforcement structural parameters on flexural properties of KSPCs and interfacial bonding compositions at the interface are investigated in detail in future sections.
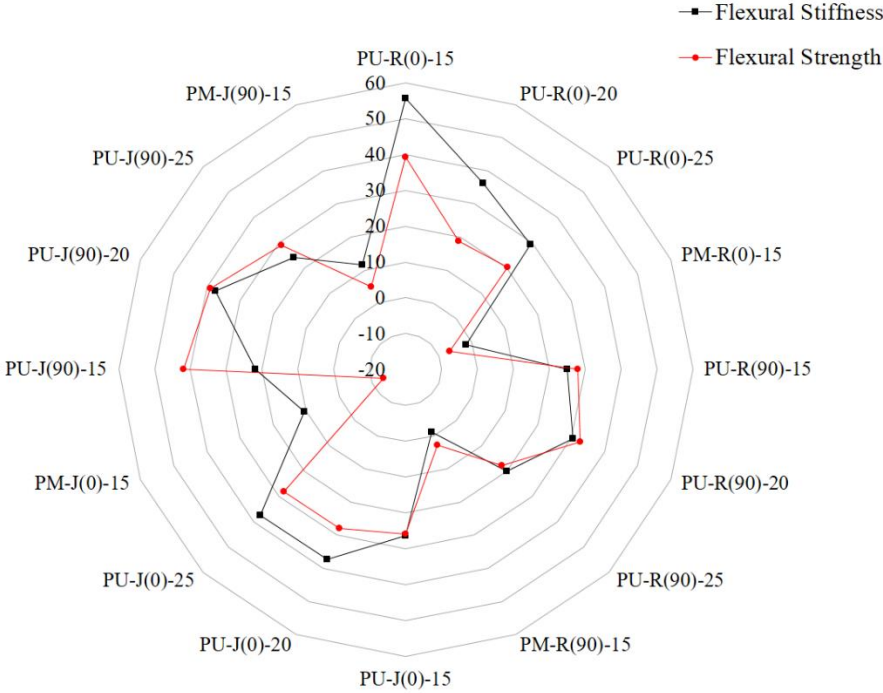
Figure 4.18. Flexural properties improvement factors of all PK-composites compared to the PN reference. The designations are presented in Table 4.3.

4.3.5. Izod impact strength of KSPCs

The impact behavior of all KSPCs was evaluated through the unnotched Izod test. Figure 4.19 shows the impact strength (I_s) of the uni-or multidirectional KSPCs. The I_s value of the neat matrix (PN), is also represented for reference. As it can be seen, embedding knitted reinforcements significantly improved the impact resistance. The impact strength of KSPCs with wale-oriented jersey reinforcements (0°) and 15 V_f,% increased up to 340% when compared to the PN reference. Moreover, the unidirectional J-A reinforced KSPCs showed better impact resistance than the R-A reinforced ones. Increasing V_f,% from 15 to 25% led to a decrease of the composite's impact strength, except for the wale-oriented R-A reinforced

KSPCs. This decrease is highly significant in the wale-oriented J-A reinforced composites (Figure 4.19). The reason can be explained by structural analysis of knitted reinforcements and crystalline morphology at the interface region in next sections. The KSPCs with 90/45/90 stacking order showed superior impact strength than those with plies embedded with 0/45/0 order. It should be noticed that the multidirectional plies orientation modified the impact strength of KSPCs.
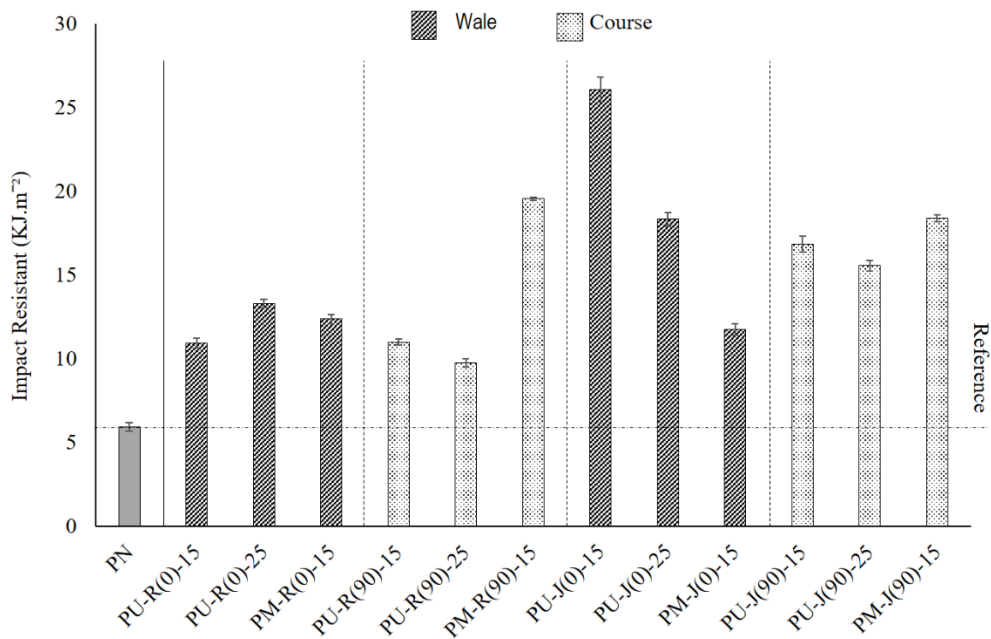
Figure 4.19. Comparison on planar Izod Impact resistant of uni-or multidirectional KSPCs with influences of knit architecture, fiber content, laminate orientation and multidirectional plie stacking

4.4.   Discussion

4.4.1. Tensile failure analysis of KSPCs

The tensile failure criteria can be characterized by composite fracture surface configuration. Figure 4.20a-c shows representative cross-section SEM fractographic tensile failure of uni-or multidirectional annealed R-A reinforced KSPCs with 15 V_{f},% fiber contents. The stress amplified linearly with increasing strain up to a knee point (≈0.5% strain) which was detected as a dropping off point from initial elastic line. The debonding of monofilament oriented normal to the testing direction is caused microcracking wherein the nucleated cracks propagate into resin-rich regions. Subsequent of knee point and before reaching an ultimate stress, the pseudo-plastic manner in the stress/strain curves (see Figure 4.11a-b) were attributed to material deformation and microfracture processes in the specimen. At plastic zone, matrix cracking is created from debonding at the interface followed by an abrupt drop in stress magnitude corresponding

to final failure of the composites resulted from a brittle failure. Fracture point coincided with peeling of monofilaments from the fracture surface and the fracture plane is bridged by unfractured filaments.

The fracture surface in Figure 4.20a-c demonstrates the advent of the crossover points which architecturally defined by the junction of the sinker loop and loop head (Figure 4.20d). In addition, knitted reinforcements were installed with slight longitudinal differences in which the loops of each plies could not be perfectly aligned upon each other. Therefore, it can be deduced that differences on plies longitudinal alignment did not cause the distinct fracture surface configuration. Meanwhile, despite the plie alignments and orientations, the fracture surface cross section of KSPCs ascertained that the highly stressed cross over points in knitted structure were responsible of tensile failure.
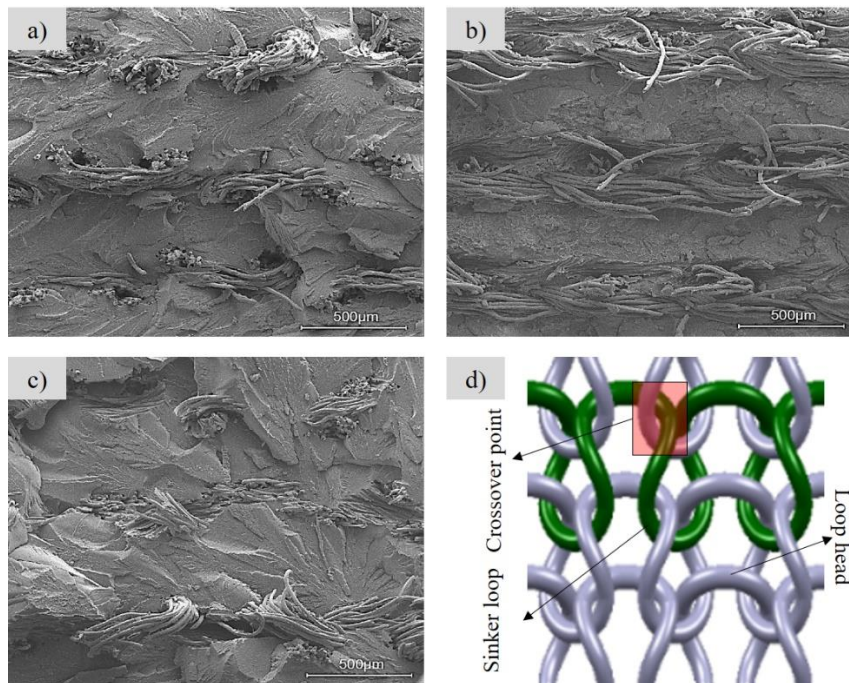
Figure 4.20. SEM fractography and fracture surface of a) PU-R(0)-15 b) PU-R(90)-15 c) PM-R(0)-15 d) Crossover point in an ordinary knit structure

As it mentioned above, the cross over points are situated on sinker loop and higher radii of curvature of the loop head. Longer loop length amended the fiber loading efficiency. Moreover, in knit fabrics the inter-filament shear is a common mode of deformation in which depends on the orientation of the reinforcement large in-plane tension and in-plane shear in different direction. The filaments are getting flatten while stresses at yarn crossover points compress the monofilaments in the filament bulk [210]. This increases the lower dynamic friction force (Figure 4.21). Therefore, during compression molding, filaments were compressed upon each other on cross section points followed by growing the stress concentrations and splashing out the matrix solution from the cross over regions.

This structural hindrance may due to feeble interfacial bonding between KSPCs components and led to form micro-voids and correspondingly accelerated the tensile and flexural stress-strain of KSPCs toward the plasticity region. Meanwhile, measuring the quantity of crossover points in annealed knitted structures enhanced to understand better feeble tensile properties of Jersey reinforced KSPCs. Figure 4.21a-b shows the breaking up of each loop into straight sections within six-degree intervals, which were projected in the wale (0°) and course (90°) directions to obtain the average loop fraction contribution- Loop Partition fraction (LPF%) - in the respective direction. This helped finding the principal orientation of filaments in the knitted structure. Moreover, measuring the length of each loop partition (Loop Partition Length -LPL) and the loop length from the simulated loop cell can support further failure analysis of KSPCs.
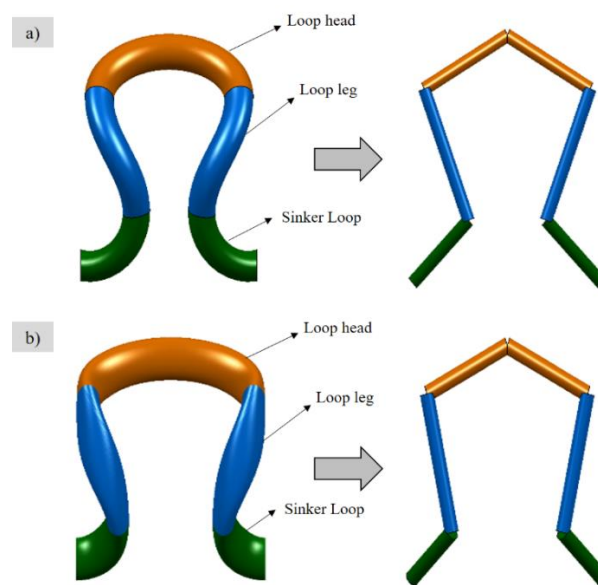
Figure 4.21. Simulated real size annealed Loop cell in a) R-A; b) J-A structure. The loop straight sections division is shown aside.

The constructional parameters of the annealed knitted fabrics were also considered to evaluate the number of cross-over points. Figure 4.22a demonstrates the plots the number of wales per centimeter (WPC), courses per centimeter (CPC) and stitch density (WPC×CPC) for the annealed knitted reinforcements. The J-A structure contains higher stitch density than R-A, hence, the number of crossover points increased for J-A reinforcements. Figure 4.22b shows the LPL magnitude of each loop for both knitted structures. As it can be observed, the sinker loop length of the jersey structure is significantly lower than that of the R-A. These two characteristics – higher stitch density together with lower sinker loop length – can lead to higher stress concentration at cross-over points, causing the earlier failure of jersey reinforced KSPCs.

98

As depicted in Figure 4.22c, the major contribution of each loop cell is in the wale direction, which can explain the higher tensile properties of unidirectional annealed R-A reinforced KSPCs in that direction (see Figure 4.11a-b). Figure 4.22c also demonstrates identical LPF in the wale and course directions for diagonal embedded knitted reinforcements. Therefore, the higher ductility and necking behavior of multidirectional KSPCs can be explained by the identical LPF value obtained in the diagonal embedded knitted reinforcements, which resulted in equal stress distribution in the cross-section. This caused the delay of tensile breakage of the middle plie (diagonally embedded) while the top and bottom plies failed.

The SEM images of surface fracture in multidirectional KSPCs prove this fact, by showing a more even fracture surface of the composite (see Figure 4.20c). Although, the weakly flexural behavior of PM series of KSPCs than PU series can be expound by identically contribution of loops in either directions (Figure 4.22c) caused reduction of radii of loop curvature and increase crossover points known as mechanically destructive structural parameter.
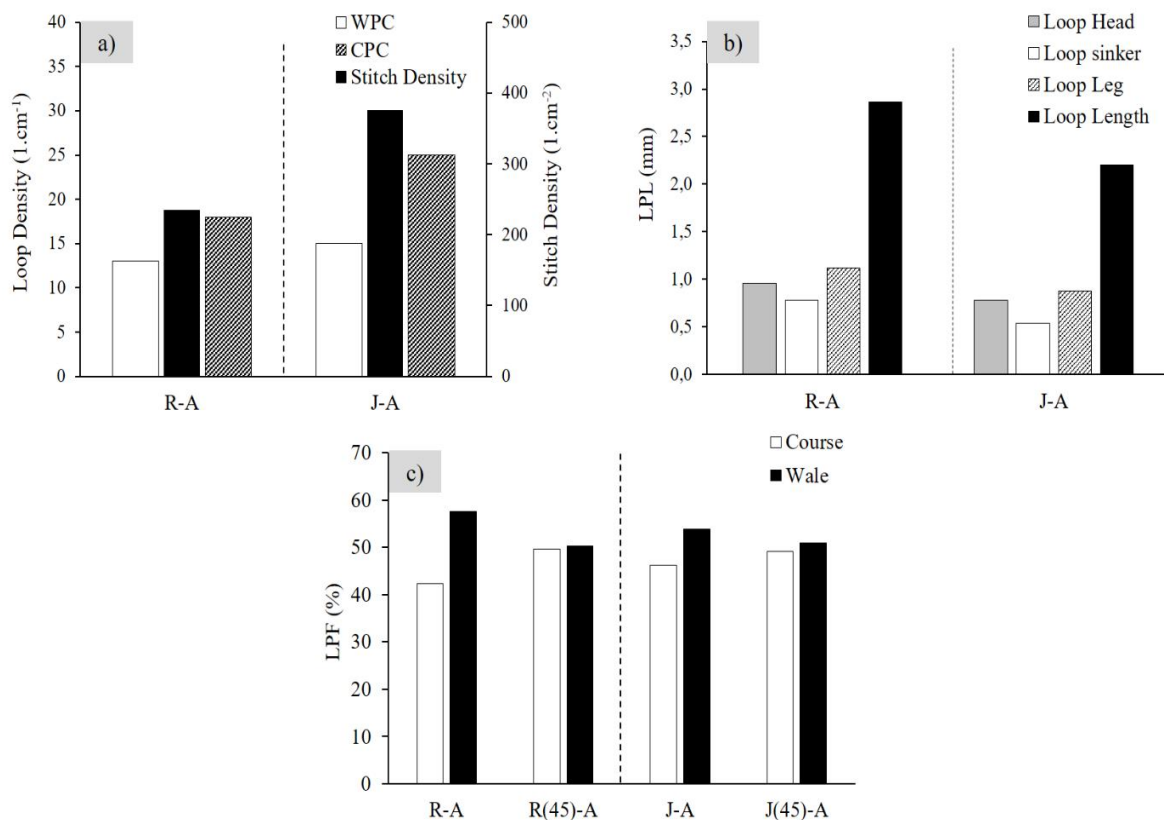
Figure 4.22. Structural analysis of knitted reinforcements based on a) loop density; b) LPL (mm); c) LPF (%)

4.4.2. Impact failure mechanism of KSPCs

To better understand the impact behavior of KSPCs, scanning electron microscopy (SEM) studies were

performed. Figure 4.23a-d shows SEM images of impact failure cross-sections of uni-or multidirectional R-A reinforced KSPCs with 15 V_f,%. To assist in the failure analysis, the fracture locations were simulated and represented by the intersection lines 1 to 5 drawn on the top view of the simulated R-A structure (Figure 4.23e).
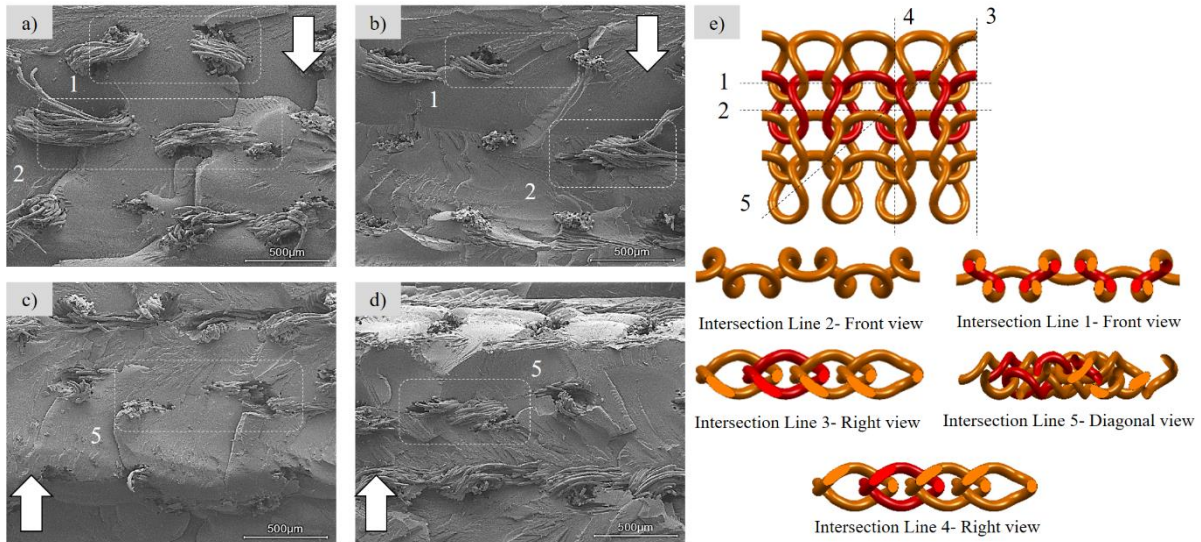
Figure 4.23. SEM fractography fracture surface of a) PU-R(0)-15; b) PU-R(90)-15; c) PM-R(0)-15; d) PM-R(90)-15; e) Simulated 5 possible observable reinforcement architecture at the impact fracture surface. The white arrows in figures represent the direction of impact strike.

The fractured surface of PU-R(0)-15 specimen demonstrates the emergence of loop heads and sinker loops due to the initiation of breakage from the highly-stressed crossover points. On PU-R (90)-15, the different plies' orientation led to a distinct fractured surface configuration, but ascertained that loop cross over points were responsible for the impact failure (Figure 4.23a-b and lines 1 and 2 in Figure 4.23e). The fractured surfaces of multidirectional R-A reinforced KSPCs is illustrated in Figure 4.23c-d. Since the plies' set comprises reinforcements installed in the bias direction, the fractured surfaces depict disordered configurations. Intersection lines 5, shown in Figure 4.23e evidence the appearance of all loop components, such as, loop head, leg and sinker loop, in the fractured surface cross section of multidirectional R-A reinforced KSPCs which may cause a better distribution of impact loads and modify the impact strength for unidirectional R-A reinforced KSPCs.

From these studies, it is apparent that the loops cross over points are primary factors for KSPCs failure. Therefore, geometrical study on a unit area of stretched-annealed knitted reinforcements can explain the better J-A reinforced KSPCs. The knitted pattern provides cross-over points and the stitch density affects the number of cross-over points per unit area. Therefore, the influence of J-A and R-A

structures on mechanical properties of composite can be compared by the same stitch density. Figure 4.24a-b shows the number of cross over point per 3×3mm unit area of stretched-annealed knitted structures. The number of cross over point per unit area was 56 and 40 for J-A and R-A reinforcements respectively. Therefore, higher cross over points in J-A structure was in contradiction with the better impact and flexural properties of J-A reinforced KSPCs.
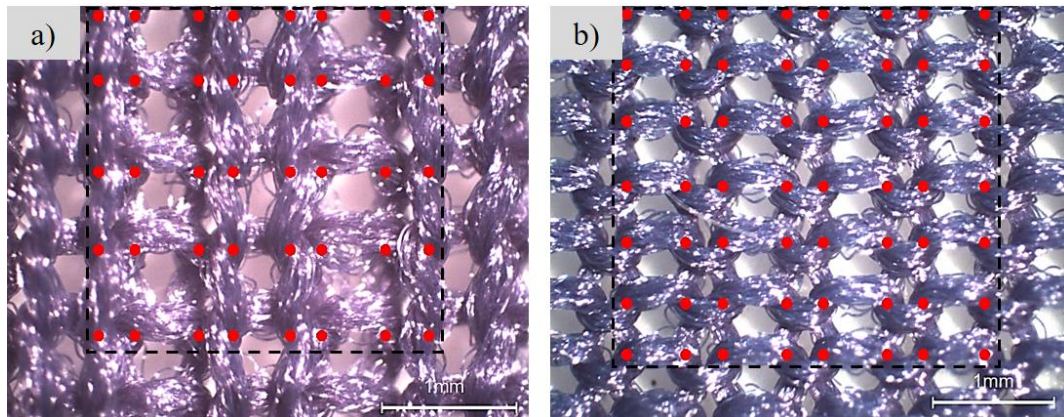
Figure 4.24. Microscopic images of 3×3mm unit area in stretched-annealed a) J-A b) R-A reinforcements; The red pointers indicate the cross over points.

Geometrical study of treated knitted reinforcements couldn't merely explain the different flexural and impact properties of reinforced KSPCs. Meanwhile, the distribution of tensile and compression stress along the body test sample during bending and izod impact experiments was investigated to reveals the causes of KSPCs mechanical failure. Figure 4.25a-c shows typical beam flexural test specimens in which a bending moment causes a beam to bend. The outside boundary, beyond the neutral plane[18] is extended although the inside boundary, below neutral plane, is contracted a little shorter [211]. In case elastical assessment, the material at the outside and the inside edges are in tension and compression respectively. The sizes of the stress distributions along tension and bended sides should be kept in balance until reaching to yield flexural strength.

The tension and compression stresses toward the surfaces proportionally increases while the neutral plan maintain at the middle of cross section (Figure 4.25a). In contrary, unsymmetrical stress distribution can be contributed by shifting neutral plane due to the better material balances on either side of it (Figure 4.25b-c). Due to the application of same matrix component with identical molding condition, a comparative study on tensile and compression behavior of knit structure particularly, could provide a

---

[18] There can only be one plane through the beam that isn't either longer or shorter than it was before the bend which is called neutral plane [211].

logical proof on failure mechanism and better flexural and izod impact properties of Jersey reinforced KSPCs.

Refer to the obtained DMA data analysis, J-A reinforcements had slightly higher complex compression modulus than R-A structures (see Figure 4.9b). Despite of the position of neutral plan, the impact properties of the composite beam were depended to the tensile properties of the knit structures wherein J-A reinforcements owned better tensile stiffness and strength than ribs in two principal directions (Figure 4.6). Therefore, at the beginning of impact collision the top lamina dissipates the strike forces and then disperse them through subsequent plies.
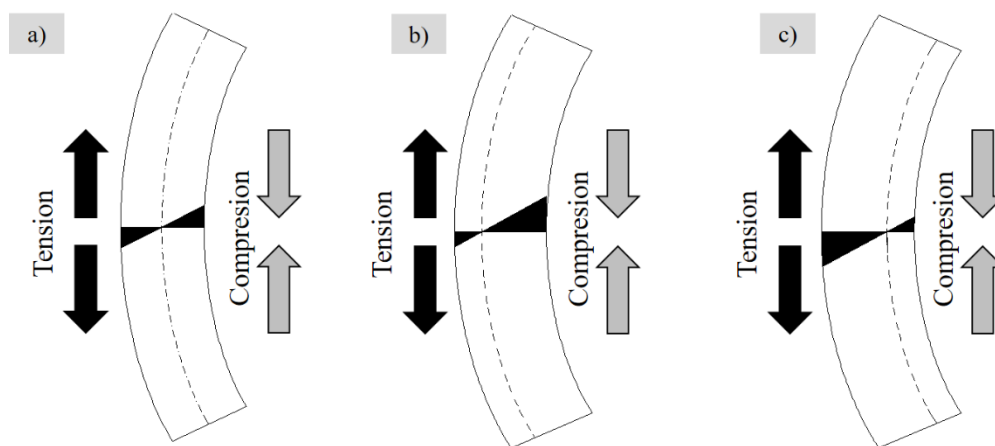
Figure 4.25. a) Schematic of annealed embedded Rib structure at moment of bending b) symmetrical Stress distribution schematic during bending c) schematic of unsymmetrical stress distribution during bending.

4.5. Conclusion

Knitted reinforced single polymer composites based on polyamide 6 (KSPCs) were successfully prepared by combination of powder impregnation and compression molding techniques (PCCM). Moreover, Nylon resin injection molding (NYRIM) was applied to produce KSPCs via in mold polymerization of ε-caprolactam (ECL) in presence of knitted reinforcements. Stretching-annealing treatment of the knitted textile reinforcements showed impressive improvement of their mechanical properties. The influence of reinforcement architecture (Rib1×1 and Jersey), fiber volume fraction (15, 2 and 25 V_f,%), reinforcement orientation (wale-0° and course-90° directions) and multidirectional stacking order (0/45/0 and 90/45/90) on the tensile properties of KSPCs was evaluated.

The results showed that the R-A reinforced KSPCs with relatively low fiber content (15 V_f,%), laminated in the wale direction, obtained the best improvement of tensile stiffness and strength when compared to

anionic and conventional PA6 polymer. The tensile fracture mechanism of the KSPCs was found to depend on the structural deformation of the knitted reinforcements, in which crossover points were the main factors responsible for tensile failure.

The NYRIM technique produced laminates with low stiffness and strength values, the reason being the formation of oligomers in the presence of the knitted textile reinforcements. This technique is advantageous for the preparation of neat PA6 plates.

The J-A reinforced KSPCs with relatively low fiber content (15 V_f,%) brought steady flexural properties and impact improvements up to 340% compare to the neat anionic PA6 matrix component. All knitted reinforced composites showed improved flexural and impact properties when compared to the neat matrix. The comparative studies performed on the tensile and compression rigidities of knitted reinforcements demonstrated that despite of the position of neutral plan, the higher impact strength of the Jersey reinforced KSPCs could be depended to the tensile properties of the Jersey structures in two principal directions in which is close to the incident side.

Chapter 5

Microstructure study of KSPCs

5.1. Introduction

Polyamide 6 are applied in many applications such as molding, extrusion and casting in which processing techniques have influence on the PA6 crystalline structure. Therefore, structural characterization of PA6 reinforcements and matrix components brings better mechanical-geometrical analogy of KSPCs. The characterization of PA6 polymer is influenced by the number of quantities.

I.   **Constitution:** average molecular weight, type and density of crosslinking, types and concentration of end-groups.

II. **Conformation:** type and extent of inter forces.

III. **Composition:** water content, monomer content, concentration and distribution of cyclic oligomers, filler content.

IV. **Crystallinity:** degree of crystallinity, composition of the crystalline phase, micromorphological structure (extended and folded chains).

V.   **Orientation:** extent of orientation of either or both the polymer chain molecules and crystalline structures.

Identification of molecular weight, crystalline orientation and thermal behavior can explain the differences on mechanical properties of KSPCs. Meanwhile, the structural relationship of knitted reinforcements are essential for any conceivable mechanical fracture analysis. The present chapter deals with the parametric study between interface status, crystallography, polymorph structure and thermal properties of KSPCs and their components. The main objectives of this study are investigation on TCL advent at the reinforcement/matrix interface and detecting the nature of TCL which may be linked with the causes of mechanical failure described in chapter 4.

5.2. Cryogenically surface topography and TCL study

Figure 5.1, schematically demonstrates the mechanism of TCL generation in KSPCs that can be resulted from different relaxation between matrix and knitted reinforcements. In this case while melt doesn't become relaxed, a void is appeared (Figure 5.1a). Fully relaxing of melt instantaneously with crystallization process led to shrinking entire system (Figure 5.1b). As a result, the density gradient will

be associated with stress field while the melt relaxes locally and maintain the crystal line body (Figure 5.1-c), creates a layer with different properties compare to the matrix/reinforcements interface [26].
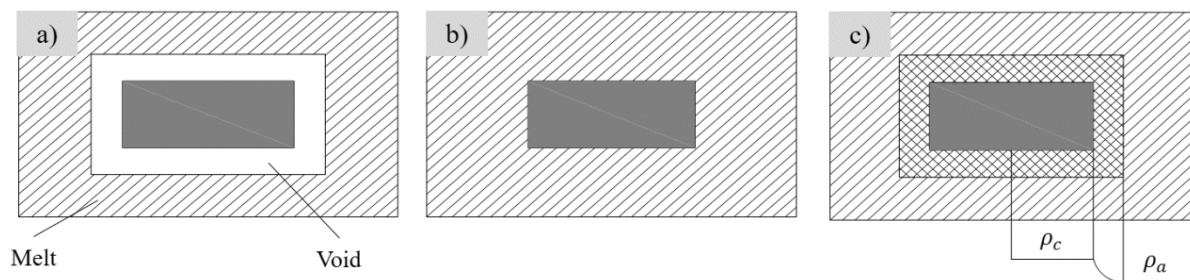
Figure 5.1. Effect of the formation of a more dense crystal in a less dense melt [26]

Polarizing light microscopy (PLM) and scanning electron microscopy (SEM) was used to characterize the KPCs materials and the components comprising knitted reinforcements and MPs. This technique was beneficial for both quantitative and qualitative studies targeted at a wide range of anisotropic specimens. Figure 5.2a shows image analysis of microscopic knitted reinforcements wherein the average thickness of monofilament measured around 17-18 µm. Figure 5.2b-f shows the PLM micrographs of the PU-R(0)-15 and PU-J(0)-15 samples in which a Rib1×1 and Jersey knit loop embedded in the matrix material. The embedded knit loop was targeted by dashed frame due to the further image analysis. Notably, the PA6 filaments from the textile structure do not show any sign of melting that would deform their circular cross-sections.

Figure 5.2b demonstrates the magnified and gamma saturated image of embedded knit loop in birefringent surface of PU-R(0)-15. A close visual inspection of the latter and of the longitudinally cut monofilaments reveals refractive index differences between the core of some textile PA6 monofilaments and their surface suggesting the presence of transcrystalline layer (TCL). As seen from both pictures in Figure 5.2c, the average thickness of the textile monofilament embedded in the KSPCs material was about 22-23 µm, whereas in the annealed knit structures, it was 17-18 µm (Figure 5.2a). It should be mentioned that the average thickness of the textile monofilament and embedded ones was obtained by 10 reads from different captured microscopic images. The thickness of this layer seems to be between 4-6 µm. This TCL would be expected to develop during the compression molding because of the epitaxial crystallization of anionic PA6 material from the matrix upon the oriented PA6 filaments of the textile structure. Such a phenomenon was observed and studied earlier in similar SPC materials obtained by reactive injection molding [86].

A micrograph of the same PU-R(0)-15 sample with crossed polarizers, which provides information on absorption color and optical path boundaries between composite components of differing refractive indices (Figure 5.2d). Polarized image allows the observation of the isotropic matrix (not birefringent) and the birefringent oriented monofilaments were displaying existence of orientation-dependent differences in refractive index, i.e., different superficial color in wale and course directions. It revealed second and third order polarization colors and their distribution across the monofilaments. The center of the stage rotation coincided with the center of the field of view due to maintaining the birefringent specimen in the exact center when rotated. Whenever the specimen was in extinction, the permitted vibration directions of light passing through which was parallel with those of either the polarizer.
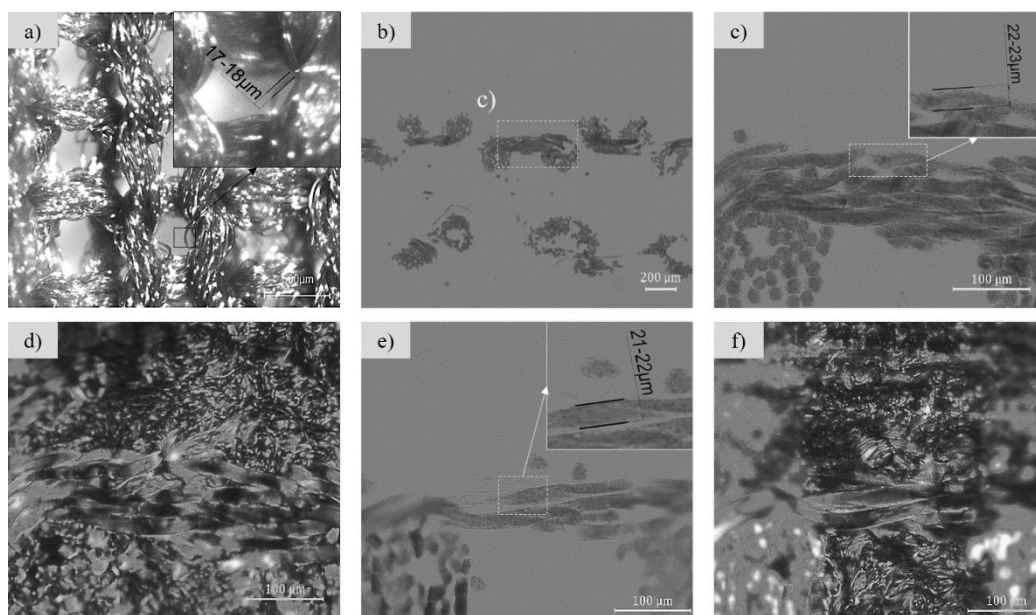
Figure 5.2. a) R-A sample with normal light and measured monofilament´s thickness; b) Light microscopy image of PU-R (0)-15; c) Identifying two distinct PLM image fields that represent the matrix component (bright field mode) and embedded monofilaments (dark field mold); d) Crossed polarized image of (c); e) Light microscopy image of PU-J (0)-15; f) Crossed polarized image (e)

Consequently, the isotropic portion include matrix component had only one refractive index and no restriction on the vibration direction of light passing through them. On the contrary, anisotropic materials which include grafted monofilament/matrix in course direction, had optical properties that vary with the orientation of incident light with the crystallographic axes (crystal facets). Identical color on monofilament and matrix in wale direction evidence similar refractive indices although TCL recognition is difficult in this direction owing to the uneven birefringent surface. In contrast, appearing the range of colors on monofilaments body in course direction may correlated with existence of TCL in interface region. This can be inferred by light-ray division and beam splitting of anisotropic components into two orthogonal portions.

This method represents a viable to strengthen the possibility of TCL advent at the matrix-reinforcement interface region. Although the DSC and X-ray analysis further strengthen the confidence in TCL appearance. Figure 5.3a-f demonstrate PLM micrographs and cross polarized of the PU-J(0)-15 sample that the average thickness of embedded monofilament was measured between 21-22 μm which was slightly less than R-A reinforced KSPCs. It can be deduced that TCL advent strengthened the reinforcement-matrix interfacial bonds and the TCL with higher thickness leading to better tensile properties of Rib reinforced KSPCs.

Figure 5.3 displays the PLM images of NK-composites, comprising 15 V_f,% of R-A and J-A reinforcements. It can be verified that the average thickness of the monofilaments embedded in NK-composites laminates lies between 19-20 μm. Since the same textile plies shown in Figure 5.2a with thicknesses of 17-18 μm were used in the NK-composites, the TCL thickness in the latter should be of 1-2 μm. In this context, it can be assumed that the thickness of the TCL in NK-composites is lower than PK-composites. Unfortunately, the PLM images of NK-composites under crossed polarizers (Figure 5.3c,f) do not clearly evidence the birefringent TCL structures at the filament-matrix interface which would be a direct proof of transcrystalinity. Most probably, the thicker TCL in the PK-composites can be somehow related with the higher pressure applied during KSPCs consolidation than in the case of NYRIM where the mold closes without making any pressure.
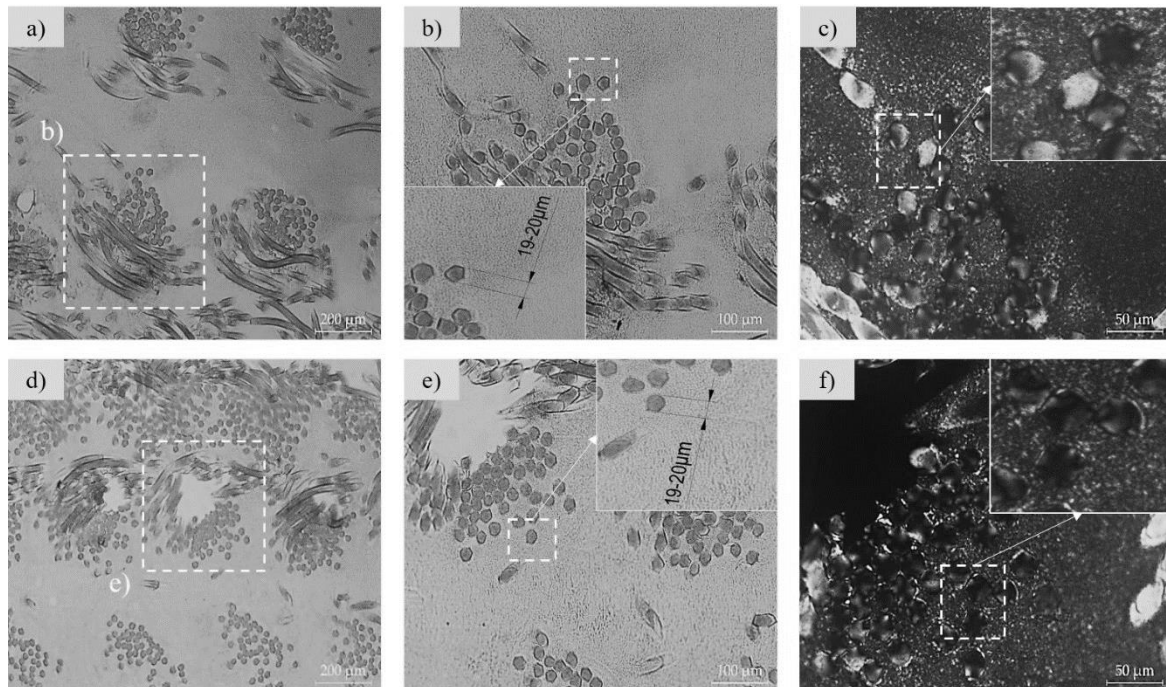
Figure 5.3. Microscopy surface topography of NYRIM prepared unidirectional annealed a-c) R-A and d-f) J-A reinforced KSPCs with 15% fiber volume fraction.

The knitted textile/matrix interface microstructure were studied additionally by SEM. Figure 5.4a-f shows representative micrographs of the PU-R-15 sample cryogenically fractured along the wale (0°) (Figure 5.4a-c) and course (90°) directions (Figure 5.4d-f). From the first three pictures, one can see that the Rib reinforcements are well embedded between relatively thick matrix layers. The monofilaments of the textile structure possess visible diameters of 22-23 μm which confirms the data of light microscopy and supports indirectly the hypothesized TCL formation. The filaments that can be observed in their longitudinal direction show no sign of melting or surface degradation. The images with higher magnification of this series Figure 5.4b-c) showed that the anionic PA6 matrix material has penetrated very well between the monofilaments wetting the well and leaving no visible voids and cracks. Therefore, a strong adhesion at the matrix-fiber interface may be expected.
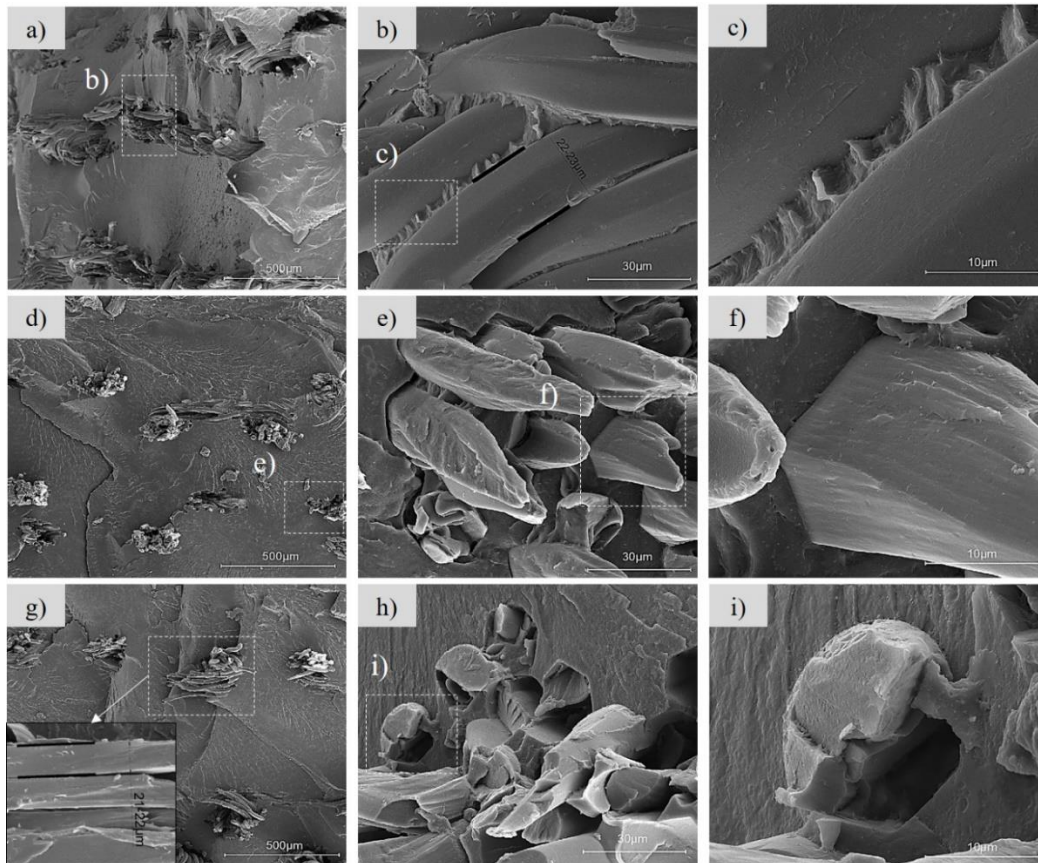
Figure 5.4. SEM images after cryofracture of PU-R-15 composite; a-c) course (90°) direction d-f) wale (0°) direction; g-i) Cryofracture SEM images of Jersey reinforced KSPCs with 15% fiber volume fraction in wale (0°) direction.

Fracturing the KSPCs in wale direction results in cohesive failure of the monofilaments with no formation of voids (Figure 5.4d-f). Larger magnifications (Figure 5.4e-f) demonstrates that the broken filaments obtain conical shapes. This is an indication of strong adhesion between the composite components that forced the filaments carry the load and break rather than to be pulled out of the matrix.

All these effects should be related to the chemical identity of both matrix and reinforcement materials, as well as to the similarity in physical properties related to their melting/recrystallization behavior.

The cryogenically surface fracture and partial pull-out of monofilament from matrix portion in PU-J(0)-15 sample is shown Figure 5.4g-i. The pulled-out monofilaments own a tube-like configuration accompanied by a circular cross section. Moreover, the SEM image in Figure 5.4g shows the average thickness of embedded monofilament, measured about 21-22 μm which agrees with image analysis in Figure 5.3e. The smooth interior portion oriented axially was surrounded by perpendicular superficial part upon it. Meanwhile, a straight boundary discriminates smooth interior and perpendicular superficial portions that may be contributed to the TCL advent (Figure 5.4i). It can be concluded that knit architecture has considerable influence on mode of fracture where cryogenically surface fracture in embedded monofilament showed a conical configuration of pulled out monofilaments. Thus, the better interfacial bonding is predicted for R-A reinforced KSPCs.

The SEM images of the NK-composite (Figure 5.5) display clear microcracks in the regions at the matrix-filaments interface. This behavior is indicative of poor filament/matrix adhesion, which could be one of the reasons that led to insufficient tensile behavior of these KSPCs. Figure 5.5a-f showed the SEM cryogenically surface fracture of NU-R(0)-15 and NU-J(0)-15. The micrographs in Figure 5.5c, f show a good wetting of the filaments by the matrix material and almost circular cross-section of the broken monofilaments that apparently did not resist the external load efficiently and displayed a fragile failure.
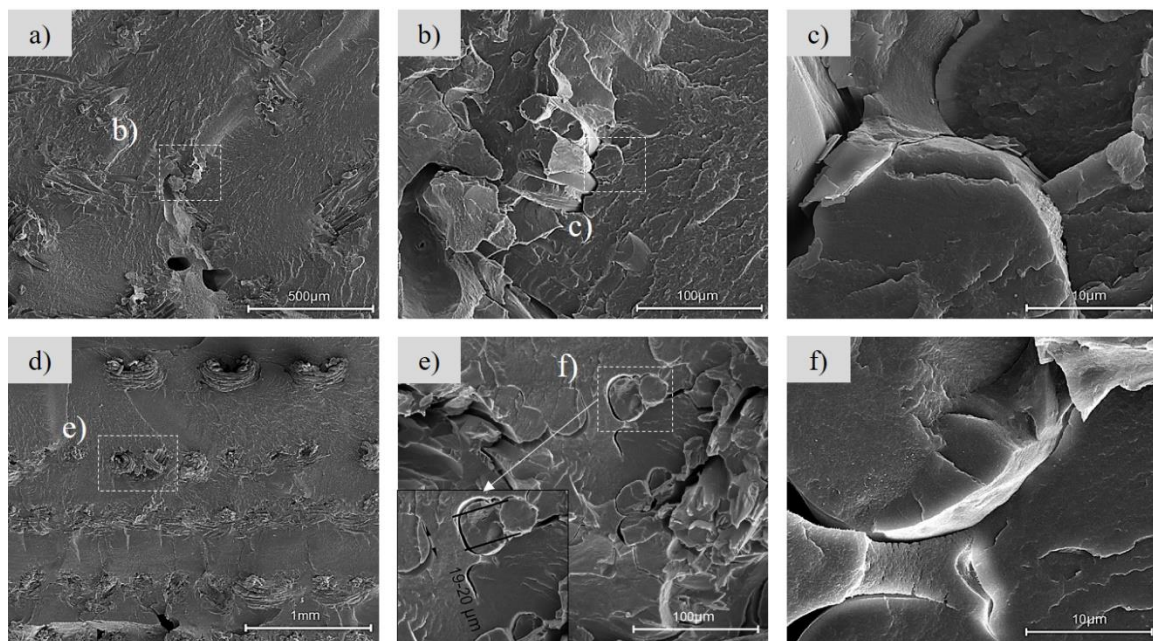
Figure 5.5. SEM images after cryofracture of NK-composites with 15% fiber volume fraction a-c) NU-R(0)-15 d-f) NU-J(0)-15

As it can be seen in Figure 5.5a,d, the cryogenically fracture surface of composites had smooth configuration where no pulled-out monofilament detected. Hence, monofilaments kept their circular configuration associated with toleration of the stresses chiefly by matrix component and proper wetting of matrix through the monofilaments is illustrated in Figure 5.5b,e. Moreover, tracking the magnified SEM images from selected zone in Figure 5.5f represents existence of narrow crystal growth changes, up to 2 μm, from the radial direction to the direction normal to the fiber surface with the 17-18 μm thickness (see Figure 5.2a). The presented achievement is in good agreement with the measured average monofilament´s thickness shown in Figure 5.3b,e. In conclusion, the failure properties of NK-composites illustrated an instantaneous breakage state due to a reedy TCL on interface region.

5.3. Crystalline phases anisotropy of KSPCs

Investigations on unique fingerprint of the crystal-amorphous relationship in the sample and of the nature of chain packing in the crystal phase of polyamide 6 is accomplished by furrier transform infrared spectroscopy techniques (FTIR). Figure 5.6a-b shows the detailed normal coordinate infrared spectra for untreated and annealed Rib1×1 reinforcements at room temperature. The FTIR band positions and intensities of un-substituted amide groups in PA6 are associated with two groups comprising the amide group itself and the intra-molecular factors affecting these bands and advent of intermolecular interactions such as H-bonds on the band positions [212,213].

As it mentioned above PA6 contains two major crystalline phase such as α-crystal form, the γ-crystal form, or a mixture of both. The amide group (CO-NH) has two specific motions such as stretching and bending vibrations (in IR range). The highest frequency amide IR absorption band is the one arising from N-H stretching mode and for amide group in the trans-conformation.

Figure 5.6a shows strong absorption band at 3286 cm^{-1} which represented the amide A, H-bonded N-H stretch vibration [214] due to fall under the same broad envelop of H-bonded N-H stretching mode. It should be mentioned that the intensity of the band cannot be directly associated with the number concentration of N-H moieties corresponding to each band because non-identical the absorptivity coefficients of the three N-H stretch bands. The Amide I band is usually the most intense in the IR spectrum of aliphatic polyamides [214]. The IR bands is fallen in frequencies of 2854, 2916 and 3070 cm^{-1} which are repetitive of C-H stretching bonds.

As Figure 5.6a demonstrates, it is fallen at 1635 cm^{-1} in the solid state which attributed to the Amide

I ($C = O$) where is sensitive to intermolecular interactions such as participation in H-bond formation as well as intra-molecular configurational. This brings discrepancies between the crystal and amorphous phases. The contribution from in-plane N-H bending mode and the stretching mode of the central amide –N-CO- bond can be classified as Amide II that is fallen at $1527 \ cm^{-1}$. Due to the better recognition, shifts in band position with the changes in crystal form from parallel to anti-parallel chain packing is its symptom. The level of disorder in the PA6 sample can be expressed by downfield shifts of Amide II and up field shift of Amide I. The more disordered is the sample the higher amide I and the lower the amide II bands are [91,212].
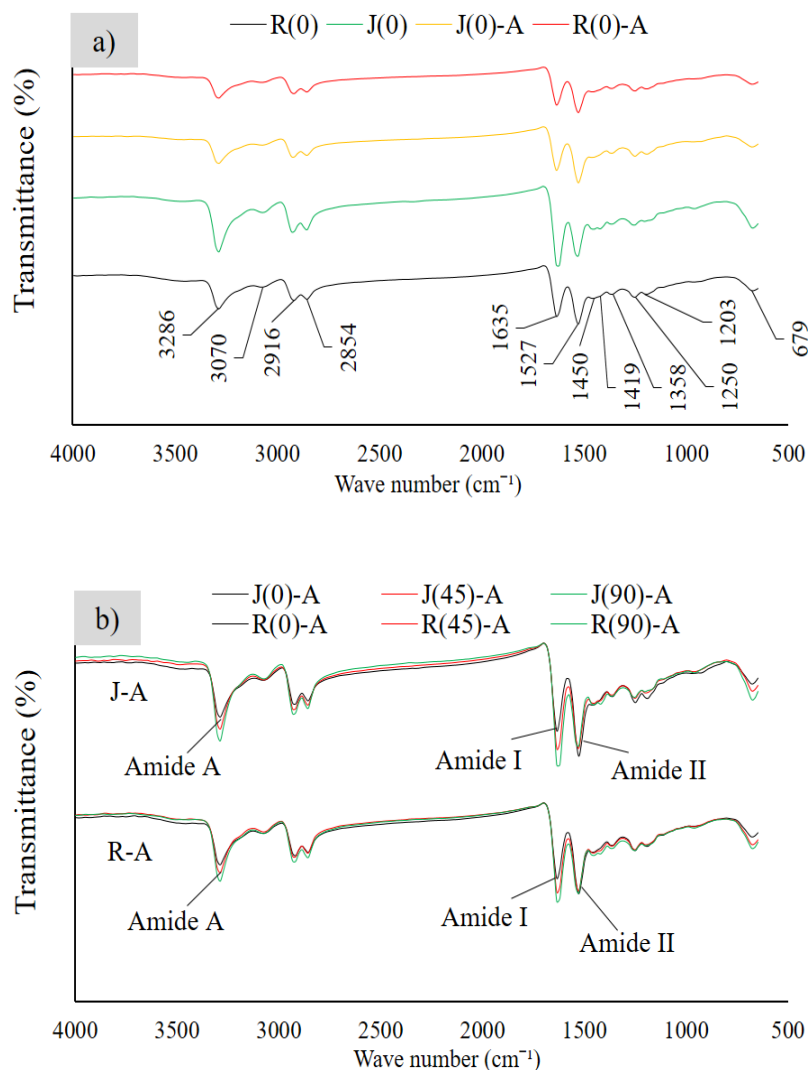
Figure 5.6. a) FTIR spectrum of untreated and annealed PA6 knit reinforcements b) Anisotropy IR spectra influenced by different incident angle IR beam

Unlike Amide II, the amide I band is insensitive to changes in the crystal form, from helical to parallel to anti-parallel chain conformation. Amide I and Amide II bands are sensitive to α-structure crystalline

[91]. Figure 5.6a illustrates gradually decadence of Amide I while the intensity of the Amide II absorption band increases for annealed Jersey reinforcements. Advent of chemical bonds of CH_2 units adjacent to NH and C=O groups were extended in conformation of α-structure of PA6 reinforcements is associated with by IR bands at 1450 and 1358 cm^{-1}. The frequency of 1250 and 1203 cm^{-1} represents the existence of Amide III in trans-structure of α-morphology crystallinity and amorphous state which is vibrated from the interactions of the C-N stretching mode and the N-H in-plane bending mode. Moreover, they represent the existence of both α and γ-crystalline phases [215]. Frequencies of 663 cm^{-1} are out of planes of bends of NH (amide V) group indicated in crystalline α-morphology [91]. All these frequencies were representatives of functional groups in trans planar conformation which had agreement with previous data related to Refs. [46,91].

Amides are derived from carboxylic acids (COOH group) where the -OH part of that group is substituted by NH_2 group. This polymorph grows the possibility of hydrogen (in the NH_2 group) bond to the oxygen atom of another molecule. In carboxylic part the carbon-oxygen double bond contains two different parts such as sigma and π bond in which pi bond sideways overlap between p orbitals on the carbon and the oxygen. Also the lone pair on the nitrogen atom ends up almost parallel to these p orbitals, and overlaps with them as they form the pi bond due to delocalizing the nitrogen lone pair [46,91]. As a result, to superior electronegativity of oxygen, the carbonyl (C=O) is a stronger dipole than the N-C dipole that let amides to become attractive for a nearby hydrogen ion (H-bond acceptors) [216]. Delocalization is due to grow stability of the molecules; hence, Amide I and Amide II bands were sensitive to α-structure crystalline and annealing process was caused transition on their IR spectra.

A comparison on infrared spectra of annealed knitted reinforcements respect to three different incident angles such as wale (0°), diagonal (45°) and course (90°) is demonstrated in Figure 5.6b. The axes of the loops were parallel to the direction of the electric field of the incoming IR in incident angle of 0°. Moreover, assume the macromolecular chains of PA6 are aligned along the monofilaments axis, the carbonyl groups (C=O) to be perpendicular to the filaments axis [217]. Consequently, absorption of the incoming IR beam by the C=O bonds is minimal while samples installed in wale direction.

On the contrary, in Amide I absorption reaches a maximum level while the filaments axis was situated perpendicular to the incident IR beam (90°). The resonance between the carbonyl stretching and the electric field of the incoming IR beam as well as becoming perpendicular to the molecular chain direction were identified the key reasons of such descendent. While annealed knitted reinforcements in course

direction shows that the molecular chains stayed parallel to the fiber direction and the N-H bending direction is almost parallel to the electrical field of the IR beam. Therefore, FTIR spectrum demonstrates the maximum intensity of Amide II absorption an incident angle of 0°.

Increasing the incident angle toward 90° the N-H bending direction becomes perpendicular to the electrical field of the IR beam was caused ascendance of Amide I for Rib1×1 structure despite in Jersey reinforcement, diagonal incident was due to increase the IR absorption of Amide I. IR spectra of all knitted reinforcements illustrated no alternation in IR absorption of Amide II. It could be deduced that unlike J-A reinforcements, R-A structures contain anisotropic crystalline polymorph regarding loop orientation.

5.4. Thermal analysis of KSPCs and the components

5.4.1. Diffraction Scanning Calorimetry study

Thermal properties of PA6 matrix components measured by DSC providing quantitative and qualitative data on endothermic (heat absorption) and exothermic (heat evolution) processes which is beneficial to determine processing windows glass transition temperature, the degree of crystallinity and crystalline phase transition. The comparative study of the first and second scan DSC thermograms of PN and NN matrix samples are demonstrated in Figure 5.7. The first DSC scan of MPs showed revealing a broad peak at the early of the heating process that is associated with the existence of humidity (Figure 5.7a). The reason lied on coinciding of its endothermic peak with boiling temperature of water (100°C). Moreover, the presented hypothesis is ascribed by elimination of the broad peak in second DSC scan shown in Figure 5.7b.

As it can be seen in Figure 5.7a, increasing the melting point of NN matrix ($T_{m(NN)}$) compared to the PN matrix ($T_{m(PN)}$) is explained by their different molecular weight. The viscometric average molecular weight M_v of PN matrix was measured by 25000 g/mol via Soxhlet extraction although NN matrix contained 58000 g/mol molecular weight. However, in both cases, the AAROP occurs at very slow rates resulting in oligomers. The higher M_v in the latter case was because the bulk AAROP takes place at higher temperature, in the polar molten ECL and in strongly basic medium.

These conditions favored complex side reactions leading to partially cross-linked PA6 characterized by molecular inhomogeneity increment. While the attraction between polymer chains become overcame by

the energy of thermal motion, the crystal structure began to break down and consequently melt the polymer. It should be mentioned that smaller molecules have greater thermal motion than big molecules owing to their proportional kinetic energy to mass and the square of velocity [218]. Although intermolecular attractive forces are raised with increasing molecular weight. Therefore, the higher melting point of NN matrix is associated with their higher molecular weight. The second DSC thermal scan was caused eliminating the thermal history and possibly, the $\alpha \rightarrow \gamma$ crystalline conversion occurred in PN and MPs samples proved by observation of small shoulder at about 200°C in the second DSC thermograph, shown in Figure 5.7b. On the contrary, the 2nd DSC scan of NN matrix doesn't show the crystalline transformation.
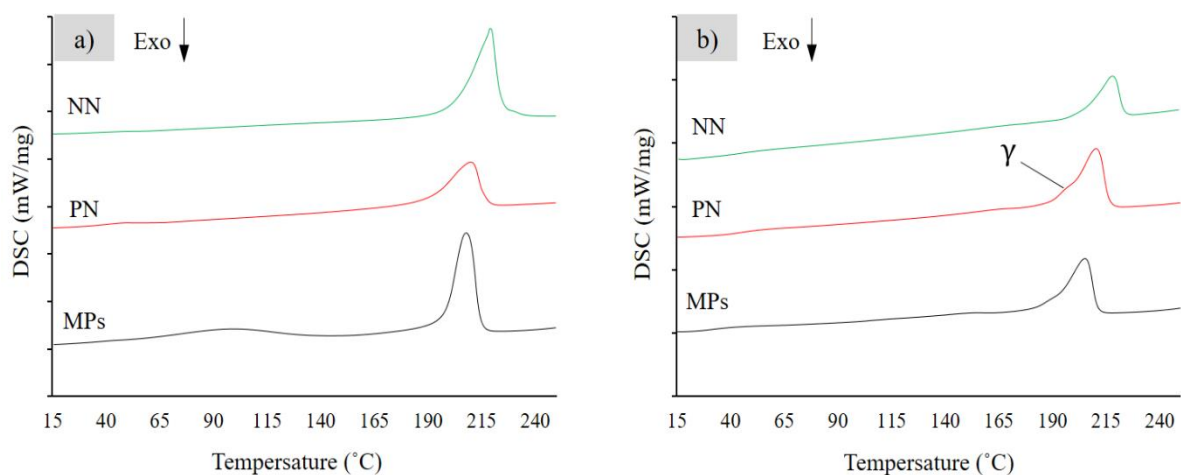
Figure 5.7. Analogy of DSCs thermograms of MPs, PN and NN matrix samples a) First Scan b) Second Scan

The detail thermal properties of PA6 matrix components are presented in Table 5.1. Polyamide 6 are semicrystalline polymers that the glass and infusion transition occur during heat increment procedure [91]. The glass transition is elevated while the polymer chains fall out of their crystal structures and become disordered. Therefore, by means of any deformation, the material are mechanically failed while the mechanical stresses exceed the resistance of motionless polymer chains [46]. The lower T_g for PN matrix evidenced higher amorphous polymorph portion compare to NN matrix which can explain their low tensile strength (see Figure 4.10).

Applying NYRIM technique increased the crystallinity of matrix component, c.a. 57% due to the $\gamma \rightarrow$ α-crystalline transition. Because of the lower T_g of MPs, high amorphous portion is predicted for hot compression molding, caused by the formation γ-crystalline from their polymer chains. Low degree of crystallinity in PN matrix and MPs compare to the NN matrix verify this fact.

Table 5.1. Calorimetry of PA6 matrix components

Samples	T_g *	T_m		T_c	χ_{cr}^{DSC} (%)
		First Scan	Second Scan		
MPs	28.2	207.8	203.8	144.7	34.88
PN	42.4	210	210.3	155.7	27.46
NN	47.1	218.8	217.7	154.1	42.98

* All the glass temperatures obtained from the second scan

A parameter of prime importance for the hot compactions of KSPCs is the width of the processing window. It can be determined by the difference in the melting temperatures (T_m) of the matrix and reinforcements materials. Thus, Figure 5.8a-b display the first and second heating scans respectively performed at 10 °C/min. A processing window width of ca. 16-17°C can be determined in Figure 5.8a, which is significantly higher than that previously found for KSPCs [72]. This fact, as evidenced by the microscopy observations above, apparently solves the problem of the undesirable fusion of the reinforcements during the hot compaction.

Figure 5.8a confirmed that the T_m of MPs is 207-208°C, while those of R, R-A and J-A textile reinforcements vary in the 223-224°C range. This observation could be explained with the already mentioned small size of the highly porous anionic MPs. The absence of side reactions during AAROP leading to cross-linking [219] can explain the inferior T_m of anionic MPs. The slightly lower M_v values in comparison with the Rib1×1 and Jersey textile reinforcements should act in the same direction.

The curves of the first heating show also that the two knitted reinforcements displayed some broad low-temperature endothermic peaks centered at 75°C (Figure 5.8a, curves 1-3) that remained not affected by the annealing with fixed ends at 170°C for 90 min, i.e., below the T_m of the textile. Since this feature disappeared completely during the second scan performed with completely molten textiles (Figure 5.8b, curves 1-3), it was associated to a relaxation processes within the knitted structure occurring right above glass transition temperature T_g.

The low-temperature peak of the MPs appearing during the first DSC scan centered at ca. 100°C could be removed by heating below melting temperature and was therefore related with the release of the humidity absorbed by the porous micron-sized MPs.

117
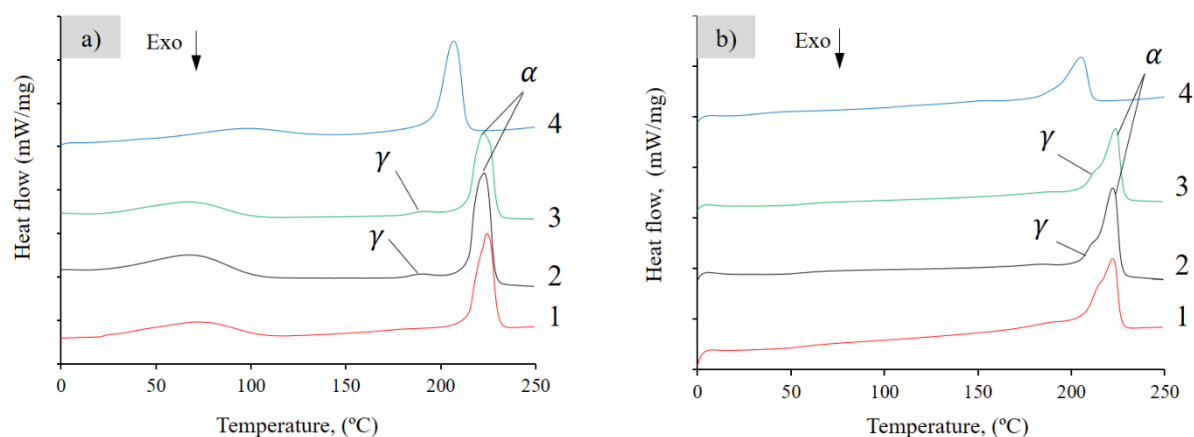
Figure 5.8. DSC curves of KSPCs building components: (a) 1st DSC scan; (b) 2nd DSC scan. 1- Rib1×1 textile reinforcement as received; 2- Annealed Rib1×1 reinforcement; 3- Annealed Jersey reinforcement; 4- Anionic MPs.

The DSC curves in Figure 5.8b reveal the T_g of all samples that were covered during the first scan by the lower temperature endotherm. In the two textile structures before and after annealing the T_g values lie between 56-57°C, while the T_g of the MPs was found to be 33°C. This observation indicates higher segmental mobility of the polymer chains in the anionic MPs as compared to those in the knitted textile reinforcements. The maxima of the melting endotherms during the second scan for the knitted structures coincided with those of the first scan being all centered at 223-224°C.

Notably, a low temperature shoulder in the 212-214°C appears in these samples during the second scan (Figure 5.8b curves 1-3) attributable to the melting of the γ-PA6 polymorph, while the T_m values above 220°C should be related to the α-PA6 polymorph [46,213,220]. The molten MPs displayed a T_g of 210°C being with 3°C higher than that during the first scan (Figure 5.8a, curve 4). This curve shows also a weak shoulder below 200°C that could be related with the melting of some amounts of anionic γ-PA6.

Figure 5.9 displays the DSC traces of laminate KSPCs reinforced by uni- and multidirectional orientation of the knitted textile plies (curves 2-5) compared to that of an anionic PA6 sample produced by compression molded MPs (curve 1). The anionic neat PA6 obtained from compression molded MPs (denominated as PN) displayed as expected a single melting peak at $T_m = 210°C$ and a T_g transition at 40°C. These data are consistent with those obtained previously in the DSC studies of neat MPs [185]. In the KSPCs with either uni- (Figure 5.9 curves 2,3) and multi-directional knitted plies (Figure 5.9 curves 4,5), a bimodal melting endotherm was registered with T_{m1}=208-210 °C and T_{m2}=218-220 °C. This dual peak should be related with the melting of PA6 originating from the anionic PA6 matrix and from the

hydrolytic PA6 textile reinforcements. It should be noted that while the in the KSPCs with unidirectional textile plies PU-R-15 and PU-J-15 only one T_g transition was clearly observed at ca. 33°C related to the anionic matrix, in the samples with multidirectional ply orientation PM-R-15 and PM-J-15, the T_g of both matrix and reinforcement PA6 were detected at 34-36°C and 48-49°C, respectively. It seems that the ply orientation in the KSPCs of this study may affect the chain mobility of the reinforcing PA6 material.
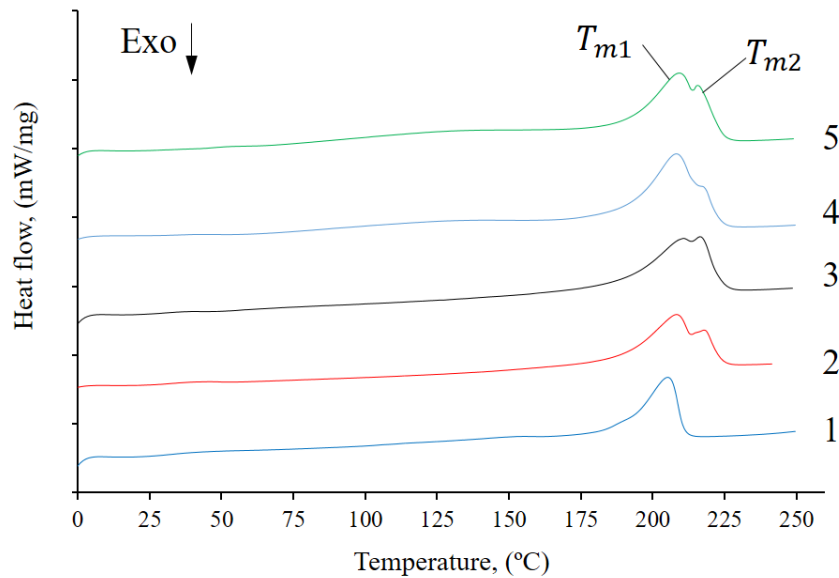
Figure 5.9. DSC curves of KSPCs from hot compacted MPs -impregnated knitted textile structures: 1- PN; 2- PU-R15; 3- PU-J15; 4- PM-R15; 5- PM-J15.

Comparing the DSC curves of NYRIM (1st NN) and PCCM (1st PN) PA6 matrices do not display low-temperature crystallization or melting processes. Figure 5.10a-b demonstrates DSC analogy of NU-R-15 specimen and its components. The NN matrix and the NK-composites own identical first order transition in their DSC thermograms where the processing window was measured about 60°C and significantly is appropriated for molding procedure and industrial benefits. It should be mentioned that the melting temperature of composite material was situated between melting points of reinforcement and NN matrix (Figure 5.10a).

The comparison on first scan DSC thermograms of NK- and PK- composites are shown in Figure 5.10b. Double and single endothermic phases are allocated to NK- and PK-composites respectively. Containing single-phase conformation during infusion in NU-R-15 specimen is contributed to better matrix impregnation through the knitted reinforcements and lack of TCL at the interface region. Analogy of second scan DSC curves in Figure 5.10c evidence absence of TCL in NYRIM prepared composites resulted from observation of no weak shoulder as appears in DSC thermogram of all PK-composites.

Appearing weak shoulder in second scan DSC thermogram of such composite represent higher portion of γ-PA6 polymorph. As conclusion, correlating the thermal analysis and topography of NK- and PK-composites verify identical nature of γ-PA6 crystalline phase and TCL polymorph. X-ray diffraction studies in next section enhance to explain better this hypothesis.
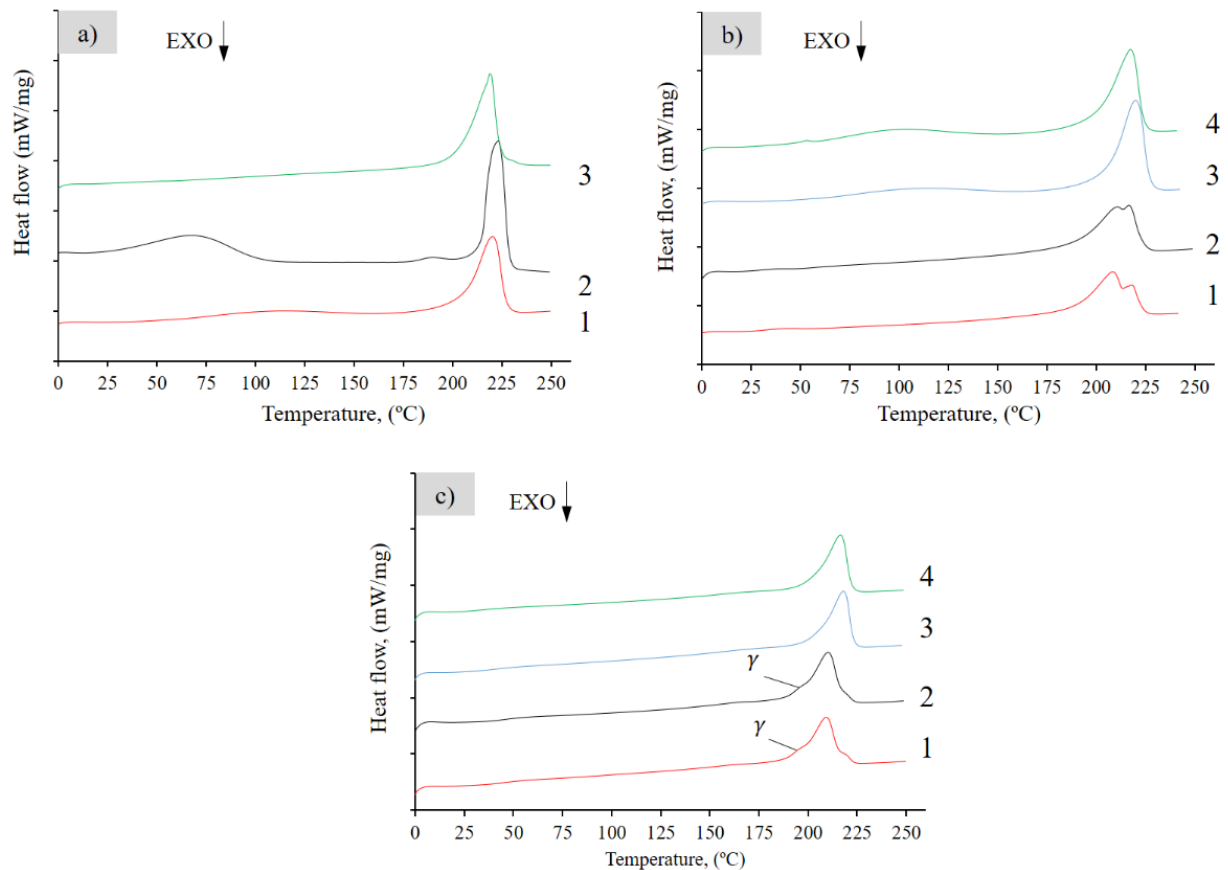
Figure 5.10. a) Comparison on DSC thermograms of NU-R-15 composite material (curve 1), annealed Rib reinforcement (curve 2) and NN matrix (curve 3); b) analogy of first scan DSC thermograms of NYRIM and PCCM prepared KSPCs. 1-PU-R-15; 2-PU-J-15; 3-NU-R-15 and 4-NU-J-1.

Interestingly, the 1st scans of the NU-J-15 and NU-R-15 composites contain broad endothermic peaks centered around 100°C (Figure 5.10b) that disappears during the second DSC scan (Figure 5.10c). Analyzing these peaks in conjunction with the morphology and mechanical data, these broad transitions can be related to the presence of oligomeric PA6 formed during the NYRIM process. These oligomers only form when the in-mold bulk AAROP is carried out in the presence of the textile structures and not in their absence, since in the case of the 1st NN curve such low-temperature transition is absent. The supposed formation of oligomers can be an indication that the textile structures inhibit the bulk AAROP due to some surface finish that was not removed during the textile pre-treatment with acetone. The weak interface at the filament/matrix interface evidenced by SEM and PLM (Figure 5.4 c, f) can also be related

with excess oligomer content in all NK-composites.

Polyamide 6 are categorized as semicrystalline (40-70% crystallinity) polymers in which two major transition orders such as glass and melting transition occur during heat increment procedure [91]. The glass transition happens while the material has amorphous polymorph portion and in return the melting process come to pass while the polymer chains fall out of their crystal structures and become a disordered liquid. Polymer chains moves around easily at the beyond T_g although below of this point they won't be able to move into new positions to relieve the stress. Therefore either the polymer chains are strong to resist to any deformation via the implied force or the material will mechanically failed while the applied forces exceed the resistance of motionless polymer chains [46].

During glass transition, the polymer chains are incapable to undergoing translational motion (chain mobility) albeit above its glass transition temperature, they move long-range segmental motion which the polymer changes from being soft and pliable (flexible the backbone chain) to being hard and brittle.

Based on the DSC traces, the crystallinity indices X_c^{DSC} of all KSPCs and their precursors were calculated according to Eq. 3-6 and presented in Table 5.2. The MPs and the anionic PA6 obtained by their compression molding (PN) possess quite low T_g values of ca. 33°C and T_m varying between 208-210°C. The X_c^{DSC} of PN becomes lower than that of MPs most probably due to the relatively faster cooling down during the compression molding.

The annealing of fixed ends of both textile reinforcement types increased their crystallinity index with up to 10%, maintaining the T_g and T_m values in the ranges of 55-57°C and 223-224°C. Therefore, the DSC data in Table 5.2 proved that the anionic PA6 matrix material and the hydrolytic PA6 of the reinforcements are quite distinct in their physical properties, being at the same time chemically identical. Each KSPCs material in Table 5.2 displayed clear bimodal character of the melting endotherms (all obtained during the 1st DSC scan).

It is logical to attribute the first T_{m1} to the matrix PA6 and the second T_{m2}– to that of the higher melting knitted textile reinforcement. Notably, while the T_{m1} values almost coincide with that of the MPs and PN, the T_{m2} values of all KSPCs are between those of the neat reinforcements and of the matrix PA6. According to previous studies on interchange reaction in polymer blends [221] interchange reactions between PA6 from the matrix and from the reinforcements can be supposed leading to the formation of block copolymers. This would result in chemical bonds across the matrix-fiber interface enhancing the

adhesion.

The lower T_g for NK-composites brought higher amorphous polymorph portion which is correlated with their low knee point and tensile properties. As it was anticipated, the crystallinity of reinforcements was elevated after annealing procedure. Increasing the melt point of NK-composites ($T_{M(NN)}$) compared to PK-composites ($T_{M(PN)}$) is resulted from different molecular weight of their own matrix component (see section 4.6.1). Applying NYRIM technique increased the crystallinity of matrix component compare to the PCCM method up to 56% although the crystallinity of KSPCs descended significantly.

Table 5.2. Crystallinity index for KSPCs and their precursors.

Sample designation	T_g (°C)	T_{m1} (°C)	T_{m2} (°C)	X_c^{DSC}, %*
MPs	28.2*	207,8	-	34,9
NN	47,1	-	218,8	43,0
PN	42.4	210	-	27,5
R	55.3*	-	224,2	34,7
J	56.2*	-	224.5	35,0
J-A	57.0*	-	223,5	41,9
R-A	56.5*	-	223,2	46,0
PU-J-15	30.3	210,2	216,5	31,0
PU-J-20	43.5	209,8	219,1	30,7
PU-J-25	41.1	209,2	219,3	30,0
PM-J-15	46.5	210,2	215,7	34.7
PU-R-15	32.3	208,2	217,8	30,9
PU-R-20	33.4	208,6	215	33,2
PU-R-25	32.6	208,2	216,9	33,6
PM-R-15	37.5	208,2	216,2	33.6
NU-J-15	29.9*	-	216.6	26.0
NU-J-20	26,7*	-	215,9	22,0
NU-J-25	25,2*	-	213,8	24,4
NU-R-15	30.7*	-	218.3	25.5
NU-R-20	33,3*	-	220	25,8
NU-R-25	32,3*	-	218,7	24,6

* T_g determined during the 2nd DSC scan

5.4.2. Thermal Gravimetry analysis

Thermogravimetric analysis (TGA) is used for the thermal degradation of polymers to study the kinetics of polymer degradations. Differential thermal analysis (DTA) of PA6 matrix component has an advantage over DSC which enables measuring changes of enthalpy in an open system while the sample mass is

simultaneously altering. Combining TGA and DTA curves allows simultaneous evaluation of enthalpy and mass changes that enhance better understanding the mechanism of enthalpy variations. Figure 5.11a represents the thermogravimetry studies of PN matrix in which three different plots including weight loss (%), differential thermal analysis (DTA, μV) and derivative thermal gravimetry (DTG, $\frac{\mu g}{min}$) versus incremental temperature are plotted overall. As it can be seen in Figure 5.11a, three characteristic points can be observed in each of the graphs. The initial decomposition temperature (IDT) represents the onset of the weight losses, TM is the melting temperature and MRD/MRDT – the temperature of maximum degradation rate. The latter is determined as the inflection point of the integral TGA curve (MRD), or as the peak of its first derivative (MRDT). The amount left after the end of the heating procedure gives the final reside (FR). The area under the derivative curve qualitatively determines the amount of that decomposed component. Figure 5.11b demonstrates comparative study on thermal decomposition of matrix components. There is similar trend can be observed in TGA thermogram of NN and PN matrix components.
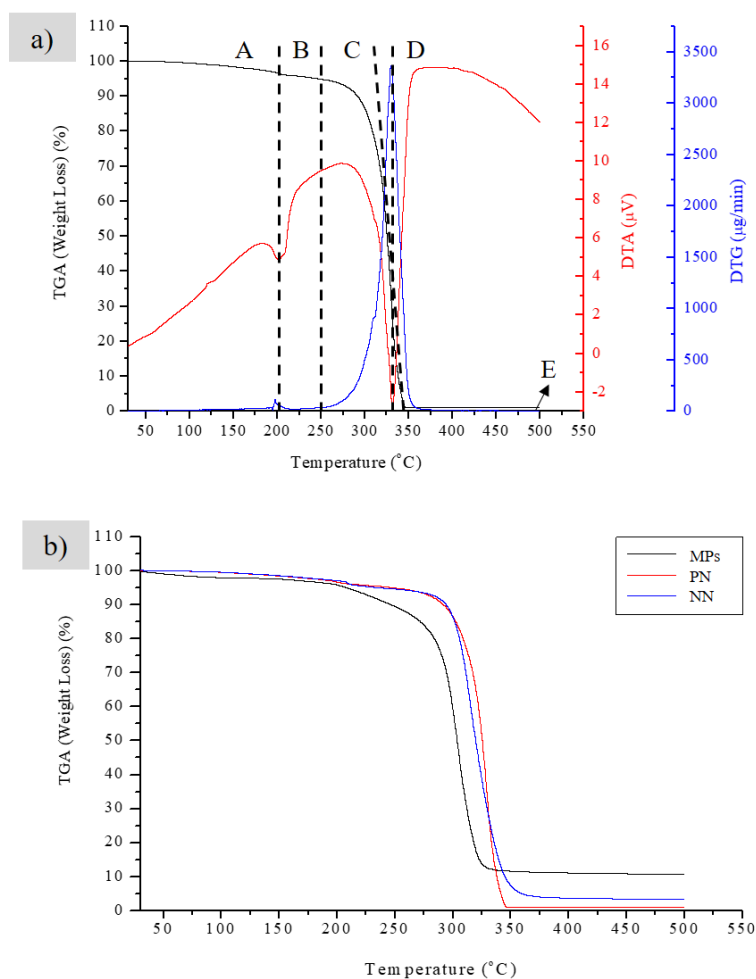
Figure 5.11. a) TGA traces of PN matrix components in N_2 atmosphere at 10 °C.min^{-1} heating rate (A=TM; B=IDT; C=MRD; D=MRDT; E=FR); b) Comparative study on thermogravimetry of MPs, NN and PN sample.

The thermogravimetric analysis of untreated and annealed Rib textile reinforcements, PU-R-15 and PM-R-15 composites are shown in Figure 5.12a-d. The Weight loss (%), Differential thermal analysis (DTA, μV) and Derivative thermal gravimetry (DTG, $\frac{\mu g}{min}$) versus became plotted versus incremental temperature. DTM, MRD, MRDT and degradation magnitude (described in chapter 4) were extracted from each plot. Figure 5.12a-b demonstrates nonsignificant changes on thermogravimetric curves of reinforcement before and after annealing procedure.

The DTA plots of R and R-A reinforcements display multiple endotherm of thermal degradation centered around 440°C although uni- and multidirectional KSPCs (Figure 5.12c-d) and PN sample (Figure 5.11a) show a single TM peak at 200°C and a strong thermal decomposition isotherm at 330°C. the differences on thermal degradation peaks in KSPCs and precursors may be linked with crosslinking of hydrolytic (reinforcements) with anionic PA6 (matrix component).
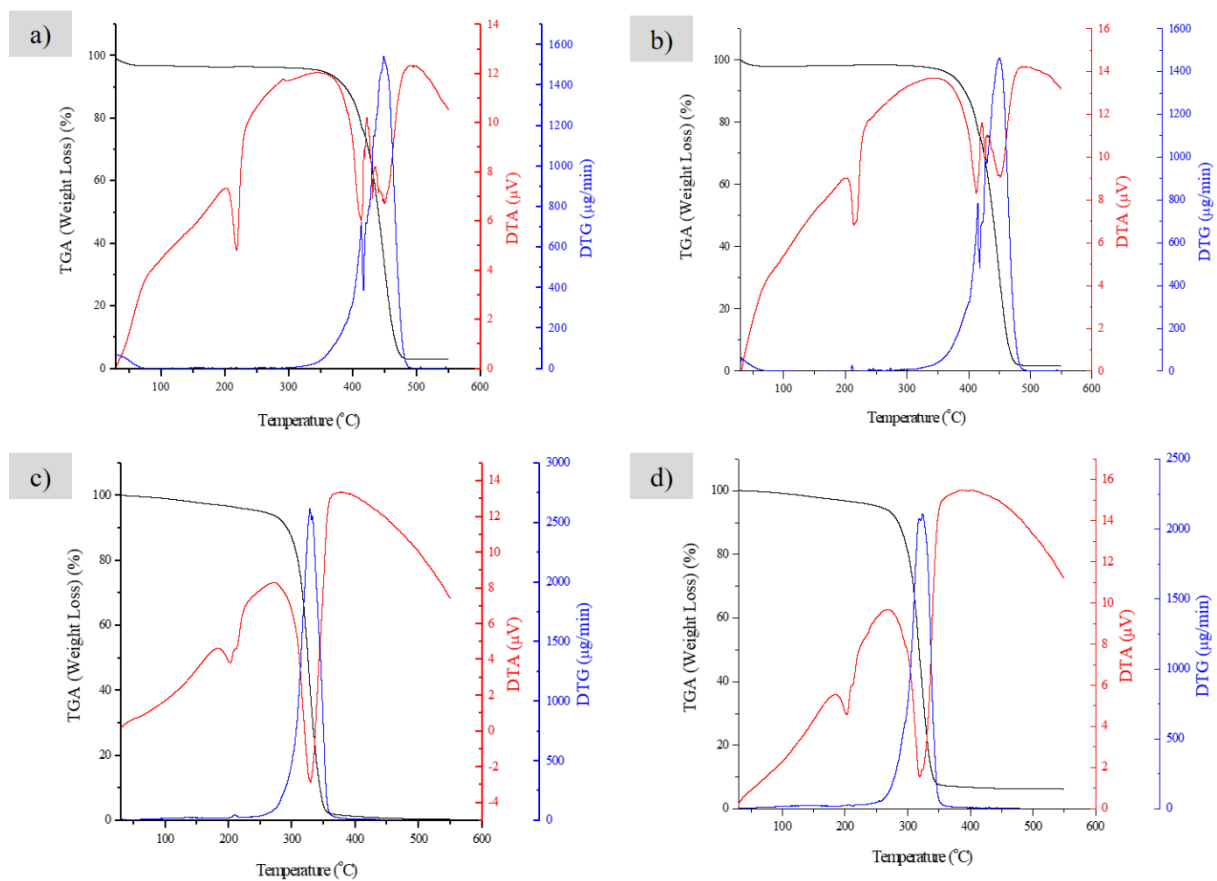
Figure 5.12. a) TGA thermographs of a) untreated Rib reinforcement; b) Annealed Rib reinforcement; c) PU-R-15; d) PM-R-15 samples (in N2 atmosphere at 10 °C.min^{-1} heating rate

TGA Thermograms of uni- or multidirectional R-A reinforced KSPCs prepared by PCCM and NYRIM molding techniques and the precursors are displayed in Figure 5.13. The untreated and treated knitted

reinforcements showed distinctly more strength under thermal degradation than KSPCs and matrices. as it can be seen in Figure 5.13, multidirectional KSPCs demonstrated feeble thermal stability compare to the unidirectional KSPCs and NK-composites.
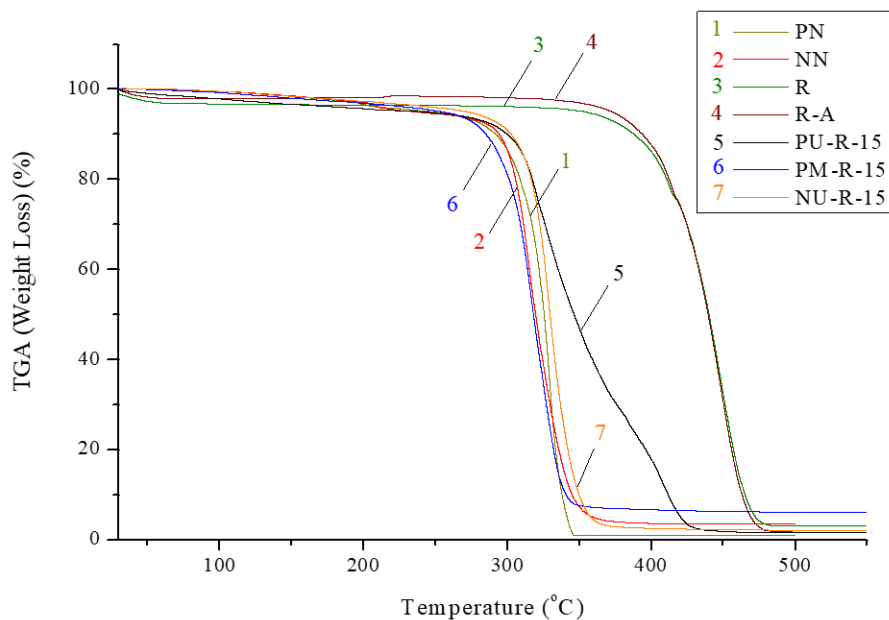
Figure 5.13. TGA thermograms of R-A reinforced KSPCs prepared by NYRIM and PCCM techniques and the precursors.

The data from TGA/DTA analyses of all samples are tabulated in Table 5.3. The thermal decomposition of NN and PN matrix (the IDT point) is around 250°C, which is with 50°C lower than the IDT of the neat textile reinforcement. Most probably, this difference is due to the orientation of the P-A sample. The carbonized residue at 550°C in the NN matrix was with 6% higher than in the PN matrix, which may be attributed to the formation of cross-linked structures in the former case, that are more difficult to depolymerize. As it can be seen in Table 5.3, MPs melted at lower temperature than the R-A textile, which is considered an advantage for the PCCM technique as a matter of raise processing window. The maximum weight loss in R and R-A reinforcements takes place around 475°C although, the ultimate degradation of composites and PN matrix is detected between 350-425°C.

The thermal stability of KSPCs was higher than the matrix component but lower than the textile reinforcement. In the presence of annealed Rib reinforcements, the thermal decomposition of composites slightly above melting temperature which is lied on volatilization temperature of the caprolactam monomer at 160°C. Tracking IDT values in Table 5.3 shows that increasing fiber content and stacking order accelerate the degradation process. Comparison on MRD values demonstrates significant decline in PU-R-15 sample that can be explained by slower rate of degradation and consequently better interfacial

125

bonding of composite components. Applying in-mold polymerization technique in NK-composites was accelerated the thermal degradation in which degradation procedure initiated over the PK-composites (252°C). It can be deduced that the thermal stability of NK-composites are higher than PK-composites although their thermal degradation exceeds at higher temperature (T>252°C).

Table 5.3. TGA data analysis for KSPCs and their precursors.

Sample	TM (°C)	IDT (°C)	MRDT (°C)		MRD (Rad)	Degradation (%)
R	218	307	413	450	1.03	93
R-A	216	301	415	450	1.07	96
MPs	204	204	-	307	1.18	85
PN	198	249	-	330	1.54	98
NN	208	225	-	317	1.15	92
PU-R-15	215	244	-	321	0.81	93
PU-R-20	202	239	-	328	1.13	95
PU-R-25	201	233	-	321	1.07	99
PM-R-15	202	231	-	318	1.16	88
NU-R-15	211	252	-	331	1.54	93

5.5. Synchrotron X-ray Diffraction Studies

Polyamide 6 (PA6) contains two crystalline forms such as α and γ phases. In α and γ crystalline structures, the plane of the amide group and that of the $(CH_2)_5$ group are parallel and perpendicular respectively. α-phase crystalline is stable crystalline form due to H-bond formation between antiparallel full-extended chains which is crystallized by slow cooling from the melt. Nevertheless, annealing process in a saturated-steam atmosphere and applying stress without any significant loss of orientation are known as the key reasons of γ crystalline structure advent [222,223].

Two different chain conformations for PA6 polymer material are considered including Straight (Figure 5.14a) and inclined chains (Figure 5.14b) where they are situated in parallel and antiparallel states. As Figure 5.14c demonstrates, H-bonds forms alternatively between antiparallel or parallel chains and creates eight possible packing orders [220]. Moreover, uncrossed (UC), shift-uncrossed (SUC) and crossed (C) are three dedicated distinct ways to stack adjacent H-bond sheets in the PA6 crystal.
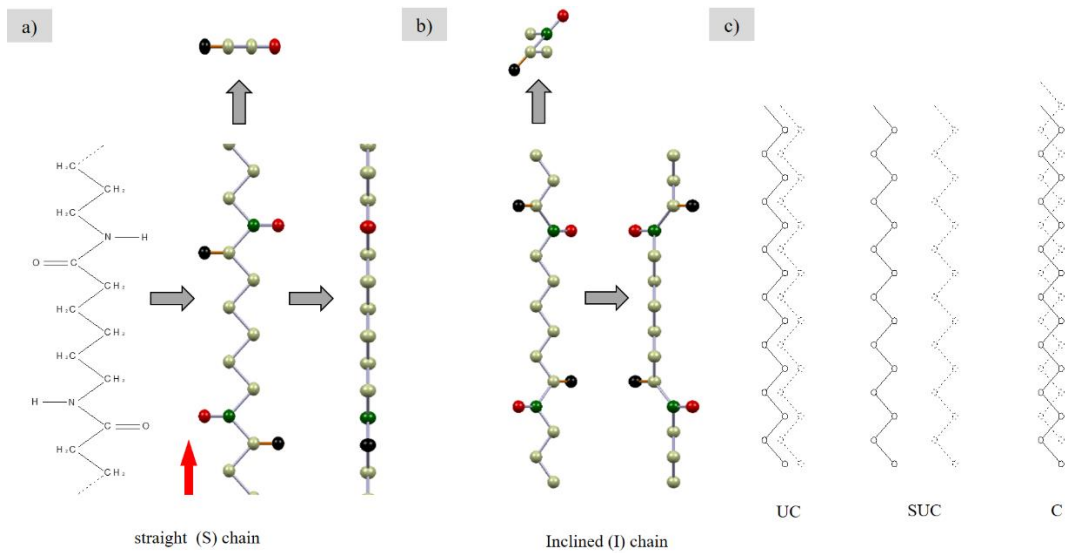
Figure 5.14. Schematic of PA6 crystalline morphology and stacking for a) α-crystalline phase; b) γ-crystalline phase; c) juxtaposition of the H-bonds in each sheet

Therefore 14 different sheet displacements for each class of PA6 crystal resulted from combining the 7 slides with C and SUC conformations (Figure 5.15a-d). As consequence, 112 regular infinite chain crystal structures in PA6 is provided by multiplying the 8 classes with the 14 stacking schemes.
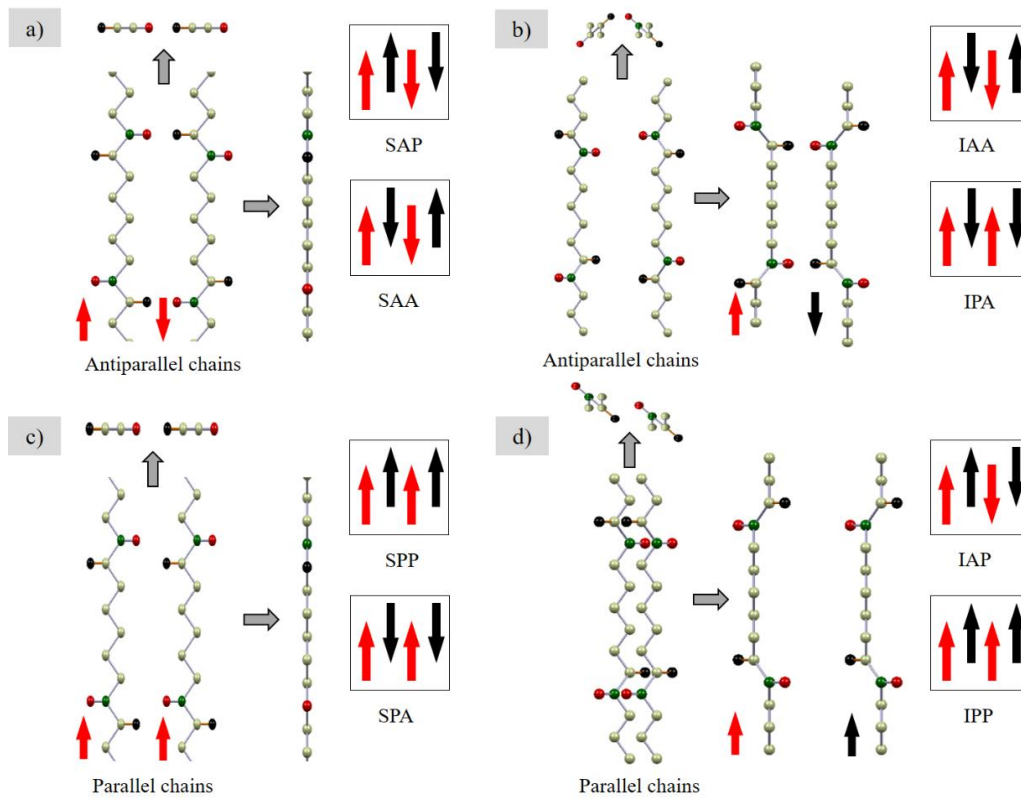
Figure 5.15. Crystalline phase conformations and possible crystal structures in Polyamide 6 constructed with different packing schemes for a, c) α b, d) γ crystalline phase. The red and black Arrows are representatives of two distinct stack adjacent H bond sheets. A, P, S and I are abbreviations of antiparallel and parallel, straight and inclined respectively.

127

PA6 polymer has large molecular weight wherein a lamella may contain more than one polymer chain. It may covalently be connected through an amorphous region to an adjacent lamella or back to the same one (one molecule). The covalent bonds are expressed by intramolecular hydrogen bonds (intra-H-bonds) [91]. Intra-H-bonds are always between antiparallel chains because the adjacent chains need to be in opposite directions. Furthermore, H-bonds can be constructed between different molecules named inter-H-bonds. The constant length 2D sheet between folds generated by molecule with intra-H-bonds (lowest enthalpy).

Van der Waals (non-Coulomb) interactions among H-bonds within sheets leading to the intermolecular interactions and consequently become packed to form a 3D structure. This stable structure represented α crystalline structure. Otherwise, in γ phase crystalline structure, parallel sheets of intramolecular bonds rotate the amide groups to make hydrogen bonds to the molecule in the adjacent sheet (inter-H-bonds). Therefore, H-bonds are intramolecular and intermolecular while they are parallel and antiparallel with the fold direction respectively. Because of the existence of intra-H-bonds, molecular mobility and formation of the H-bond sheet inside the molecule are formed. Inter-H-bonds favored γ phase wherein created in the amorphous region from melt and Intra-H-bonds represented α phase crystalline polymorph.

Commonly the suitable thermomechanical treatments like annealing procedure are caused appearing an intermediate crystalline phase between α and γ phase using (e.g., extending the PA6 filaments upper their elasticity) [206]. The heating treatment which shifts the interchanging γ to α crystalline phase. The transformation between α to γ require breaking and converting new H-bonds and altering chain conformation.

Respect to the Figure 5.16a-d, three major transformation steps had been predicted [220]. As Figure 5.16a demonstrated that in a molecule, the chains connected by folds in which amide units in the adjacent molecules were not at the same height (intra- H-bond). Therefore, sliding adjacent H-bond sheet maintains the amide units at the same height. All amide units twist about 10° although H-bonds between two adjacent amides retained which is called Pseudo α phase. Continuing the amide unit twist breaks half of intra-H-bonds. Hence, the inter-H-bonds are generated while the other half of the intra-H-bonds were maintained. This structure is representative of β structure [224,225] (Figure 5.16b) which is responsible for appearing strong diffraction. The reason is explained by the same height of the amide units leading disorder in the chain conformation [225,226]. In the second stage, the remaining intra-H-bonds are broken to form complete inter-H-bonds and generate δ crystalline phase [224] (Figure 5.16c).

At the end, the inclined amide units are caused complete rotation of chains and complete transition of α to γ phase (Figure 5.16d).
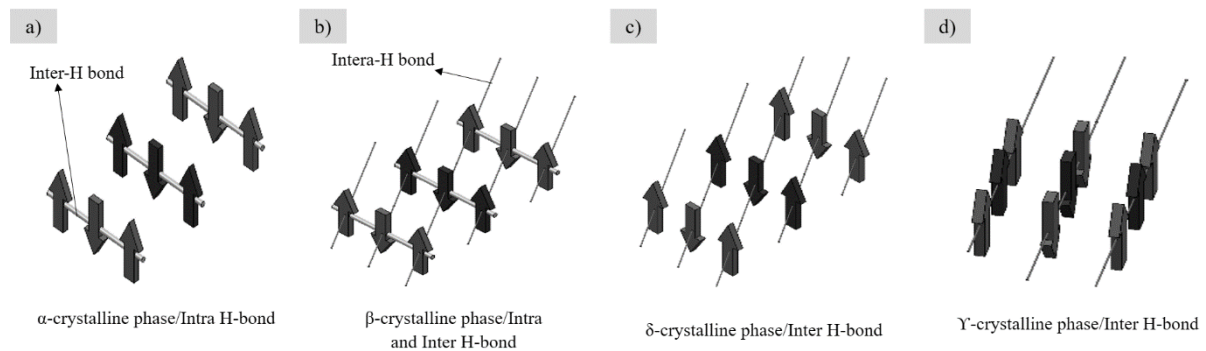
Figure 5.16. Transition mechanism between alpha and gamma forms.

Crystallization occurs during both isothermal and non-isothermal processes. Chemical structure comprising amide group concentration and symmetry, is very important for the crystallization. With decreasing amide concentration, the crystallization will be faster because of increasing chain flexibility. The length of the repeat unit is important and contain an remarkable influence opposite to that of the amide concentration, that is, faster crystallization for shorter repeat units [227]. At a given amide concentration, the polyamides with the highest degree of symmetry (e.g., even-even) will have the highest rate of crystallization. Molecular mass (chain length) affects crystallization through the increase in viscosity that it causes [213]. This factor becomes important above a certain threshold value in which the lower molecular mass crystallizes faster. The distribution of molecular masses is significant, and segregation of different fractions can occur in extreme cases. Therefore, NN samples with higher molecular weight contain more perfect crystallization which in this case is α-crystalline phase.

During cooling, the crystallization rate is low at temperatures close to the melting temperature and large crystal sizes are achieved [228,229]. At lower temperatures, far below melting, the crystallization rate is quicker, but smaller crystals are formed. The presence of homogeneous or heterogeneous nuclei obviously affects the overall crystallization rate by facilitating the initial nucleation step [230]. The reason is that even in the melt some H-bonds remain fixed and result in effective nucleation sites on cooling. This "memory effect" is more obvious in samples with higher amide-group concentration (higher nucleation density) and causes higher overall crystallization rates [91,231].

To better understand the differences and similarities between the PA6 matrix and reinforcement in KSPCs and their precursors, X-ray diffraction studies were performed. The linear diffraction patterns of

representative samples were collected and deconvoluted by peak fitting. Eq. 3-9 was implemented to calculate the total crystallinity index and the specific content of α- and γ-PA6 polymorphs. According to previous findings [221], a monoclinic unit cell lattice was assumed for the α-PA6 form characterized by two peaks corresponding to α[200] and α[002/202] crystalline planes with 2θ being centered in the studied samples at ca. 20° and 23°, respectively.

For the γ-crystalline form, non-hexagonal unit cell was supposed for all samples, as suggested by Samon et al. [232]. Therefore, fits with two Gaussian peaks corresponding to γ[001] and γ[200] crystalline planes were performed with 2θ being between 21 and 22°. The diffuse scattering of the amorphous PA6 component was presented by two wide Gaussian peaks (halos). This procedure led to very good fits with fitting coefficients $r^2 \approx 0.99$. Representative X-ray patterns and their deconvolutions are shown in Figure 5.17a-e.
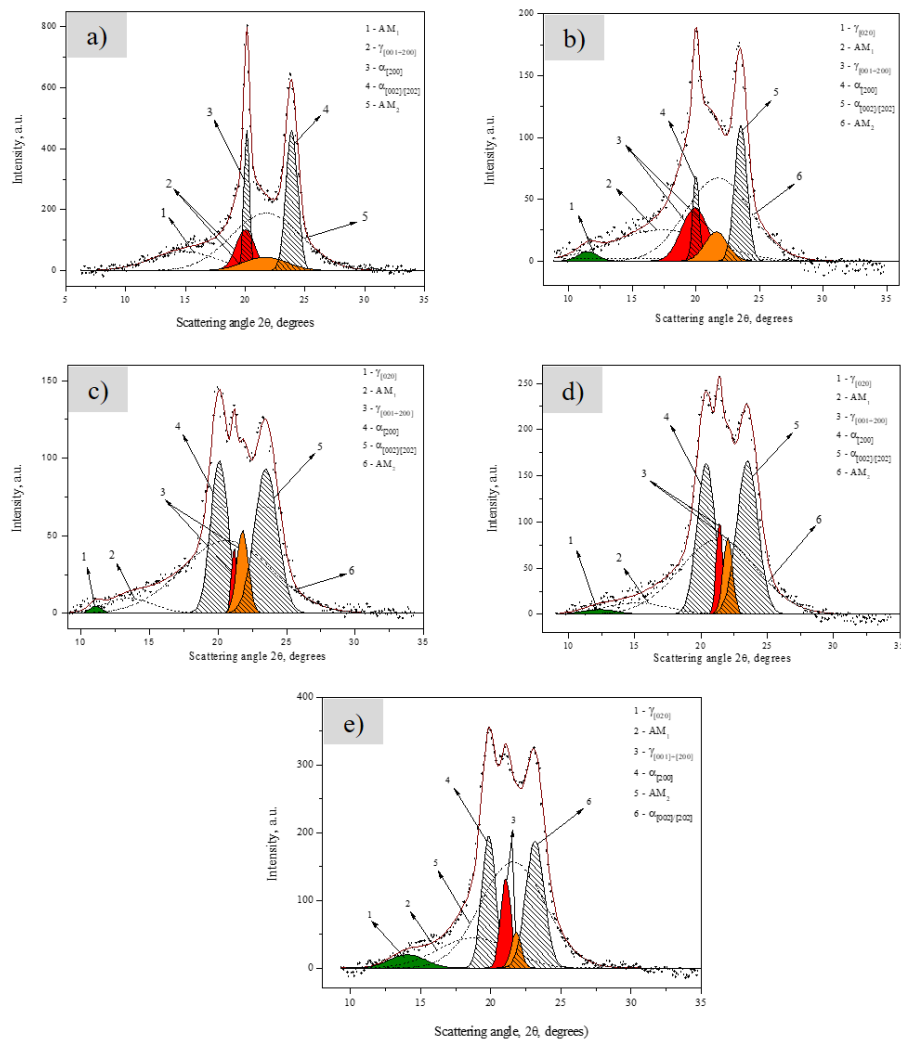
Figure 5.17. WAXS patterns and their fits of SPCs building components: a) PA6 microparticles MPs; b) PN; c) R; d) R-A; e) J-A. AM=amorphous portion

Let´s first consider the XRD patterns of the matrix precursors in KSPCs, the MPs and PN (Figure 5.17a-b). These patterns belong to non-oriented samples, in which the α-PA6 reflections are narrower than those of the γ-polymorph.

In the PN sample obtained after melting/recrystallization of MPs the α[200] reflection is weaker than the α[002/202] peak. This indicates that during their recrystallization from the melt, the α-crystallites in this sample display a descendant growth along the plane determined by the H-bonds. On the contrary, in the patterns of the R, R-A and J-A samples (Figure 5.17c-e), both PA6 polymorphs are fitted with narrow and symmetric (in the case of α-PA6) crystalline peaks, which is typical for oriented PA6. In addition, comparing visually the widths of the α-PA6 peaks in Figure 5.17a-b allows the conclusion that the anionic PA6 of the MPs and the plates obtained thereof (PN) comprises smaller but more perfect crystallites than the hydrolytic PA6 of the knitted textile reinforcements.

The fitted XRD patterns of the KSPCs in Figure 5.18a-f allowed the clear separation of the α[200] and α[002/202] reflections of the anionic matrix PA6 and the hydrolytic PA6 of the textile structures. For the peaks of the two γ-polymorphs, however, such separation was impossible. In all KSPCs the α-PA6 matrix peaks are wider than those of the textile reinforcements. This is logical since the anionic PA6 melted and recrystallized during the KSPCs preparation thus forming less perfect and non-oriented matrix crystallites, while the PA6 from the knitted textile filaments did not melt remaining oriented. Notably, in most all the KSPCs samples the two α-reflections of the textile reinforcements are asymmetric with the α[002/202] peak becoming stronger.

Since no melting of the reinforcing monofilament occurred as shown by the microscopy study above, a recrystallization of the matrix material should be supposed at the temperature of the compression molding (215°C). Apparently, this has led to a preferred growth of the α-crystallites along the direction of the van de Waals forces between the PA6 molecules forming the crystalline plane. The crosslinking between adjacent molecules influence the physical behavior and mechanical properties of long chain polymers.

Association of such molecules, known as crosslinking, is a permanent chemical bonding between separate molecules and it is caused entanglement of polymer chains, rigidity in the glassy state, crystallinity and hydrogen bonding. In PA6, the crosslinking occurs through C-C bonds which depends on the density, molecular mobility and distribution of these crosslinks. Different molecular weights for

hydrolytic (PA6 knitted reinforcements) and anionic (PA6 matrix) polymerized may cause branching monomers at the interface. The branching in semicrystalline polymers like PA6, restricts the size of ordered domains wherein the branch points are not fit into crystal lattice. Due to this fact, the γ-crystalline phase appeared in the region between matrix and reinforcement components can be attributed to the TCL advent at the interface.
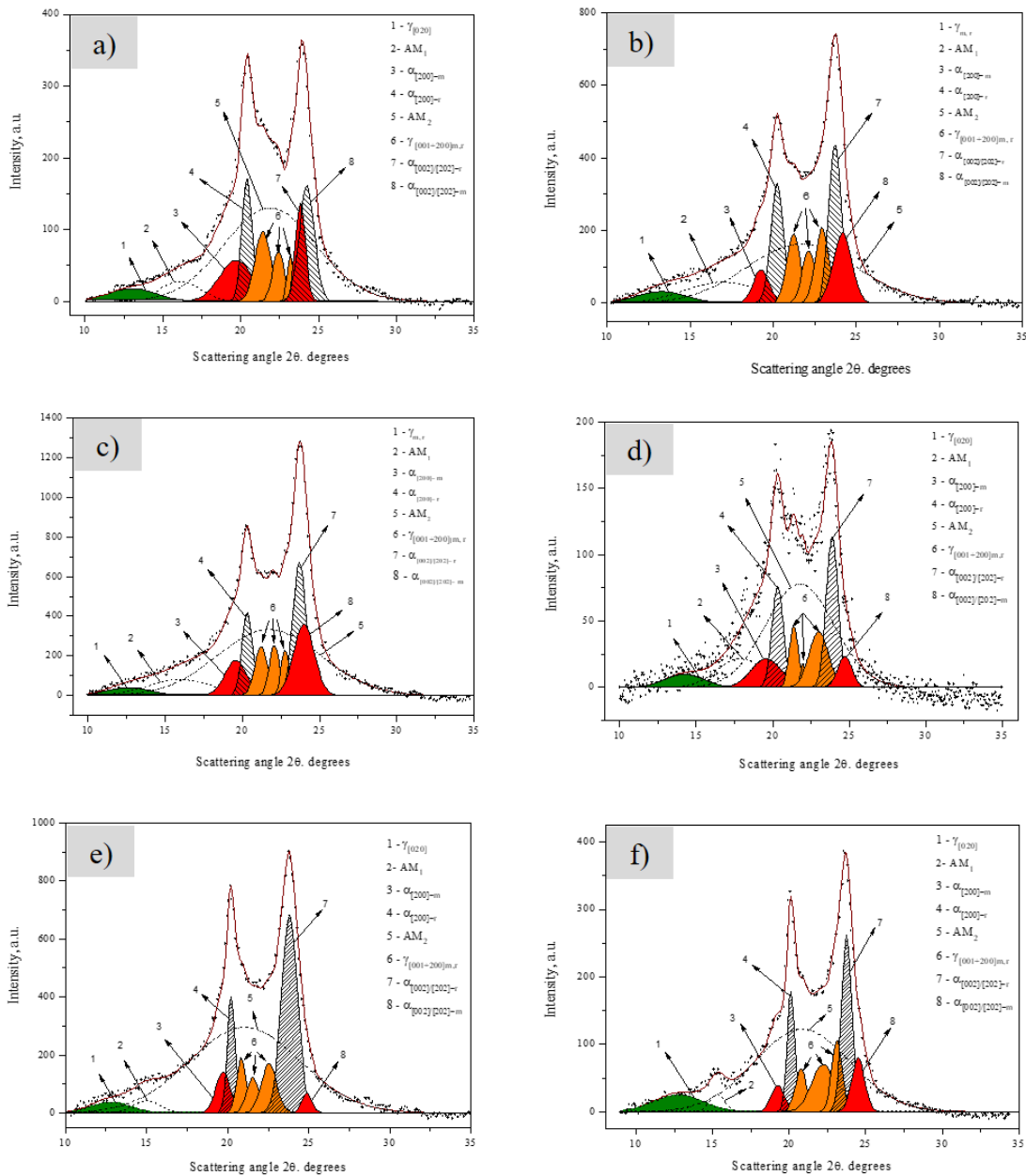
Figure 5.18. WAXS patterns and their fits of PK-composites: a) PU-J-15; b) PU-J-20; c) PU-J-25; d) PU-R-15; e) PM-J-15; f) PM-R-15.

The fitted XRD patterns of NK-composites with 15% fiber content are illustrates Figure 5.19a-b. In all KSPCs the dual α-PA6 matrix peaks are wider than those of the textile reinforcements. This means that

the anionic PA6 matrix material formed during the NYRIM or PCCM formed less perfect and non-oriented matrix crystallites, while the PA6 from the knitted textile filaments did not melt, remaining oriented. Notably, in all of KSPCs samples the two α-reflections of the textile structures have become asymmetric, with the α[002/202] peak becoming stronger.

Since no melting of the reinforcing monofilament occurred, as shown by the microscopy study above (Figure 5.3c, f), recrystallization of matrix PA6 upon the oriented textile filaments during the laminate consolidation can be hypothesized with a preferred growth of the α-crystallites along the direction of the van de Waals forces between the PA6 molecules forming the crystalline plane. This is one more proof, although indirect, for the possibility of TCL formation during the KSPCs preparation by either NYRIM. In-mold crystallization of ECL was caused descend of γ[020] portion. The crystalline reflection of knitted reinforcements showed higher intensity in XRD pattern of NK-composites.
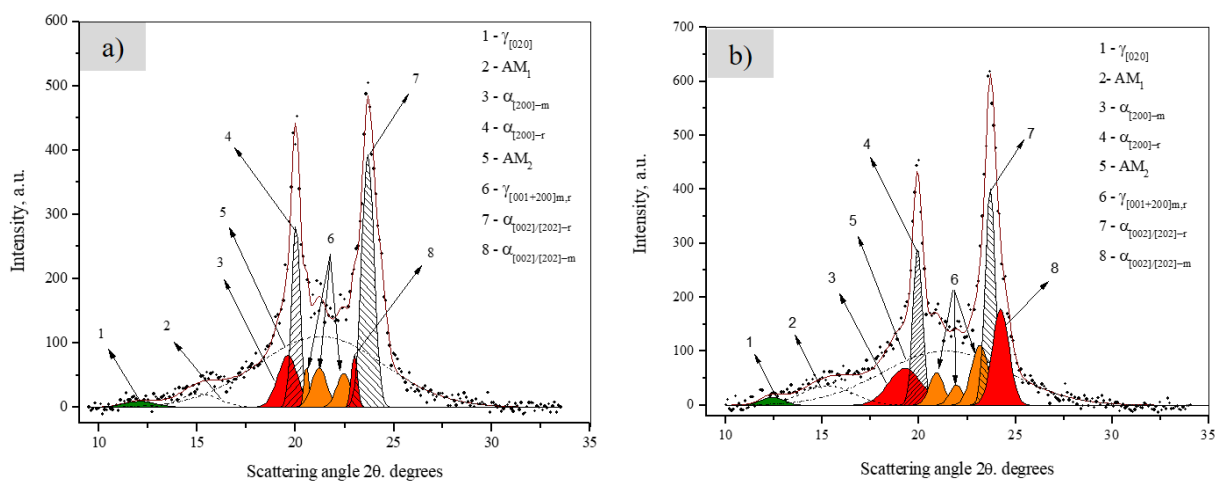
Figure 5.19. WAXS patterns and their fits of NK-composites: a) NU-R-15; b) NU-J-15

More conclusions about the crystalline structure and the crystallinity index X_c^{XRD} of the materials under investigation can be made based on the data in Table 5.4. The d-spacings for all α- and γ-PA6 reflections were also calculated and tabulated. Comparing the MPs and PN samples indicates that transforming the anionic microparticles into matrix of the MPs by melting at 215°C is associated with some decrease of X_c^{XRD} from 42% to 35% and a significant drop in the α/γ ratio, i.e., and α- to γ-polymorph transition takes place.

The knitted textile reinforcements before any treatment seem to have X_c^{XRD} values of ca. 40%, i.e., like that of MPs and lower than PN. The untreated Rib1×1 structure, however, is significantly richer in α-PA6 than the former two anionic samples with its α/γ ratio being above 3. Stretching the knitted textile

133

reinforcements to 30% accompanied with annealing at 170°C for 90 min results in a massive growth of the crystallinity index with about 10% reaching values 53-54% that are very high for PA6. At the same time, the α/γ ratio is maintained between 3 and 4.

These observations can be related with the higher total crystallinity index of the J-A and R-A samples observed by either DSC or XRD compared to the untreated samples, the difference reaching 13% in the Rib reinforcements. As seen from Figure 5.17c-e, it is the α-PA6 content that increases during the stretching/annealing whereas the γ-PA6 remains relatively constant. These results are consistent with previous studies on the structure-mechanical properties relationship in oriented PA6 annealed in the 170-200°C [209]. Therefore, the big increase in E and σ_{max} values upon annealing were proved to be related to a γ-to-α form transition.

Table 5.4. Data from the deconvolution of the XRD patterns of SPCs, textile structures and anionic PA6 precursors

Sample	α^*%	γ %	X_c^{XRD}, %	$\dfrac{\alpha}{\gamma}$	$d_{\alpha(200)}$ Å	$d_{\alpha(002/202)}$ Å	$d_{\gamma(020)}$ Å	$d_{\gamma(001)}$ Å	$d_{\gamma(200)}$ Å
MPs	26.5	15.2	41.7	1.74	4.29	3.62	-	4.31	3.99
PN	17.4	17.5	34.9	1.00	4.32	3.68	7.48	4.33	4.00
NN	28.3	16.5	44.8	1.72	4.24	3.6	-	3.7	3.53
J-A	41.0	11.8	52.8	3.47	4.35	3.74	6.13	4.10	3.96
R-A	42.9	10.7	53.6	4.00	4.24	3.68	6.97	4.04	3.93
R	31.0	9.5	40.5	3,26	4.30	3.68	7.78	4.08	3,97
PU-J-15	13.0 [R] 18.0 [M] **31.0 [T]**	14.9	45.9	2.08	4.38 [R] 4.23 [M]	3.57 [R] 3.63 [M]	6.57	4.03	3.86 [R] 3.73 [M]
PU-J-20	10.9 [R] 20.9 [M] **31.8 [T]**	19.3	51.1	1.65	4.48 [R] 4.27 [M]	3.58 [R] 3.65 [M]	6.45	4.07	3.91 [R] 3.77 [M]
PU-J-25	15.4 [R] 18.3 [M] **33.7 [T]**	12.5	46.2	2.69	4.42 [R] 4.25 [M]	3.61 [R] 3.65 [M]	6.78	4.07	3.92 [R] 3.80 [M]
PU-R-15	8.7 [R] 19.7 [M] **28.4 [T]**	15.3	43.7	1.86	4.41 [R] 4.25 [M]	3.51 [R] 3.63 [M]	6.06	4.04	3.94 [R] 3.75 [M]
PM-J-15	4.7 [R] 24.2 [M] **28.9 [T]**	12.7	41.6	2.28	4.37 [R] 4.27 [M]	3.48 [R] 3.63 [M]	6.71	4.15	4.01 [R] 3.84 [M]
PM-R-15	7.0 [R] 17.7 [M] **24.7 [T]**	21.1	45.8	1.17	4.48 [R] 4.26 [M]	3.53 [R] 3.64 [M]	6.72	4.16	3.89 [R] 3.74 [M]
NU-J-15	22.8 [R] 17.3 [M] **40.1 [T]**	7.9 4.0 11.9	51.9	3.37	4.45 [R] 4.60 [M]	3.75 [R] 3.67 [M]	7.32	4.25 [R] 4.20 [M]	4.05 [R] -
NU-R-15	18.8 [R] 15.3 [M] **34.1 [T]**	7.5 5.8 13.3	47.4	2.57	4.43 [R] 4.54 [M]	3.76 [R] 3.68 [M]	7.02	3.97 [R] 4.31 [M]	3.84 [R] 4.19 [M]

R: Reinforcement
M: Matrix
T: Total

Notably, the γ[020] reflection of the annealed Jersey (J-A sample) is better revealed as compared to that in the R-A meaning that the different textile architecture may result in different crystallization behavior during the stress-relaxation of the knitted textile reinforcements and the hot compaction procedure. According to Table 5.4, a general common feature of the KSPCs is that the α-PA6 content in the matrix is always lower than that in the incrusted textile structure. The difference between the two values seems to be dependent on the type of the knitting pattern and the alignment of the textile ply in one or more direction.

The X_c^{XRD} values of the studied KSPCs vary between 42% (PM-J-15) and 51% (PU-J-20) and the α/γ ratio – between 1.2 for PM-J-15 and 2.7 for PU-J-25. Such differences can be considered significant. It seems that the different textile ply pattern and alignment can really affect the crystallization process which is expected to result in different mechanical behavior. Table 5.4 allows also the conclusion that the long spacings values d_{hkl} that determine the unit cell edges of the matrix and reinforcement PA6 components in KSPCs differ only slightly, the difference being in the margin of the experimental error.

The crystallinity of KSPCs varied between 42% (PM-J-15) to 51% (PU-J-20) which was located between X_c^{XRD} values matrix (lower case) and the annealed knitted reinforcements (upper case). Despite sample PM-R-15, all KSPCs contained higher α/γ ratio (1.2-2.7) than matrix components and lower than annealed knitted reinforcements. Higher α/γ for J-A reinforced KSPCs than those reinforced by Rib structure represent great portion of α than γ-crystalline phase.

Respect to the microscopic image analysis, shown in Table 5.4, TCL measured thicker in R-A reinforced KSPCs which is in good agreement with WAXS data analysis Table 5.4. Therefore, γ-polymorphs in KSPCs reinforced by R-A structures can represent the nature of TCL at the interface. In this study, it believes that TCL advent weaken the flexural of the KSPCs. As conclusion, J-A reinforced KSPCs showed better flexural and Izod impact properties because of having less γ- polymorph fraction in their crystalline structure and TCL with narrow thickness.

According to Table 5.4, NK-composites contain few portions of γ-phase which properly fitted with lack of TCL at the interface. The NK-composites displayed slightly higher crystallinity indices, approaching 50%. The rate of cooling in the semiautomatic NYRIM mold is lower than in compression molding process, which determines the higher X_c^{XRD} values in the former case. In the PK-composites, the α/γ ratio is closing or slightly above 2.0, while in the NK-composites it is in the 2.5-3.3 range. Again, this should be

attributed to the different temperature profiles in the NYRIM and PCCM process. Also, in the compression molding technique one deals with melting of already existing PA6, whereas in the NYRIM technology the PA6 matrix is formed in-situ and only crystallizes during the process, without any melting. This causes the higher values of the total crystallinities and the α-polymorph content in the latter case.

Table 5.4 also presents the values of the evolution of the d-spacings of all neat PA6 samples obtained by PCCM and NYRIM and in the respective laminates containing 15% R-A and J-A structures. Quite notably, the $d_{\gamma(020)}$ of the PK-composites varying between 6.0-6.6 Å is lower than the respective values of the NYRIM materials being in the range of 7.0-7.3 Å. With the other long spacings the differences are smaller. Apparently, the crystalline cell type and dimensions are not strongly affected by the parameters of the consolidation techniques.

It should be noted that in many cases in Table 5.4, it was possible to distinguish the crystalline planes of the PA6 matrix obtained by NYRIM or PCCM and those of the oriented PA6 from the reinforcements. Unfortunately, having in mind that the XRD patterns in this study are produced by standard XRD equipment with a certain level of noise, the differences between the d-values of the matrix and reinforcement PA6 are too small to be interpreted.

The monoclinic inter and intra-sheet distances are strongly affected by crystal perfection [233]. Comparing the d-spacing in KSPCs shows remarkable increase for in-mold polymerizing ECL in presence of knitted reinforcements. Therefore, feeble tensile properties of KSPCS molded by NYRIM technique is attributed with the higher inter-sheet distances (d-spacing) of their α and γ crystalline structures. Moreover, the increase in d-spacing of crystal lattice can explain the lower average thickness of TCL in NK-composites.

5.6. Conclusion

The fracture mechanism of KSPCs at the interface was linked with the existence of TCL, identified through polarized light microscopy (PLM) and SEM studies. Overall, the TCL advent significantly modified the tensile properties of the studied composites. XRD analysis performed enable explaining the formation of this TCL at the interface related with the α to γ-phase crystalline conversion. The higher quantity of γ-phase in the PK-composites proved to be correlated to the thicker TCL in the interphase layer between reinforcement and matrix components. The obtained XRD data was in good agreement with the DSC data

analysis performed. In conclusion, the failure properties of NK-composites seem to be essentially due to a thin TCL on the reinforcement-matrix interface region. The thicker TCL at the interface in R-A reinforced PK-composites technique explained their higher tensile properties. Otherwise, better flexural and impact properties of PK-composites reinforced by Jersey structure can be linked with the lower TCL thickness and lower.

The microscopy results and indirectly the XRD studies suggested the formation of a transcrystalline layer at the fiber-matrix interface in both NYRIM and PCCM materials being slightly thicker in the latter case. Structural studies by thermal methods and XRD indicated the importance of the stretch-annealing of the textile reinforcements and of the temperatures for sample consolidation in both processes. Further improvement of the KSPCs mechanical behavior will require novel reinforcements´ architecture, e.g. the use of woven textiles, optimization of their surface finishing and studying the interlaminar shear strength of the KSPCs as a function of ply the amount and alignment.

Chapter 6

Development and structural-mechanical analysis of WSPCs

6.1. Introduction

The present chapter present a systematic study on the relationship between the woven reinforcement geometry, fiber volume fraction, ply orientation with overall mechanical properties of Polyamide 6 based woven reinforced single polymer composites (WSPCs). The development and fully mechanical, thermal and polymorph characterization of this class of composite materials is not known available in currently available open-access literature. Stitched woven fabrics (developed by Jackob Muller AG[®] Company) are a promising novel class of woven fabrics and were applied as reinforcements, for the first time in this study. They are composed of two main partitions including the base woven structure (i.e., plain pattern) and diagonal filaments that are stitched on determined points and form an integrated structure. The mechanical properties (tensile, flexural and impact) of WSPCS reinforced with stitched woven and conventional woven fabrics are analyzed and compared with KSPCs terms of reinforcements´ structural parameters. The mechanical failure behavior of WSPCs has been investigated by electron microscopy complemented by simulation and fractography studies using image processing techniques.

6.2. Mechanical properties of woven reinforcement

6.2.1. Woven fabric structural simulation

Computer-aided technologies are applied to improve the efficiency of production processes. However, virtual simulations of fabrics demanded very complex work due to the combination of techniques including physical-mechanical simulation, collision detection, and user interface techniques. The real size modeling of all stretched-annealed woven reinforcements was performed to enable a parametric fracture study of mechanical properties of WSPCs. There are many different models of representative fabric´s geometry by textile researchers [234–238].

Unit-cell (or repeat) architecture was simulated to deal with the micromechanics of reinforcements. A repeating network of identical unit-cells in the form of crimp waves and constant yarn cross-section in the woven structure was determined. The systematic study of woven fabric geometry started in 1937 by Peirce [234] (Figure 6.1a). In this model, a two-dimensional unit-cell of plain woven fabric was built by superimposing linear and circular yarn segments in which the yarns were assumed to be circular in cross-section and highly incompressible, but at the same time perfectly flexible.

The Peirce's model is unrealistic, as it doesn't consider the flattening of yarns due to the inter-yarn pressure developed during weaving. Thus, the circular cross section of yarns in fabric structure change into an elliptical configuration. Kemp [235] proposed a racetrack section to modify the cross-sectional shape (Figure 6.1b). This model consists of a rectangular cross-section attached by two semicircular ends, which brings relatively simple relations of circular configuration geometry. Therefore, the Kemp racetrack model was selected to simulate all stretched-annealed woven reinforcements in this study.
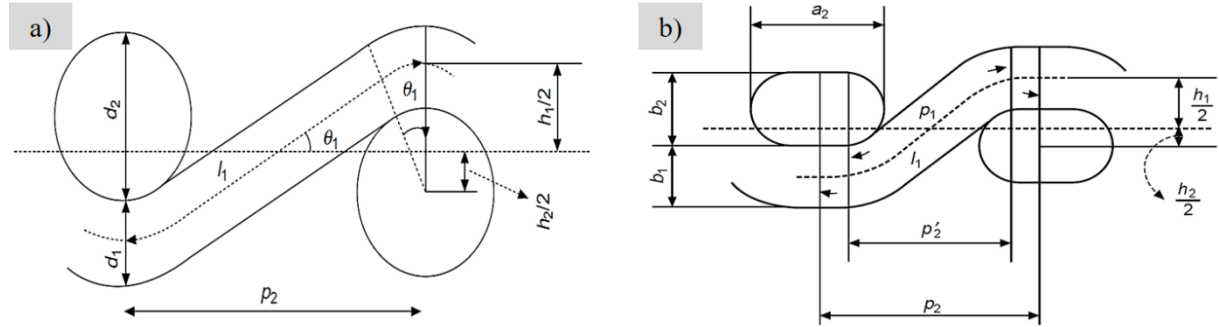
Figure 6.1. Peirce's circular cross-section geometry of plain-weave fabrics; b) Kemp's racetrack section geometry of plain-weave fabrics

The equations for Kemp´s model and its derivatives are presented in 6-1:

$$
\begin{cases}
p_i = a_i - b_i + \left(l'_j - D\theta_j + D \sin\theta_j\right) \\
h_i = (l'_i - D\theta_i) \sin\theta_i + D(1 - \cos\theta_i) \\
l'_i = l_i - a_i + b_i \\
h_1 + h_2 = b_1 + b_2 = D \\
l_{cj} = D_i\theta_i + a_i - b_i \\
e_i = \dfrac{a_i}{b_i} \\
T = h_1 + b_1 = h_2 + b_2 \\
n = \dfrac{1}{p}
\end{cases} \tag{6-1}
$$

where,

d – Free circular-yarn diameter

D – Sum of circular diameters

a – Major diameter of flattened yarn

b – Minor diameter of flattened yarn

e – Yarn flattening coefficient

h – Height of crimp wave

T – Fabric thickness

141

p – Average yarn spacing for the fabric as a whole

n – Average number of yarns per unit length

c – Yarn crimp

l – Length of thread axis between planes containing the axes of consecutive cross threads

l_c – Contact length of yarn

Subscripts i, j– represent the warp and weft directions respectively

Ten digitalized microscopic images captured form top surface of annealed woven reinforcements, using Leica Application Suite 4.4 software and their kernel geometry were subject to analysis by Kemp´s structural model. Ultimately the measured kernel geometry was imported to SolidWorks software (version 2014-2015) and the cross-section profile was swept over it (Figure 6.2a-c). Three major variables were considered for the simulation simplification procedure 1) the filament cross section was considered elliptical 2) the constant sweeping of elliptical cross section through the kernel geometry 3) No dimensionally deformation at cross over points. To perform a contact interface assessment, the simulated samples were virtually clash tested. Figure 6.2a-c illustrates the final product of the isometric and three side views of simulated annealed plain, satin (5 harness) and stitched plain 30° (as representative of stitched plain fabrics category) structures respectively.
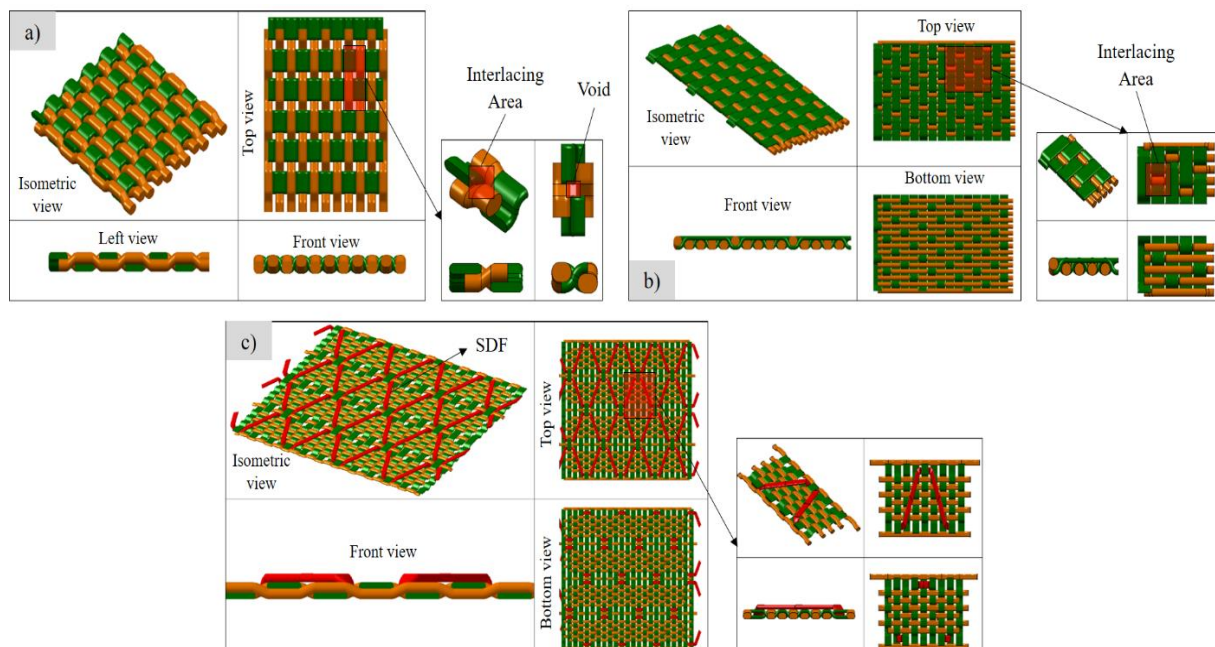
Figure 6.2. Simulated 3D model of real size annealed woven reinforcements a) Plain b) Satin c) Stitched plain with 30° SDF

6.2.2. Tensile properties of woven reinforcements

The typical tensile stress-strain behavior of plain and satin reinforcements in wale direction, with and without stretching-annealing treatment, is presented in Figure 6.3a-d. For untreated woven reinforcement, the initial zone showed a low slope due to the decrimping and crimp-interchange (up to 10% tensile strain). Afterward, the stress-strain curve gradient increased steeply reaching its peak which could be caused by the induced filament elongation. Moreover, the peak amplitude in the tensile stress-strain graph was governed by the level of yarn crimp and the filaments distortion. After the yield strength, the reinforcement´s structure never returned to its original dimension due to the viscoelastic nature of woven fabrics (residual strains).

The stretching-annealing treatment caused the release of strain residuals generated by converting the amorphous to crystal portion of the filaments [239]. Therefore, the tensile rigidity and strength of woven reinforcements were significantly modified by applying a stress-relaxing procedure (Figure 6.3a). Figure 6.3b-d displays a deformed structure of all woven reinforcements after the treatment through which the porosity of the structures was increased. Due to this fact, better matrix impregnation and interfacial bonding between composite components are predicted.
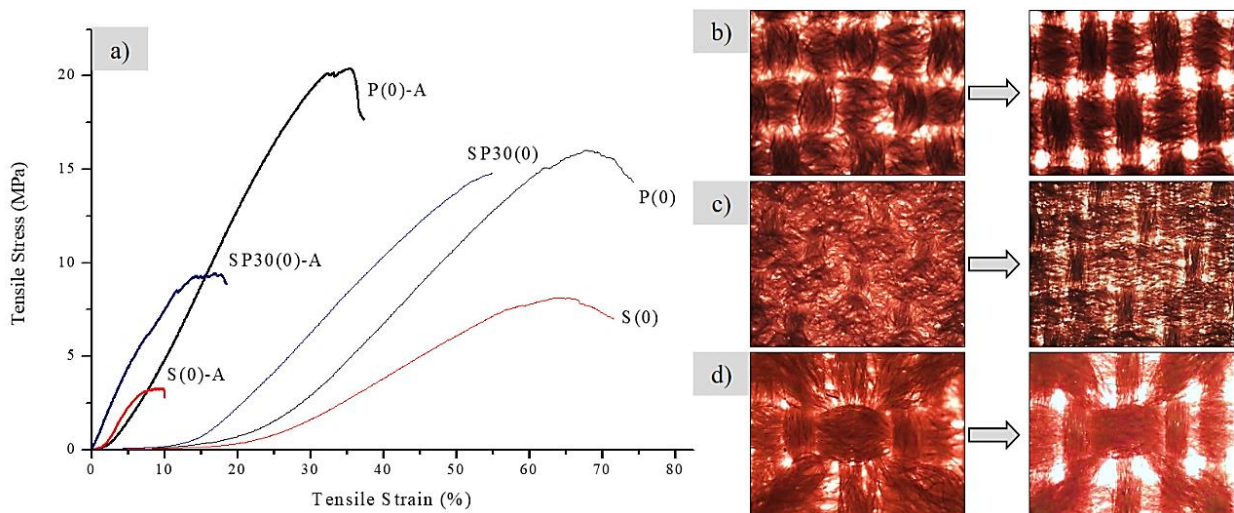
Figure 6.3. a) Typical stress–strain graph of untreated and stretched-annealed representative Plain and Satin reinforcements in warp direction; Structural deformation of b) Plain; c) Satin; d) SP45 before and after annealing from left to right. Sample designations are presented in Table 3.1 and Table 3.2.

The tensile properties of plain and satin reinforcements in two main directions including warp (0°) and weft (90°) are presented in Table 6.1. The stretching-annealing process significantly improved the tensile stiffness and strength of all reinforcements. The S-A structure showed higher tensile rigidity than P-A

wherein the elastic zone of reinforcements was associated with a tensile strain of 0.5-1.5 %. Moreover, Satin structures had more anisotropic tensile behavior due to considerable differences between their tensile properties in plies orientations. The P-A reinforcements contained higher tensile strength than satin in the two main directions. The reason lays on better aligning and straightening of crimped filaments in the direction of tensile stresses in plain fabrics.

The interlace points in woven structures brought about a decline in weave angle. Hence, filaments became deformed from flat-like into circular cross-section accompanied by crimp-interchanging. At interlacing point (Figure 6.2), one set of filaments increases the crimp gradient while the other decreases. Therefore, a woven pattern containing the less interlacing points like S-A reinforcements, the less crimp interchange exists, and all tensile loads are endured by straight filaments [240]. Consequently, in this study, it is believed that treated plain structures (P-A) play a beneficial role in tensile properties of WSPCs.

Table 6.1. Data about the tensile properties of Plain and Satin reinforcements with and without stretching-annealing treatment.

Specimens	Young´s modulus E(GPa)	Stress at max σ_{Max}(Mpa)	Strain at break ε_{Br}(Mpa)
P(0)	0.8 ± 0.1	15.4 ± 0.8	67.2 ± 0.7
P(90)	2.2 ± 0.2	17.4 ± 0.4	61.1 ± 1.8
S(0)	0.9 ± 0.1	8.1 ± 0.2	65.0 ± 1.4
S(90)	0.8 ± 0.1	9.3 ± 0.6	66.9 ± 0.8
P(0)-A	21.7 ± 1.1	19.4 ± 1.0	28.1 ± 1.0
P(90)-A	3.4 ± 0.3	19.0 ± 1.0	46.2 ± 1.4
S(0)-A	43.2 ± 1.7	3.4 ± 0.1	10.0 ± 0.8
S(90)-A	1.4 ± 0.1	16.5 ± 1.0	45.1 ± 1.5

Tensile stress-strain curves of all stitched plain reinforcements with and without treatment in two main directions are displayed in Figure 6.4. The stretching-annealing treatment modified significantly the tensile properties of all Stitched plain reinforcements. The best tensile behavior was achieved in the warp direction. Even if with SP45 sample, increasing of SDF gradient improved the tensile properties (Figure 6.4) of stitched plain reinforcements.
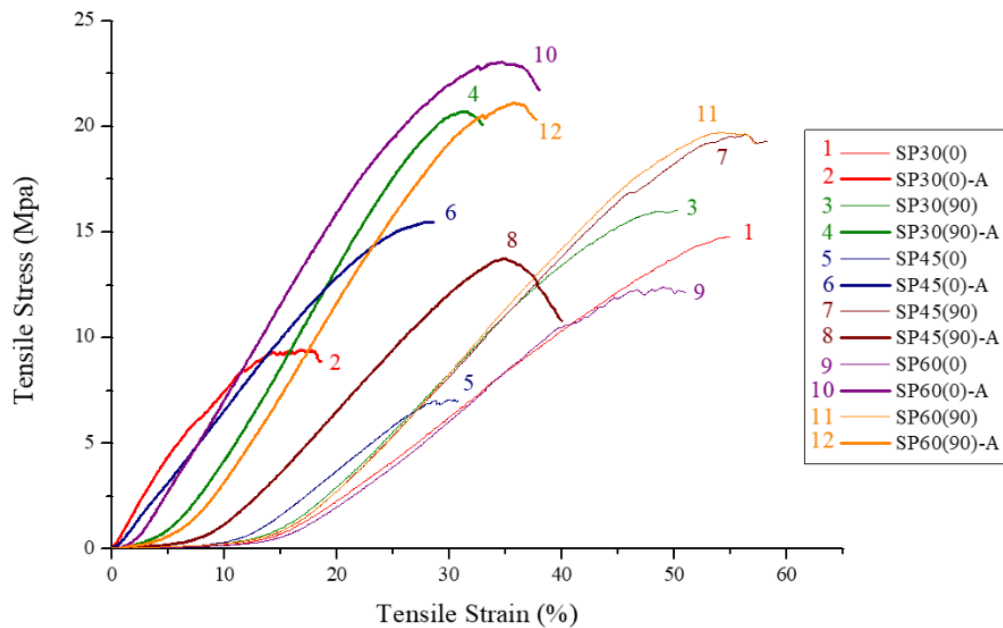
Figure 6.4. Stress-strain curves in tension of all woven reinforcements before and after the stretching-annealing treatment applying strain at two principal directions. For sample designation see Table 3-1 and Table 3-2.

The data analysis on tensile properties of all SP reinforcements before and after treatment is tabulated in Table 6.2. The effect of SDF gradient on tensile properties of SP textile fabrics in either directions was investigated. Introducing SDFs in plain base structure improved the tensile properties of plain structures although the physical properties of the plain substrate became preserved.

Comparing the data analysis on tensile properties of untreated and annealed plain and stitched woven plain reinforcements (Table 6.2 and Table 6.1) evidenced that applying SDFs significantly strengthens the elastic modulus of plain reinforcement (as substrate) up to 360% and 20 % in warp and weft directions respectively. Increasing the SDF gradient did not significantly change the elastic modulus of treated stitched plain reinforcements in the two principal orientations. The treated SP30 sample contained the highest tensile stiffness in warp (101MPa) and weft (7MPa) directions. On the other hand, the SP45 samples showed the lowest Young modulus in either directions.

In general, the tensile behavior of stitched plain reinforcements dropped by 45° inclination of SDFs and then leveled up while SDFs gradient approached to 60° of inclination. Noticeably, treated SP60 reinforcements showed the highest tensile strength in any directions between stitched plain structures. However, treated SP60 depicted the lowest and the highest ductile behavior in warp and weft directions respectively.

145

Table 6.2. Data about the tensile properties deduced from the mechanical tests in tension of Stitched plain reinforcements with and without annealing treatment respect to the 30°, 45° and 60° SDFs gradient. For sample designation see Table 3-1 and Table 3-2.

Specimens	Young´s modulus E(GPa)	Stress at max σ_{Max}(Mpa)	Strain at break ε_{Br}(Mpa)
SP30(0)	1.4 ± 0.1	13.2 ± 0.5	53.1 ± 2.2
SP45(0)	1.7 ± 0.1	7.8 ± 0.7	32.1 ± 1.5
SP60(0)	1.2 ± 0.03	12.4 ± 0.5	50.6 ± 2.8
SP30(90)	2.0 ± 0.1	17.7 ± 0.9	53.4 ± 2.3
SP45(90)	1.9 ± 0.1	19.2 ± 1.0	55.3 ± 2.0
SP60(90)	1.9 ± 0.1	19.7 ± 0.7	53.3 ± 2.1
SP30(0)-A	101.1 ± 2.7	9.2 ± 0.5	26.7 ± 2.1
SP45(0)-A	74.8 ± 2.2	15.9 ± 0.6	28.6 ± 1.6
SP60(0)-A	85.8 ± 2.1	23.2 ± 0.1	17.1 ± 0.3
SP30(90)-A	7.0 ± 0.8	20.0 ± 0.8	31.1 ± 0.01
SP45(90)-A	2.2 ± 0.2	14.1 ± 0.4	35.7 ± 1.2
SP60(90)-A	3.7 ± 0.3	22.4 ± 1.2	37.5 ± 2.4

The quasi-static analysis of treated stitched plain reinforcements enabled a better explanation on of different tensile responses of stitched plain structures concerning the increase of SDFs gradient. Three captured images at the onset, middle and end tensile elongation of representative SP45(0)-A and SP45(90)-A reinforcements are presented in Figure 6.5. Tracking the reinforcement structural deformation in warp and weft-tested samples evidenced that SDFs compressed and centralized the warps and weft filaments in their domain (Figure 6.5a$_3$,b$_3$).

In case of warp-wise tension, the side compression of SDFs columns increased the transversal strain in that domain (Figure 6.5a$_3$). Due to this observation, the Poisson´s ratio of stitched plain reinforcements is integrated by two distinct transversal strains consisting the differential transversal strain of the entire structure (ε_{y1}) and that of SDFs domain (ε_{y2}). Therefore, as seen in Figure 6.5a$_3$, the discrepancy between ε_{y1} and ε_{y2} caused a gap between two adjacent SDFs at the terminal elongation.

In the case of weft-wise elongation, the SDFs compressed the wefts in their domain and by raising the longitudinal strains, the gap between adjacent SDFs was increased (Figure 6.5b$_3$). Due to this fact, two distinct differential longitudinal strains existed, being the former considered for the entire structure (ε_{x1}) and the later for SDFs domain (ε_{x2}). The stitched reinforcement´s structure showed unique longitudinal (ε_x) and transversal (ε_y) strains while they were stretching in warp and wept direction respectively.
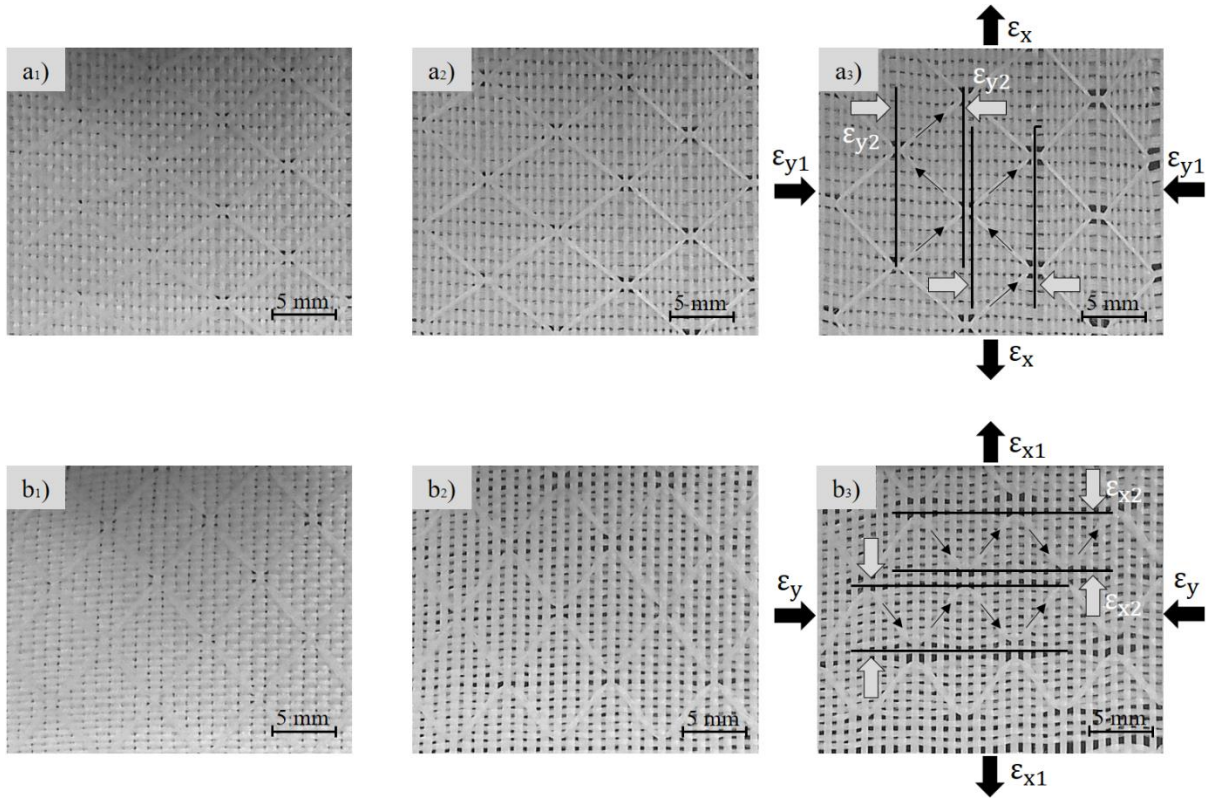
Figure 6.5. Static-Strain analysis of SP45 a_i) Warp; b_i) Weft orientations. The figure subscript i represents the deformation status at onset (i=1), mid (i=2) and terminal (i=3) of tensile elongation.

Assuming that the stitched plain reinforcements are stretched along warp and weft directions, Poisson´s ratio is measured by the following equation:

$$\nu = -\frac{\delta\varepsilon_y}{\delta\varepsilon_x} \rightarrow \begin{cases} \nu_{\text{warp}} = -\dfrac{\delta\varepsilon_{y1}+\delta\varepsilon_{y2}}{\delta\varepsilon_x} \\ \nu_{\text{weft}} = -\dfrac{\delta\varepsilon_y}{\delta\varepsilon_{x1}-\delta\varepsilon_{x2}} \end{cases} \tag{6-2}$$

As equation 6-2 demonstrated, the ν_{warp} and ν_{weft} are increased with respect to the incremental differential transversal strains and subtractive longitudinal strains in warp and weft directions respectively. Higher Poisson´s ratio in weft direction was identified by applying image analysis of Figure 6.5a_3,b_3, through which the $\delta\varepsilon_{x1}$, $\delta\varepsilon_{x2}$, $\delta\varepsilon_{y1}$, $\delta\varepsilon_{y2}$ values were measured. Lower ν_{warp} yielded less reinforcement´s structural distortion and consequently higher tensile properties in warp than weft direction could be explained logically.

To bond the tensile properties with geometrical deformation of stitched plain reinforcements, the resultant SDFs length was divided into longitudinal (warp) and transverse (weft) components (Figure 6.6)
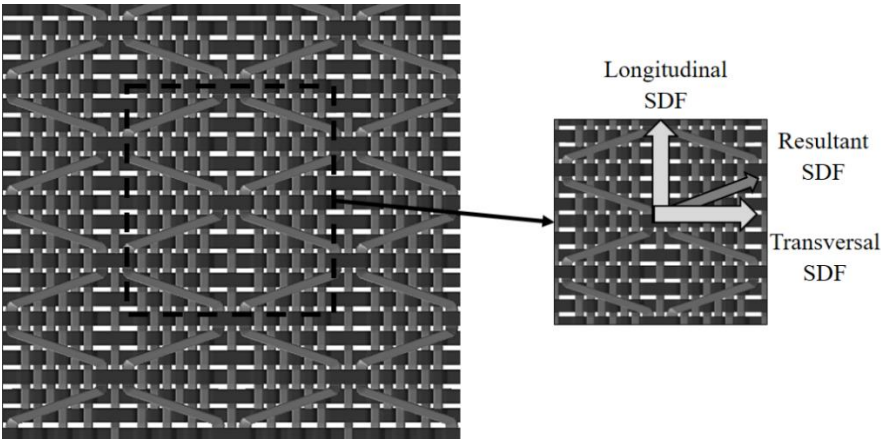
Figure 6.6. Visualized top view of SP30-A and dissolution of SDF in to longitudinal (warp) and transversal (weft) components

The length of resultant SDFs in all treated stitched plain reinforcements was measured by image processing with Leica Application Suite 4.4 software (Figure 6.7-a). The SDFs quantities $(\frac{1}{m})$ in the transverse and longitudinal directions were presented to calculate SDFs participation factor (%) in corresponding directions per reinforcements length (mm) (Figure 6.7-b).
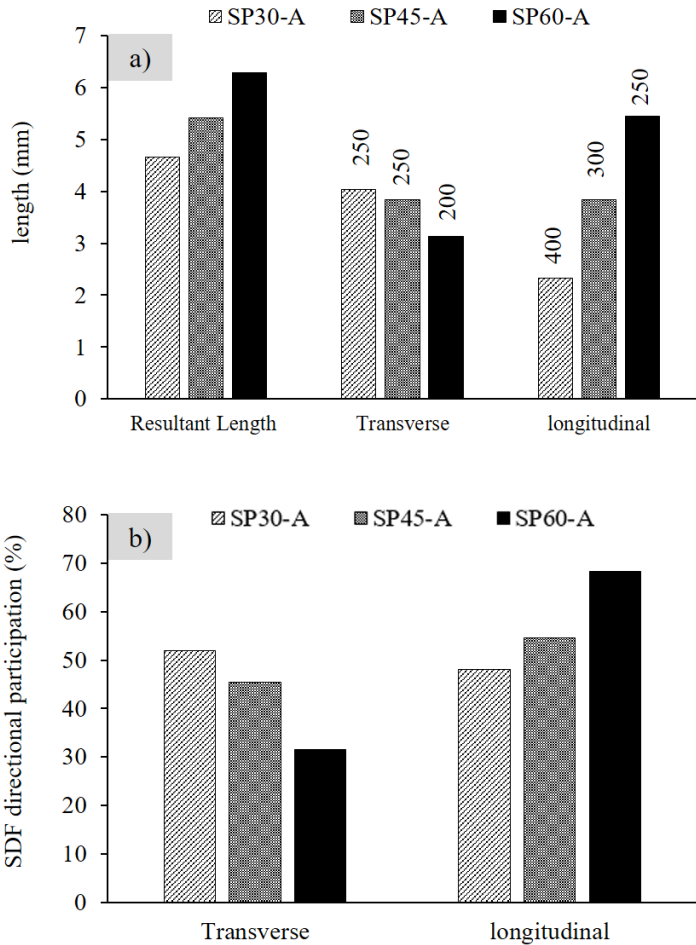
Figure 6.7. a) Comparative study on length (mm) of SDF resultant and the components. The SDFs quantities (1/m) are shown in the corresponding direction; b) SDFs directional participation (%) in either directions.

148

Surprisingly, treated SP30 showed a balanced geometry due to the symmetrical participation of SDFs in both directions. On the contrary, increasing the SDFs gradient unbalanced the reinforcements´ structures. Meanwhile, the identical SDFs participations in treated SP30 reinforcements contributed to a better tension in plain substrates causing a better tensile behavior.

6.2.3. Bending properties of woven reinforcements

The study of the bending behavior of woven fabrics is important and may be linked to the final flexural properties of composite material. The influence of orientation, architecture and reinforcement technical face on the bending rigidity of all woven reinforcements is displayed in Table 6.3, calculated by Pierce equation (Eq.3-12). As it can be seen in Table 6.3, the annealing treatment decreased the bending rigidity of the reinforcements. S-A samples showed 147% and 52% improvement of bending rigidity compared to the P-A in the technical front and back faces respectively.

In the case of stitched plain reinforcements, inserting SDFs improved the bending rigidity of the plain structure in both directions. Increasing the SDF gradient didn't significantly improve the bending rigidity of stitched plain reinforcements.

Table 6.3. Comparison on bending rigidity of all woven reinforcements influenced by test direction, technical faces and annealing treatment

Specimens	Bending rigidity ($\mu N.m$)		Specimens	Bending rigidity ($\mu N.m$)	
	Technical front face	Technical back face		Technical front face	Technical back face
P(0)	11.59 ± 0.00	11.16 ± 0.49	P(0)-A	4.33 ± 0.23	4.14 ± 0.18
S(0)	28.13 ± 1.37	4.44 ± 0.25	S(0)-A	10.68 ± 0.41	6.30 ± 0.29
SP30(0)	9.82 ± 0.44	11.99 ± 0.51	SP30(0)-A	8.52 ± 0.35	8.34 ± 0.37
SP45(0)	7.75 ± 0.35	8.41 ±0.61	SP45(0)-A	9.02 ± 0.33	6.89 ± 0.28
SP60(0)	8.33 ± 0.34	8.33 ± 0.34	SP60(0)-A	5.21 ± 0.23	4.52 ± 0.19
P(90)	6.87 ± 0.33	6.75 ± 0.33	P(90)-A	3.50 ± 0.21	4.16 ± 0.20
S(90)	3.16 ± 0.18	8.38 ± 0.40	S(90)-A	3.06 ± 0.17	6.27 ± 0.30
SP30(90)	9.77 ± 0.41	3.44 ± 0.19	SP30(90)-A	4.64 ± 0.25	2.34 ± 0.13
SP45(90)	8.27 ± 0.36	2.54 ± 0.15	SP45(90)-A	5.43 ± 0.26	2.70 ± 0.15
SP60(90)	8.43 ± 0.37	5.58 ± 0.28	SP60(90)-A	5.05 ± 0.25	3.75 ± 0.19

6.2.4. Dynamic mechanical spectroscopy of woven reinforcements

The isothermal compression dynamic mechanical spectroscopy of all woven reinforcements such as Storage modulus (E'), loss modulus (E''), tangent delta (δ) and complex compression modulus (E^*) before and after stretching-annealing treatment is shown in Figure 6.8. The DMA testing of all woven reinforcements explains the influence of reinforcements' architecture on impact properties of WSPCs. Figure 6.8a shows that the stretching-annealing procedure reduced the damping properties (Tan δ) of woven reinforcements. The damping properties of stitched plain structures were slightly higher than treated plain and satin reinforcements. Knowing the damping (energy dissipation) properties of reinforcements provide quantitative information about their performance in WSPCs during impact test.
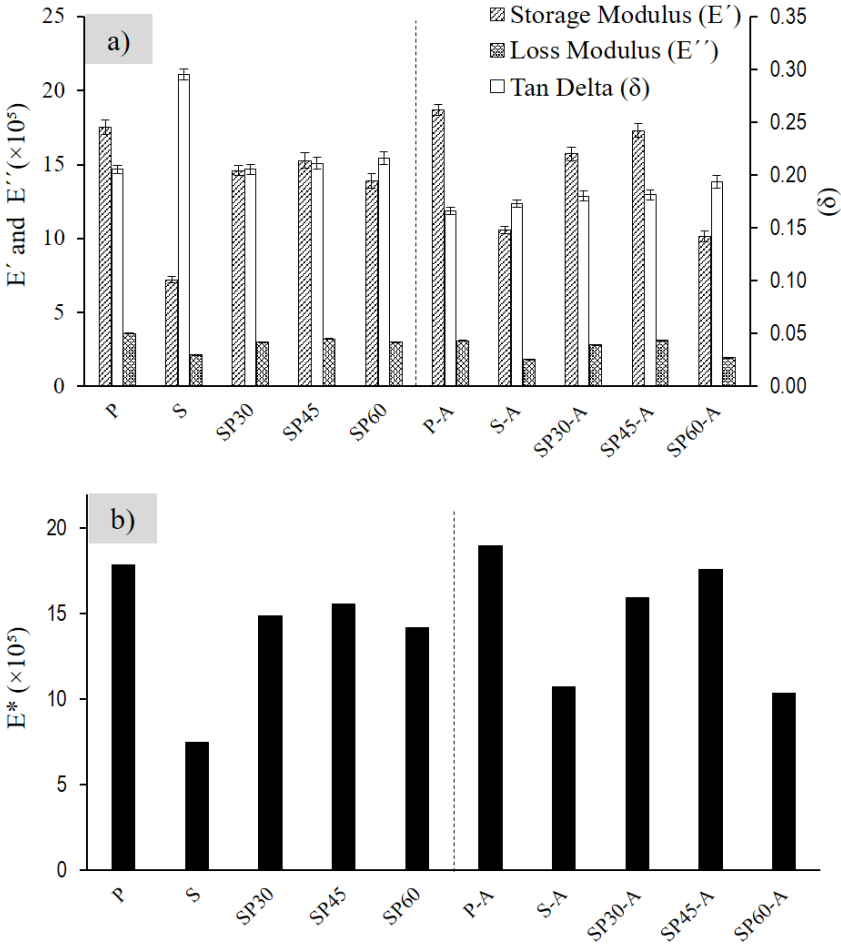
Figure 6.8. Dynamic mechanical analysis (DMA) of woven reinforcements before and after annealing procedure; a) Storage modulus, loss modulus and tangent delta; b) Complex compression modulus (E^*).

Except in sample SP60, the compression stiffness of all reinforcements increased with stretching-annealing treatment. Figure 6.8b, demonstrates that the compression stiffness of the treated plain structure is the highest among all woven reinforcements. The complex modulus of treated stitched plain

reinforcements changed by SDFs gradient increased from 30° to 45°. But It dropped abruptly from 60° becoming identical to the E* value of treated satin structures.

6.3. Mechanical Properties of WSPCs

The mechanical properties of all WSPCs prepared by PCCM (PW-composite) and NYRIM (NW-composite) techniques were studied in relation to the woven reinforcement architecture, fiber volume fraction, ply orientation and stacking orders. Table 6.4 presents all NW- and PW-composite samples and explains their designations. Unlike KSPCs, the woven reinforcements were unidirectionally oriented. As such WSPCs with three fiber contents were prepared, i.e., 15, 20 and 25 V_f%.

Table 6.4. The designation and detail description of WSPCs prepared by PCCM and NYRIM techniques.

WSPCs designation	Woven reinforcement architecture	V_f,%	Plies Number (PCCM)	Plies Number (NYRIM)
P/N[a]U-P([b])-15	Annealed Plain reinforcement	15	3	6
P/N[a]U-P([b])-20		20	4	8
P/N[a]U-P([b])-25		25	5	10
P/N[a]U-S([b])-15	Annealed Satin reinforcement	15	3	6
P/N[a]U-S([b])-20		20	4	8
P/N[a]U-S([b])-25		25	5	10
PU-SP[c](0)-15	Annealed Stitched Plain reinforcement	15	3	-
PU-SP[c](90)-25		25	5	-

[a] P or N represent the PCCM and NRIM molding techniques respectively in this study.

[b] Unidirectional laminating of woven textile reinforcements in which 0° for warp or 90° for weft directions.

[c] The gradient (°) of SDF in stitched plain reinforcements are shown by 30, 45 and 60.

6.3.1. Tensile properties of PW-composites

Anisotropic material behavior of woven reinforced composites is a result of the reorientation and redistribution of monofilaments in reinforcements´ structure. Figure 6.9a-b shows representative stress-strain curves of WSPCs wherein the influences of reinforcement orientation, architectures and fiber volume fractions were inspected. Nonlinear elastic behavior is followed by pseudo-plastic before reaching an ultimate stress gained at the early stages of tensile loading. The achieved nonlinearity in stress-strain graph of WSPCs postulated by shear deformation of the longitudinal filaments, extensional deformation of the matrix component and transverse cracking of the filaments known as micromechanical deformations [241,242]. Figure 6.9a-b demonstrates superior tensile properties of WSPCs than PN

reference.

The WSPCs showed different configurations in their tensile stress-strain graph after their yield point in the two main directions. The tensile behavior of WSPCs showed a plastic deformation in warp direction (Figure 6.9a) represented by the plateau region after 3-4% stain. The warp (0°) tested samples demonstrated more ductile behavior due to their higher strain at break. Otherwise, stress-strain behavior of WSPCs in weft (0°) direction (Figure 6.9b) was tracked by an abrupt drop in stress magnitude which represented their brittle failure mode.
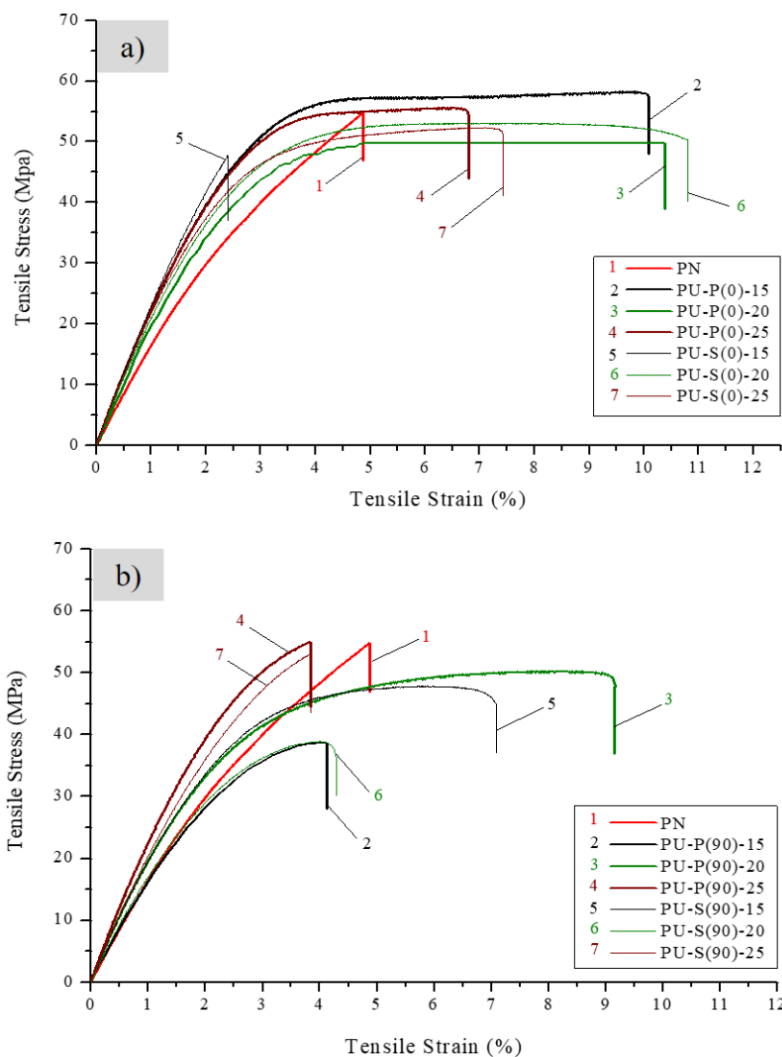
Figure 6.9. Stress-strain curves in tension of annealed plain and satin reinforced WSPCs: (a) Strain applied along the unidirectional alignment of the ply set; (b) Strain normal to the ply set alignment; For sample designation see Table 6.4.

Figure 6.10a-c, shows a comparative study on tensile properties of WSPCs such as young modulus (E), tensile strength (σ) and tensile strain at break (ε). The effect of reinforcement orientation, architectures, and volume fractions was investigated. All WSPCs contained better tensile behavior than

152

the PN reference. Unlike weft tested plain reinforced WSPCs, mounting the unidirectional laminates didn't modify the elastic modulus of WSPCs (Figure 6.10a).

Figure 6.10b presents a comparison of tensile stress at max (σ_{max}) of all WSPCS. Surprisingly, there was no improvement in tensile strength of WSPCs compare to the PA6 neat matrix component (Figure 6.10b). As it can be seen in Figure 6.10c, increasing V_f%, raised the ductility of WSPCs in warp orientation although it didn't change significantly in weft direction. As it can be seen in Figure 6.10a, b, raising the fiber content up to 25 V_f,% increased the isotropic behavior of WSPCs due to the identical tensile stiffness and strength in both directions. However, the degree of anisotropy increased by reduction of V_f%.
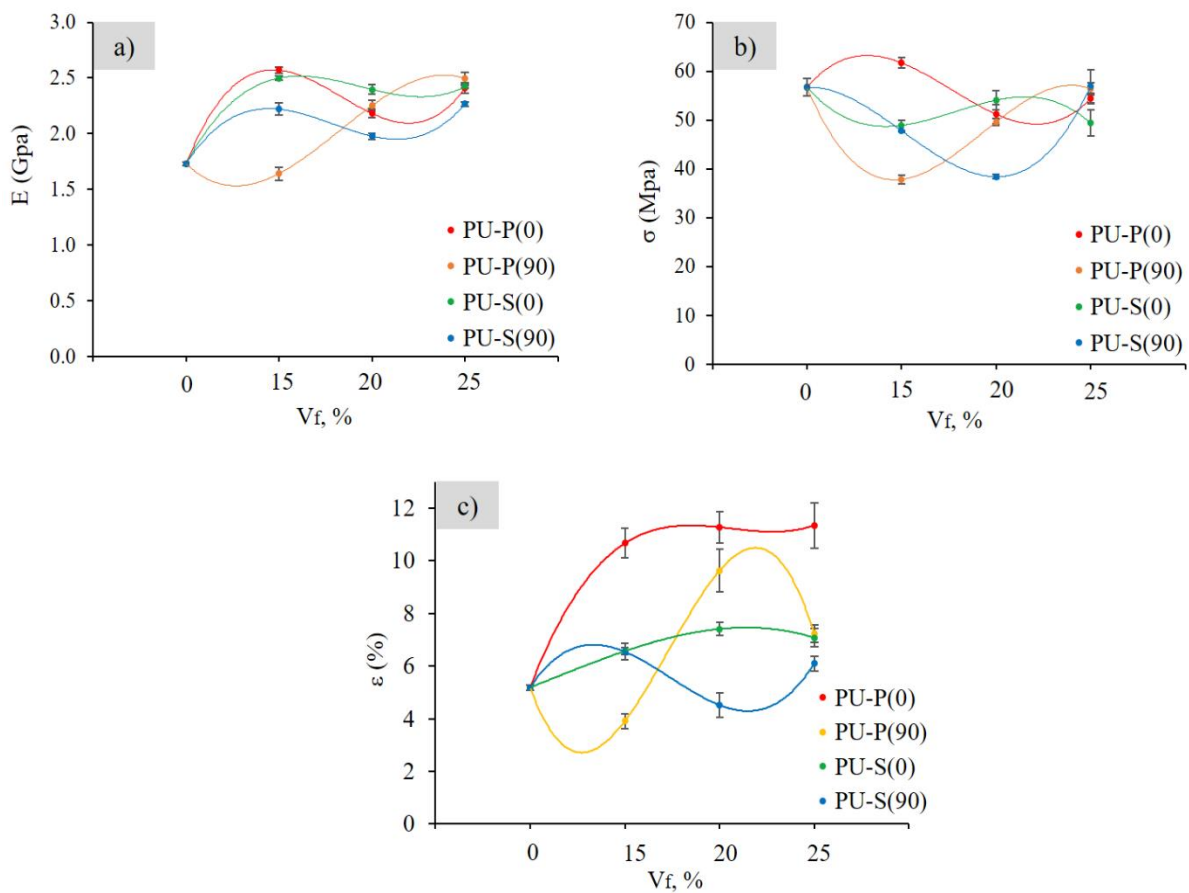
Figure 6.10. Comparison on a) Tensile stiffness (GPa); b) Tensile stress (MPa) at max; c) Tensile strain of unidirectional WSPCs respect to the woven architecture, fiber volume fraction and plie orientation. For sample designation see Table 6.4

A deep analysis of tensile properties of WSPCs is shown in Table 6.5 whereby the influence of reinforcement orientation, architectures, and volume fractions had been evaluated. The discrepancies between σ_{max} and σ_{Break} values represent the necking phenomenon where the engineering stress starts to decrease with an increasing strain. Embedding P-A reinforcements improved 60% and 9% tensile stiffness and strength of WSPCs respectively compared to the PN reference. The following observations

can be drawn based on the analysis of the tensile properties of WSPCs (Table 6.5) and KSPCs (Table 4.5):

i) Embedding woven reinforcements increased the tensile stiffness (E, GPa) of composites.

ii) Unlike WSPCs, embedding the knitted structures increased the tensile strength (σ_{max}, MPa) of KSPCs compared to the PN reference.

iii) WSPCs had higher tensile stiffness and lower tensile strength than KSPCs.

iv) Embedding woven reinforcement in PA6 matrix caused necking behavior of WSPCs whereas the tensile stress-strain graph of KSPCs demonstrated a brittle behavior.

v) The WSPCs are more ductile than KSPCs due to the high strain at failure in their stress-strain graph.

Table 6.5. Data about the tensile properties of WSPCs. For sample designation see Table 6.4 and the text.

Sample designation	Young´s modulus E, (Gpa)	Tensile stress at max σ_{max}, (MPa)	Tensile stress at break σ_{br}, (MPa)	Tensile strain at break ε_{br}, (%)
PN	1.73 ± 0.02	57.3 ± 0.9	56.7 ± 1.8	5.2 ± 0.1
Durethan B30S*	1.03 ± 0.04	51.2 ± 2.0	65.5 ± 1.3	37 ± 6.0
PU-P (0)-15	2.57 ± 0.03	61.7 ± 1.1	55.8 ± 1.6	10.7 ± 0.5
PU-P (0)-20	2.18 ± 0.04	51.1 ± 1.9	51.1 ± 1.9	11.3 ± 0.5
PU-P (0)-25	2.41 ± 0.05	54.3 ± 1.1	54.0 ± 0.7	11.3 ± 0.8
PU-P (90)-15	1.64 ± 0.06	37.9 ± 0.8	37.9 ± 0.8	3.9 ± 0.2
PU-P (90)-20	2.25 ± 0.05	49.6 ± 0.8	46.9 ± 0.6	9.6 ± 0.8
PU-P (90)-25	2.49 ± 0.06	56.4 ± 1.3	55.9 ± 0.7	7.2 ± 0.3
PU-S (0)-15	2.50 ± 0.02	48.9 ± 1.1	46.3 ± 1.4	6.6 ± 0.1
PU-S (0)-20	2.40 ± 0.04	54.1 ± 1.9	51.8 ± 1.9	7.4 ± 0.2
PU-S (0)-25	2.42 ± 0.01	49.4 ± 2.7	51.9 ± 0.9	7.1 ± 0.3
PU-S (90)-15	2.22 ± 0.05	47.8 ± 0.5	46.1 ± 1.4	6.5 ± 0.3
PU-S (90)-20	1.98 ± 0.03	38.4 ± 0.5	38.2 ± 0.7	4.5 ± 0.4
PU-S (90)-25	2.27 ± 0.02	57.0 ± 3.4	56.8 ± 1.3	6.1 ± 0.2

* Commercial neat hydrolytic PA6 of BASF, Germany, compression molded granulate [209]

For the selection of the best tensile properties of plain reinforced WSPCs with 15 and 25% fiber volume fractions, unidirectional stitched plain reinforced WSPCs have been prepared and characterized mechanically. Figure 6.11a-b, presents an inductive study of warp and weft-wise stress-strain graphs of stitched plain reinforced WSPCs, and stress-strain plots of PN matrix and plain reinforced WSPCs (with

corresponding fiber content) are presented as references. Assessment of the elastic zone in Figure 6.11a-b shows that applying stitched woven reinforcements remarkably improved the tensile stiffness and strength of the reference samples.
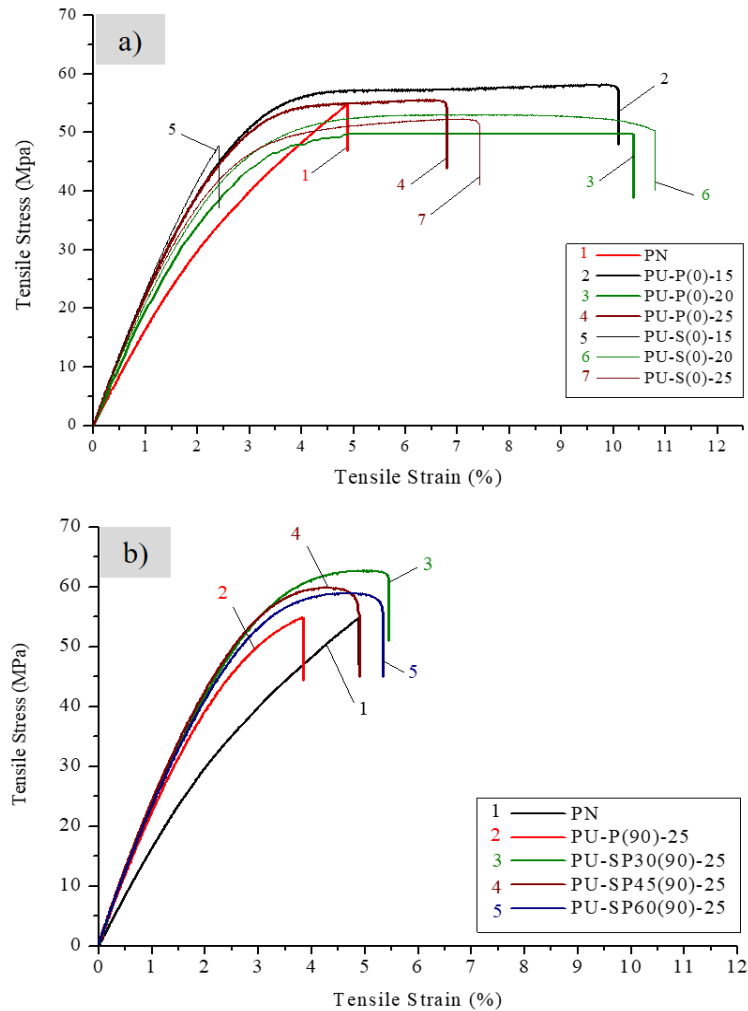
Figure 6.11. Stress-strain curves in tension of annealed stitched plain reinforced WSPCs: (a) Strain applied along the unidirectional alignment of the ply set; (b) Strain normal to the ply set alignment; In all stress-strain curves the neat anionic matrix PN is presented for reference. For sample designation see Table 6.4.

WSPCs reinforced by P-A and S-A reinforcements showed plastic behavior in stress-strain curve (Figure 6.11a). Embedding the P-A structures in WSPCs was caused strain hardening followed by an increase in their stress-strain curve reaching the tensile failure point. On its side, stitched plain reinforced WSPCs demonstrated a necking state in the plastic zone, detected by gradually steepening their stress-strain curve after ultimate strength. Increasing the SDF gradient up to 60° raised the ductility of warp-tested stitched plain reinforced WSPCs. In general, SP45-A reinforced WSPCs showed distinct tensile properties in comparison with those reinforced by treated SP30 and SP60. The detailed comparison of tensile properties of WSPCs reinforced by stitched plain structures is presented on Figure 6.12a-c. Changing the

155

strain direction to 90° in relation to the wales direction resulted in the stress-strain curves in Figure 6.12b. The PN matrix component and P-A reinforced WSPCs are presented as references. Applying the SDFs increased remarkably the tensile stiffness and strength of WSPCs compared to those reinforced by a plain structure.

Increasing the SDF gradient up to 60° improved 10% and 63% the tensile stiffness of composites compared to plain reinforced WSPCs (with corresponding fiber content) and PN matrix respectively (Figure 6.12a). WSPCs reinforced with SP45 reinforcements showed the highest tensile stiffness (2,78 GPa) in weft direction and the lowest elastic modulus (2.61GPa) in warp direction among stitched plain reinforced WSPCs. Figure 6.12b illustrates the comparative study of tensile stress at max wherein embedding SP30 reinforcements modified the tensile strength slightly up to 10.5% compare to P-A reinforced WSPCs with the corresponding V_f,%. As seen in Figure 6.12c, treated stitched plain structures didn't change considerably the ductility of plain reinforced WSPCs.
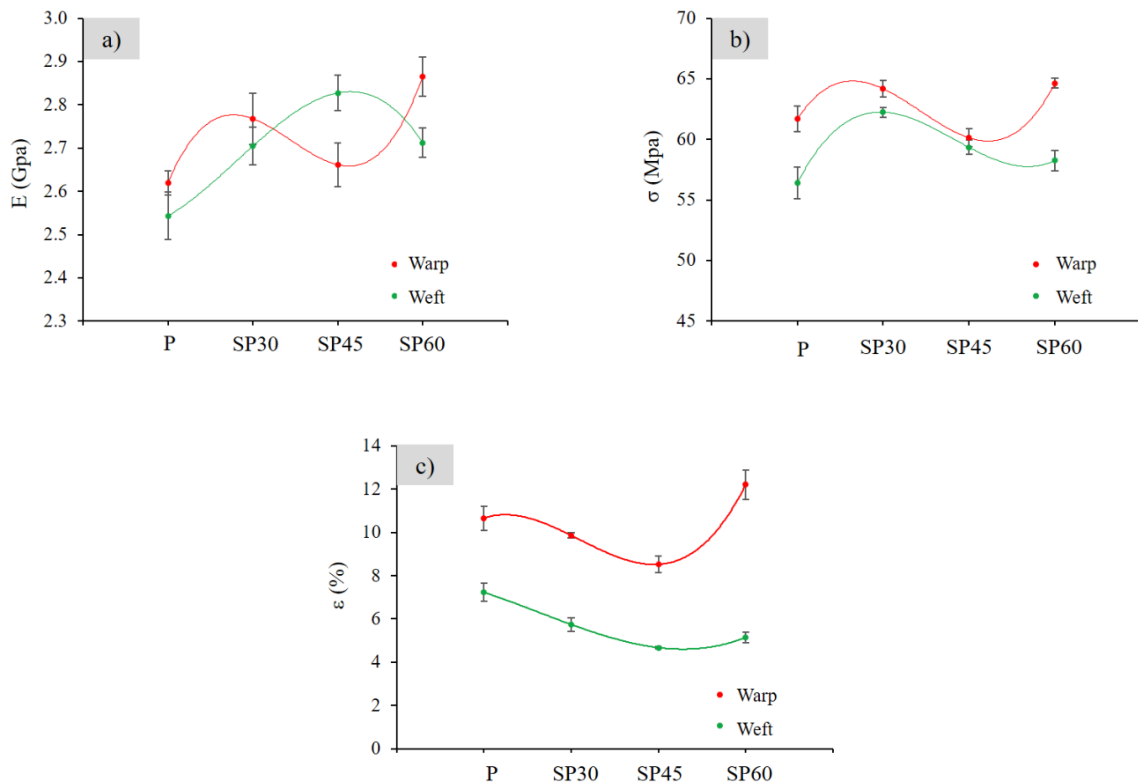
Figure 6.12. Comparison on a) Tensile stiffness (GPa) b) Tensile stress (MPa) at max and break c) Tensile strain of unidirectional stitched reinforced WSPCs influenced by the SDF gradient and plie orientation; For sample designation see Table 6.4.

The further evaluation of the tensile properties of stitched plain reinforced WSPCs is presented in Table 6.6. Like P-A reinforced WSPCs, applying stitched reinforcements in warp direction caused the a necking

effect due to the discrepancies between σ_{max} and σ_{Break} values. However, weft wise PW-composites showed a brittle behavior resulting from the identical stresses at max and break magnitudes. However, higher tensile properties of stitched plain reinforced WSPCs can be correlated with quasi-static analysis of fabric structures.

As seen in Figure 6.5, the SDFs in stitched plain reinforcements maintained the warp and weft filaments in the position during tensile loading. They showed dual differential transversal and longitudinal strains in warp and weft direction respectively. Lower ν_{Warp} may cause reduction of the shear traction (stress fields) at the interface region between reinforcement-matrix. Thus, shear force dissipation between the filament and matrix contact points may explain better the higher tensile properties of warp wise stitched plain reinforced WSPCs.

Table 6.6. Data about the tensile properties of stitched plain reinforced WSPCs. For sample designation see Table 6.4 and the text.

Specimens	Young´s modulus E, (Gpa)	Tensile stress at max σ_{max}, (MPa)	Tensile stress at break σ_{br}, (MPa)	Tensile strain at break ε_{br}, (%)
PN	1.73 ± 0.02	56.71 ± 1.77	56.71 ± 1.77	5.2 ± 0.1
PU-P(0)-15	2.57 ± 0.03	61.68 ± 1.07	55.75 ± 1.63	10.66 ± 0.56
PU-SP30(0)-15	2.72 ± 0.06	64.17 ± 0.70	60.43 ± 1.20	9.86 ± 0.13
PU-SP45(0)-15	2.61 ± 0.05	60.13 ± 0.75	61.30 ± 0.63	8.52 ± 0.37
PU-SP60(0)-15	2.82 ± 0.05	64.63 ± 0.41	58.98 ± 0.78	12.21 ± 0.69
PU-P(90)-25	2.49 ± 0.06	56.38 ± 1.30	55.93 ± 0.79	7.23 ± 0.34
PU-SP30(90)-25	2.65 ± 0.04	62.24 ± 0.40	57.12 ± 1.01	5.74 ± 0.34
PU-SP45(90)-25	2.78 ± 0.04	59.34 ± 0.58	58.71 ± 0.42	4.67 ± 0.12
PU-SP60(90)-25	2.66 ± 0.03	58.26 ± 0.84	57.65 ± 1.21	5.15 ± 0.15

The radar chart of calculated IF_{PN} value of tensile stiffness, stress at max and stress at break of all WSPCs is presented in Figure 6.13. The radar plots shifted towards the stitched plain reinforced WSPCs, which is attributed to the better tensile properties of this class of composite materials. The supreme value of 62% IF_{PN} was obtained for PU-SP60(0)-15 samples. The differences between the areas of stress at max and break represented the necking phenomena. Therefore, higher necking behavior is observed for stitched plain reinforced WSPCs due to an extreme overlapping area of stress at max on stress at break. As a conclusion, introducing SDF on the plain structure with 30° and 60° gradients is considered the best pattern to improve the tensile properties of WSPCs.
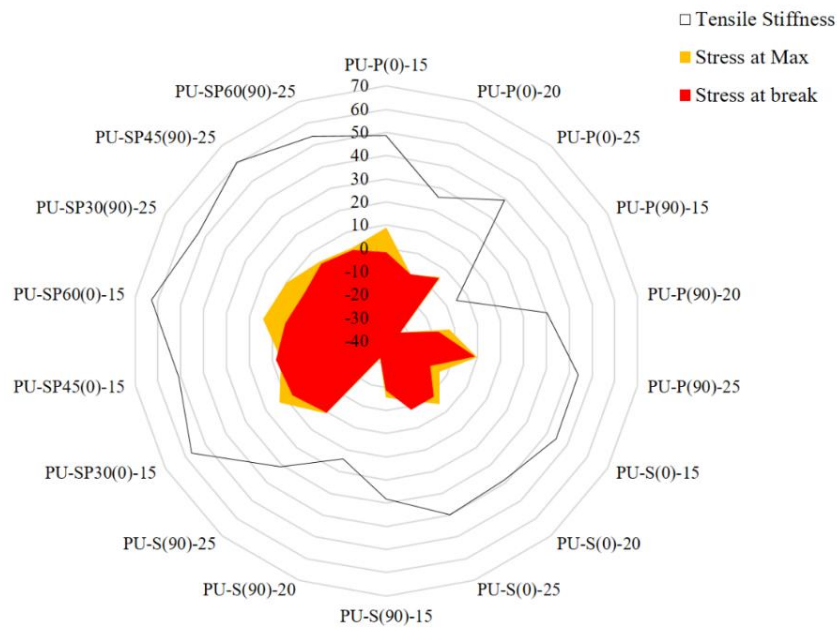
Figure 6.13. Calculated improvement factors on tensile stiffness, stress at max and stress at break of all WSPCs compared to the PN reference. For sample designation see Table 6.4.

6.3.2. Tensile properties of NW-composites

Comparison of tensile behavior of WSPCs prepared by PCCM and NYRIM techniques are illustrated in Figure 6.14. The stress-strain graphs of PN, NN and PU-P(0)-15 samples are presented as references to observe the influence of applying in-mold polymerization on tensile properties of WSPCs. The in-mold polymerization of ECL in the presentation of NW-composites caused an in-crease in the ductility and tensile strength of the neat matrix (NN) compared to the PN sample produced from compression molded MPs. Figure 6.14 also shows that the NW-composites, similarly to NK-composites showed significant feeble tensile properties compare to their matrix component (NN) and PW-composites. The reason is related with the existence PA6 oligomers produced during the NYRIM processing. This elevated oligomer levels should be attributed to impediments in the matrix-forming AA-ROP that takes place in the presence of PA6 textiles, in which the filament finishing had not been removed completely by the acetone washing.
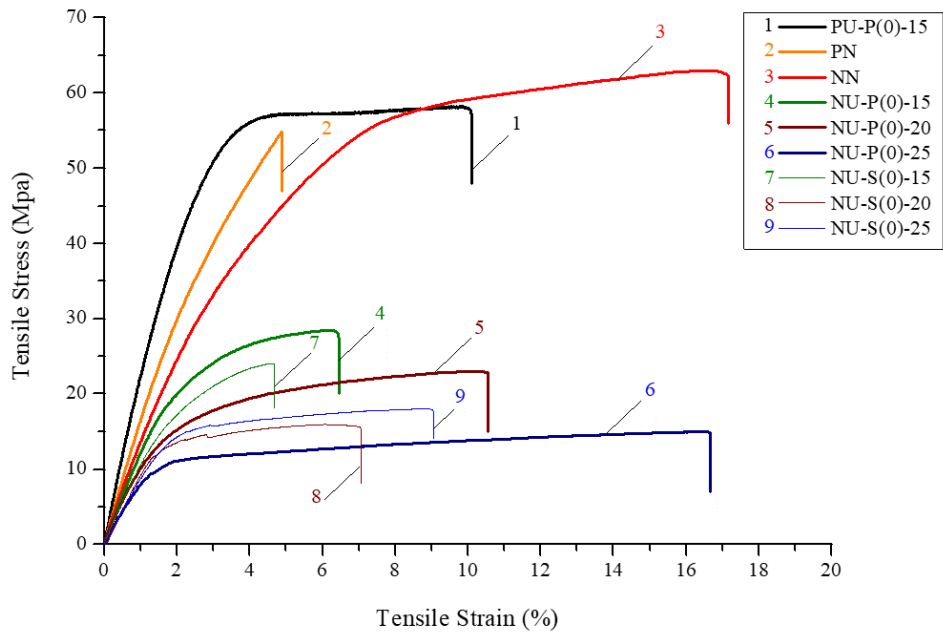
Figure 6.14. Comparative study on stress–strain characteristics for NW-composites influenced by reinforcement architectures and fiber volume fraction. For sample designation see Table 6.4.

The tensile properties data sheet of NW-composites is presented in Table 6.7. Applying NYRIM technique didn't cause the necking effect due to the identical max and failure stress values. Thus, comparing the Table 6.5 and Table 6.7 evidenced that the in-mold polymerization of ECL in presence of woven textile reinforcements was not an appropriate method to produce WSPCs. It should be noticed that all WSPCs designations in the following sections refer to PW-composites only.

Table 6.7. Data about the tensile properties of NW-composites. For sample designation see Table 6.4.

Specimens	Young´s modulus E, (Gpa)	Tensile stress at max σ_{max}, (MPa)	Tensile stress at break σ_{br}, (MPa)	Tensile strain at break ε_{br}, (%)
PN	1.73 ± 0.02	56.71 ± 1.77	56.71 ± 1.77	5.19 ± 0.11
NN	1.38 ± 0.05	67.82 ± 0.96	66.44 ± 1.08	12.65 ± 0.54
NU-P(0)-15	1.28 ± 0.07	27.00 ± 1.42	26.18 ± 1.05	7.82 ± 0.99
NU-P(0)-20	1.21 ± 0.01	23.40 ± 0.37	23.01 ± 0.22	11.02 ± 0.03
NU-P(0)-25	0.94 ± 0.03	14.37 ± 0.58	15.90 ± 1.02	16.17 ± 0.71
NU-S(0)-15	1.25 ± 0.07	22.91 ± 1.02	22.46 ± 1.28	5.06 ± 0.12
NU-S(0)-20	1.06 ± 0.01	21.08 ± 0.21	14.63 ± 0.93	7.77 ± 0.22
NU-S(0)-25	0.97 ± 0.05	19.21 ± 1.17	18.71 ± 0.99	8.73 ± 0.81

To evaluate the influence of tensile properties of woven reinforcements for WSPCs, Figure 6.15 displays stress-strain curves of wale-wise plain and stitched plain reinforced WSPCs with 15% fiber content and their precursors. Woven reinforcements demonstrated significantly lower tensile properties in

comparison with the matrix component. It is believed that the weak tensile behavior of the woven reinforcements cannot explain the improvement of tensile properties in WSPCs compared to the PN matrix component.
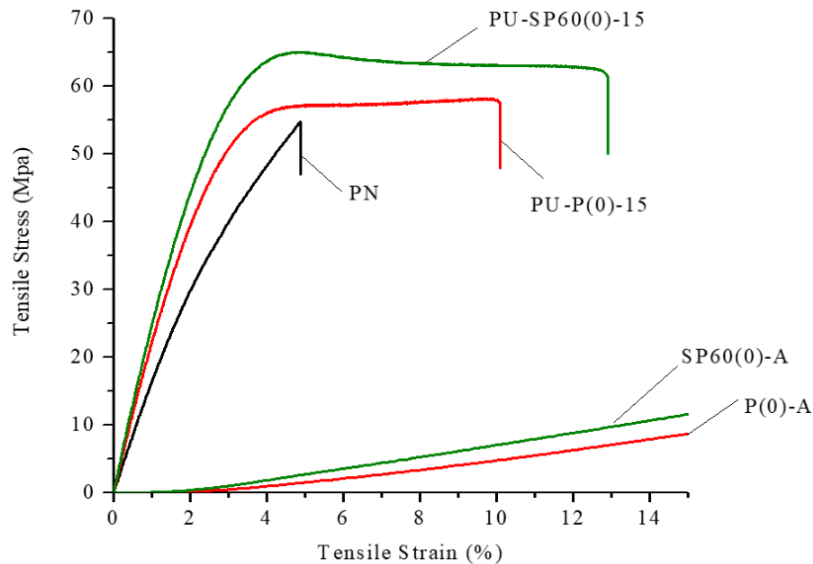
Figure 6.15. Comparison on stress-strain graph of PU-P(0)-15, PU-SP60(0)-15 and their components.

6.3.3. Flexural properties of WSPCs

Flexural strength and stiffness are not rudimentary material properties and are a combination of a material's basic tensile, compressive and shear properties. When a flexural loading is applied to a specimen, all three of the material's basic stress states are induced. Therefore, material failure, is dictated by which of the three basic stresses is the first to approach to its strength. Despite the obvious complexities implied in the above, flexural testing is common. The data analysis of flexural properties of all WSPCs influenced by their reinforcements´ architecture, fiber volume fraction, test direction and SDF gradient are shown in Table 6.8.

All WSPCs showed weaker flexural properties than their matrix component. Neither reinforcement architectures nor fiber volume fraction increment had modification on bending properties of WSPCs. Furthermore, stitched plain reinforcements didn't improve the flexural properties of WSPCs compare with those reinforced with plain structures. Only, replacing stitched plain with 30° gradient by plain structures could modify the flexural strength of plain reinforced WSPCs by ca. 24% $\text{IF}(\%)_{\text{PU}-\text{P}(0)-15}$ and 34% $\text{IF}(\%)_{\text{PU}-\text{P}(90)-25}$.

Table 6.8. Data analysis of flexural properties of unidirectional WSPCs respect to the reinforcement's architecture, fiber volume fraction, SDF gradient and test direction. For sample designation see Table 6.4.

Speciments	Flexural Modulus (Gpa)	IF_{PN} (%)	Flexural Strength (Mpa)	IF_{PN} (%)
PN	2.32 ± 0.02	-	91.68 ± 4.54	-
P(0)P-15	2.44 ± 0.01	5.08	83.79 ± 3.59	-8.61
P(0)P-20	1.44 ± 0.01	-37.98	60.05 ± 2.28	-34.50
P(0)P-25	1.99 ± 0.02	-14.21	81.54 ± 1.74	-11.06
P(90)P-15	1.62 ± 0.01	-30.34	63.94 ± 2.36	-30.26
P(90)P-20	1.74 ± 0.01	-25.15	69.42 ± 1.50	-24.28
P(90)P-25	1.77 ± 0.01	-23.80	71.36 ± 1.57	-22.16
P(0)S-15	1.77 ± 0.03	-24.05	70.21 ± 4.30	-23.42
P(0)S-20	1.87 ± 0.03	-19.39	71.52 ± 2.95	-21.99
P(0)S-25	1.89 ± 0.04	-18.50	84.38 ± 2.66	-7.96
P(90)S-15	1.54 ± 0.02	-33.62	59.91 ± 2.80	-34.66
P(90)S-20	0.73 ± 0.01	-68.80	27.55 ± 1.30	-69.95
P(90)S-25	1.74 ± 0.02	-25.08	70.63 ± 0.98	-22.96
P(0)SP30-15	2.53 ± 0.05	9.02	103.41 ± 2.14	12.80
P(0)SP45-15	2.04 ± 0.03	-12.01	83.92 ± 2.50	-8.47
P(0)SP60-15	2.52 ± 0.02	8.31	98.08 ± 4.44	6.98
P(90)SP30-25	1.99 ± 0.04	-14.18	85.56 ± 3.58	-6.68
P(90)SP45-25	1.31 ± 0.02	-43.60	52.94 ± 1.66	-42.25
P(90)SP60-25	1.98 ± 0.07	-14.94	82.80 ± 2.55	-9.69

6.3.4. Impact properties of WSPCs

The relation between impact resistance (I_s) of WSPCs with the reinforcements architecture, test direction, fiber volume fraction and SDF gradient is presented in Figure 6.16a-b. In general, embedding the woven reinforcements elevated the impact strength to ca. $IF(\%)_{PN} = 50\%$ for PU-P(0)-15 sample. Unlike PU-P(90) samples, all WSPCs showed alternative impact behavior respect to the fiber content increment (Figure 6.16a). Once more, WSPCs with 20% fiber content displayed more anisotropic behavior due to high discrepancies between their I_s values. Increasing fiber volume fraction had no significant effect on impact resistance of P-A and S-A reinforced WSPCs.

Embedding plain reinforcements with low fiber content caused better impact properties in comparison with the satin reinforced WSPCs. Figure 6.16b shows that applying the stitched plain structures with complementary angles didn't change the impact strength of composites compared to the plain reinforced WSPCs. However, PU-SP45-15 samples demonstrated significant impact strength improvement ca., $IF(\%)_{PN}$=118% and $IF(\%)_{PU-P(0)-15}$= 41%. Moreover, the I_s value of SP45 reinforced WSPCs in warp (0°) direction was improved by ca. 101% to those reinforced by weft-wise SP45 structures.
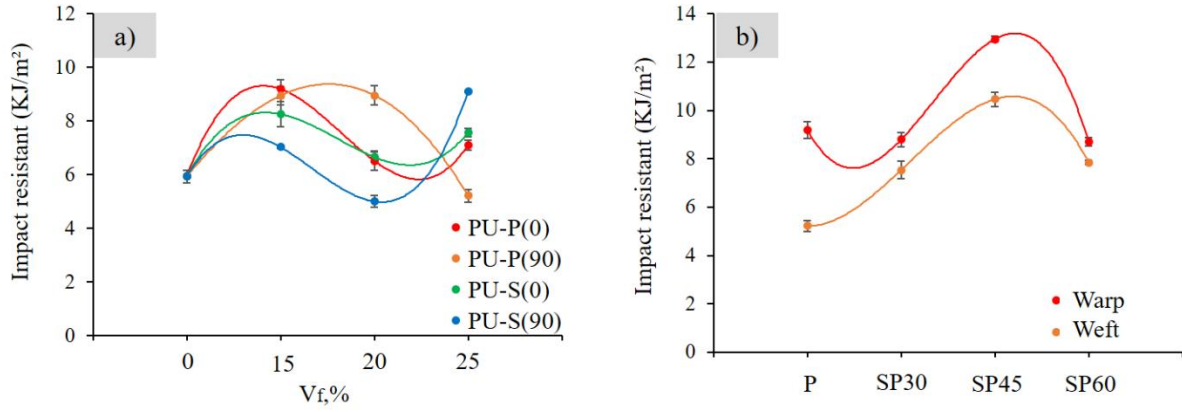
Figure 6.16. Comparison on planar Izod Impact resistant of a) Unidirectional Plain and Satin reinforced WSPCs b) Unidirectional Stitched plain reinforced WSPCs with influences of reinforcements architecture, fiber content, test orientation and SDFs gradient. For sample designation see Table 6.4.

6.4. Discussion

6.4.1. Tensile failure mechanism in WSPCs

A woven fabric is assembled with two systems of filaments perpendicularly interlaced with each other in a two-dimensional format. Hence the interactions between the two filaments and filament strength are taken into account in fabric strength. By neglecting the interactions between filaments in the woven reinforcement, the tensile strength of system considers as filaments systems in all directions. The filament-filament shear traction is known as a remarkable factor in the final tensile strength of WSPCs. Shear force was a certain force required to pull a yarn out of the fabric by overcoming the resistances between the filament contact points.

The shear traction (τ_f) which resisted any attempt of relative yarn movement at the contact area was a sum of pressure-related frictional force (τ_{f1}) and pressure-independent adhesive force termed (τ_{f2}). The pressure is generated while tensile load is exerted uniaxially or biaxially causing a tightening effect to the fabric at the interlacing area. The interactions at the interlacing points between warp and weft filaments remarkably changed the filament behavior from its ex-situ state [23]. Figure 6.17 shows the external stresses at a differential portion d_x presented by the following equations [243,244].

$$\frac{L_f}{2}\tau_f n_f d_x = d\sigma_y \tag{6-3}$$

$$L_f = 1.51\pi(b_f + a_f) - \sqrt{a_f b_f} \tag{6-4}$$

Where, $\frac{L_f}{2}$ is the actual contact length between filaments for one contact point, τ_f is the shear resistance, and n_f is the number of filaments per fabric length (Fabric Count), a_f and b_f are the long and short axes of the filament cross section respectively.
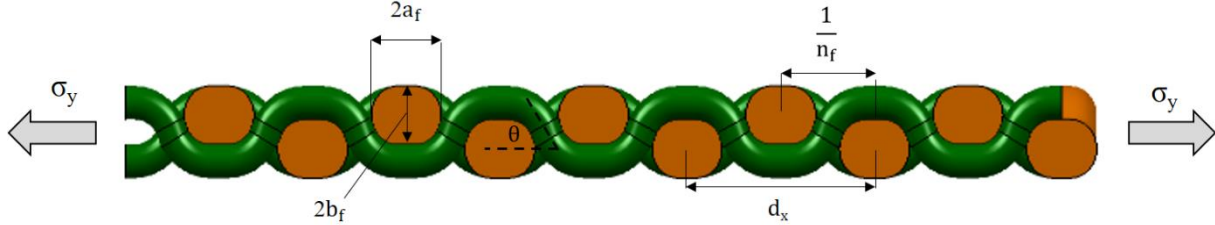
Figure 6.17. Applied stresses in situ tensile breaking load of the filament

The warp and weft filaments behave in mutual restraints that reacts as a series of sub-bundle systems made of links of length. The filament critical length is given into the equation (6-3) because of an increasing in-situ tensile breaking load of the filament (σ_y).

$$\begin{cases} \frac{L_f}{2}\tau_f n_f l_c = \sigma_y \\ l_c = \frac{2}{L_f n_f} \frac{\sigma_y}{\tau_f} \end{cases} \tag{6-5}$$

where, L_f is the circumference of the yarn cross section. The weaved original filaments in woven fabric structure are treated as a chain of statistically independent yarn segments of length l_c in which the filaments strength, size and interface interaction are its major parameters. By applying biaxial external tensions including σ_0 (warp direction) and σ_{90} (weft direction) the external tensions create a pressure P at an interlacing area with circumference L_f (Figure 6.18). This force created frictional force μP where μ is frictional coefficient of filaments and is in equilibrium with shear stress τ_{f1}. According to the ASTM D3108, frictional coefficient (μ) of PA6 filaments measured was 0,27.

$$\begin{cases} \tau_{f1}\frac{L_f}{2} = \mu P \\ \tau_{f1} = \frac{2\mu P}{L_f} \end{cases} \tag{6-6}$$

As it can be seen in Figure 6.18, P is the product of biaxial stresses. θ_0 and θ_{90} are interlacing angles at the longitudinal and transversal directions, respectively.

$$P = (2\sigma_0 \sin\theta_0 + 2\sigma_{90} \sin\theta_{90}) \tag{6-7}$$

$$\theta = \arctan\left(\frac{2b_f}{\frac{1}{2n_f}}\right) = \arctan(4b_f n_f) \tag{6-8}$$
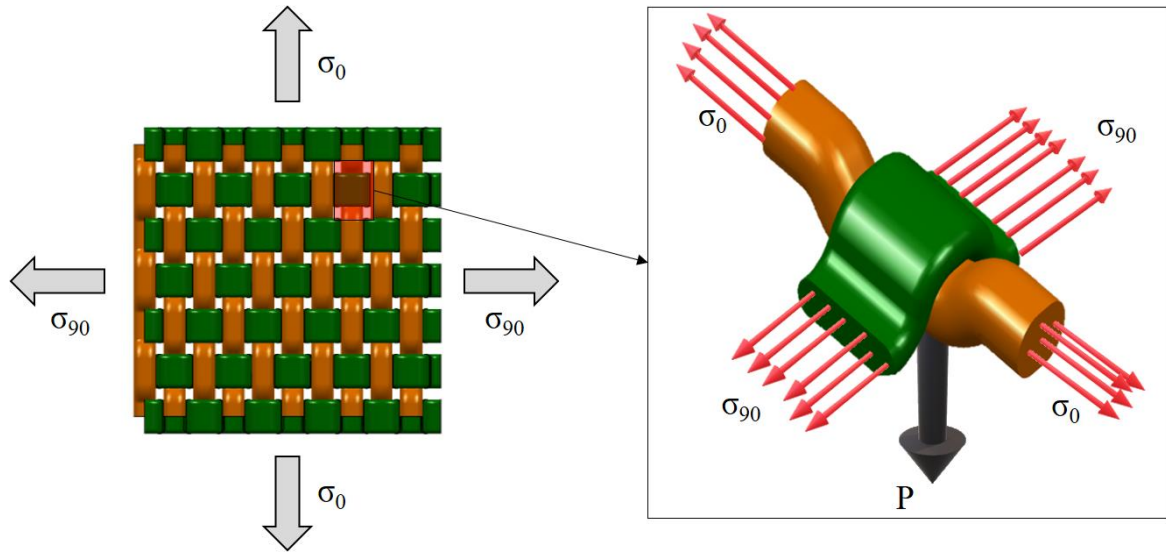
Figure 6.18. Various forces on a plain weave reinforcement a) Biaxial loading on the reinforcement; b) Tensile stress at interlacing point

Increasing of σ_0 declines θ_0 and a similar correlation exist between σ_{90} and θ_{90}. Meanwhile, a proportional relationship supported an identical geometry in both directions of the woven reinforcements.

$$\frac{\sigma_0}{\sigma_{90}} = \frac{\sin\theta_{90}}{\sin\theta_0} \tag{6-9}$$

$$\begin{cases} P = 4\sigma_{90}\sin\theta_{90} \\ \qquad\text{or} \\ P = 4\sigma_0\sin\theta_0 \end{cases} \tag{6-10}$$

Merging equations (6-6), (6-8) and (6-10) yielded the first shear resistance component as

$$\tau_{f1} = \frac{8\mu}{L_f}\sigma_{90}\sin\left[\arctan(4b_f n_f)\right] \tag{6-11}$$

As mentioned above the shear stress was divided into two components in which the second τ_{f2} resulted from pulling out of filaments from fabric structure [245]. The maximum adhesive surface force P_m at one contact point is derived as.

$$P_m = \frac{2\tau_s a_f}{\rho}\tanh(2\rho a_f) \tag{6-12}$$

where τ_s is the elastic shear strength of the contact area. The geometrical and mechanical properties of the filament are presented by ρ.

$$\rho = \frac{1}{b_f} \sqrt{\frac{G_f}{\pi E_f}} \tag{6-13}$$

where $\frac{G_f}{E_f}$, is the ratio of the longitudinal shear modulus and tensile modulus of the filament. Likewise, the maximum adhesive surface force equilibrated by τ_{f2}.

$$\tau_{f2} \frac{L_f}{2} = P_m \tag{6-14}$$

$$\tau_{f2} = \frac{4\tau_s a_f b_f}{L_f \sqrt{\frac{G_f}{\pi E_f}}} \tanh\left(\frac{2a_f}{b_f} \sqrt{\frac{G_f}{\pi E_f}}\right) \tag{6-15}$$

The second derived component of shear stress is independent of the loading situation and directions, filament mechanical properties $\frac{G_f}{E_f}$ and geometrical property $\frac{a_f}{b_f}$.

$$\tau_f = \tau_{f1} + \tau_{f2} = \frac{8\mu\sqrt{\frac{G_f}{\pi E_f}}\sigma_{90} \sin\left[\arctan(4b_f n_f)\right] + 4\tau_s a_f b_f \tanh\left(\frac{2a_f}{b_f} \sqrt{\frac{G_f}{\pi E_f}}\right)}{L_f \sqrt{\frac{G_f}{\pi E_f}}} \tag{6-16}$$

Because of extremely low magnitudes for τ_s, the effect of τ_{f2} component was neglected. In general, the influence of frictional component is more dominant than the adhesive surface force ($\tau_{f2} = 0$) when external load exists.

$$\tau_f \approx \tau_{f1} \tag{6-17}$$

In conclusion, the shear stress τ_f (shear bonding strength of the filament-filament at interlacing area) is related to external tensile stresses and filament surface frictional properties. Regarding the Eq.(6-11), there is a linear correlation between external tensile stresses with pressure-related frictional stress τ_{f1}. Therefore, a higher ellipticity (flatter yarn) of the yarn cross-sectional area ($\frac{a_f}{b_f}$) leads to a lower shear stress (τ_{f1}). When the filament count (tex) and fiber volume fraction V_f are high, more monofilaments exist in air extruded filament causing higher τ_{f1}.

The relation between the critical length upon the original filament (fabric) length, $\frac{L_c}{L_o}$ displays filaments interactions in both directions during tensile strain. When $\frac{L_c}{L_o} < 1$, the mean fabric strength per yarn is greater than the mean filament strength. While $\frac{L_c}{L_o} = 1$, the minimum value of tensile stress is obtained resulting in a stronger fabric. However, the nature of filament-filament interaction is correlated with various weave architectures. In what regards the idealized illustration of Satin (5 harness) reinforcement structures, the compression force per yarn-yarn contact point can be upgraded by [244].

$$P = \frac{12}{5}\,\sigma_0 \sin \theta_0 = \frac{12}{5}\,\sigma_{90} \sin \theta_{90} \tag{6-18}$$

$$\tau_{f1} = \frac{24\mu}{5L_f}\sigma_{90} \sin \left[\arctan(4b_f n_f)\right] \tag{6-19}$$

An $\frac{L_c}{L_o} = 1$ yields to a stronger reinforcement. Thus, by applying the same matrix component, the tensile properties of WSPCs are associated with the ratio of $\frac{L_c}{L_o}$ and with the combination of equations (6-4), (6-8) and (6-10) a rational correlation is set between l_c and reinforcement geometrical parameters.

$$\begin{cases} l_{c-Plain} = \dfrac{0.25}{n_f\mu \sin\left[arctan(4b_f n_f)\right]} \\ l_{c-Satin} = \dfrac{0.42}{n_f\mu \sin\left[arctan(4b_f n_f)\right]} \end{cases} \tag{6-20}$$

To obtain the value of l_c, an image analyzing technique was employed to measure the geometrical parameters of the reinforcements presented in equation (6-20). Ten digitalized microscopic images captured from the top surface of annealed reinforcements, using Leica Application Suite 4.4 software.

The ratio of $\frac{L_c}{L_o}$ for annealed plain reinforcements in warp and weft direction was 0.95 and 0.80 respectively. Moreover, warp and weft wise $\frac{L_c}{L_o}$ in annealed Satin reinforcements yield 0.97 and 0.90 correspondingly. Therefore, all annealed woven reinforcements in this study had higher $\frac{L_c}{L_o}$ ratio in warp than weft direction causing higher tensile properties in that orientation. The higher $\frac{L_c}{L_o}$ ratio resulted from filament´s lower crimp ratio (straight configuration) in the reinforcement structure. Thus, treated stain reinforcements have straight geometrical configuration or higher $\frac{L_c}{L_o}$ ratio in either direction, which is attributed to the better tensile properties of stain reinforced WSPCs.

A structural analysis of the woven reinforcements was performed to be linked with the mechanical properties of WSPCs. Figure 6.19a-d shows representative cross sectional SEM fractographic from tensile failure of PU-P(0)-15, PU-P(90)-25, PU-SP30(0)-15 and PU-SP30(90)-25. The tensile failure configuration demonstrates filament breakage, delamination and longitudinal splitting. There is no transversal crack detected and the tensile failure formed near crimp regions (interlacing points). The filament longitudinal splitting was merely observed in the two principal directions of all WSPCs (Figure 6.19a-d).

The splits only presented superficially at the tensile breakage surface through thickness. Transversal strain resulted from mismatch in the Poisson's ratio of warp and weft filaments in embedded woven structure which is caused by longitudinal splitting tensile failure [246,247]. The distance between two adjacent crimps, the length of the undulating region (crimp length), the filament width at the crimp region and filament thickness were identified as key parameters to characterize their fracture mechanism.
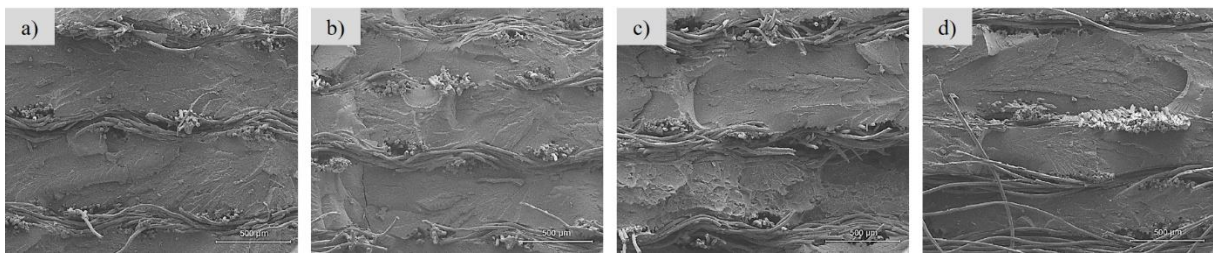
Figure 6.19. SEM fractography of tensile fractured surface of a) PU-P(0)-15; b) PU-P(90)-25; c) PU-SP30(0)-15 and d) PU-SP(90)-25

To connect the reinforcement-matrix bonding condition to the final tensile properties of WSPCs, all SEM images, shown in Figure 6.19a-d were imported to MATLAB software as a greyscale image. The matrix data of images comprising X and Y pixels and Z level were extracted. Image matrices contained numbered columns and rows which were mapped to linearly spaced X and Y values respectively. Each cell value in a matrix of SEM image represented a Z (gray level) that is in the XY plane by the cell's X and Y pixels. Therefore, higher indentation in a surface plot evidenced that the composites were broken at alternative levels and represented higher tensile strength of monofilaments at the plane of stress. As it can be seen in Figure 6.20a-d, weft-oriented WSPCs showed flatter surface plots compared to the warp-oriented ones. Appearing scattered high intensity Z values (gray level) in particular points in surface plot of PU-P(90)-25 and PU-SP30(90)-25 are resembled by tensile stress concentrations at those points.
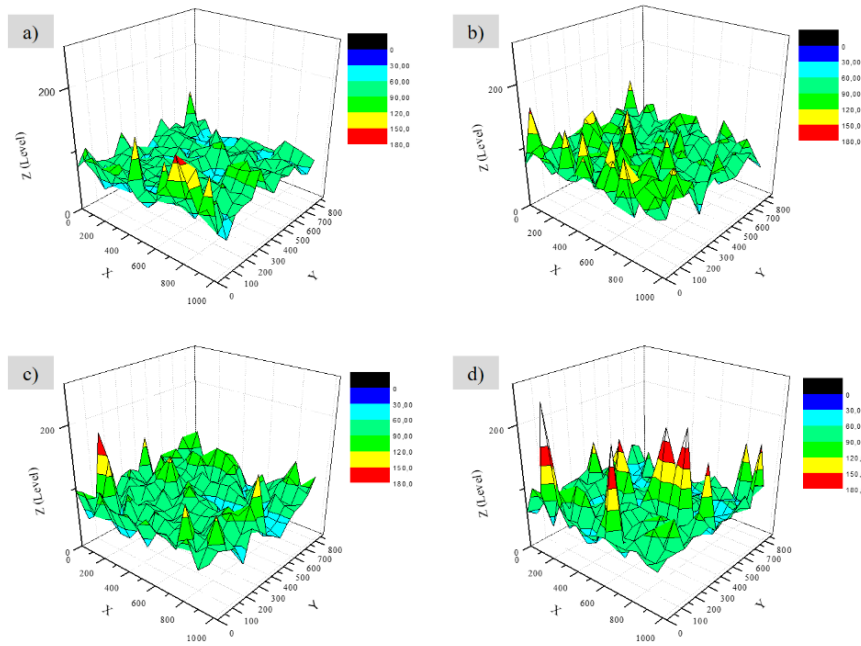
Figure 6.20. Color map surface of SEM tensile fractured surface of a) PU-P(0)-15; b) PU-P(90)-25; c) PU-SP30(0)-15 and d) PU-SP(90)-25

To have a better observation of evenness of surface fractography in WSPCs, the top surface contour plots of Figure 6.20a-d are presented in Figure 6.21a-d. The higher intensity Z level in PU-P(90)-25 sample is correlated with the existence of higher stress concentration which is attributed to the feeble tensile properties of this class of WSPCs.
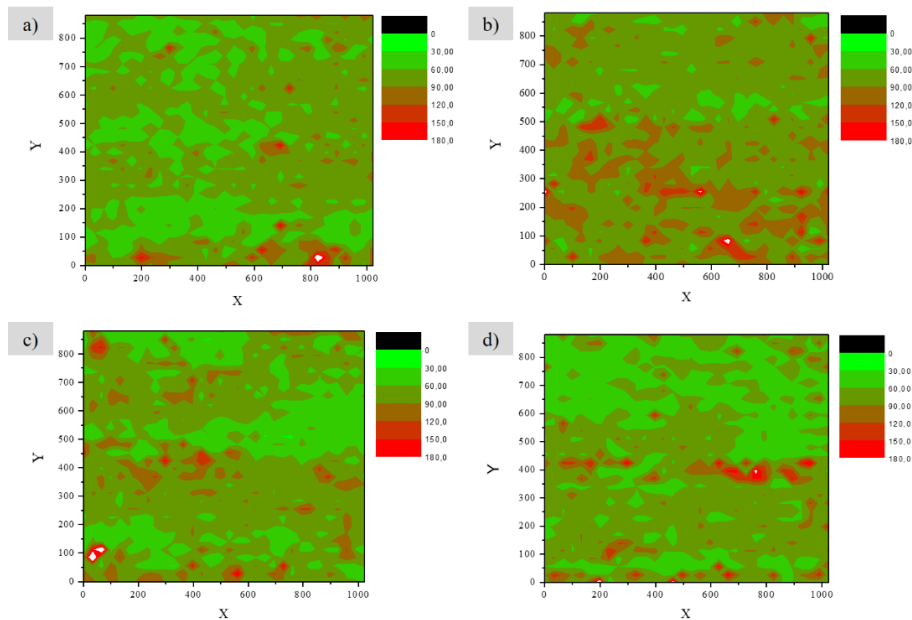
Figure 6.21. Contour plot from top surface of fractography plot shown in Figure 6.21; a) PU-P(0)-15; b) PU-P(90)-25; c) PU-SP30(0)-15 and d) PU-SP(90)-25

To reach a logical statement and analyze the tensile stresses distribution at the plane of stress, color segmentation of contour plots shown in Figure 6.21a-d was required to distinguish each range of Z level. Image segmentation was applied to divide each contour plot (Figure 6.21) into multiple parts which was targeted to measure the area of each Z value ranges. Figure 6.22 depicts the color segmentation of representative contour plots into Z levels of 0-60, 60-90, 90-120 and 120-150 via MATLAB software. Afterwards image enhancement techniques were utilized to improve the distanced object edges with morphological operations on MATLAB binary images.
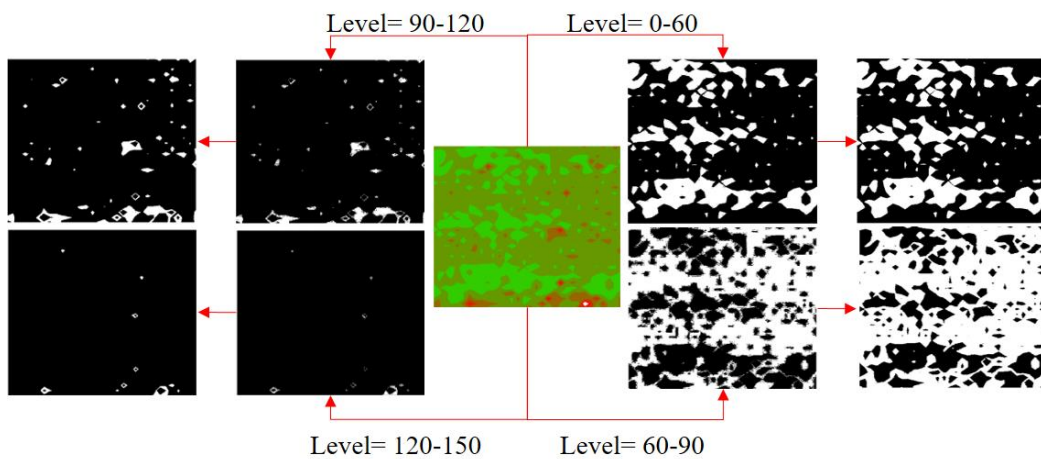
Figure 6.22. Image segmentation followed by image enhancement techniques, applied to distinguish the Z level ranges in contour plot of representative PU-P(0)-15;

As it can be seen in Figure 6.23, all measured areas of Z levels in different ranges were plotted to explain the mechanical properties of WSPCs better. All WSPCs presented the highest Z value in the range between 60-90 and the lowest in the range of 120-150. The sample PU-P(90)-25 showed the highest and lowest Z value in the ranges 90-120 and 0-60 respectively.
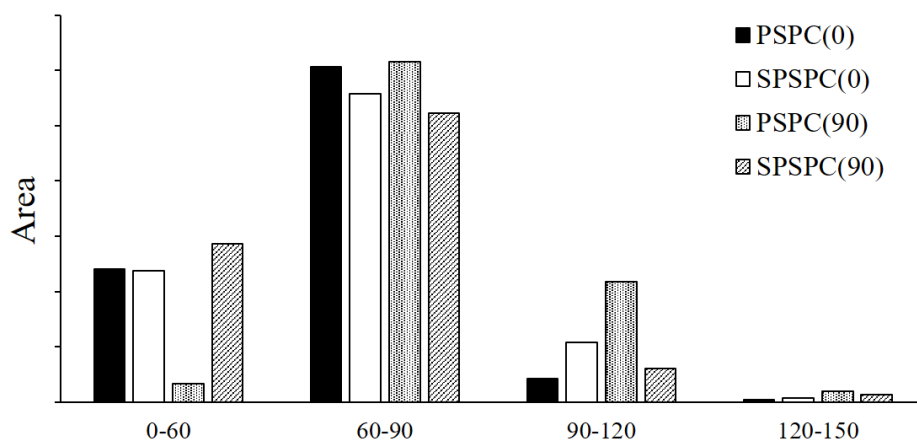
Figure 6.23. Comparing the Z level ranges of all stitched reinforced WSPCs;

169

The schematics of reinforcements, laminated WSPCs and composites´ cross-section in the two principal directions are illustrated in Figure 6.24a-c, to present better description of the relation between area of Z levels (Figure 6.23), and tensile properties of WSPCs. The distribution of stresses arises in arbitrary direction at the fractured surface of WSPCs and can be decomposed into the sum of a normal stress (σ_n) and a shear stress (σ_s) distribution (Figure 6.24d).

In an elastic state, the external and internal normal and shear stresses are identical. Moreover, the tangential stresses take on any value and the element will still be in equilibrium with the applied stresses. After the yield point this equilibrium becomes distorted. Consequently, the aspect ratio of filaments influences shear distribution during tensile test. As Figure 6.24d shows, weft filament has higher aspect ratio than warps. Thus, while the tensile stresses are applying in warp direction the shear stress is implied on weft filaments at the plane of stress. Due to the higher aspect ratio in weft filaments, the shear stresses are distributed evenly along the fractured surface. Otherwise, in the case of weft oriented WSPCs, the shear stresses are applied in warp filaments with lower aspect ratio causing an increase of stress concentration on the plane of stress (see Figure 6.21).
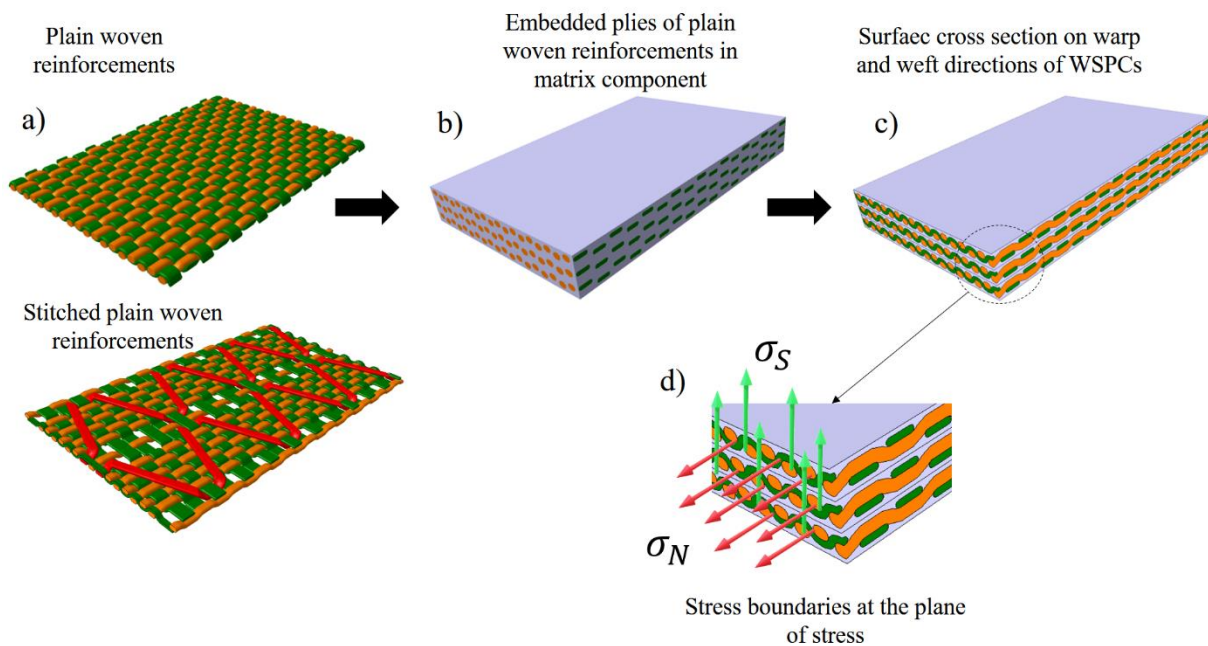
Figure 6.24. a) Plain and Stitched plain woven reinforcements; b) a representative schematic of SPC reinforced by plain textile structure; c) Plane surface cut of in biaxial directions d) Stress boundary conditions comprising projection of implied tensile stresses into the resulting normal and shear stress distributions.

The image analysis procedure was used to measure the aspect ratio of embedded filaments and prove their influence on the shear (tangential) stress distribution on warp and weft direction at the plane of

stress. At the beginning, superficial microscopic images were captured from two main WSPCs cross-section and then image analyzed with Leica Application Suite 4.4. Figure 6.25 presents the measurement of the major and minor axis of warp and weft monofilament´s bundles in which the appendixes 1 and 2 are designated as warp and weft directions respectively. Aspect ratio of filaments in the two directions were calculated by $\frac{b_i}{a_i}$, i=1, 2.
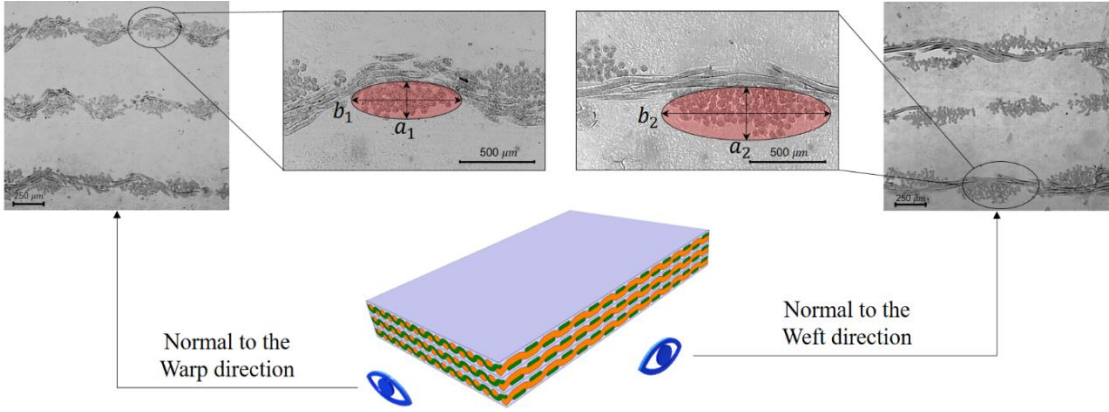
Figure 6.25. Microscopic image capturing of composite cross-section and measuring the embedded filaments on two principal directions

Figure 6.26 shows the calculated aspect ratio of warp and weft filaments in embedded plain and stitched plain woven reinforcements. All embedded filaments showed higher aspect ratio in weft direction which is in good agreement with the better tensile properties in warp direction of WSPCs (Figure 6.25). The embedded filaments in stitched plain reinforced WSPCs had higher aspect ratio than those reinforced with plain structures. Thus, it can be deduced that the tangential stresses are distributed better in embedded stitched plain reinforcements due to higher aspect ratio of embedded filaments causing an increase of their tensile properties.
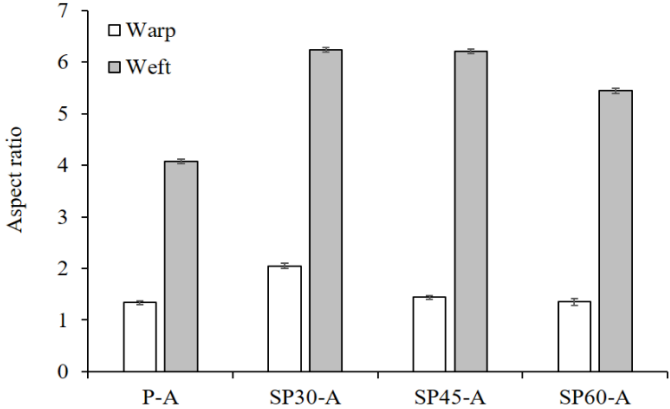
Figure 6.26. Comparison on measured aspect ratio of embedded warp and weft filaments in plain and stitched plain SPCs

To evaluate the quality of the fracture surface along the plane of stresses, the matrix data of converted binary images was generated and arranged in a virtual matrix. By obtaining the virtual matrices, cross-section profiles of contour plots, along vertical and horizontal lines were illustrated in Figure 6.27a. However, the study of vertical profile from contour plots of a binary image in WSPCs, enabled to evaluate the uniformity of the fractured surface only. For noise filtration of vertical profile from each sample´s contour plot, the Savitzky-Golay filter technique was applied by local polynomial regression around each point, and a new, smoothed value for each data point was created. By applying this method data features, such as peak height and width were preserved.
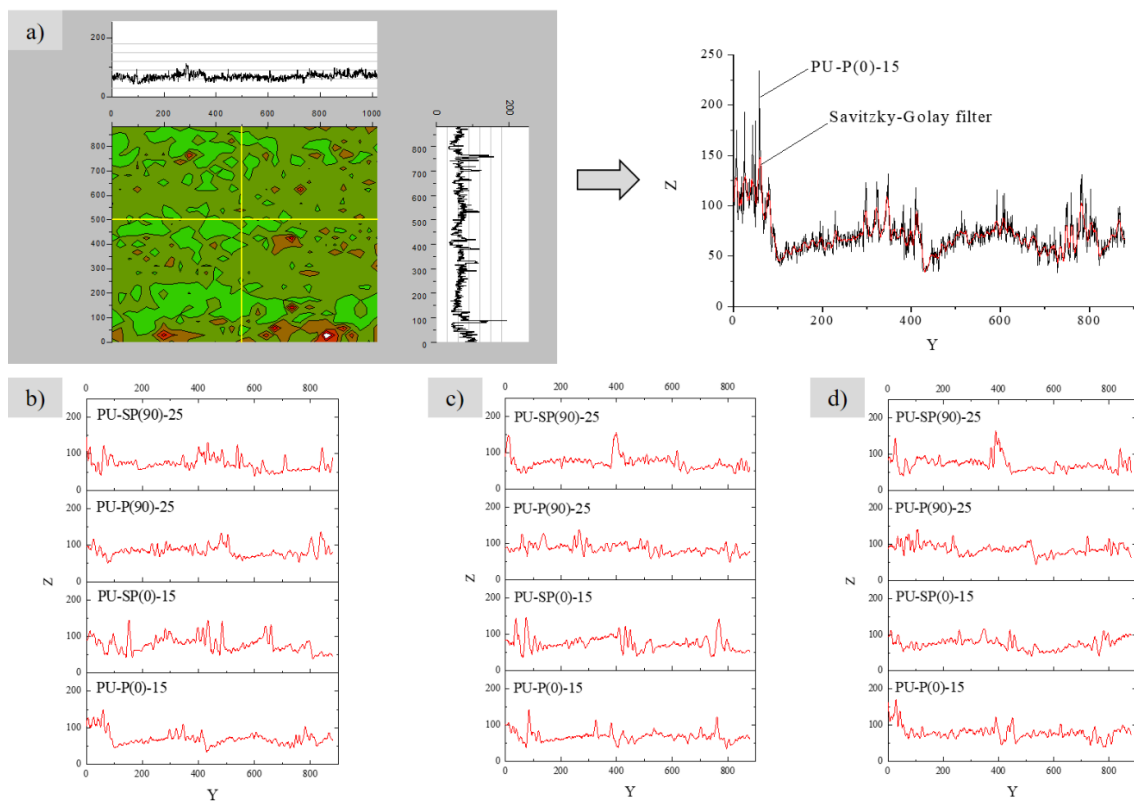
Figure 6.27. a) vertical and horizontal color map profile from contour plot of fractured surface in representative PU-P(0)-15 sample and noise omitting procedure; b) Comparing the smoothed vertical profile from contour plot of all WSPCs at selected horizontal pixels, b) 200; c) 500 and d) 800

The final smoothed vertical profile from contour plot of all WSPCs at selected horizontal pixels of 200, 500 and 800 are depicted in Figure 6.27b-d respectively. It can be deduced that samples with higher signals showed lower uniformity which explain higher tensile strength because of gliding the monofilament over each other. Otherwise, samples with lower signals evidence higher uniformity of fractured surface at the plane of stress which is followed by an abrupt breakage of monofilaments at tensile failure. As seen in Figure 6.27b-d, warp oriented WSPCs demonstrated higher signals on their vertical profile comparing

172

to the weft-oriented ones. In contrast, PU-P(90)-25 showed the lowest signals in their vertical profile resulting the sudden breakage of embedded monofilaments and in increasing the shear stresses during tensile failure. As a conclusion, the higher signal in vertical profile of warp oriented WSPCs are in good agreement with their better tensile properties.

To evaluate matrix and reinforcement bonding conditions in fractography of P-A and S-A reinforced WSPCs, the cross sectional SEM fractographic from tensile failure of PU-P(0)-15 and PU-S(0)-15 are shown in Figure 6.28a-b. All SEM images were imported to MATLAB software to convert greyscale image and extract the images matrix data such as X and Y pixels and Z level (gray level). The contour graphs of the extracted image matrix data were plotted. To analyze the tensile stresses distribution at the plane of stress, color segmentation of contour plots was carried out to distinguish the area of Z level into 0-60, 60-90, 90-120 and 120-150 (Figure 6.28). Subsequently, image enhancement techniques were applied to modify the distanced object edges with morphological operations on binary images.
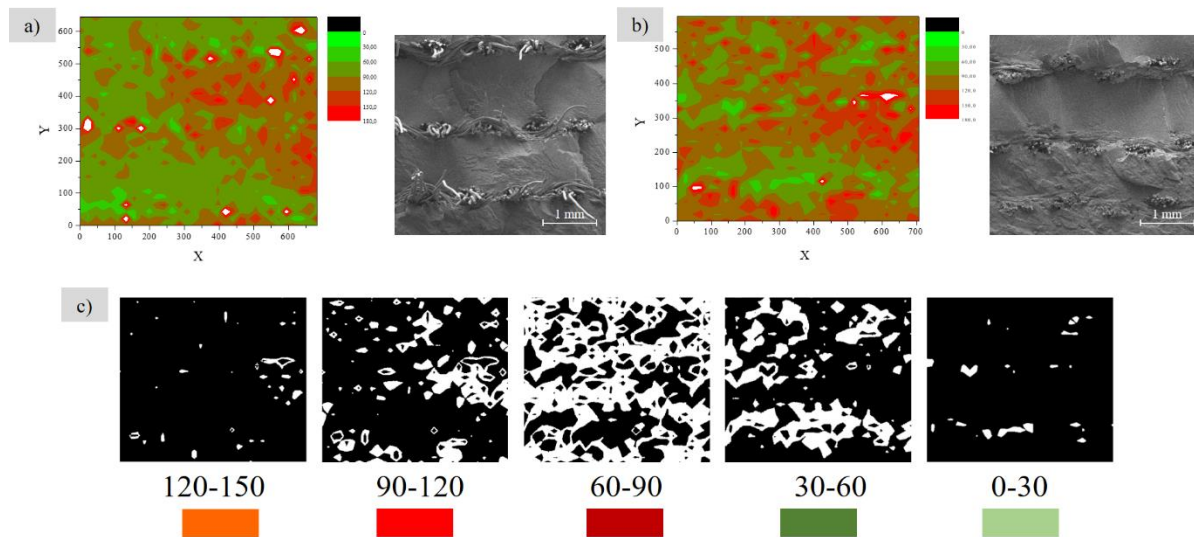
Figure 6.28. Contour plot of SEM surface fractured image of a) PU-P(0)-15 sample; b) PU-S(0)-15; c) Image segmentation followed by image enhancement techniques, applied to distinguish the Z level ranges in contour plot of WSPCs using MATLAB software

Figure 6.29 presents the measured Z levels area at determined ranges. plain and satin reinforced WSPCs showed the highest Z level in the range between 60-120 and the lowest magnitudes in the ranges 0-60 and 150-180. The sample PU-P(0)-15 showed a descending trend on their Z level magnitude while the ranges were increasing. Notwithstanding, PU-S(0)-15 sample showed a proportional distribution on its Z level. Due to this observation, it can be concluded that WSPCs reinforced with satin structures break instantaneously after the tensile failure at the plane of stress.
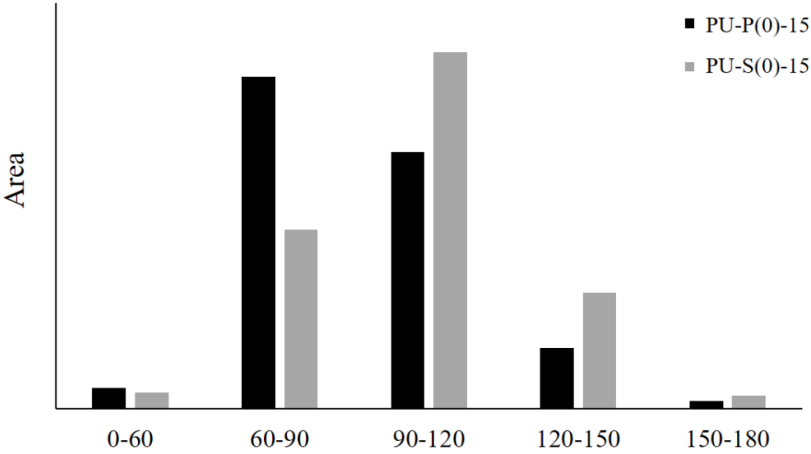
Figure 6.29. Comparison on the Z level ranges of all Plain and Satin reinforced SPCs.

Figure 6.30 illustrates the representative simulated Satin reinforcement and laminated satin reinforced WSPCs. Image analysis techniques were employed to measure the aspect ratio of embedded filaments from cross sectional microscopic images of WSPCs in the two principal directions using MATLAB software.
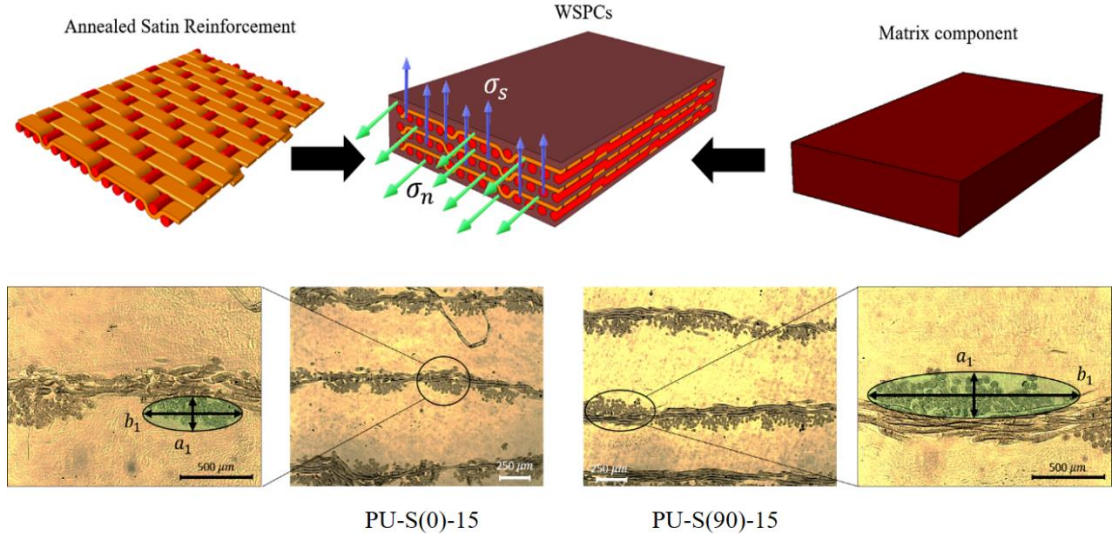
Figure 6.30. Microscopic image capturing of composite cross-section and measuring the embedded filaments in the two principal directions

The measured aspect ratio of warp and weft embedded filaments in plain and satin woven reinforcements (Figure 6.30) is presented in Figure 6.31. Satin reinforced SPCs contained higher embedded warp filament´s aspect ratio than those reinforced with plain structures. Due to this fact the WSPCs reinforced with a satin structure showed better tensile behavior in weft direction than those reinforced with plain. However, the image analysis of the cross section surface of plain reinforced WSPCs

depicted higher values for embedded weft filaments. Moreover, different fiber volume fraction brought alternation on aspect ratio of embedded filaments in the two principal directions.

It can be concluded that the tangential stresses at the plane of stress are distributed better in embedded warp wise plain reinforcements due to higher aspect ratio of embedded weft filaments. At the same time, the higher tensile properties of plain reinforced WSPCs in warp direction can be explained by this fact too.
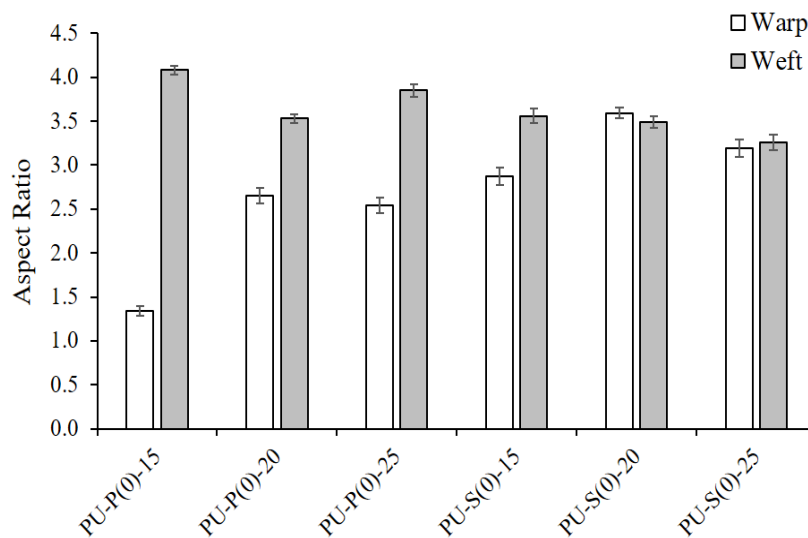
Figure 6.31. Microscopic image capturing of composite cross-section and measuring the embedded filaments on two principal directions

6.4.2. Impact failure mechanism in WSPCs

The feeble flexural properties of WSPCs may lay on outstanding discrepancies between storage and loss modulus of the annealed woven reinforcements. Due to this fact, woven structures have more energy storage than dissipation during compression loads which increase their viscoelastic behavior. The resulting strain and stress will be in a perfectly elastic solid, although, there is a 90° phase lag of strain with respect to stress in a purely viscous fluid. Therefore, the viscoelastic behavior of stretched-annealed reinforcements occurs when the stress is applied, and the strain lags behind. Meanwhile, the stress concentration increases in interlacing points due to low energy dissipation.

To better understand the impact behavior of WSPCs, scanning electron microscopy (SEM) studies were performed. Figure 6.32a-d shows SEM images of impact failure cross-sections of unidirectional plain and stitched plain WSPCs with 15% fiber content (V_f) in the two principal directions. The fractured surface of all

175

specimen demonstrates the emergence of interlace points due to the initiation of breakage from the highly-stressed points. Comparison with SEM fractography of impact fracture cross sections in WSPCs shows several alternative concavities whereas KSPCs demonstrated a stepwise fracture configuration. Therefore, it can be deduced that the impact energy is dissipated through each ply in KSPCs wherein the laminas are shattered one by one after the strike point. In the case of WSPCs the plies are not broken sequentially. This means that the plies away from the collision point are fractured prior to those that are near the strike point.
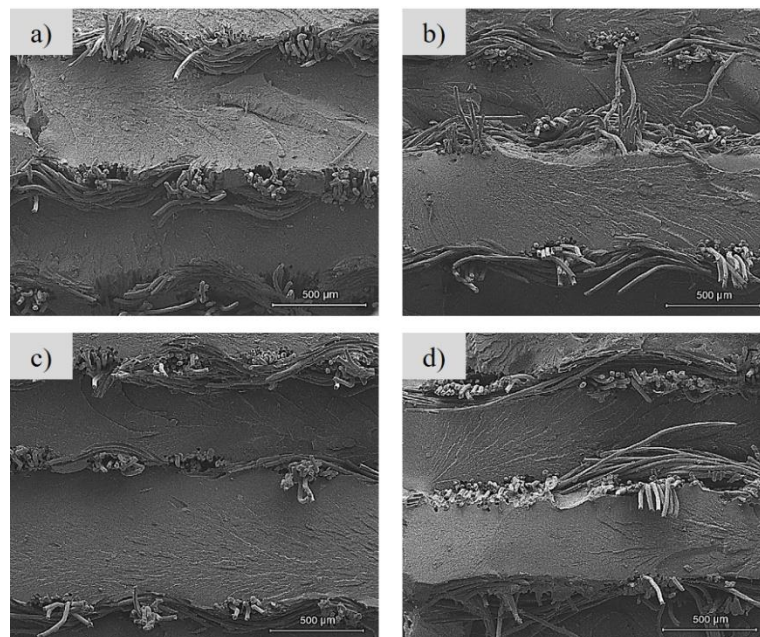
Figure 6.32. SEM fractography of impact fracture surface in a) PU-P(0)-15 b) PU-P(90)-25 c) PU-SP(0)-15 d) PU-SP(90)-25

The differences of impact fracture surface configuration of WSPCs and KSPCs can be linked with damping properties of the reinforcements on stress distribution and dissipation through the thickness of the composite bar test sample. Correspondingly, the higher tan delta value of knitted (Figure 4.9a) than woven reinforcements (Figure 6.8a) is attributed to the high reduction of damping forces in knitted structures. Due to this fact, the fractography of impact fracture surface in KSPCs followed a step wise breaks and consequently, their impact resistance is higher than WSPCs.

The effect of the position of the neutral plane and the tensile and compression stresses distribution in a composite bar test was shown in Figure 4.9a-c. Due to the application of the same matrix component with identical molding conditions, a comparative study on tensile and compression behavior of woven structures could provide a logical evidences on impact failure mechanisms of WSPCs. As Figure 6.16 demonstrated plain reinforced WSPCs featured higher impact strength than those reinforced by a satin

structure. Hence, it can be predicted that regardless the position of the neutral plane, the reason lays on the higher compression modulus of the treated plain reinforcement (Figure 6.8-b). Nevertheless, their tensile stiffness, was lower in warp direction compared to the treated satin structure (Table 6.5). As a result, at the beginning of the impact collision the top lamina dissipates the strike forces and then disperses them through subsequent plies. The impact properties of WSPCs reinforced by SP45 structure, exclusively, were higher than those reinforced by plain textile fabrics. The reason can be explained by identical complex modulus and tan delta as well as higher tensile stiffness of SP45 compared to the plain reinforcements.

6.5. Conclusions

Nylon resin injection molding (NYRIM) was applied to produce woven reinforced single polymer composites based on polyamide 6 (WSPCs) via in mold polymerization of ε-caprolactam in presence of woven reinforcements. Furthermore, WSPCs were successfully prepared by combination of powder impregnation and hot compaction techniques (PCCM). Stretching-annealing treatment of the woven textile reinforcements demonstrated considerable perfection of their mechanical properties. The influence of reinforcement architecture (plain, satin and stitched plain), fiber volume fraction (15, 20 and 25 V_f,%), reinforcement orientation (warp,0° and weft,90° directions) in the mechanical properties of WSPCs was evaluated.

The results show that embedding the woven reinforcements in WSPCs with relatively low fiber content (15%), laminated in the wale direction, brought the best improvement of tensile properties compared to the PA6 matrix component as a reference. Applying the stitched diagonal filament on plain substrates modified tensile properties of plain reinforced WSPCs up to 25%. SEM fractography and fracture surface studies of composites evidenced a link between failure mechanism and structural interlacing points in reinforcements. Using NYRIM technique lowered the tensile properties of composites than NN and PW-composites.

In general, WSPCs showed higher tensile stiffness and lower tensile strength in comparison with KSPCs. The tensile stress-strain graphs of KSPCs demonstrated a brittle behavior whereas WSPCs showed necking and ductile behavior after the yield strength. Unlike KSPCs, WSPCs did not improve the flexural properties of the matrix component although their impact resistance recovered up to 118%. The significant improvement of impact properties of plain reinforced composites was explained by the

differences between the compression and tensile properties of the reinforcements. Regardless the position of the neutral plane, higher compression properties of the treated plain reinforcement compared to satin explained the superior impact properties of plain reinforced WSPCs. Lower impact properties of WSPCs compared to KSPCs lays on differences between compression storage and loss modulus of annealed woven reinforcements when compared with knitted structures.

SEM fractography and fracture surface studies of composites evidenced a link between failure mechanism and structural interlacing points in reinforcements. Image processing was applied to further analysis of fractured surfaces of composites at tensile failure. The results showed that all warp oriented WSPCs distributed shear stresses widely along the cross section at the plane of stress due to a measured higher aspect ratio of embedded weft filaments. Moreover, higher tensile properties of stitched plan reinforced WSPCs were linked to their higher filaments aspect ratio in comparison with the embedded plain and satin reinforced composites. Microstructure analysis of WSPCs and their precursors was carried out and linked with their mechanical properties in this study.

Microstructure characterization of WSPCs

7.1.   Introduction

Processing conditions, molecular weight, and molecular weight distribution of the polymer influence the physical and mechanical properties of PA6 polymers. In recent years, considerable number of studies exist in the literature in respect to the microstructure characterization of PA6 polymers by various characterization techniques [213,215,248,249]. The microstructure properties, comprising crystallinity, chain orientation and crystalline orientation of polyamides have been investigated by several researchers [250,251].

This chapter, reports on the study about the relationship between the matrix-reinforcements crystalline structure, interfacial bonding and the mechanics of WSPCs reinforced by different woven architecture, fiber volume fraction and orientation. DSC and TGA experiences have been performed to evaluate the thermal stability of the composites. WAXS patterns were obtained for composites and their precursors to detect their crystalline fractions in relation with their mechanical properties. The biaxial stretching-annealing of all woven reinforcement up to 30% was resulted an increase of the modulus E and yield stress, and σ values were correlated with microstructure analysis at the interface region of WSPCs. The crystalline structure at the matrix/reinforcement interface was also related to structural changes in the amorphous phase and α-to-γ transition.

7.2.   Thermal analysis of WSPCs and the components

7.2.1.   Diffraction Scanning Calorimetry

Differential scanning calorimetry was used to investigate the response of composite materials to heating induction. Key parameters such as the windows processing, glass temperature transition and crystalline degree of WSPCs and components were extracted from the DSC thermograms. Figure 7.1a demonstrates the first heating scan of all woven reinforcements and MPs, performed at 10°C/min. The processing window was calculated at about 24°C which was sufficient to produce WSPCs with no risk of monofilaments fusion and degradation during hot compaction. Lower melting temperature of aniconic MPs ($T_{m-MPs,\alpha} \approx 207°C$) than reinforcements ($T_{m-R,\alpha} \approx 224°C$) could also be related with the slightly lower M_v of WSPCs. Similar to the DSC thermogram of knitted reinforcements, the broad low-temperature endothermic peaks (centered at 85°C) appeared in DSC thermogram of untreated woven reinforcements (Figure 7.1a). Appearing low-temperature endothermic peaks were attributed to the release of the

humidity absorbed by the filament´s bulkiness. Although, stress-relaxing treatment caused an increase of about 10°C of the broad peak in treated woven reinforcements. Stretching-annealing treatment of woven reinforcements caused low temperature endothermic peak in the first DSC scan that may be attributed to the melting of the γ-PA6 polymorph ($T_{mR,\gamma}$<200°C) [46,220] (Figure 7.1a). The maximum of the melting endotherms should be related to the α polymorph of PA6 ($T_{mR,\alpha}$≈223°C) because of formation of strong hydrogen bonds between antiparallel chains [213]. Figure 7.1b, shows the second DSC scan of composite precursors wherein the T_g of all samples was revealed after eliminating the thermal history. Higher segmental mobility of the polymer chains in the anionic MPs lied on lower T_g of MPs (≈33°C). Moreover, melting of some amount of anionic γ-PA6 polymorph yielded advent of a weak shoulder below 200°C.
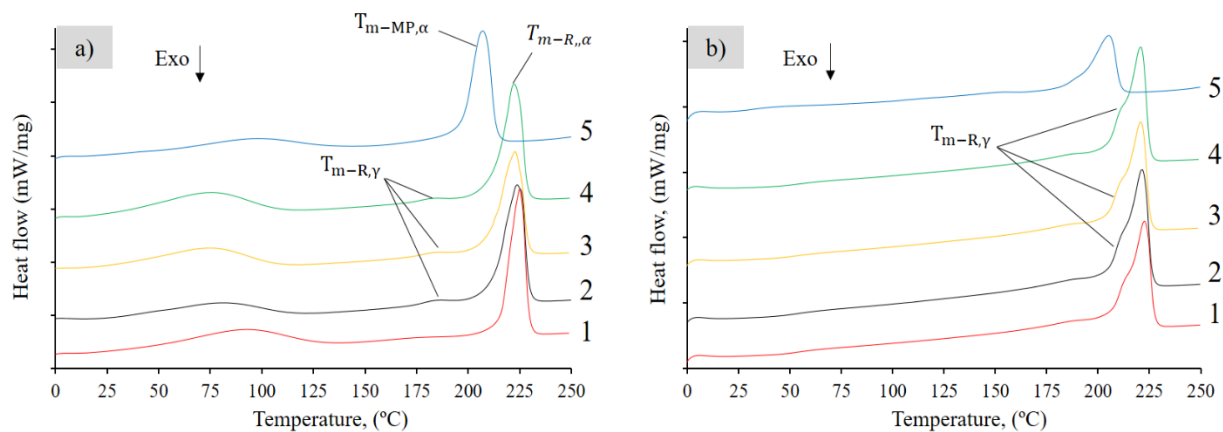
Figure 7.1. DSC thermograms of WSPCs building components: (a) 1st DSC scan; (b) 2nd DSC scan. 1- Untreated Plain reinforcement; 3- Annealed Plain reinforcement; 4- Annealed Satin reinforcement; 4- Annealed SP30 reinforcement 5- Anionic MPs. For sample designation see Table 6.4

The first and second DSC scans of unidirectional WSPCs (curve 2-4) compared to that of an anionic PA6 sample produced by compression molded MPs (curve 1) is shown in Figure 7.2a-b respectively. The first scan DSC thermogram of PN illustrated a single melting peak (T_{m-PN}=210°C) although a bimodal melting endotherm was registered for WSPCs with $T_{m-SPC,1}$= 208-210°C and $T_{m-SPC,2}$= 214-219°C (Figure 7.2a). The former can be related with melting of PA6 originating from the matrix component and the later was allocated to the hydrolytic PA6 woven reinforcements. The second DSC scan of PN and WSPCs samples show a weak shoulder prior to their melting temperature which can be linked with the existence of γ-PA6 crystalline phase (Figure 7.2b).
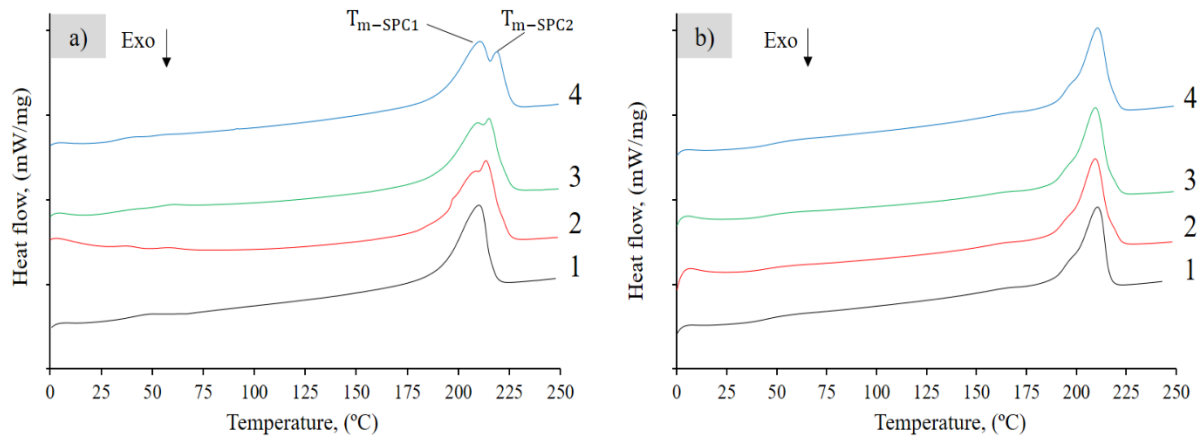
Figure 7.2. DSC curves of WSPCs from hot compacted MPs -impregnated woven textile structures: (a) 1st DSC scan; (b) 2nd DSC scan.: 1 – PN; 2 – PU-P-15; 3 –PU-S-15; 4 –PU-SP30-15. For sample designation see Table 6.4.

The crystallinity indices X_c^{DSC} of all WSPCs and their precursors are shown in Table 7.1 which were calculated according to Eq.3-8.

Table 7.1.Crystallinity index for WSPCs and their precursors

Sample designation	T_g (°C)	T_{m1} (°C)	T_{m2} (°C)	X_c^{DSC}, %
MPs	32.3*	207.8	-	34.9
PN	33.3	210	-	27.5
P & S	50.7*	-	224.9	37.2
P-A	48.1*	-	223.5	41.8
S-A	48.9*	-	222.5	38.3
SP30-A	52.4*	-	222.2	39.2
SP45-A	51.8*	-	224.8	35.7
SP60-A	50.9*	-	222.2	37.3
P-P(0)-15	32.9	208.7	213.6	33.0
P-P(0)-20	30.8	209.5	215.8	31.9
P-P(0)-25	30.3	209.8	217.3	31.0
P-S(0)-15	31	209.6	215	32.5
P-S(0)-20	30.8	209.4	217.2	30.6
P-S(0)-25	33.1	209.4	218.6	32.2
P-SP30(0)-15	34.1	210.5	219.2	30.9
P-SP45(0)-15	30.8	209.7	215.7	34.0
P-SP60(0)-15	33.5	210.7	217.7	33.4
P-SP30(0)-25	33	209.9	217	30.9
P-SP45(0)-25	33.7	211.1	217.8	33.8
P-SP60(0)-25	32.4	210.4	217.6	29.6

*T_g determined during the 2nd DSC scan

Total crystallinity of woven structure becomes slightly improved after stretching-annealing treatment although the reinforcements architecture didn't change the degree of crystallinity (X_c^{DSC}) significantly. As it can be seen in Table 7.1, all WSPCs demonstrated bimodal endothermic melting peaks, which correlate

with the melting point of matrix component in a range between 208-210°C. Similarly to KSPCs, this dual peak should be related with the melting of PA6 originating from the anionic PA6 matrix and with the hydrolytic PA6 textile reinforcements.

Fiber volume fraction and reinforcement architecture had no significant changes on glass transition temperature and degree of crystallinity in WSPCs. It should be mentioned that embedding the woven reinforcements lowered the T_g of WSPCs at the same level as PN sample and MPs showing high amorphous portion after molding procedure. Lower X_c^{DSC} value of PN than MPs could result from relatively faster cooling down during the compression molding.

7.2.2. Thermal gravimetry analysis

The thermogravimetric experiments demonstrated a clear difference between the thermochemical properties of WSPCs and precursors. Figure 7.3a-c shows the thermogravimetric analysis of P-A reinforcement, PN matrix and PU-P-15 composite. The DTM, MRD, MRDT and degradation magnitude (explained in chapter 5) were extracted from synchronized plotting of the weight loss (%), differential thermal analysis (DTA, μV) and derivative thermal gravimetry (DTG, $\frac{\mu g}{min}$) versus incremental temperature (Figure 7.3a). The DTA plots of PN matrix displayed unique peak configuration (Figure 7.3b) whereas annealed woven textile reinforcements contained double-peak form during decomposition (Figure 7.3a).

It should be noticed that the double-peak configuration in stretched-annealed knitted structure was discrete and evenly proportional (see Figure 5.11a-b), whereas it is asymmetric and attached in treated woven reinforcements. This may be explained by a different crystalline division in knitted and woven reinforcement after stretching-annealing treatment. The existence of double-peak conformation in DTA thermograph in PU-P-15 sample can explain the distinct behavior of WSPCs precursors at interface region which forms crosslinking of hydrolytic with anionic PA6 polymorph (Figure 7.3c). Due to this fact, appearing interphase layer with different properties than matrix and reinforcement component can be predicted.
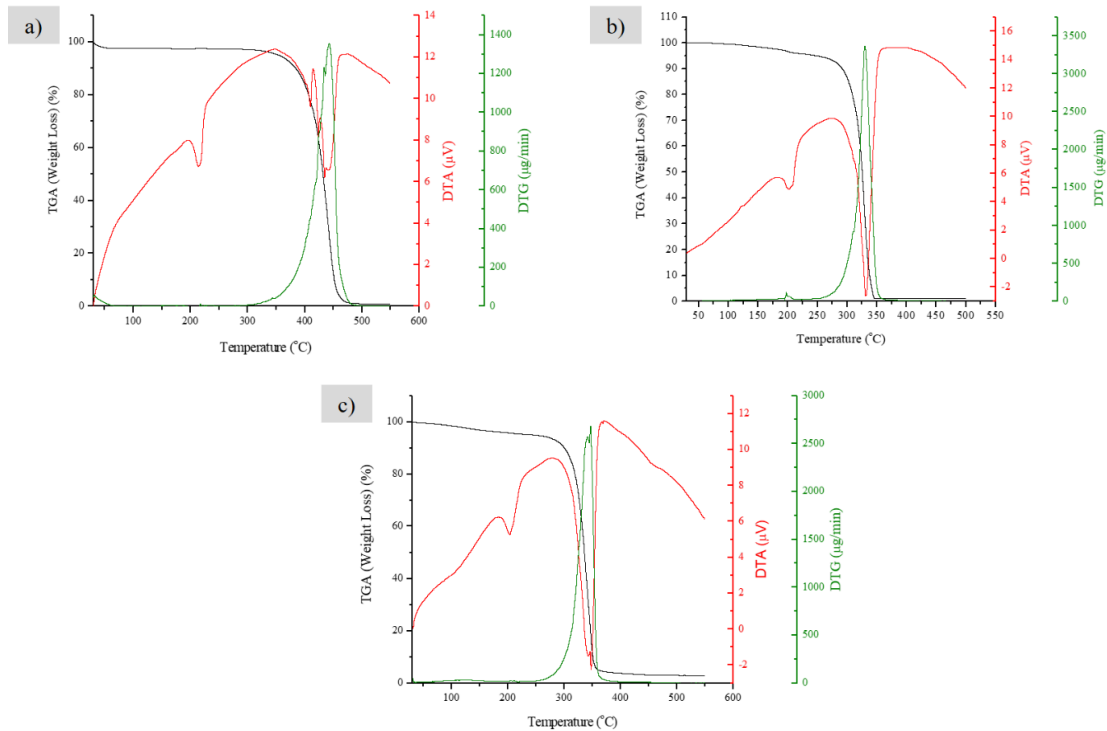
Figure 7.3. Thermogravimetric analysis (in N2 atmosphere at 10 $^{\circ}$C.min^{-1} heating rate) of a) Annealed Plain; b) PN; c) PU-P-15

The thermogravimetric of unidirectional WSPCs and its components is shown in Figure 7.4. Thermogravimetry parameters comprising DTM, IDT, MRDT, MRD and degradation quantities were tabulated in Table 7.2. Generally, all woven reinforcements demonstrated higher thermal stability than the matrix component and WSPCs. All WSPCs in this study thermally decomposed in the same way and there were no considerable differences on their thermal stability. The remarkable differences on thermal stability of woven reinforcements and MPs enable the possibility of increasing mold pressure that could cause better matrix impregnation and crystalline lattice formation at the interface region (Figure 7.4).
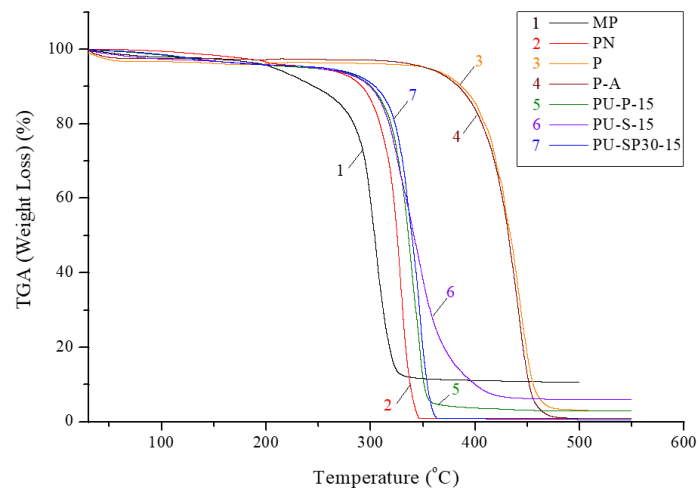
Figure 7.4. Thermogravimetry curves of WSPCs and the precursors.

184

The thermal decomposition of composites was slightly above melting temperature is related with the volatilization temperature of the caprolactam monomer at 160°C (Table 7.2). The annealing treatment of woven reinforcements decreased IDT value to 9°C. As shown in Table 7.2, MPs degraded faster than woven reinforcements that can be regarded an advantage to elevate the processing window. The thermal stability of WSPCs was higher than matrix component but lower than woven reinforcements. The weight loss of WSPCs and PN sample (heat rate of 10°C/min) took place in the range of 325-375°C, whereas it was about 400-450°C for woven reinforcements. The comparison of MRD values evidenced that matrix component degraded faster than WSPCs and reinforcements. Moreover, increasing fiber volume fraction delayed the degradation rate. At the end of the heating procedure (up to 550°C), woven reinforcements contained residues that can be attributed to the crosslinking effect.

Table 7.2. TGA data analysis for WSPCs and their precursors.

Sample	DTM (°C)	IDT (°C)	MRDT (°C)	MRD (Rad)	Degradation (%)
P	217	311	444	1.09	92.4
P-A	213	302	441	1.12	95.4
PN	198	198	330	1.30	98.0
MPs	204	204	307	1.18	85.0
PU-P-15	204	252	346	1.20	92.7
PU-P-20	202	226	332	1.11	99.2
PU-P-25	201	224	351	0.74	97.1
PU-S-15	203	234	343	0.92	89.0
PU-SP30-15	204	243	347	1.20	97.7
PU-SP45-15	203	216	338	1.06	89.4
PU-SP60-15	203	229	349	1.00	98.4

7.3.   Infrared Spectroscopy of WSPCs

The detailed normal coordinate infrared spectra for PA6 untreated and annealed Plain and Satin woven reinforcements at room temperature are demonstrated in Figure 7.5. Transform Infrared Spectroscopy techniques (FTIR) have been applied to accomplish unique fingerprint of the crystal-amorphous relationship in the sample and of the nature of chain packing in the crystal phase of PA6. Because similar infrared spectra for annealed Knitted and Woven textile structures can be seen, the peak description is presented in section 5-3.
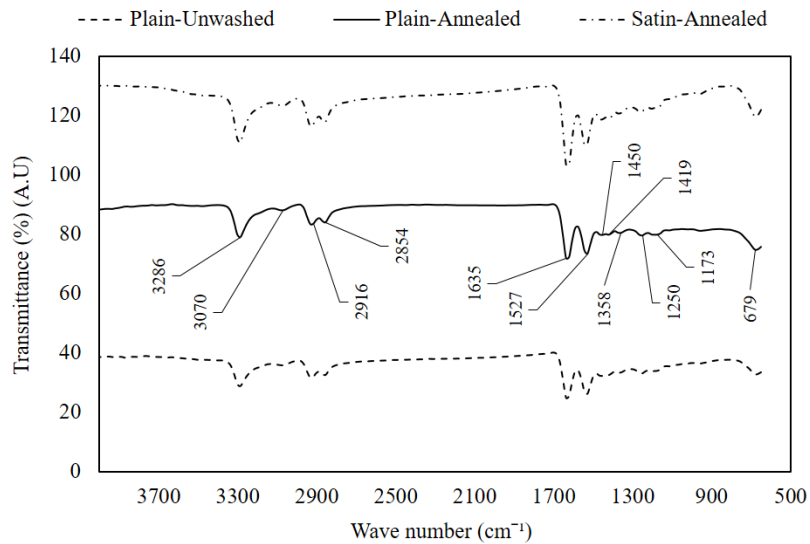
Figure 7.5. FTIR spectrum of untreated and annealed woven reinforcements before and after stretching-annealing process

Figure 7.6 illustrates a comparative study on infrared spectra of annealed stitched plain reinforcements with SDF gradient increment. The IR spectra of annealed Plain structure are shown as reference. The axes of the warp filaments were parallel to the direction of the electric field of the incoming IR in incident angle of 0°. IR spectra of all treated Stitched plain reinforcements showed an increase in IR absorption of Amide I while the gradient of SDFs grows. As it mentioned before, Amide I and Amide II bands were sensitive to α-structure crystalline. Therefore, increasing stitching angle of SDFs on plain substrate raised the IR absorption intensity of Amide I and Amide II which may be linked to the different α-crystalline portions in their molecular structures. More exploration can be found in WRD study of WSPCs and precursors.
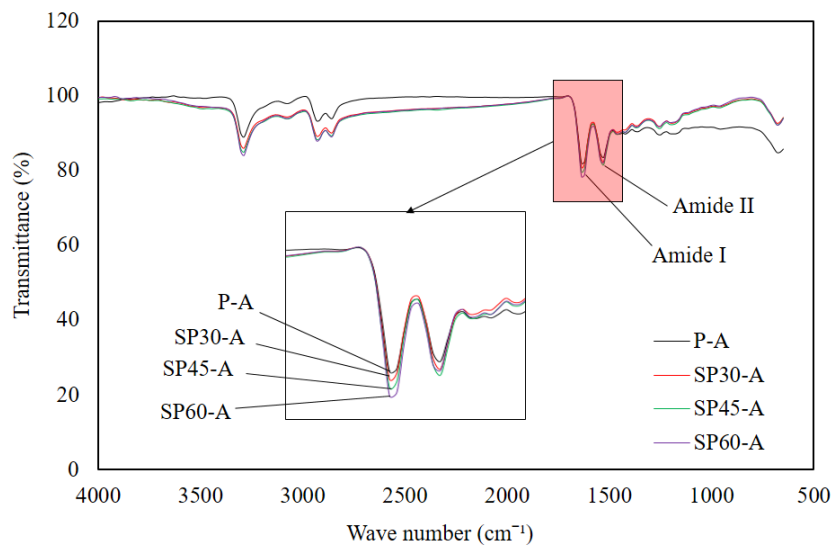
Figure 7.6. Anisotropy IR spectra of stretched-annealed Stitched plain reinforcements. The FTIR spectrum of treated Plain reinforcements is presented as reference sample.

186

7.4.   Cryogenically surface topography of WSPCs

In composite materials, evaluation of bonding condition at the fiber-matrix interface is essential to understand their mechanical performance. To characterize the interface status of the WSPCs produced by PCCM technique, microstructural studies were carried out. Polarized light microscopy (PLM), and scanning electron microscopy (SEM) were used to identify TCL occurrence, in connection with the structural characteristics of the woven reinforcements. X-ray diffraction and differential scanning calorimetry (DSC) were used to investigate composites' crystallography and inner morphology of the transcrystalline layer (TCL).

Frequently, the preparation of SPCs and other polymer-polymer composites includes a stage in which the molten matrix-forming polymer crystallizes epitaxially upon oriented crystalline fibers of other material whereby a transcrystalline layer (TCL) is formed on the fiber surface [252,253]. The simplest method to detect the formation of TCL is to compare the thickness of the reinforcement´s monofilaments in the neat textile structure to that in the final laminate composite. Due to proof of TCL at interface region in WSPCs, polarized light microscopy (PLM) had been applied. Figure 7.7a demonstrates the microscopy and PLM images of PU-P(0)-15 sample. The isotropic component (Matrix) and the anisotropic (reinforcements) were illustrated with yellowish and dark portions respectively. The distinct color and optical path boundaries between monofilaments and matrix component evidenced a narrow TCL around filaments in interface region (Figure 7.7b).

The perceived brightness of PLM images was not dependent merely upon the conditions of illumination but also on the sensitivity and linearity of the detector that acquired the image. This influenced the intensity distribution and interrelationship of contrast between light and dark regions in birefringence[19]. Therefore, by applying Gamma correction in this study, the overall brightness of an image has been controlled as illustrated by the images either bleached out, or too dark images in Figure 7.7b. Therefore, the TCL can be detected as a thin halo around the embedded monofilament.

The microscopic image of stretched-annealed plain reinforcement is shown in Figure 7.7c. The average diameter of each monofilament has been measured via image analysis using Leica Application Suite 4.4 software and calculated by 22-23 µm (Figure 7.7c). A micrograph of the same PU-P (0)-15 sample with crossed polarizers is shown in Figure 7.7d. Similar refractive indexes of monofilament and

---

[19] Birefringence is the optical property of a material having a refractive index that depends on the polarization and propagation direction of light. These optically anisotropic materials are said to be birefringent.

matrix in warp direction accompanied by advent of the colors ranges on monofilaments body in weft direction caused difficulties on TCL recognition. Accordingly, cryogenically fractured surface of WSPCs via SEM would facilitate the TCL thickness measurement.
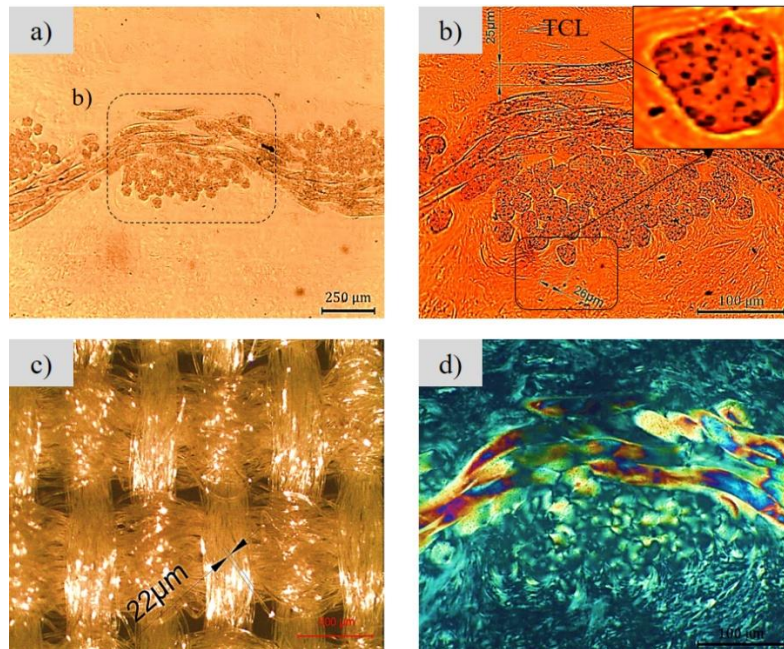
Figure 7.7. Microscopy surface topography of PU-P(0)-15 a) embedded monofilament bundle in matrix component; b) gamma ray saturated microscopic images of monofilaments bundle and TCL observation; c) Overview of magnified top image of annealed Plain reinforcement; d) Polarized topography of Figure 7b.

WSPCs was fabricated by melting the PA6 microcapsules, while the reinforcements were partially melted and then isothermally cooled to crystallization temperature. The representative SEM cryogenically fractured surface of WSPCs reinforced by plain, satin and stitched plain structures with 15 V_f,% is visualized in Figure 7.8. The even cryogenically fracture surface in WSPCs is demonstrated by no longitudinal splitting (Figure 7.8a-c). No cracks or other defects at the fiber-matrix interface were observed. Observing non-instantaneous failure configuration at interface (Figure 7.8d-f) contributed to the appearance of the non-circular configuration in the breakage region. Hence, the conical configuration of monofilaments was correlated with gliding the monofilament along their axes at the failure point result in strong bonding between WSPCs components.

Figure 7.8b illustrates average thickness of the textile monofilament embedded in WSPCs was about 25-26 µm and 22-23 µm in the annealed plain reinforcement (Figure 7.7c). The average thickness of the textile monofilaments and embedded ones was obtained by 10 reads using alternative microscopic images. Consequently, the formation of TCL with a supposed thickness of 2-4 µm is evidenced. To detect

TCL, the partial pulled-out monofilament (Figure 7.8g-i) showed that superficial part (TCL orientation) was perpendicular to the axially oriented interior portion (monofilament axis). Meanwhile, a straight boundary discriminated these two orientations.
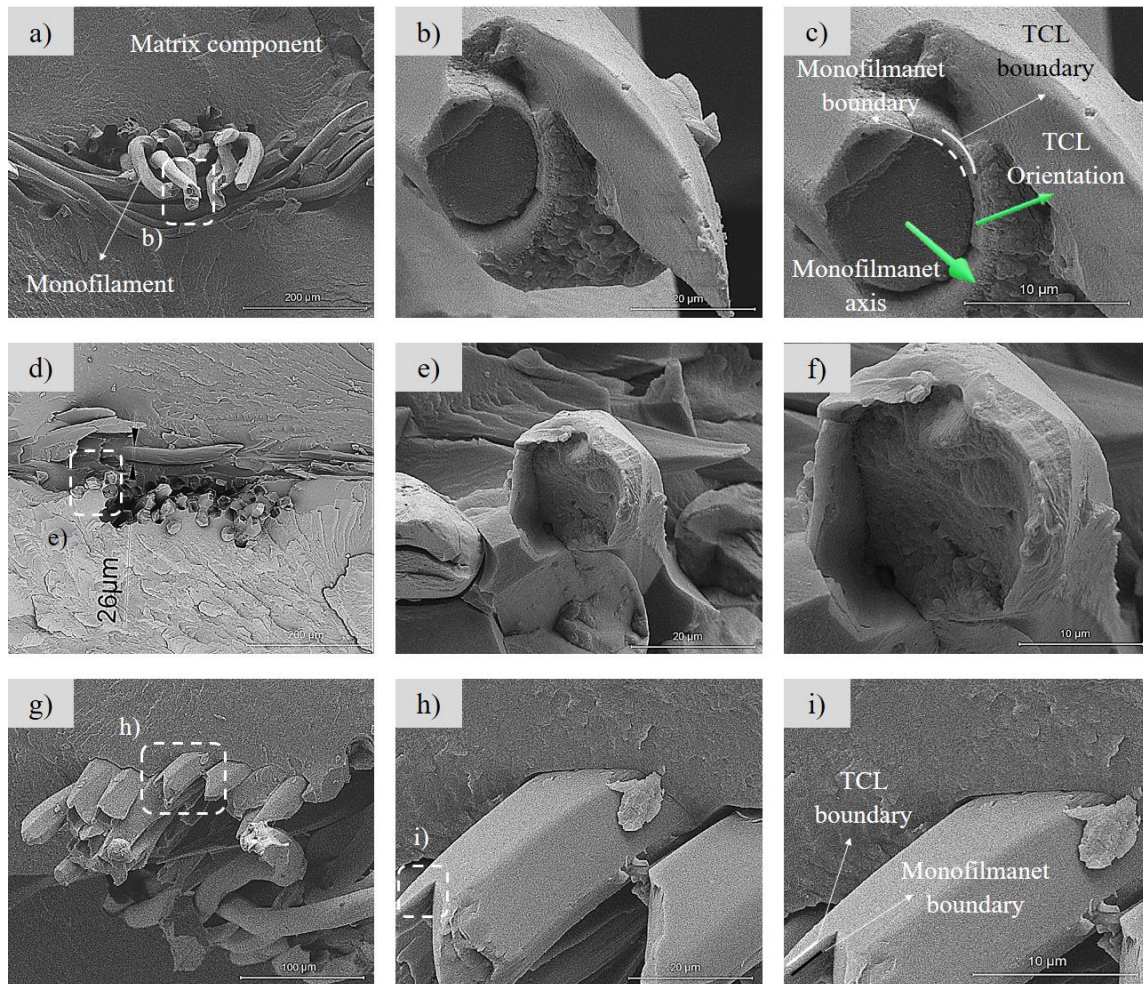
Figure 7.8. SEM surface topography with 15% fiber volume fraction of WSPCs reinforced by a-c) Plain d-f) Satin g-i) Stitched Plain 30

7.5. Synchrotron X-ray diffraction studies

To present an alternative technique to evaluate the influence of TCL on mechanical properties of WSPCs, X-ray diffraction studies were carried out. Peak fitting procedure has been performed by deconvoluting the linear diffraction patterns of representative samples with fitting coefficients $r^2 \approx 0.99$. Representative X-ray patterns and their deconvolutions of Plain reinforcement before and after treatment are shown in Figure 7.9a-b respectively. In respect to the previous studies [221,232], two peaks with 2θ being centered at ca. $20°$ and $23°$ were detected corresponding to $\alpha[200]$ and $\alpha[002/202]$ crystalline planes of α-phase monoclinic unit cell lattice respectively. Two Gaussian peaks corresponding to $\gamma[001]$

and γ[200] crystalline planes were identified with 2θ being between 21 and 22° in γ-crystalline form, non-hexagonal unit cell. Two wide Gaussian peaks (halos), represented by AM_1 and AM_2 show the diffuse scattering of the amorphous PA6 component. The XRD pattern of untreated plain structure shows broader α-crystalline phase reflections than those of the γ-polymorph (Figure 7.9a). Otherwise, α-polymorphs are fitted with narrow and symmetric (Figure 7.9b) in annealed Plain reinforcement.
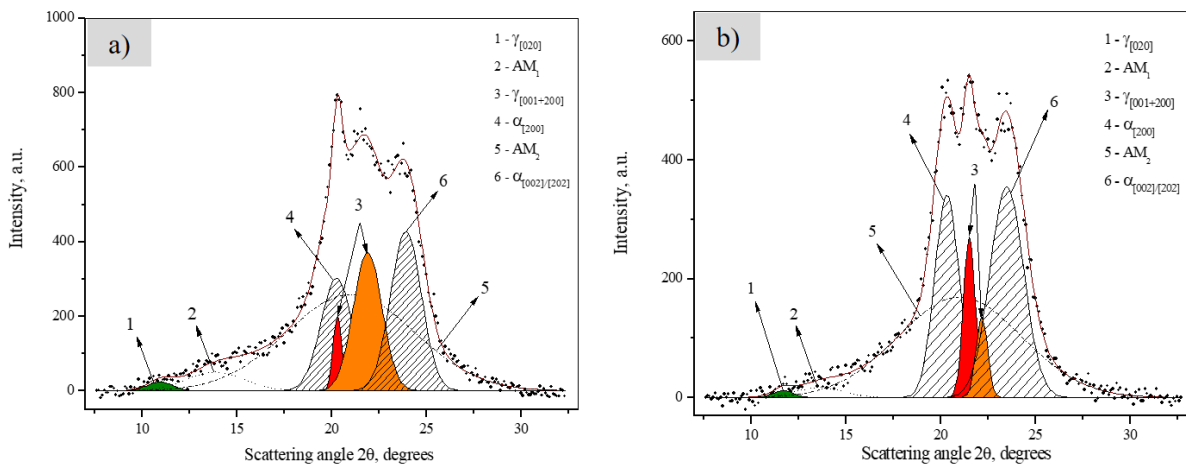
Figure 7.9. WAXS patterns and their fits of SPCs building components: a) untreated Plain reinforcement; b) stretched-annealed Plain reinforcement. AM=amorphous portion

The fitted XRD patterns of WSPCs are shown in Figure 7.10a-f. In what regards the fitted XRD patterns of PN matrix component (Figure 5.17b) and woven reinforcements (Figure 7.9b), X-ray diffraction of composite materials were convoluted by the clear separation of α[200] and α[002/202] reflections of anionic matrix PA6 and the hydrolytic PA6 of reinforcements. It should be mentioned that the peak separation of γ-crystalline phase was impossible. However, four convoluted fits for γ-crystalline phase were detected in XRD pattern of WSPCs whereas KSPCs contained three γ-phase fractions in their crystalline polymorphs (see Figure 5.18).

The initial state of the PA6 matrix component was the mesomorphic β-form (Figure 5.17b) that can be transformed into the more stable crystal forms under hot compression molding. The broad and short peaks of α-polymorph in both representative composite samples correspond to recrystallization of anionic MPs during the WSPCs preparation, and form less perfect and non-oriented matrix crystallites. In contrast, the long α-crystal peaks represent the annealed embedded knitted reinforcements which did not melt.

Comparison of X-ray diffractions of WSPCs and KSPCs demonstrate the existence of larger and intense convoluted peak for reinforcement α-crystalline phase in composite reinforced by woven structures.

Otherwise, the matrix α-crystalline fractions were shorter and broader in WSPCs. It can be deduced that woven crystalline fractions of the reinforcements have key influence on the final mechanical properties of WSPCs.
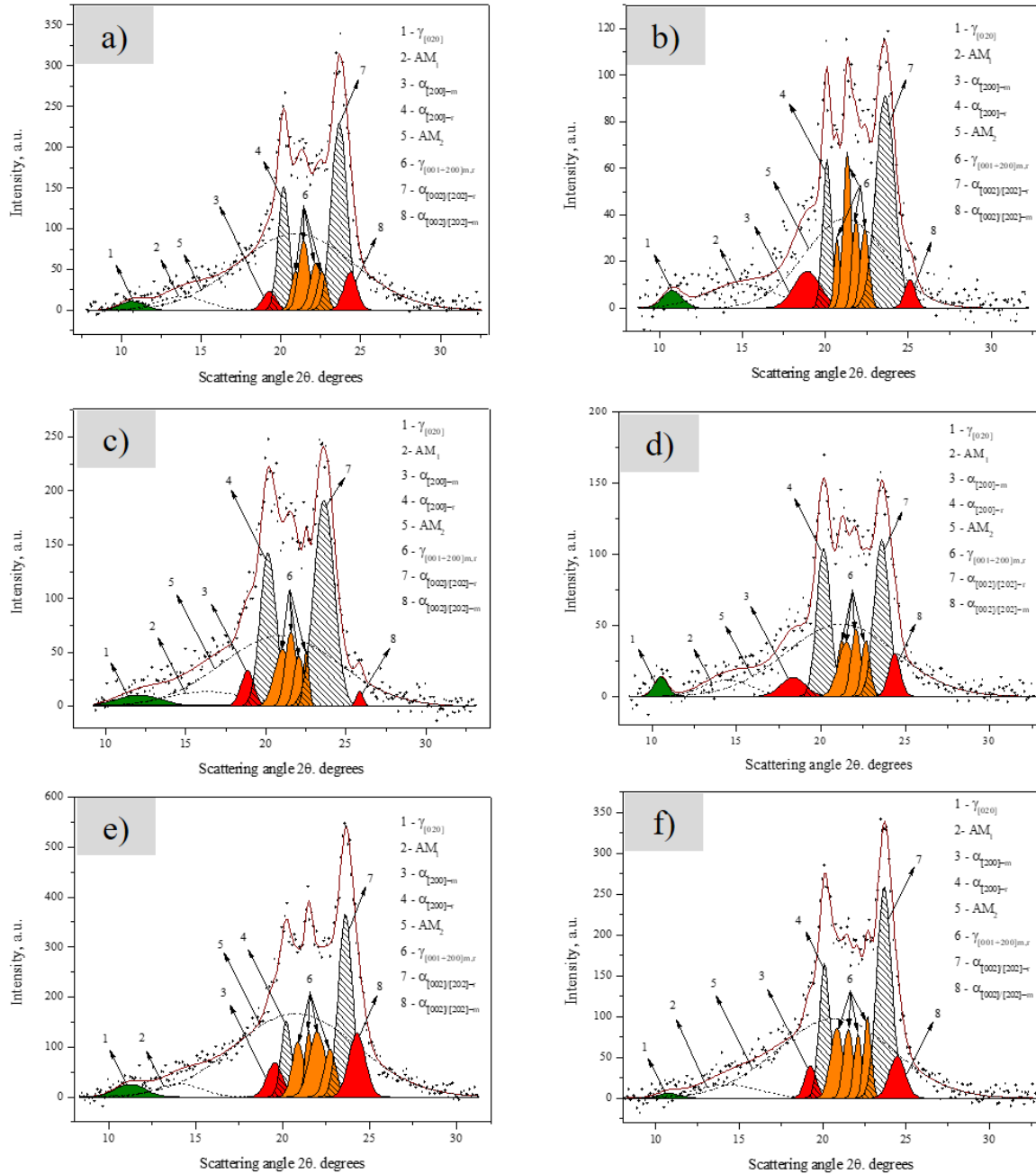
Figure 7.10. WAXS patterns and their fits of PCCM prepared WSPCs materials: a) PU-P(0)-15; b) PU-P(0)-20; c) PU-P(0)-25; d) PU-S(0)-15; e) PU-SP30(0)-15; f) PU-SP30 (90)-25.

The crystalline structure and the degree of crystallinity X_c^{XRD} in all WSPCs and the components are presented in Table 7.3. Notably, different crystalline reflection of WSPCs and the precursors demonstrate that different woven architectures may result in different crystallization behaviors during the stretching-

annealing of the woven textile reinforcements and the hot compaction procedure. The total crystallinity index and the specific content of α- and γ-PA6 polymorphs were calculated by Eq. 3-9. The transition of α- to γ-crystalline phase after molding MPs to PN caused a decrease of X_c^{XRD} (from 42% to 35%) and the α/γ ratio. Table 7.3, shows that stretching-annealing treatment of woven reinforcements cause a decreasing γ[020] reflection. Due to this fact, the crystallinity of untreated Plain structure (50%) slightly increased (54%) after treatment.

Table 7.3. Data from the deconvolution of the XRD patterns of WSPCs, textile structures and anionic PA6 precursors

Sample	$\alpha\%$	$\gamma\%$	X_c^{XRD}, %	$\dfrac{\alpha}{\gamma}$	$d_{\alpha(200)}$ Å	$d_{\alpha(002/202)}$ Å	$d_{\gamma(020)}$ Å	$d_{\gamma(001)}$ Å	$d_{\gamma(200)}$ Å
MP	26.5	15.2	41.7	1.74	4.29	3.62	-	4.31	3.99
PN	17.4	17.5	34.9	1.00	4.32	3.68	7.48	4.33	4.00
P	31.48	18.20	49.68	1.73	4.38	3.75	8.09	4.37	4.06
P-A	43.12	10.66	53.78	4.05	4.36	3.78	7.58	4.13	4.01
PU-P(0)-15	25.27[R]	8.81[R]	43.13	2.25	4.40[R]	3.76[R]	8.27	4.14[R]	4.00[R]
	4.59[M]	4.46[M]			4.60[M]	3.65[M]	-	4.24[M]	3.93[M]
	29.86[T]	**13.27**[T]							
PU-P(0)-20	27.68[R]	12.13[R]	52.35	1.93	4.41[R]	3.77[R]	8.20	4.16[R]	4.06[R]
	6.81[M]	5.73[M]			4.69[M]	3.55[M]		4.29[M]	3.97[M]
	34.49[T]	**17.86**[T]							
PU-P(0)-25	33.63[R]	9.13[R]	51.99	2.37	4.41[R]	3.76[R]	7.28	4.12[R]	4.03[R]
	2.91[M]	6.32[M]			4.70[M]	3.44[M]		4.22[M]	3.95[M]
	36.54[T]	**15.45**[T]							
PU-S(0)-15	25.84[R]	10.59[R]	48.01	1.93	4.40[R]	3.77[R]	8.40	4.13[R]	4.03[R]
	5.78[M]	5.800[M]			4.83[M]	3.65[M]		4.18[M]	3.92[M]
	31.62[T]	**16.39**[T]							
PU-SP30(0)-15	17.46[R]	10.13[R]	42.55	1.56	4.39[R]	3.76[R]	7.86	4.13[R]	4.04[R]
	8.46[M]	6.500[M]			4.54[M]	3.66[M]		4.25[M]	3.91[M]
	25.92[T]	**16.63**[T]							
PU-SP30(90)-25	24.62[R]	6.93[R]	45.34	2.02	4.41[R]	3.75[R]	8.21	4.12[R]	4.02[R]
	5.73[M]	8.06[M]			4.60[M]	3.63[M]		4.26[M]	3.92[M]
	30.35[T]	**14.99**[T]							

R: Reinforcement
M: Matrix
T: Total

The crystallinity of WSPCs varied between 42 to 53% and was located between X_c^{XRD} values matrix (lower case) and the annealed woven reinforcements (upper case). Applying the SDFs to Plain reinforcements didn't change significantly the X_c^{XRD} index of WSPCs. All WSPCs contained an higher α/γ ratio (1.6-2.4) than matrix components (≈1) and lower than the annealed knitted reinforcements (≈4.5). Comparison of α/γ ratio of all composites (Table 7.3 and Table 5.4) evidenced slightly lower γ-crystalline phase fraction for WSPCs. This achievement is in good agreement with the advent of TCL at the reinforcement/matrix interface in WSPCs.

The long spacing values d_{hkl} in Table 7.3 brought the conclusion that the unit cell edges of the matrix and reinforcement PA6 components in WSPCs differ only slightly, and the difference being in the margin of the experimental error. Although, analogy of d-spacing in all composites evidenced that embedding woven reinforcements in anionic PA6 polymer increased slightly, the spacing between successive (d_{hkl}) planes are a matter of atoms and particles. The reason of feeble tensile strength in WSPCs and not in KSPCs, may be explained by their longer $d_{\gamma(020)}$ value requiring low energy to break the H-bonds in inter and intra sheet. As a conclusion, the nature of TCL seems to be found on γ- polymorphs in WSPCs and comparative study on the effect of reinforcement architecture in crystalline fractions of WSPCs and KSPCs can evidence a logical correlation between TCL advent and its thickness with final mechanical properties of composites.

7.6. Conclusion

Microstructure analysis of WSPCs and its precursors has been carried out and linked with their mechanical properties in this study. Combination of powder impregnation and hot compaction techniques (PCCM was performed to produce WSPCs. plain, satin and stitched plain woven were selected as reinforcements and a stretching-annealing treatment was applied to stabilize their geometrical properties. The DSC scan of WSPCs and components show a weak shoulder prior to their melting temperature which can be linked with the existence of γ-PA6 crystalline phase. The transcrystalline layer (TCL) at the matrix/reinforcements interface were detected via PLM and SEM experiments and the formation of TCL with a supposed thickness of 2-4 μm is observed. The comparative study of DSC and TGA thermograms with X-ray spectroscopy of all composites and their components brought a conclusion of similar nature of TCL and γ-crystalline fraction in WSPCs. The narrow TCL and low γ-crystalline fraction at the interface in WSPCs compare to the KSPCs could explain less durable and stiffer properties of WSPCs.

Recycling of SPCs and mechano-morphological studies

8.1. Introduction

In this chapter, an attempt is made to recycle mechanically fractured SPCs prepared by NYRIM and PCCM techniques via injection molding method. Meanwhile, the recycled SPCs are classified based on their polymerization techniques and the reinforcement types. Moreover, the conventional PA6 neat matrix injection molded to provide the reference sample. The tensile and flexural properties of recycled SPCs are also compared to PN and NN reference samples to evaluate the possibility of reproducible composite material. Their mechanical properties are correlated with their thermal properties.

8.2. Tensile properties of recycled SPCs

Table 8.1 shows the sample designation of recycled composite material based on the reinforcement architectures and molding techniques.

Table 8.1. Sample designation and properties of weft knitted reinforcements used

Recycled SPCs designation		Description
IN		Injection molded conventional PA6 neat plate
RP	KRP	Recycled PCCM prepared SPCs reinforced by knitted fabrics
	WRP	Recycled PCCM prepared SPCs reinforced by woven fabrics
RN	KRN	Recycled NYRIM prepared SPCs reinforced by knitted fabrics
	WRN	Recycled NYRIM prepared SPCs reinforced by woven fabrics

The engineering stress-strain curve for IN sample known as semicrystalline thermoplastic, demonstrated a proportional limit followed by a maximum value at which necking takes place (Figure 8.1a). At yield stress, the sample flow has begun at earlier strains ($25 < \varepsilon_{necking} < 50\%$). The neck does not continue shrinking in IN sample until the specimen fails. Therefore, the IN sample in the neck stretches only to a "natural draw ratio" correlated with the temperature and specimen processing. Beyond necking stage, a new state of IN sample was appearing while the neck propagated until it spans the full gage length of the specimen and become drawn ($50 < \varepsilon_{Draw} < 100\%$). As it can be seen in Figure 8.1a, the stress-strain graph contains an upward trend reaching the breaking point ($100 < \varepsilon_{br} < 150\%$). The reason lies on the strengthened microstructure in IN resulting from necking process. The breaking load is greater than that needed to induce necking in the untransformed material just outside the neck. The

stress-strain graphs of recycled SPCs is demonstrated in Figure 8.1b. The tensile stress-strain graph of anionic PA6 matrix component prepared by NYRIM, PCCM and injection molded techniques are presented as references.

The latter sample showed lower tensile stiffness and strength as compared to the neat NN and PN matrices, but a much clearer ductile behavior. As to the recycled samples in Figure 8.1b, the tensile properties of the WRP and KRP sample were significantly higher than the WRN and KRN material, evidencing a significant influence of the prior molding technique on the mechanical properties of recycled composites. Tensile stress-strain plot of KRP and WRP samples showed a brittle behavior due to coincidence of the maximum stress with the abrupt fracture. Although the tensile behavior of KRN and WRN samples was similar with the injection molded PA6 sample.
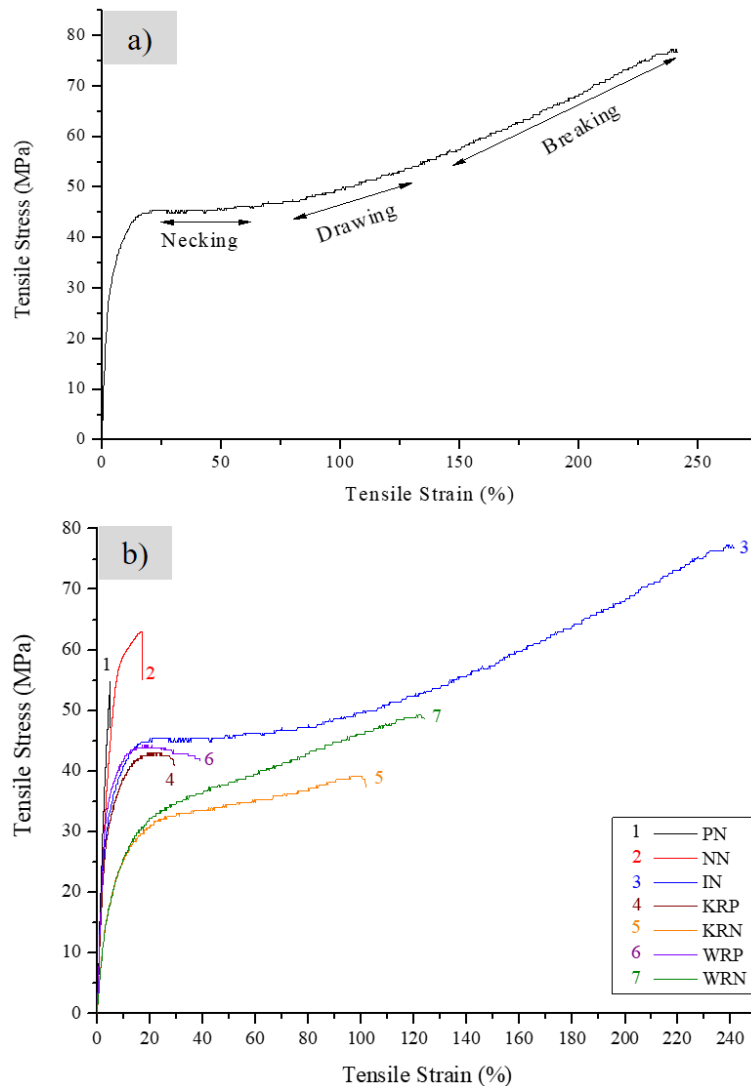
Figure 8.1. a) Tensile stress-strain curves in tension of IN sample; b) Comparative study on stress-strain curves of recycled SPCs. The stress-strain graph of PN, IN and NN sample are presented as references.

As seen in the averaged mechanical data in Table 8.2, the reinforcement architecture influenced the tensile properties of the recycled composites. Samples WRP and KRP showed higher tensile stiffness 300 % and 200% than WRN and KRN samples respectively. In general, sample WRP showed stiffer behavior among all recycled composites. Moreover, WRP had higher tensile stiffness than the anionic IN sample (28.5 IF_{IN}%) and NN (38.5 IF_{NN}%) reference samples.

Table 8.2. Data about tensile properties of all recycled composites. Tensile properties of PN and NN neat matrix are presented as references. Designations are presented in Table 8.1

Specimens	Young´s modulus E,(Gpa)	tensile stress at max σ_{max} (Mpa)	tensile stress at break $\sigma_{at\ break}$ (%)	tensile strain at break $\varepsilon_{at\ Break}$ (%)
PN	1.73 ± 0.02	56.7 ± 1.8	56.7 ± 1.8	5.19 ± 0.1
NN	1.38 ± 0.05	66.2 ± 3.0	67.8 ± 1.0	12.1 ± 1.1
IN	1.32 ± 0.08	76.4 ± 1.1	75.9 ± 1.1	225.7 ± 3.3
WRP	1.81 ± 0.04	43.1 ± 1.2	41.1 ± 1.0	38.0 ± 0.9
KRP	1.34 ± 0.02	43.2 ± 0.5	41.4 ± 1.6	28.8 ± 0.8
WRN	0.64 ± 0.02	50.2 ± 0.9	49.0 ± 1.4	122.5 ± 1.4
KRN	0.61 ± 0.01	32.2 ± 1.2	32.4 ± 0.5	100.0 ± 1.9

8.3. Flexural properties of recycled SPCs

The analogical study on flexural stress-strain graphs and analytical flexural properties of recycled SPCs, IN and PN matrix component are presented in Figure 8.2.
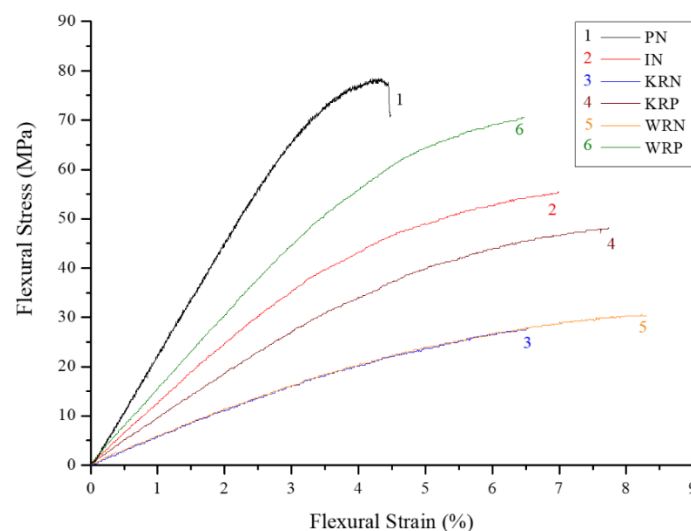
Figure 8.2. Analogical study on flexural stress-strain plots of recycled SPCs respect to the reinforcement's architecture and polymerization type. The stress-strain graph of PN and IN sample are presented as references. Designations are presented in Table 8.1

The flexural properties of WRP were the highest among other recycled SPCs and IN samples. Although, PN matrix samples demonstrated better the flexural properties. WRP had better flexural stiffness (IF_{KRP}=62,5%) and strength (IF_{KRP}=21,2%) than KRP. It should be mentioned that no changes were observed in flexural stress-strain graph of RN samples.

Deep analysis of tensile properties of recycled SPCs are shown in Table 8.3 concerning the influence of reinforcement architectures, and molding techniques. Comparing the tensile and flexural properties of WRP with IN samples is an evidence of the promising application of recycled SPCs.

Table 8.3. Analogical study on flexural stress-strain plots and analytical flexural properties of recycled SPCs respect to the reinforcement's architecture and the molding techniques. The stress-strain graph of PN and IN sample are presented as references. Designations are presented in Table 8.1

Specimens	Flexural modulus E_f,(Gpa)	Flexural stress at max $\sigma_{f,max}$ (Mpa)	Flexural strain at max $\varepsilon_{f,at\,max}$ (%)
PN	2.32 ± 0.02	91.7 ± 4.5	4.4 ± 0.1
IN	1.18 ± 0.02	49.0 ± 0.8	6.3 ± 0.2
WRP	1.56 ± 0.02	50.3 ± 0.4	6.4 ± 0.2
KRP	0.96 ± 0.04	41.5 ± 0.9	7.5 ± 0.2
WRN	0.59 ± 0.01	30.6 ± 0.2	6.3 ± 0.1
KRN	0.64 ± 0.01	28.2 ± 0.4	6.4 ± 0.1

8.4. Calorimetry of SPCs components

The processing temperature influences the quality of the molded part. When applying low temperature, higher pressure is needed to deliver the polymer melt into the mold cavity. If the temperature is too high, the risk of material degradation increases. If the injection pressure is too low, a short shot could result whereas with high pressure the mold is flashed. Figure 8.3a-b shows the DSC thermographs of all recycled SPCs and IN sample as reference. Figure 8.3a confirmed that the melting temperature of IN sample is about 225°C, while those of recycled composites vary in the 213-215°C range. The DSC curves in Figure 8.3b reveals the T_g of all samples that were covered during the first scan with a lower temperature endotherm.

The RP samples contained higher T_g values than RN, showing higher segmental mobility of the polymer chains. The small shoulder in endothermic melting peak in RP and IN samples may be related to the transition of α- to γ-crystalline phase as depicted in the second DSC scan of all reinforcements

(see Figure 5.8b). Hence, a low temperature shoulder in the 212-214°C range can be attributed to the melting of the γ-PA6 polymorph [46,213,220].
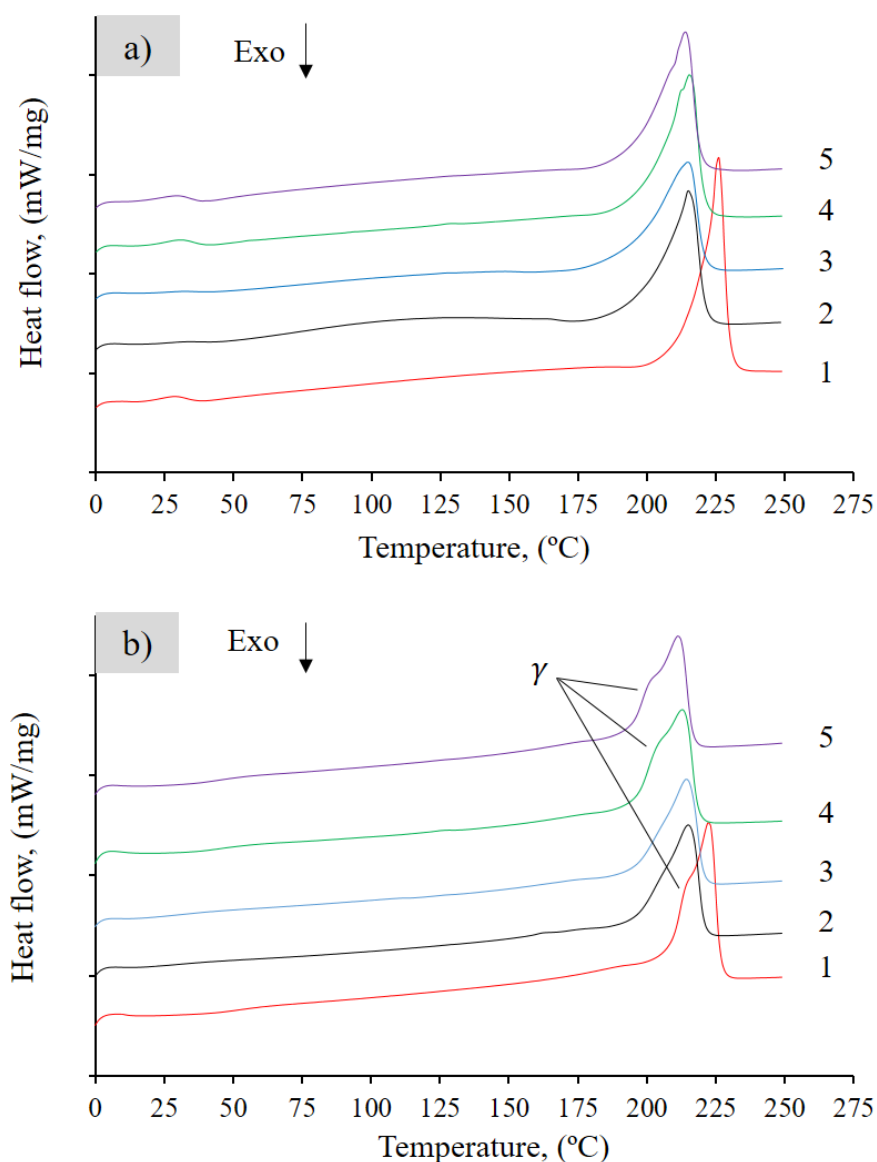
Figure 8.3. DSC thermograms of recycled SPCs from injected molded: (a) 1st DSC scan; (b) 2nd DSC scan.: 1- IN; 2- KRN; 3- WRN; 4- KRP; 5- WRP. Designations are presented in Table 8.1.

Surprisingly, the first scans of the KRN and WRN samples have broad endothermic peaks centered around 125°C that disappear during the second DSC scan. Similar to DSC thermograms of KSPCs, shown in Figure 5.9, the broad transitions can be linked to the presence of oligomeric PA6 even after recycling NYRIM prepared SPCs. An oligomer is a molecule including a few monomer units and has different physical properties as compared with the polymer.

As mentioned above, the broad endothermic transition was eliminated by the 2nd DSC scan of SPCs

produced by NYRIM technique. The final temperature of the DSC experiment was set on 250°C which should be sufficient to break the bonds in oligomers and interlock them with the polymer chain. But, the temperature of the heater was set between 195-200°C which was less than the melting point of PA6. It can be deduced that the heat was not enough to break the oligomers and covalently bond the new monomer with the PA6 polymer chains. The weak mechanical properties of RN samples can also be related with excess oligomer content.

The DSC data analysis of all recycled composites and conventional PA6 injection molded samples are presented in Table 8.4. It should be noted that the reinforcement's type of recycling process changed the T_g transition having RP samples shown twice a greater T_g value (≈44 °C) than RN samples (20-23°C). The DSC curves of all recycles SPCs displays narrow single melting peaks in the range of 213-215°C albeit IN sample had higher melting temperature at T_{m-IN}=226°C (Table 8.4).

No significant changes in DSC crystallinity of IN and RP was observed. However, the X_c^{DSC} value of RN samples was the lowest (≈26°C). As a conclusion, the different thermal characteristics of recycled SPCs obviously clarified their different molecular and crystalline morphologies with the copolymerization of two PA6 polymerization techniques such as hydrolytic and anionic ring opening polymerization. Hence, the application of different molding technique and applying different reinforcement architectures cause different thermal and mechanical properties for recycled SPCs.

Table 8.4. Crystallinity index for SPCs and their precursors. Designations are presented in Table 8.1.

Sample designation		T_g (°C)	T_{m1} (°C)	T_{m2} (°C)	X_c^{DSC}. %
Neat PA6	MPs	28.2	207.8	-	34.9
	PN	42.4	210	-	27.5
	NN	47.1	-	218.8	43.0
	IN	49.2	-	225.8	31.97
PCCM prepared SPCs	PU-J-15	45.3	210.6	216.5	31.0
	PU-R-15	34	208.2	217.8	27.1
	PU-P-15	42.7	208.7	213.6	33.0
	PU-S-15	44.9	209.6	215	32.4
	PU-SP30-15	45.4	210.5	219.2	30.9
NYRIM prepared SPCs	NU-J-15	26.1	-	217.5	32.6
	NU-R-15	27.7	-	218.2	30.0
Recycled SPCs	KRN	23.9	-	215	26.63
	WRN	20.4	-	215.1	26.45
	KRP	44.2	-	215.4	30.20
	WRP	44.3	-	213.9	29.07

8.4.1. Thermal stability of recycled SPCs

Differential thermal analysis (DTA) of WSPCs and matrix components enables measuring the changes of enthalpy in an open system, while the sample mass is simultaneously altering. Combining TGA and DTA curves allows complementary evaluation of enthalpy and mass changes, providing in such a way better understanding of the crystallization, melting and degradation of the samples. Figure 8.4a-d represents the combined thermal studies of P IN, RN and RP samples. They include three different plots as a function of the temperature, namely the weight loss (TGA, %), enthalpy/entropy changes (DTA, μV) and derivative thermal gravimetry (DTG, μg/min).

As it can be seen in Figure 8.4a, NN matrix sample had higher IDT value (≈ 350°C) compare to the recycled SPCs. IN and RP samples contained a smooth single endothermic peak in their DTA vs temperature plot whereas the DTA thermogram of KRN showed a double peak conformation (Figure 8.4b). Bimodal endothermic peaks in DTA thermograms of KRN may be connected to improper branching and interlocking of molecular groups to the chains. Hence, exitance of oligomers in RN are proven by bimodal endothermic peaks in their DTA thermogram. This is caused a quick thermal degradation and low thermal stability.
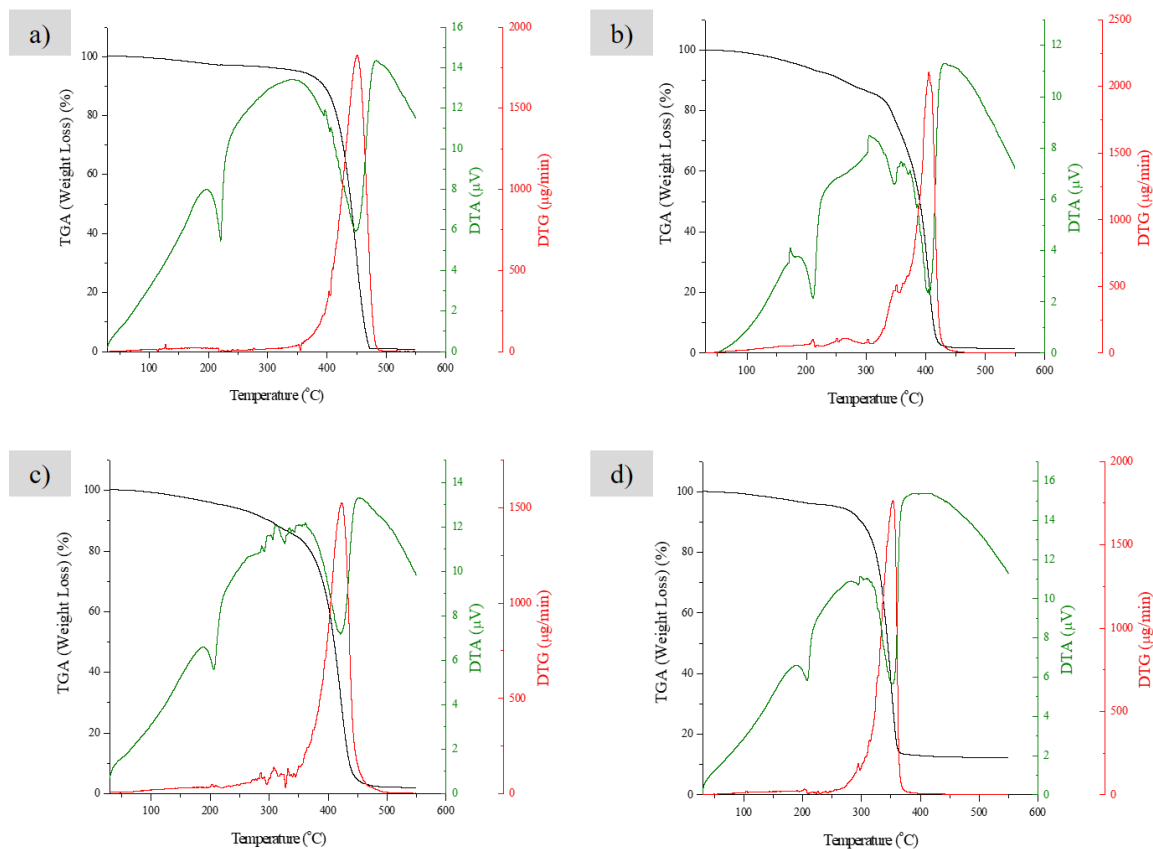
Figure 8.4. Thermogravimetric analysis (in N2 atmosphere at 10 °C.min^{-1} heating rate) of a) IN; b) KRN; c) KRP; d) WRP.

A comparative study of TGA thermogravimetric graphs of IN and recycled SPCs to analyze their structural morphology and thermal stability is shown in Figure 8.5. The DTM, MRD, MRDT and degradation magnitude were extracted from simultaneous plotting of the weight loss (%), DTA (μV) and DTG ($\frac{\mu g}{min}$) versus incremental temperature. Figure 8.5 shows the percent mass dissipation as a function of sample temperature for the IN and recycled SPCs under a nitrogen purge.

The TGA results demonstrated that the IN sample undergoes thermal degradation beginning at 451°C with a total mass loss of 98.2%. On the other hand, recycled SPCs were decomposed at lower temperature and showed inferior total mass loss due to the disruption of copolymerizing the reinforcements and matrix components after recycling procedure. The higher degradation rate (MRD values) of recycled SPCs compared with the IN sample evidenced their low thermal stability.
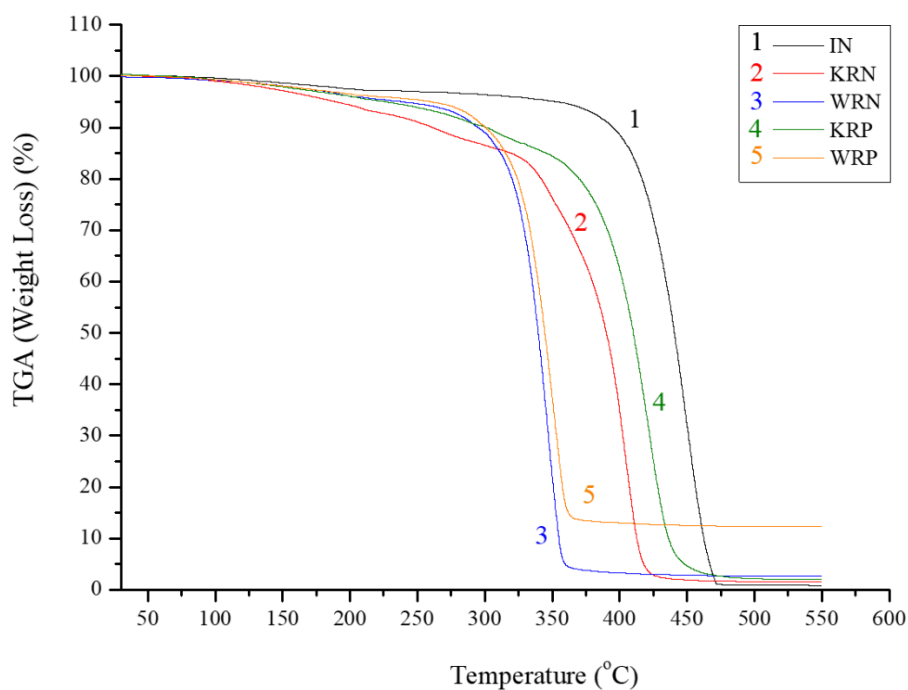
Figure 8.5. Thermogravimetry plots of IN, RN and RP samples

Thermogravimetry parameters comprising DTM, IDT, MRDT, MRD and degradation quantities are shown in Table 8.5. The explanation of the data in Figure 8.5 and Table 8.5 should be related to small differences in the thermal degradation mechanisms in each of the samples studied. There exist six main degradation mechanisms including main-chain scission, side group scission, elimination, depolymerization, cyclization and cross-linking [254]. All these processes could occur in a different way and to different extent depending on the PA6 matrix synthetic route (hydrolytic polymerization or AAROP), the presence of oligomers, traces of catalysts and/or low molecular finishing substances and stabilizers

203

related to the textile reinforcements. Therefore, higher residuals remaining in WRP may represent the existence of crosslinking and good chain interlocking during injection molding.

Table 8.5. TGA data analysis for recycled-SPCs and IN neat polymer as reference sample.

Sample	DTM (°C)	IDT (°C)	MRDT (°C)	MRD (Rad)	Degradation (%)
IN	220	331	451	1.08	98.2
RN-KSPC	210	210	405	1.09	83.6
RN-WSPC	205	246	347	1.22	91.6
RP-KSPC	205	205	422	1.03	86.7
RP-WSPC	207	239	353	1.13	82.85

8.5. Conclusion

In this study, injection molding techniques were applied to reprocess the mechanically fractured KSPCs and WSPCs test samples prepared by NYRIM and PCCM techniques. The conventional PA6 granules were fed to the injection molding machine to produce the reference sample. The mechanical and thermal properties of recycled SPCs were compared to the two neat matrix types and to injection molded neat commercial PA6.

The results showed that the reinforcement architecture affected the tensile properties of the recycled composites. WRP samples had higher tensile stiffness than anionic neat PA6 matrix (28.5 IF_{IN}%) and conventional PA6 (38.5 IF_{NN}%). Generally, RP samples showed significantly better tensile properties than RN samples. The recycled SPCs, depicted feeble flexural properties compare to the PN matrix component. Although, RP had better flexural properties among other recycled SPCs and IN sample. The alternative thermal behavior of RP and RN samples could be explained by their different molecular and crystalline morphology resulted from copolymerization of two PA6 polymerization techniques such as hydrolytic and anionic ring opening polymerization.

The DSC thermograms and DTA derivatives of RN evidenced existence of oligomers in their chemical structure and explained their weak mechanical properties although, RP samples didn't contain the oligomers in their polymorph structure. As conclusion, investigation on mechanical and thermal behavior of WRP samples accomplished the possibility of substituting recycled SPCs with the neat polymer material.

Chapter 9

Conclusion and future perspective

9.1. Conclusion

Outstanding mechanical performance, optimum durability and low weight are basic requirements for industrial polymer composites. Nowadays, there exists an additional important demand for their easy recycling and reprocessing. In conventional composite materials reprocessing could be a major challenge due to their inherent heterogeneity, i.e., the matrix and the reinforcements are quite different in their physical and chemical nature. An elegant solution of the reprocessing problem would be if the matrix and the reinforcement polymers are the same, as is in the case single-polymer composites (SPCs).

In the present study, SPCs based on polyamide 6 (PA6) are developed via nylon reactive injection molding (NYRIM) or powder coating/compression molding (PCCM). In the NYRIM process, activated anionic ring-opening polymerization (AAROP) of ε-caprolactam (ECL) to PA6 is carried out in a specially designed semiautomatic mold, in the presence of PA6 plain-woven textile plies. In the case of PCCM, the AAROP of ECL is performed in solution to synthesize PA6 microcapsules (PAMCs). They represent fine powders with grain sizes in the 15-25 µm range and were used to powder-coat the same plain woven textile structures, which were then subjected to compression molding to get the final SPC.

For both NYRIM and PCCM three fiber volume fractions V_f were used, namely 15, 20 and 25%. The effect of V_f on the tensile properties of the PA6-pased SPCs resulting from the NYRIM and PCCM techniques were investigated and compared. Microscopic image analysis was applied to detect transcrystalline layer (TCL) at the fiber-matrix interface. The results showed that applying PCCM technique increased the tensile stiffness of SPC by ca. 50% as compared to the neat matrix component. This effect was related to the good interface resulting between the PA6 matrix and the PA6 textile filaments. Optimization of the molding conditions, applying the alternative reinforcements with different morphologies are also studied. Some SPCs were reprocessed and the resulting PA6 molded plates showed morphology and mechanical properties very similar to those of commercial hydrolytic neat PA6.

Two principal type of textile reinforcements such as Knit and Woven fabrics had been employed. Two basics Rib and Jersey architectures were selected for knit reinforcements and Plain and Satin patterns were chosen for Woven fabric reinforcements. Moreover, Stitched Woven Fabrics were applied as reinforcements which they are promising novel class of woven fabrics patented by Jackob Muller Company AG ®. Stitched woven reinforcements own two segments comprising the base woven structure and the stitched diagonal filaments (SDFs) that are stitched on instated points. The plain architecture

206

were selected as substrate woven structure.

Mechanical properties of SPCs were investigated in correlation with the reinforcement's structural parameters, orientation, fiber content and stacking order. All reinforcements in this study were annealed prior molding procedure. Due to better understanding the fracture mechanism and detection of transcrystalline layer (TCL) on the interface region, post-failure examination including stereo-optical and scanning electron microscopy (SEM) image analysis performed. Wide angle x-ray scattering (WAXs) and differential scanning calorimetry (DSC) applied due to analyze the crystallography, polymorph structure and thermal properties of SPCs. The following conclusions may be derived from this research work:

A. Preparation and optimization of anionic PA6 matrix component:

To select an anionic PA6 matrix component with better mechanical properties, two distinct molding techniques such as Compression molding of polyamide 6 microparticles MPs (PN) and Nylon resin injection molding (NN) were applied for producing PA6 isotropic plates. The tensile behavior of PA6 matrix components was evaluated and compared by analyzing their tensile stress-strain graphs. By comparing the stress-strain plots of PA6 matrix plates demonstrated higher tensile stiffness for PN samples whereas the NN samples showed higher hardening and ductile properties. Their thermal properties, crystal structures, monoclinic inter and intra-sheet distances and crystalline fractions were studied to correlate their tensile failure with microstructural state. The $\alpha \rightarrow \gamma$ transition was observed in endothermic shoulder on the DSC thermograms of PN samples although DSC thermogram of NN sample did not indicated such transition. The X-ray diffraction of all PA6 plates illustrated advent of γ_{020} crystalline phase in PN matrix component in which was attributed to the observed small endothermic shoulder on its DSC thermograms. Higher $\frac{\alpha}{\gamma}$ ratio as well as lower d-spacing in NN samples were linked with their better tensile strength.

B. Developing the KSPCs and structural-mechanical properties:

Knitted reinforced single polymer laminate composites based on polyamide 6 (KSPCs) were produced by compression molding of polyamide 6 microparticles powder-coating annealed PA6 Rib or Jersey knitted textile structures (PCCM). The MPs were synthesized by solution/precipitation activated anionic ring-opening polymerization of ɛcaprolactam. The tensile properties of KSPCs were studied in relation to the

knitted reinforcement architecture, fiber volume fraction (15, 20 and 25% V_f,%), ply orientation (wale,0° and course,90° directions) and stacking orders (0/45/0 and 90/45/90). The tensile stiffness and strength of the newly prepared KSPCs with fiber content of 15% showed significant improvements as compared to the neat anionic PA6 matrix and to commercial hydrolytic PA6 (HPA6).

The fracture behavior of KSPCs was investigated by electron microscopy complemented by simulation studies. The better tensile stiffness and strength were achieved for the Rib reinforced KSPCs with relatively low fiber content (15%), laminated in the wale direction compare to the PN reference. The tensile fracture mechanism of the KSPCs was explained by structural deformation of the knit loops elements during elongation. The crossover points were detected as weak points causing advent of microcracks and the tensile failure was the latter consequence. All KSPCs modified the flexural and impact properties compare to the PA6 neat matrix. Despite feeble tensile properties, the KSPCs reinforced by 15 % Jersey knitted stricture showed steady flexural properties and impact improvements up to 340% of PN reference.

C. Comparative structural and mechanical studies on KSPCs prepared by different reactive processing techniques:

To compare the mechanical properties of KSPCs, two determined techniques such as NYRIM and PCCM techniques were employed in this study. In both cases volume fractions of 15-25% of textile reinforcements were applied. The PA6 microparticles for the first method were prepared prior to the compression molding by anionic polymerization in suspension. In the second process, a similar anionic polymerization process was applied but carried out in situ in the bulk and directly in the NYRIM mold. It was found out that the PCCM process can produce single polymer laminates with good mechanical properties in tension. The best modulus and maximal strength values, with improvements of 12% and 18% respectively, were shown by the composite containing a volume fraction of 15% of Rib textiles. The NYRIM technique produced laminates with low stiffness and strength values, the reason being the formation of oligomers in the presence of the knitted textile reinforcements.

The NYRIM technique is advantageous for the preparation of neat PA6 plates. If textile reinforcement should be used, any sizing or coloring should be carefully eliminated in order not to impede the AAROP and create weak phase boundaries in the composite. The microscopy results and indirectly the XRD studies suggested the formation of a transcrystalline layer at the fiber-matrix interface in both NYRIM and PCCM materials being thicker in the latter case. Structural studies by thermal methods and X-ray

diffraction indicated the importance of the stretching-annealing of the textile reinforcements and of the temperatures for sample consolidation in both processes. Further improvement of the KSPCs mechanical behavior will require alternative reinforcement´s architecture, optimization of their surface and studying the interlaminar shear strength of the KSPCs as a function of ply amount and alignment.

D. Development and mechanical properties of WSPCs

Similar to the KSPCs, NYRIM and PCCM techniques were employed to produce WSPCs. For the first time, novel Stitched plain reinforcements patented by Jackob Muller company AG® were applied in this study. Stitched plain reinforcements were produced including the plain structure as substrate and the stitched diagonal filaments (SDFs) as supportive structure. Stretching-annealing treatment of the woven textile reinforcements demonstrated considerable perfection on their mechanical properties. The mechanical properties of woven textile reinforcements demonstrated considerable perfection on their mechanical properties. The influence of reinforcement architecture (Plain, satin and stitched plain), fiber volume fraction (15, 20 and 25% V_f,%), reinforcement orientation (warp,0° and weft,90° directions) on the tensile properties of WSPCs was evaluated. The results showed that applying the stitched diagonal filament on plain substrates modified their tensile stiffness of plain reinforced WSPCs up to 25%. SEM fractography and fracture surface study of composites evidenced a link between failure mechanism with structural interlacing points in reinforcements. Applying NYRIM technique did not improved the tensile properties of composites compare to the NN sample.

Comparing the mechanical properties WSPCs and KSPCs, demonstrated WSPCs had higher tensile stiffness (IF_{KSPCs}= 50%) and lower tensile strength (IF_{KSPCs}= -8%) compare to KSPCs. Embedding treated stitched plain reinforcements made composite stiffer in comparison with knitted structures. In general, KSPCs depicted a brittle manner whereas WSPCs showed necking and ductile behavior after the yield strength.

Applying woven reinforcements in WSPCs did not change the flexural properties of the matrix component. KSPCs contained extremely higher bending rigidity than WSPCs with max improvement factor of 60%.

Applying treated knitted and woven reinforcements was led to significant modification of impact resistance in KSPC (IF_{PN}= 330%) and WSPCs (IF_{PN}= 120%) compare to the PN reference sample.

Embedding knitted reinforcements increased the impact properties of KSPCs than WSPCs ($IF_{WSPCs}=$ 210%). However, the superiority of impact resistance in KSPCs was explained by differences on compression storage and loss modulus of annealed woven reinforcements compare to the knitted structures.

E. Microstructure characterization of WSPCs

The DSC scan of WSPCs and precursors evidenced appearing a weak shoulder prior their melting temperature attributing with γ-PA6 crystalline phase advent. The transcrystalline layer (TCL) at the matrix/reinforcements interface were detected via PLM and SEM experiments and the feeble tensile strength of WSPCs. α to γ-phase crystalline transition was correlated with the existence of TCL. The nature of TCL in WSPCs was attributed with the γ-crystalline fraction. WSPCs showed narrow TCL and low γ-crystalline fraction compare to the KSPCs. Due to this fact, less durable and stiffer properties of WSPCs are explained.

F. Recycling of SPCs and comparing their thermal-mechanical properties

The injection molding technique was employed to recycle the mechanically fractured all SPCs prepared by NYRIM (N-type) and PCCM (P-type) techniques. The results depicted that the reinforcement architecture affected the tensile properties of the recycled composites. Samples prepared by RP had better tensile properties than RN samples. Merely, sample WRP had higher tensile stiffness than anionic neat PA6 matrix (28.5 IF_{IN}%) and conventional PA6 (38.5 IF_{NN}%). The recycled SPCs, showed feeble flexural properties compare to the PN matrix component. Unlike RP samples, the DSC thermograms and DTA derivatives of RN samples depicted existence of oligomers in their chemical structure which can be attributed to their weak mechanical properties. Better mechanical and thermal behavior of WRP samples provides further explorations on substituting recycled-SPCs with the neat polymer material.

9.2. Future perspectives

There are a wide range of applications such as automotive, aerospace and renewable energy industries in which the thermoset composite materials are applied, however to their inherent nature of heterogeneity, they have not been properly recycled. The recycling based on the current and future waste management

and environmental legislations will lead to resource and energy saving that will accompanied by various technologies, mostly focusing on reinforcement fibers and yet to be commercialized. The major obstacles in this way are costly recycling, unknown and inadequate markets and low quality of the recyclates. Therefore, the extensive research and focusing on developing new commercial composite materials is obligatory. The obvious perspective by year 2030, the production process will become more sustainable as well as less composite wastes would be emerged. From resource availability point of view, it will be hard to imagine the burring of EOL wind turbine blades or incinerating of composite car parts those mixed with plastics.

Estimating the adhesion properties of materials is considered as point of view of thermodynamic and kinetic aspects of wetting. Atmospheric pressure plasma deposition has been presented more than 20 years ago. The diffuse dielectric barrier discharge (DBD) recently is most utilized in surface treatment of the polymers and it is led to removing the weak cohesive layer (surface cleaning). DBD may thus be used as an efficient technique to assist the adhesion properties of the PA6 fibrous reinforcement in comparison with the matrix. The interfacial bonding behavior of PA-6 samples before and after surface treatment indicates that DBD could be a convenient tool to induce a controlled roughness of the polymer fibers.

Due to widespread applications such as automobile, house- hold, and electrical industries, particle-filled polymer composites have attracted strong interest. Applying nanotubes, montmorillonite, in-situ produced inorganic nanoparticles modify the physical, mechanical properties, thermal resistance and chemical reagent resistance. Moreover, they can provide cost effective high-performance materials. Addition of rigid particles to a thermoplastic matrix component leads in an increase in strength, stiffness, and dimensional stability. Extrinsic include mechanical properties of matrix component, interfacial adhesion, morphology and intrinsic variables like specimen geometry, strain rate, temperature influence the brittle-to-ductile transition of polymer blends or composites.

The laminated composites exhibit excellent in-plane properties, causing relatively low damage tolerance and impact resistance. Fabrics are used as reinforcements to improve inter-laminar properties. Therefore, study of the mechanical behavior of such composites is essential to figure out their potential. Both fabrics and matrix are responsible for bearing the mechanical loads while the matrix shields the filaments from external stresses. The stiffness and strength of composites depend upon the fabric architecture and material properties of fiber and matrix. The future works would focus on modeling the elastic and plastic behavior of the KSPCs and WSPCs, using the finite element method. A novel 3D finite element

symmetrical discretization of KSPCs and WSPCs are developed based on geometrical measurements from photomicrographs (Figure 9.1). The final results are compared with experimental results. Eventually, the optimized FEM model conditions are applied to a representative volume elements (RVE) which is the repeating element (unit cell) that represents the whole SPCs.
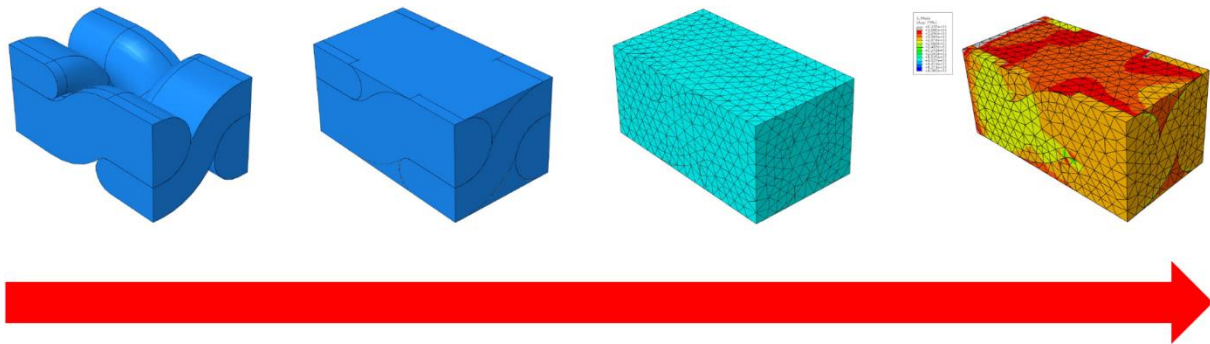
Figure 9.1. 3D model of representative volume elements (RVE)

It can be concluded by now there exist very few initial studies in the field of PA6-based SPCs and that the whole potential of these materials has not been disclosed yet. No systematic studies exist on the relationship between the parameters of the reinforcing textile structures and the morphology, structure and overall mechanical properties of PA6-based SPC materials produced by reactive injection molding. Applying PA6-based SPC reinforced with newly developed reinforcement materials is caused that the fundamental inconsistency between the heterogeneity and recyclability would become less critical. With the constantly developed new expertise and knowledge and the joint efforts from all involved parties, we can turn many today's dreams in composite world to reality in the coming 30–40 years. The conventional PA6 thermoplastic matrices will be significantly replaced by end of life PA6 base SPCs. A promising approach to composites recycling followed by specific economic and ecological advantages with less final mechanical degradation has had in mind.

"Neither you nor I understand the mysteries of pre-eternity.

Neither you nor I can read this enigma's solution.

Our talk with one another takes place behind a curtain.

Once the curtain drops, neither you nor I will remain."

Omar Khayyam, Rubaiyat

References:

[1] E. Harkin-Jones, R.J. Crawford, Mechanical properties of rotationally molded nyrim, Polym. Eng. Sci. 36 (1996) 615–625.

[2] M.M. Schwartz, M. Schwartz, Composite materials handbook, McGraw-hill New York, 1984.

[3] N. Capiati, R. Porter, The concept of one polymer composites modelled with high density polyethylene, J. Mater. Sci. 10 (1975) 1671–1677.

[4] D.N. Saheb, J.P. Jog, Natural fiber polymer composites: A review, Adv. Polym. Technol. 18 (1999) 351–363.

[5] N.-M. Barkoula, T. Peijs, T. Schimanski, J. Loos, Processing of single polymer composites using the concept of constrained fibers, Polym. Compos. 26 (2005) 114–120.

[6] D.E.W. (AVK), M.K. (CCeV) Thomas Kraus, Composites Market Report 2016, 2016.

[7] M. Buggy, L. Farragher, W. Madden, Recycling of composite materials, J. Mater. Process. Technol. 55 (1995) 448–456.

[8] D. Hull, T.W. Clyne, An introduction to composite materials, Cambridge university press, 1996.

[9] F.R. Jones, Handbook of polymer-fiber composites, Essex Longman Sci. Tech. (1994) 279.

[10] K.K. Chawla, Composite materials: science and engineering, Springer, 2012.

[11] D. Gay, S. V Hoa, S.W. Tsai, Composite materials: design and applications, CRC press, 2002.

[12] N.K. Naik, P.S. Shembekar, M. V Hosur, Failure behavior of woven fabric composites, J. Compos. Technol. Res. 13 (1991) 107–116.

[13] M. Mariatti, M. Nasir, H. Ismail, Influence of different woven geometry and ply effect in woven thermoplastic composite behaviour-Part 2, Int. J. Polym. Mater. 47 (2000) 499–512.

[14] A.G. Prodromou, S. V Lomov, I. Verpoest, The method of cells and the mechanical properties of textile composites, Compos. Struct. 93 (2011) 1290–1299.

[15] T. Ishikawa, T.-W. Chou, Elastic behavior of woven hybrid composites, J. Compos. Mater. 16 (1982) 2–19.

[16] M. Epstein, S. Nurmi, Near net shape knitting of fiber glass and carbon for composites, in: Int. SAMPE Symp. Exhib. 36 Th, San Diego, CA, 1991: pp. 102–113.

[17] S. Ramakrishna, H. Hamada, N.K. Cuong, Z. Maekawa, Mechanical properties of knitted fabric reinforced thermoplastic composites, in: Proc. ICCM, 1995: pp. 245–252.

[18] K.H. Leong, S. Ramakrishna, Z.M. Huang, G.A. Bibo, The potential of knitting for engineering

composites—a review, Compos. Part A Appl. Sci. Manuf. 31 (2000) 197–220.

[19]   B. Gommers, I. Verpoest, P. Van Houtte, Analysis of knitted fabric reinforced composites: Part I. Fibre orientation distribution, Compos. Part A Appl. Sci. Manuf. 29 (1998) 1579–1588.

[20]   A. Miravete, 3-D textile reinforcements in composite materials, Woodhead Publishing, 1999.

[21]   T.E. Meink, S. Huybrechts, M.-H.H. Shen, Processing induced warpage of filament wound composite cylindrical shells, J. Compos. Mater. 36 (2002) 1025–1047.

[22]   D. Kugler, T.J. Moon, Identification of the most significant processing parameters on the development of fiber waviness in thin laminates, J. Compos. Mater. 36 (2002) 1451–1479.

[23]   N.C.W. Judd, Voids and their effects on the mechanical properties of composites–an appraisal, (1978).

[24]   Y.K. Hamidi, L. Aktas, M.C. Altan, Three-dimensional features of void morphology in resin transfer molded composites, Compos. Sci. Technol. 65 (2005) 1306–1320.

[25]   B.D. Harper, G.H. Staab, R.S. Chen, A note on the effects of voids upon the hygral and mechanical properties of AS4/3502 graphite/epoxy, J. Compos. Mater. 21 (1987) 280–289.

[26]   A.J. Blake, W. Clegg, Crystal structure analysis: principles and practice, Oxford University Press, 2009.

[27]   D.P.R. Thirumalai, T.L. Andersen, A. Lystrup, Influence of moisture absorption on properties of fiber reinforced polyamide 6 composites, in: Proc. 26th Annu. Tech. Conf. Am. Soc. Compos. 2011 2nd Jt. Us-Canada Conf. Compos., DEStech Publications, 2011.

[28]   K. Banik, T.N. Abraham, J. Karger-Kocsis, Flexural Creep Behavior of Unidirectional and Cross-Ply All-Poly(propylene) (PURE®) Composites, Macromol. Mater. Eng. 292 (2007) 1280–1288.

[29]   R.M. Bonner, Nylon Plastics, edited by M. Kohan, J, (1973).

[30]   Á. Kmetty, T. Bárány, J. Karger-Kocsis, Self-reinforced polymeric materials: A review, Prog. Polym. Sci. 35 (2010) 1288–1310.

[31]   K.P. Matabola, A.R. Vries, F.S. Moolman, A.S. Luyt, Single polymer composites: a review, J. Mater. Sci. 44 (2009) 6213–6222.

[32]   C. Gao, L. Yu, H. Liu, L. Chen, Development of self-reinforced polymer composites, Prog. Polym. Sci. 37 (2012) 767–780.

[33]   D.M. Barry, H. Kanematsu, European Union (EU) directives and regulations, in: Corros. Control Surf. Finish., Springer, 2016: pp. 89–96.

[34]   J.L. Thomason, Micromechanical parameters from macromechanical measurements on glass reinforced polypropylene, Compos. Sci. Technol. 62 (2002) 1455–1468.

[35]   R. Piñero-Hernanz, C. Dodds, J. Hyde, J. García-Serna, M. Poliakoff, E. Lester, M.J. Cocero, S. Kingman,

S. Pickering, K.H. Wong, Chemical recycling of carbon fibre reinforced composites in nearcritical and supercritical water, Compos. Part A Appl. Sci. Manuf. 39 (2008) 454–461.

[36]   Y. Bai, Z. Wang, L. Feng, Chemical recycling of carbon fibers reinforced epoxy resin composites in oxygen in supercritical water, Mater. Des. 31 (2010) 999–1002.

[37]   J.G. Poulakis, P.C. Varelidis, C.D. Papaspyrides, Recycling of polypropylene-based composites, Adv. Polym. Technol. 16 (1997) 313–322.

[38]   I.M. Ward, Developments in oriented polymers, 1970–2004, Plast. Rubber Compos. 33 (2004) 189–194.

[39]   J. Karger-Kocsis, T. Bárány, Single-polymer composites (SPCs): Status and future trends, Compos. Sci. Technol. 92 (2014) 77–94.

[40]   J.M. Thomas, R. Raja, Design of a "green" one-step catalytic production of ɛcaprolactam (precursor of nylon-6), Proc. Natl. Acad. Sci. U. S. A. 102 (2005) 13732–13736.

[41]   G. Dahlhoff, J.P.M. Niederer, W.F. Hoelderich, ɛCaprolactam: new by-product free synthesis routes, Catal. Rev. 43 (2001) 381–441.

[42]   R.S. Kulkarni, P.P. Kanekar, Bioremediation of ɛcaprolactam from nylon-6 waste water by use of Pseudomonas aeruginosa MCM B-407, Curr. Microbiol. 37 (1998) 191–194.

[43]   R. Li, D. Yao, Preparation of single poly(lactic acid) composites, J. Appl. Polym. Sci. 107 (2008) 2909–2916.

[44]   W. Prosser, P.J. Hine, I.M. Ward, Investigation into thermoformability of hot compacted polypropylene sheet, Plast. Rubber Compos. 29 (2000) 401–410.

[45]   A. Izer, T. Bárány, Hot consolidated all-PP composites from textile fabrics composed of isotactic PP filaments with different degrees of orientation, Express Polym Lett. 1 (2007) 790–796.

[46]   M.I. Kohan, Nylon plastics handbook, Hanser Publishers Cincinnati, 1995.

[47]   A.R. Tripathy, W.J. MacKnight, S.N. Kukureka, In-situ copolymerization of cyclic poly (butylene terephthalate) oligomers and ɛcaprolactone, Macromolecules. 37 (2004) 6793–6800.

[48]   J. Karger-Kocsis, L. Kiss, Attempts of separation of the polymerization and crystallization processes by means of DSC thermograms of activated anionic polymerization of ɛcaprolactam, Die Makromol. Chemie. 180 (1979) 1593–1597.

[49]   A. Lustiger, C.N. Marzinsky, R.R. Mueller, H.D. Wagner, Morphology and damage mechanisms of the transcrystalline interphase in polypropylene, J. Adhes. 53 (1995) 1–14.

[50]   C.-M. Wu, M. Chen, J. Karger-Kocsis, The role of metastability in the micromorphologic features of

215

sheared isotactic polypropylene melts, Polymer (Guildf). 40 (1999) 4195–4203.

[51]   D. Rolel, E. Yavin, E. Wachtel, H.D. Wagner, Experimental study of transcrystallinity in UHMWPE/LLDPE composites, Compos. Interfaces. 1 (1993) 225–242.

[52]   H. Li, X. Zhang, Y. Duan, D. Wang, L. Li, S. Yan, Influence of crystallization temperature on the morphologies of isotactic polypropylene single-polymer composite, Polymer (Guildf). 45 (2004) 8059–8065.

[53]   B.L. Deopura, R. Alagirusamy, M. Joshi, B. Gupta, Polyesters and polyamides, Elsevier, 2008.

[54]   J.H. V Roberts, D.B. James, L.M. Cook, Reaction injection molding, (2004).

[55]   P.-E. Bourban, N. Bernet, J.-E. Zanetto, J.-A.E. Månson, Material phenomena controlling rapid processing of thermoplastic composites, Compos. Part A Appl. Sci. Manuf. 32 (2001) 1045–1057.

[56]   I.P. Orench, F.J. Calleja, P.J. Hine, I.M. Ward, A microindentation study of polyethylene composites produced by hot compaction, J. Appl. Polym. Sci. 100 (2006) 1659–1663.

[57]   F. v. Lacroix, M. Werwer, K. Schulte, Solution impregnation of polyethylene fibre/polyethylene matrix composites, Compos. Part A Appl. Sci. Manuf. 29 (1998) 371–376.

[58]   Y. Gong, G. Yang, Single polymer composites by partially melting recycled polyamide 6 fibers: Preparation and characterization, J. Appl. Polym. Sci. 118 (2010) 3357–3363.

[59]   K. van Rijswijk, H.E.N. Bersee, Reactive processing of textile fiber-reinforced thermoplastic composites – An overview, Compos. Part A Appl. Sci. Manuf. 38 (2007) 666–681.

[60]   P.J. Hine, R.H. Olley, I.M. Ward, The use of interleaved films for optimising the production and properties of hot compacted, self reinforced polymer composites, Compos. Sci. Technol. 68 (2008) 1413–1421.

[61]   N.D. Jordan, D.C. Bassett, R.H. Olley, P.J. Hine, I.M. Ward, The hot compaction behaviour of woven oriented polypropylene fibres and tapes. II. Morphology of cloths before and after compaction, Polymer (Guildf). 44 (2003) 1133–1143.

[62]   N. Dencheva, Z. Denchev, S. Lanceros-Méndez, T. Ezquerra Sanz, One-Step In Situ Synthesis of Polyamide Microcapsules With Inorganic Payload and Their Transformation into Responsive Thermoplastic Composite Materials, Macromol. Mater. Eng. 301 (2016) 119–124.

[63]   S. Bourbigot, L. Garnier, B. Revel, S. Duquesne, Characterization of the morphology of iPP/sPP blends with various compositions, EXPRESS Polym. Lett. 7 (2013) 224–237.

[64]   D. Yao, R. Li, P. Nagarajan, Single-polymer composites based on slowly crystallizing polymers, Polym. Eng. Sci. 46 (2006) 1223–1230.

[65]   M.J. Jenkins, P.J. Hine, J.N. Hay, I.M. Ward, Mechanical and acoustic frequency responses in flat hot-

compacted polyethylene and polypropylene panels, J. Appl. Polym. Sci. 99 (2006) 2789–2796.

[66]   Z.A. Ishak, K.G. Gatos, J. Karger-Kocsis, On the in-situ polymerization of cyclic butylene terephthalate oligomers: DSC and rheological studies, Polym. Eng. Sci. 46 (2006) 743–750.

[67]   P.J. Hine, I.M. Ward, Hot compaction of woven poly(ethylene terephthalate) multifilaments, J. Appl. Polym. Sci. 91 (2004) 2223–2233.

[68]   V. Nanthagopal, T. Senthilram, V.R.G. Dev, Flexural and impact studies on stitched self-reinforced polypropylene composites, J. Thermoplast. Compos. Mater. 27 (2014) 1504–1514.

[69]   J. Karger-Kocsis, Polypropylene: an AZ reference, Springer Science & Business Media, 2012.

[70]   P.K. Bajpai, I. Singh, J. Madaan, Tribological behavior of natural fiber reinforced PLA composites, Wear. 297 (2013) 829–840.

[71]   S. Fakirov, Transreactions in condensation polymers, John Wiley & Sons, 2008.

[72]   D. Bhattacharyya, P. Maitrot, S. Fakirov, Polyamide 6 single polymer composites, Express Polym Lett. 3 (2009) 525–532.

[73]   L. Shavit-Hadar, D.M. Rein, R. Khalfin, A.E. Terry, G.W.J.C. Heunen, Y. Cohen, Compacted UHMWPE fiber composites: Morphology and X-ray microdiffraction experiments, J. Polym. Sci. Part B Polym. Phys. 45 (2007) 1535–1541.

[74]   S. Ratner, A. Weinberg, G. Marom, Morphology and mechanical properties of crosslinked PE/PE composite materials, Polym. Compos. 24 (2003) 422–427.

[75]   S. Ratner, A. Pegoretti, C. Migliaresi, A. Weinberg, G. Marom, Relaxation processes and fatigue behavior of crosslinked UHMWPE fiber compacts, Compos. Sci. Technol. 65 (2005) 87–94.

[76]   T. Ogawa, H. Mukai, S. Osawa, Mechanical properties of ultrahigh-molecular-weight polyethylene fiber-reinforced PE composites, J. Appl. Polym. Sci. 68 (1998) 1431–1439.

[77]   T. Xu, R.J. Farris, Comparative studies of ultra high molecular weight polyethylene fiber reinforced composites, Polym. Eng. Sci. 47 (2007) 1544–1553.

[78]   T. Xu, R.J. Farris, Shapeable matrix-free Spectra® fiber-reinforced polymeric composites via high-temperature high-pressure sintering: Process-structure-property relationship, J. Polym. Sci. Part B Polym. Phys. 43 (2005) 2767–2789.

[79]   P.J. Hine, I.M. Ward, Hot compaction of woven nylon 6, 6 multifilaments, J. Appl. Polym. Sci. 101 (2006) 991–997.

[80]   L.M. Morgan, B.M. Weager, C.M. Hare, G.R. Bishop, G.M. Smith, Self reinforced polymer composites: Coming of age, Self. 5 (2009) 13–24.

[81]   J. Loos, T. Schimanski, J. Hofman, T. Peijs, P.J. Lemstra, Morphological investigations of polypropylene single-fibre reinforced polypropylene model composites, Polymer (Guildf). 42 (2001) 3827–3834.

[82]   L. Shavit-Hadar, R.L. Khalfin, Y. Cohen, D.M. Rein, Harnessing the Melting Peculiarities of Ultra-High Molecular Weight Polyethylene Fibers for the Processing of Compacted Fiber Composites, Macromol. Mater. Eng. 290 (2005) 653–656.

[83]   B. Alcock, N.O. Cabrera, N.-M. Barkoula, A.B. Spoelstra, J. Loos, T. Peijs, The mechanical properties of woven tape all-polypropylene composites, Compos. Part A Appl. Sci. Manuf. 38 (2007) 147–161.

[84]   B. Alcock, N.O. Cabrera, N.-M. Barkoula, J. Loos, T. Peijs, The mechanical properties of unidirectional all-polypropylene composites, Compos. Part A Appl. Sci. Manuf. 37 (2006) 716–726.

[85]   Y. Gong, A. Liu, G. Yang, Polyamide single polymer composites prepared via in situ anionic polymerization of εcaprolactam, Compos. Part A Appl. Sci. Manuf. 41 (2010) 1006–1011.

[86]   N. Dencheva, Z. Denchev, A.S. Pouzada, A.S. Sampaio, A.M. Rocha, Structure–properties relationship in single polymer composites based on polyamide 6 prepared by in-mold anionic polymerization, J. Mater. Sci. 48 (2013) 7260–7273.

[87]   L. Kiss, J. Karger-Kocsis, DSC investigations on the alkaline polymerization of εcaprolactam, J. Therm. Anal. 19 (1980) 139–141.

[88]   C.W. Macosko, RIM: fundamentals of reaction injection molding, Hanser Munich, 1989.

[89]   L.J. Lee, Polyurethane reaction injection molding: Process, Materials, and Properties, Rubber Chem. Technol. 53 (1980) 542–599.

[90]   C. Wu, C. Huang, Melting and crystallization behavior of copolymer from cyclic butylene terephthalate and polycaprolactone, Polym. Eng. Sci. 51 (2011) 1004–1013.

[91]   S.M. Aharoni, n-Nylons, their synthesis, structure, and properties, Wiley, 1997.

[92]   J. Kalantar, L.T. Drzal, The bonding mechanism of aramid fibres to epoxy matrices, J. Mater. Sci. 25 (1990) 4186–4193.

[93]   T. Peijs, Composites for recyclability, Mater. Today. 6 (2003) 30–35.

[94]   J. Wang, Q. Mao, J. Chen, Preparation of polypropylene single-polymer composites by injection molding, J. Appl. Polym. Sci. 130 (2013) 2176–2183.

[95]   curve® advantages, (n.d.). http://www.curvonline.com/products/index.html.

[96]   The principle of PURE®, (n.d.). http://www.ditweaving.com/about_pure.php?page=pure_technology.

[97]   Armordon ®, (n.d.). http://www.donlow.co.uk/gb/en/markets/armordon/.

[98]   Composites, (n.d.). http://www.vonroll.com/en/products/composites/?id=77c606d6.

[99] Self reinforced HDPE, (n.d.). https://www.neocomposite.com/neohdpe-more.

[100] S. Fakirov, Nano- and Microfibrillar Single-Polymer Composites: A Review, Macromol. Mater. Eng. 298 (2013) 9–32.

[101] G. Rusu, M. Rusu, E. Rusu, A. Stoleriu, C.A. Teaca, Direct centrifugal molding of nylon 6-based products from ε‑caprolactam, Polym. Plast. Technol. Eng. 39 (2000) 233–247.

[102] K. Kircher, Chemical reactions in plastics processing, Hanser Munich, 1987.

[103] L. Ricco, S. Russo, G. Orefice, F. Riva, fa, Macromolecules. 32 (1999) 7726–7731.

[104] R. Puffr, V. Kubanek, Lactam-based Polyamides: Polymerization Structure, CRC Press, 1991.

[105] R.M. Joyce, D.M. Ritter, US Pat. 2,251,519 (1941); WE Hanford and RM Joyce, J. Polym. Sci. 3 (1948) 167.

[106] W.E. Hanford, R.M. Joyce, Polymeric amides from epsilon‑caprolactam, J. Polym. Sci. 3 (1948) 167–172.

[107] W. Griehl, S. Schaaf, Zur anionischen ε‑caprolactam‑polymerisation. Versuche über die viskositätsstabilisierung, Die Makromol. Chemie. 32 (1959) 170–183.

[108] O. Wichterle, J. Králíček, The anionic polymerization of caprolactam, in: Fortschritte Der Hochpolym., Springer, 1961: pp. 578–595.

[109] N. Yoda, A. Miyake, Polymerization of α‑piperidone by alkali metal and certain acyl compounds, J. Polym. Sci. 43 (1960) 117–136.

[110] H. Yumoto, K. Ida, N. Ogata, On the Ring Opening Reaction of ε‑Caprolactam Derivatives, Bull. Chem. Soc. Jpn. 31 (1958) 249–252.

[111] R. Puffr, J. Šebenda, Anionic polymerization of caprolactam—XLIV: Polymerization in the presence of complex-forming metal cations, Eur. Polym. J. 8 (1972) 1037–1044.

[112] K. Udipi, R.S. Davé, R.L. Kruse, L.R. Stebbins, Polyamides from lactams via anionic ring-opening polymerization: 1. Chemistry and some recent findings, Polymer (Guildf). 38 (1997) 927–938.

[113] H.K. Reimschuessel, K.C. Frisch, Ring Opening Polymerization, NY Marcel Dekker. (1969).

[114] H.K. Reimschuessel, Nylon 6. Chemistry and mechanisms, J. Polym. Sci. Macromol. Rev. 12 (1977) 65–139.

[115] N. Mougin, C.A. Veith, R.E. Cohen, Y. Gnanou, Anionic polymerization of lactams in the presence of metal dialkoxyaluminum hydrides: presentation of a new mechanism, Macromolecules. 25 (1992) 2004–2016.

[116] T. Saegusa, E. Goethals, Ring-opening polymerization, ACS Publications, 1977.

[117] J. Zimmerman, Polyamides, Wiley-Interscience, Encycl. Polym. Sci. Eng. Second Ed. 11 (1988) 315–381.

[118] E.W. Pietrusza, Anionic Polymerization of Lactams with Symmetrical Triazine as Cocatalyst, (1969).

[119] J. Kříž, J. Stehlíček, J. Dybal, J. Hauer, P. Schmidt, Study of the propagation centre in the anionic polymerization of lactams, 1. Spectroscopic and theoretical study of the activated monomer in dimethyl sulfoxide, Macromol. Chem. Phys. 197 (1996) 467–482.

[120] J. Kříž, J. Stehlíček, J. Dybal, J. Hauer, Study of the propagation centre in the anionic polymerization of lactams, 2. Model study of the interaction between an activated monomer and N-acyllactam in dimethyl sulfoxide, Macromol. Chem. Phys. 197 (1996) 483–495.

[121] C. Jia, P. Chen, W. Liu, B. Li, Q. Wang, Surface treatment of aramid fiber by air dielectric barrier discharge plasma at atmospheric pressure, Appl. Surf. Sci. 257 (2011) 4165–4170.

[122] M. Duhovic, P. Maitrot, S. Fakirov, Polyamide 66 polymorphic single polymer composites, Open Macromol. J. 3 (2009) 37–40.

[123] P.J. Hine, I.M. Ward, N.D. Jordan, R. Olley, D.C. Bassett, The hot compaction behaviour of woven oriented polypropylene fibres and tapes. I. Mechanical properties, Polymer (Guildf). 44 (2003) 1117–1131.

[124] Y. Gong, G. Yang, Manufacturing and physical properties of all-polyamide composites, J. Mater. Sci. 44 (2009) 4639–4644.

[125] N. Vasileva Dencheva, D. Manso Vale, Z. Zlatev Denchev, Dually reinforced all-polyamide laminate composites via microencapsulation strategy, Polym. Eng. Sci. 57 (2017) 806–820.

[126] S.D. Tohidi, A.M. Rocha, N.V. Dencheva, Z. Denchev, Single polymer laminate composites by compression molding of knitted textiles and microparticles of polyamide 6: Preparation and structure-properties relationship, Compos. Part A Appl. Sci. Manuf. 109 (2018) 171–183.

[127] F. Oliveira, N. Dencheva, P. Martins, S. Lanceros-Méndez, Z. Denchev, A new approach for preparation of metal-containing polyamide/carbon textile laminate composites with tunable electrical conductivity, J. Mater. Sci. 53 (2018) 11444–11459.

[128] O.A. Khondker, T. Fukui, M. Inoda, A. Nakai, H. Hamada, Fabrication and mechanical properties of aramid/nylon plain knitted composites, Compos. Part A Appl. Sci. Manuf. 35 (2004) 1195–1205.

[129] E. Kim, S. An, H. Kim, Graft copolymerization of ∈-Caprolactam onto Kevlar-49 fiber surface and properties of grafted Kevlar fiber reinforced composite, J. Appl. Polym. Sci. 65 (1997) 99–107.

[130] S.N. Kukureka, C.J. Hooke, M. Rao, P. Liao, Y.K. Chen, The effect of fibre reinforcement on the friction and wear of polyamide 66 under dry rolling–sliding contact, Tribol. Int. 32 (1999) 107–116.

[131]   D.B. Eagles, B.F. Blumentritt, S.L. Cooper, Interfacial properties of kevlar-49 fiber-reinforced thermoplastics, J. Appl. Polym. Sci. 20 (1976) 435–448.

[132]   D.H. Gordon, S.N. Kukureka, The wear and friction of polyamide 46 and polyamide 46/aramid-fibre composites in sliding–rolling contact, Wear. 267 (2009) 669–678.

[133]   A. Bolvari, S. Glenn, R. Janssen, C. Ellis, Wear and friction of aramid fiber and polytetrafluoroethylene filled composites, Wear. 203 (1997) 697–702.

[134]   N. Klein, G. Marom, E. Wachtel, Microstructure of nylon 66 transcrystalline layers in carbon and aramid fibre reinforced composites, Polymer (Guildf). 37 (1996) 5493–5498.

[135]   Z. Yu, A. Ait-Kadi, J. Brisson, Nylon/Kevlar composites. I: mechanical properties, Polym. Eng. Sci. 31 (1991) 1222–1227.

[136]   H. Nuriel, N. Klein, G. Marom, The effect of the transcrystalline layer on the mechanical properties of composite materials in the fibre direction, Compos. Sci. Technol. 59 (1999) 1685–1690.

[137]   H. Nuriel, N. Kozlovich, Y. Feldman, G. Marom, The dielectric properties of nylon 6, 6/aramid fibre microcomposites in the presence of transcrystallinity, Compos. Part A Appl. Sci. Manuf. 31 (2000) 69–78.

[138]   N. Klein, D. Selivansky, G. Marom, The effects of a nucleating agent and of fibers on the crystallization of nylon 66 matrices, Polym. Compos. 16 (1995) 189–197.

[139]   H.F. Shi, Y. Zhao, X. Dong, C.C. He, D.J. Wang, D.F. Xu, Transcrystalline morphology of nylon 6 on the surface of aramid fibers, Polym. Int. 53 (2004) 1672–1676.

[140]   A. Feldman, M.F. Gonzalez, G. Marom, Transcrystallinity in surface modified aramid fiber reinforced nylon 66 composites, Macromol. Mater. Eng. 288 (2003) 861–866.

[141]   A.Y. Feldman, E. Wachtel, N.E. Zafeiropoulos, K. Schneider, M. Stamm, R.J. Davies, A. Weinberg, G. Marom, In situ synchrotron microbeam analysis of the stiffness of transcrystallinity in aramid fiber reinforced nylon 66 composites, Compos. Sci. Technol. 66 (2006) 2009–2015.

[142]   J.C. Chen, C.M. Wu, F.C. Pu, C.H. Chiu, Fabrication and mechanical properties of self-reinforced poly (ethylene terephthalate) composites, Structure. 30 (2011) 228–237.

[143]   E.G. Chatzi, J.L. Koenig, Morphology and structure of Kevlar fibers: a review, Polym. Plast. Technol. Eng. 26 (1987) 229–270.

[144]   E.G. Chatzi, S.L. Tidrick, J.L. Koenig, Characterization of surface hydrolysis of Kevlar-49 fibres by diffuse reflectance, Am. Chem. Soc., Div. Polym. Chem., Polym. Prep. 28 (1987) 13–14.

[145]   Z. Yu, A. Ait-Kadi, J. Brisson, Nylon/Kevlar composites. II: Investigation of interfaces, Polym. Eng. Sci. 31 (1991) 1228–1232.

[146] M. Raimo, On the origin of transcrystalline morphology in polymers and their composites: re-evaluation of different views, Mater. Today Commun. 3 (2015) 137–140.

[147] R.A. Naik, Failure analysis of woven and braided fabric reinforced composites, J. Compos. Mater. 29 (1995) 2334–2363.

[148] S. Ramakrishna, Characterization and modeling of the tensile properties of plain weft-knit fabric-reinforced composites, Compos. Sci. Technol. 57 (1997) 1–22.

[149] J. Richard, L. Richard, Warp knitted fabric, (1973).

[150] S. Mukherjee, Weft-Knitted Fabrics, Text. Cloth. Des. Technol. (2017).

[151] S.D. Tohidi, A.A.A. Jeddi, H. Nosrati, Analyzing of the Woven Fabric Geometry on the Bending Rigidity Properties, Int. J. Text. Sci. 2 (2013) 73–80.

[152] S. Ramakrishna, Energy absorption characteristics of knitted fabric reinforced epoxy composite tubes, J. Reinf. Plast. Compos. 14 (1995) 1121–1141.

[153] D. Philips, I. Verpoest, J. Van Raemdonck, Sandwich panels produced from 3D-knitted structures, in: Proc. 40th Int. SAMPE Symp. Exhib., 1995: pp. 957–965.

[154] I. Verpoest, J. Dendauw, Mechanical properties of knitted glass fibre/epoxy resin laminates, in: Proc. 37th Int. SAMPE Symp. Exhib., 1992: pp. 369–377.

[155] B. Gommers, T.K. Wang, A. De Heusch, I. Verpoest, Mechanical properties of warp knitted fabric reinforced composites, in: Proc. 40th Int. SAMPE Symp. Exhib., 1995: pp. 966–976.

[156] S. Ramakrishna, H. Hamada, R.W. Rydin, T.W. Chou, Impact damage resistance of knitted glass fiber fabric reinforced polypropylene composites, Sci. Eng. Compos. Mater. 4 (1995) 61–72.

[157] S. Ramakrishna, D. Hull, Energy absorption capability of epoxy composite tubes with knitted carbon fibre fabric reinforcement, Compos. Sci. Technol. 49 (1993) 349–356.

[158] C.D. Rudd, M.J. Owen, V. Middleton, Mechanical properties of weft knit glass fibre/polyester laminates, Compos. Sci. Technol. 39 (1990) 261–277.

[159] S. Chou, H.-C. Chen, C.-C. Lai, The fatigue properties of weft-knit fabric reinforced epoxy resin composites, Compos. Sci. Technol. 45 (1992) 283–291.

[160] S. Ramakrishna, D. Hull, Tensile behaviour of knitted carbon-fibre-fabric/epoxy laminates—Part I: Experimental, Compos. Sci. Technol. 50 (1994) 237–247.

[161] S. Ramakrishna, Bolted joints of knitted fabric reinforced composites., in: Proc. 7th Japan-US Conf. Kyoto, 1995: pp. 633–640.

[162] S. Ramakrishna, H. Hamada, N.K. Cuong, Fabrication of knitted glass fibre fabric reinforced

thermoplastic composite laminates, Adv. Compos. Lett.(UK). 3 (1994) 189–192.

[163]   C.Z.P. Júnior, L.H. De Carvalho, V.M. Fonseca, S.N. Monteiro, J.R.M. d'Almeida, Analysis of the tensile strength of polyester/hybrid ramie–cotton fabric composites, Polym. Test. 23 (2004) 131–135.

[164]   T. Osada, A. Nakai, H. Hamada, Initial fracture behavior of satin woven fabric composites, Compos. Struct. 61 (2003) 333–339.

[165]   F. Gao, L. Boniface, S.L. Ogin, P.A. Smith, R.P. Greaves, Damage accumulation in woven-fabric CFRP laminates under tensile loading: Part 1. Observations of damage accumulation, Compos. Sci. Technol. 59 (1999) 123–136.

[166]   F. Gao, L. Boniface, Sl. Ogin, P.A. Smith, R.P. Greaves, Damage accumulation in woven-fabric CFRP laminates under tensile loading: 2. Modelling the effect of damage on macro-mechanical properties, Compos. Sci. Technol. 59 (1999) 137–145.

[167]   O. Asi, Effect of different woven linear densities on the bearing strength behaviour of glass fiber reinforced epoxy composites pinned joints, Compos. Struct. 90 (2009) 43–52.

[168]   S.V. Lomov, D.S. Ivanov, T.C. Truong, I. Verpoest, F. Baudry, K. Vanden Bosche, H. Xie, Experimental methodology of study of damage initiation and development in textile composites in uniaxial tensile test, Compos. Sci. Technol. 68 (2008) 2340–2349.

[169]   S.D. Pandita, G. Huysmans, M. Wevers, I. Verpoest, Tensile fatigue behaviour of glass plain-weave fabric composites in on-and off-axis directions, Compos. Part A Appl. Sci. Manuf. 32 (2001) 1533–1539.

[170]   K.H. Leong, M. Nguyen, I. Herszberg, The effects of deforming knitted glass fabrics on the basic composite mechanical properties, J. Mater. Sci. 34 (1999) 2377–2387.

[171]   O.A. Khondker, I. Herszberg, K.H. Leong, An investigation of the structure-property relationship of knitted composites, J. Compos. Mater. 35 (2001) 489–508.

[172]   O.A. Khondker, K.H. Leong, I. Herszberg, H. Hamada, Impact and compression-after-impact performance of weft-knitted glass textile composites, Compos. Part A Appl. Sci. Manuf. 36 (2005) 638–648.

[173]   T.B. Bini, S. Ramakrishna, Z.M. Huang, C.T. Lim, Structure–tensile property relationship of knitted fabric composites, Polym. Compos. 22 (2001) 11–21.

[174]   T. Alpyildiz, B.M. Icten, R. Karakuzu, A. Kurbak, The effect of tuck stitches on the mechanical performance of knitted fabric reinforced composites, Compos. Struct. 89 (2009) 391–398.

[175]   O. Kayacan, A. Kurbak, Basic studies for modeling complex weft knitted fabric structures part IV: Geometrical modeling of miss stitches, Text. Res. J. 78 (2008) 659–663.

[176]   A. Kurbak, O. Kayacan, Basic studies for modeling complex weft knitted fabric structures part V: Geometrical modeling of tuck stitches, Text. Res. J. 78 (2008) 577–582.

223

[177]   I. Putnoki, E. Moos, J. Karger-Kocsis, Mechanical performance of stretched knitted fabric glass fibre reinforced poly (ethylene terephthalate) composites produced from commingled yarn, Plast. Rubber Compos. (2013) 40–46.

[178]   J. Karger-Kocsis, T. Czigany, Interfacial effects on the dynamic mechanical behavior of weft-knitted glass fiber fabric-reinforced polypropylene composites produced of commingled yarns. Tensile and flexural response, Appl. Compos. Mater. 4 (1997) 209–218.

[179]   T.G. Kannan, C.M. Wu, K.B. Cheng, Effect of different knitted structure on the mechanical properties and damage behavior of Flax/PLA (Poly Lactic acid) double covered uncommingled yarn composites, Compos. Part B Eng. 43 (2012) 2836–2842.

[180]   Z.-M. Huang, Progressive flexural failure analysis of laminated composites with knitted fabric reinforcement, Mech. Mater. 36 (2004) 239–260.

[181]   S.D. Pandita, D. Falconet, I. Verpoest, Impact properties of weft knitted fabric reinforced composites, Compos. Sci. Technol. 62 (2002) 1113–1123.

[182]   J. Karger-Kocsis, Q. Yuan, J. Mayer, E. Wintermantel, Transverse impact behavior of knitted carbon-fiber fabric-reinforced thermoplastic composite sheets, J. Thermoplast. Compos. Mater. 10 (1997) 163–172.

[183]   A. Aktaş, M. Tercan, M. Aktaş, F. Turan, Investigation of knitting architecture on the impact behavior of glass/epoxy composites, Compos. Part B Eng. 46 (2013) 81–90.

[184]   M. Todo, K. Takahashi, P. Béguelin, H.H. Kausch, Strain-rate dependence of the tensile fracture behaviour of woven-cloth reinforced polyamide composites, Compos. Sci. Technol. 60 (2000) 763–771.

[185]   C. Brêda, N. Dencheva, S. Lanceros-Méndez, Z. Denchev, Preparation and properties of metal-containing polyamide hybrid composites via reactive microencapsulation, J. Mater. Sci. 51 (2016) 10534–10554.

[186]   F. Dan, C. Vasiliu-Oprea, Anionic polymerization of caprolactam in organic media. Morphological aspects, Colloid Polym. Sci. 276 (1998) 483–495.

[187]   C.A. Veith, R.E. Cohen, Synthesis of poly (dimethylsiloxane)-nylon-6 diblock copolymers, in: Makromol. Chemie. Macromol. Symp., Wiley Online Library, 1991: pp. 241–258.

[188]   F. Oliveira, N. Dencheva, P. Martins, S. Lanceros-Méndez, Z. Denchev, Reactive microencapsulation of carbon allotropes in polyamide shell-core structures and their transformation in hybrid composites with tailored electrical properties, EXPRESS Polym. Lett. 10 (2016) 160–175.

[189]   M.A. Rahman, L.A. Renna, D. Venkataraman, P. Desbois, A.J. Lesser, High crystalline, porous polyamide 6 by anionic polymerization, Polymer (Guildf). 138 (2018) 8–16.

[190]   A.B. Strong, Fundamentals of composites manufacturing: materials, methods and applications, Society of Manufacturing Engineers, 2008.

[191] T.S. Lundström, S. Toll, J.M. Håkanson, Measurement of the permeability tensor of compressed fibre beds, Transp. Porous Media. 47 (2002) 363–380.

[192] M. Matusiak, Investigation of the thermal insulation properties of multilayer textiles, Fibres Text. East. Eur. 14 (2006) 98–102.

[193] I. Frydrych, G. Dziworska, J. Bilska, Comparative analysis of the thermal insulation properties of fabrics made of natural and man-made cellulose fibres, Fibres Text. East. Eur. 10 (2002) 40–44.

[194] M. Yoneda, S. Kawabata, A theoretical consideration on the objective measurement of warm/cool feeling, Text. Mach. Soc. Japan. (1982) 393–406.

[195] G. Rusu, K. Ueda, E. Rusu, M. Rusu, Polyamides from lactams by centrifugal molding via anionic ring-opening polymerization, Polymer (Guildf). 42 (2001) 5669–5678.

[196] M.N. Bureau, J. Denault, K.C. Cole, G.D. Enright, The role of crystallinity and reinforcement in the mechanical behavior of polyamide-6/clay nanocomposites, Polym. Eng. Sci. 42 (2002) 1897–1906.

[197] Y.P. Khanna, W.P. Kuhn, Measurement of crystalline index in nylons by DSC: complexities and recommendations, J. Polym. Sci. Part B Polym. Phys. 35 (1997) 2219–2231.

[198] N. Dencheva, T. Nunes, M.J. Oliveira, Z. Denchev, Microfibrillar composites based on polyamide/polyethylene blends. 1. Structure investigations in oriented and isotropic polyamide 6, Polymer (Guildf). 46 (2005) 887–901.

[199] F.T. Peirce, 26—The "handle" of cloth as a measurable quantity, J. Text. Inst. Trans. 21 (1930) 377–416.

[200] A. Kurbak, Plain knitted fabric dimensions (Part II), Text. Asia. 78 (1998) 36–44.

[201] A. Kurbak, G. Amreeva, Creation of a geometrical model for Milano rib fabric, Text. Res. J. 76 (2006) 847–852.

[202] A. Kurbak, Geometrical models for balanced Rib knitted fabrics part I: Conventionally knitted 1× 1 Rib fabrics, Text. Res. J. 79 (2009) 418–435.

[203] A. Kurbak, Some Effects of Substituting a Presser-foot for Take-down Tension in Weft Knitting, 1982.

[204] A. Kurbak, A. Yagci, An Investigation Upon the Dimensional Properties of Various Rib Knitted Fabrics, Tekst. ve Tek. 4 (1988) 40–71.

[205] L.A. De Godoy Oriani, A.L. Simal, Structure of heat-treated nylon 6 fibers. I. Application of the arrhenius equation, J. Appl. Polym. Sci. 46 (1992) 1973–1985.

[206] N.S. Murthy, H. Minor, R.A. Latif, Effect of annealing on the structure and morphology of nylon 6 fibers, J. Macromol. Sci. Part B Phys. 26 (1987) 427–446.

[207]   V.B. Gupta, Heat setting, J. Appl. Polym. Sci. 83 (2002) 586–609.

[208]   K.P. Menard, Dynamic mechanical analysis: a practical introduction, CRC press, 2008.

[209]   N. Dencheva, Z. Denchev, M.J. Oliveira, S.S. Funari, Relationship between crystalline structure and mechanical behavior in isotropic and oriented polyamide 6, J. Appl. Polym. Sci. 103 (2007) 2242–2252.

[210]   M. Duhovic, D. Bhattacharyya, Simulating the deformation mechanisms of knitted fabric composites, Compos. Part A Appl. Sci. Manuf. 37 (2006) 1897–1915.

[211]   N.E. Dowling, Mechanical behavior of materials, Pearson, 2012.

[212]   O. Olabisi, K. Adewale, Handbook of thermoplastics, CRC press, 2016.

[213]   N.S. Murthy, S.A. Curran, S.M. Aharoni, H. Minor, Premelting crystalline relaxations and phase transitions in nylon 6 and 6, 6, Macromolecules. 24 (1991) 3215–3220.

[214]   D.J. Skrovanek, S.E. Howe, P.C. Painter, M.M. Coleman, Hydrogen bonding in polymers: infrared temperature studies of an amorphous polyamide, Macromolecules. 18 (1985) 1676–1683.

[215]   D.R. Salem, R.A.F. Moore, H. Weigmann, Macromolecular order in spin-oriented nylon 6 (polycaproamide) fibers, J. Polym. Sci. Part B Polym. Phys. 25 (1987) 567–589.

[216]   A.S. Radhakrishna, M.E. Parham, R.M. Riggs, G.M. Loudon, New method for direct conversion of amides to amines, J. Org. Chem. 44 (1979) 1746–1747.

[217]   Y. Liu, L. Cui, F. Guan, Y. Gao, N.E. Hedin, L. Zhu, H. Fong, Crystalline morphology and polymorphic phase transitions in electrospun nylon-6 nanofibers, Macromolecules. 40 (2007) 6283–6290.

[218]   J.B. Austin, A relation between the molecular weights and melting points of organic compounds, J. Am. Chem. Soc. 52 (1930) 1049–1053.

[219]   H. Sekiguchi, B. Coutin, Polymerizability and related problems in the anionic polymerization of lactams, J. Polym. Sci. Polym. Chem. Ed. 11 (1973) 1601–1614.

[220]   Y. Li, W.A. Goddard, Nylon 6 crystal structures, folds, and lamellae from theory, Macromolecules. 35 (2002) 8440–8455.

[221]   N. Dencheva, T. Nunes, M.J. Oliveira, Z. Denchev, Microfibrillar composites based on polyamide/polyethylene blends. 1. Structure investigations in oriented and isotropic polyamide 6, Polymer (Guildf). 46 (2005) 887–901.

[222]   I. Abu-Isa, α-γtransition in nylon 6, J. Polym. Sci. Part A-1 Polym. Chem. 9 (1971) 199–216.

[223]   K. Miyasaka, K. Makishima, Transition of nylon 6 γphase crystals by stretching in the chain direction, J. Polym. Sci. Part A-1 Polym. Chem. 5 (1967) 3017–3027.

[224]   N.S. Murthy, Metastable crystalline phases in nylon 6, Polym. Commun. 32 (1991) 301–305.

[225]   F. Auriemma, V. Petraccone, L. Parravicini, P. Corradini, Mesomorphic form (β of nylon 6, Macromolecules. 30 (1997) 7554–7559.

[226]   D.R. Holmes, C.W. Bunn, D.J. Smith, The crystal structure of polycaproamide: Nylon 6, J. Polym. Sci. 17 (1955) 159–177.

[227]   K. Miyasaka, K. Ishikawa, Effects of temperature and water on the γ–αcrystalline transition of nylon 6 caused by stretching in the chain direction, J. Polym. Sci. Part B Polym. Phys. 6 (1968) 1317–1329.

[228]   H. Arimoto, α-γTransition of nylon 6, J. Polym. Sci. Part A Gen. Pap. 2 (1964) 2283–2295.

[229]   R. Androsch, M. Stolp, H. Radusch, Crystallization of amorphous polyamides from the glassy state, Acta Polym. 47 (1996) 99–104.

[230]   N.S. Murthy, S.M. Aharoni, A.B. Szollosi, Stability of the γform and the development of the αform in nylon 6, J. Polym. Sci. Polym. Phys. Ed. 23 (1985) 2549–2565.

[231]   J.P. Parker, P.H. Lindenmeyer, On the crystal structure of Nylon 6, J. Appl. Polym. Sci. 21 (1977) 821–837.

[232]   J.M. Samon, J.M. Schultz, B.S. Hsiao, Study of the cold drawing of nylon 6 fiber by in-situ simultaneous small-and wide-angle X-ray scattering techniques, Polymer (Guildf). 41 (2000) 2169–2182.

[233]   E.E. Vinken, Polyamides: Hydrogen bonding, the Brill transition, and superheated water, (2008).

[234]   F.T. Peirce, 5—The geometry of cloth structure, J. Text. Inst. Trans. 28 (1937) 45–96.

[235]   A. Kemp, An extension of Peirce's cloth geometry to the treatment of non-circular threads, (1958).

[236]   J.W.S. Hearle, W.J. Shanahan, An energy method for calculations in fabric mechanics part I: Principles of the method, J. Text. Inst. 69 (1978) 81–91.

[237]   J.L. Hu, J.G. Teng, Computational fabric mechanics: Present status and future trends, Finite Elem. Anal. Des. 21 (1996) 225–237.

[238]   G.A. V Leaf, R.D. Anandjiwala, A generalized model of plain woven fabric, Text. Res. J. 55 (1985) 92–99.

[239]   J. Hu, Structure and mechanics of woven fabrics, Elsevier, 2004.

[240]   S. De Jong, R. Postle, 39—an Energy Analysis of Woven-Fabric Mechanics by Means of Optimal-Control Theory Part I: Tensile Properties, J. Text. Inst. 68 (1977) 350–361.

[241]   T. Ishikawa, T.-W. Chou, Stiffness and strength behaviour of woven fabric composites, J. Mater. Sci. 17 (1982) 3211–3220.

[242]   T. Ishikawa, T.-W. Chou, Nonlinear behavior of woven fabric composites, J. Compos. Mater. 17 (1983) 399–413.

[243]   A.A. Shahpurwala, P. Schwartz, Modeling woven fabric tensile strength using statistical bundle theory,

Text. Res. J. 59 (1989) 26–32.

[244]   N. Pan, Analysis of woven fabric strengths: prediction of fabric strength under uniaxial and biaxial extensions, Compos. Sci. Technol. 56 (1996) 311–327.

[245]   N. Pan, M.-Y. Yoon, Behavior of yarn pullout from woven fabrics: theoretical and experimental, Text. Res. J. 63 (1993) 629–637.

[246]   T. Fujii, S. Amijima, K. Okubo, Microscopic fatigue processes in a plain-weave glass-fibre composite, Compos. Sci. Technol. 49 (1993) 327–333.

[247]   J.E. Bailey, P.T. Curtis, A. Parvizi, On the transverse cracking and longitudinal splitting behaviour of glass and carbon fibre reinforced epoxy cross ply laminates and the effect of Poisson and thermally generated strain, in: Proc. R. Soc. London A Math. Phys. Eng. Sci., The Royal Society, 1979: pp. 599–623.

[248]   J.L. Hutchison, N.S. Murthy, E.T. Samulski, Deuterium NMR studies of water in oriented nylon 6 fibers, Macromolecules. 29 (1996) 5551–5557.

[249]   N.S. Murthy, Hydrogen bonding, mobility, and structural transitions in aliphatic polyamides, J. Polym. Sci. Part B Polym. Phys. 44 (2006) 1763–1782.

[250]   I. Sandeman, A. Keller, Crystallinity studies of polyamides by infrared, specific volume and X-ray methods, J. Polym. Sci. Part A Polym. Chem. 19 (1956) 401–435.

[251]   N.S. Murthy, R.G. Bray, S.T. Correale, R.A.F. Moore, Drawing and annealing of nylon-6 fibres: studies of crystal growth, orientation of amorphous and crystalline domains and their influence on properties, Polymer (Guildf). 36 (1995) 3863–3873.

[252]   H. Quan, Z.-M. Li, M.-B. Yang, R. Huang, On transcrystallinity in semi-crystalline polymer composites, Compos. Sci. Technol. 65 (2005) 999–1021.

[253]   N. Dencheva, A. Stribeck, Z. Denchev, Nanostructure development in multicomponent polymer systems characterized by synchrotron X-ray scattering, Eur. Polym. J. 81 (2016) 447–469.

[254]   J. Chiu, Thermogravimetry for chemical analysis of polymers, Carl Hanser Verlag, Appl. Polym. Anal. Charact. Recent Dev. Tech. Instrumentation, Probl. Solving,. (1987) 175–215.